



**Nanoparticles for Plasma Immunoglobulin  
Immunosensor for Alzheimer's disease**

**A thesis submitted by**

**Orlando Ketebu**

**For the Degree of Doctor of Philosophy**

**School of Chemical Engineering and Advance Materials  
Newcastle University**

**May 2014**

## Abstract

Nanoparticles are known for their unique and exceptional properties and are widely used in biomedical, bioelectronics, pharmacology and environmental fields. This thesis looks at the synthesis of iron oxide nanoparticles ( $\text{Fe}_3\text{O}_4$  and  $\gamma\text{-Fe}_2\text{O}_3$ ), iron oxide core-gold shell nanoparticles ( $\gamma\text{-Fe}_2\text{O}_3\text{-Au}$ ), their characterization and application in the development of plasma immunoglobulin immunosensor electrode as a biomarker for Alzheimer's disease (AD). Iron oxide coated with gold shell was used in the development of the immunosensor electrode in order to improve on the sensitivity, low plasma immunoglobulin concentration detection, stability and reproducibility of the immunosensor electrode for AD monitoring and detection. This is achieved by taking advantage of the increased surface area obtained from combining iron oxide core and gold shell nanoparticles for biomolecules binding, their biocompatibility that allows biomolecules to regenerate and the electron conducting properties of gold nanoparticles.

Iron oxide nanoparticles in this thesis were synthesized through oxidative alkaline hydrolysis of ferrous salt and the synthesis parameters altered to see how it affects the nanoparticles properties, structure, purity and size. The synthesized iron oxide nanoparticles ( $\text{Fe}_3\text{O}_4$ ) showed changes in shape and size and also the formation of side products or impurities mixed with  $\text{Fe}_3\text{O}_4$  nanoparticles such as akaganeite ( $\beta\text{-FeOOH}$ ) nano-rods,  $\alpha\text{-Fe}_2\text{O}_3$  (hematite) and lepidocrocite ( $\gamma\text{-FeOOH}$ ). Gold shell nanoparticles average size 24 nm was formed as a shell on  $\gamma\text{-Fe}_2\text{O}_3$  nanoparticles (50 nm) through the iterative reduction of chloroauric acid with hydroxylamine. The iron oxide core-gold shell nanoparticles with average particles size 74 nm was used in the development of the immunosensor electrode. The immunosensor electrode and nanoparticles were characterized using physical and electrochemical techniques.

The immunosensor electrode for the direct detection of plasma immunoglobulin as biomarker for AD is a novel work since no work has been carried out on direct electrochemical detection of plasma immunoglobulin for AD. The electrode was developed with a view to addressing the problems currently facing present Alzheimer's disease biomarkers such as being too expensive, technically challenging, rarely

available and inability to control repeated sampling for regular monitoring of AD. In developing the immunosensor electrode, depleted plasma immunoglobulin was used as the biomarker and polyclonal rabbit Anti-human IgA, IgG, IgM as the antibody specific for plasma conjugation. Gold electrode and  $\gamma$ -Fe<sub>2</sub>O<sub>3</sub>-Au nanoparticles were used as the immobilizing substrate for the immunosensor electrode. The immunosensor electrodes showed good response, sensitivity and reproducibility in differentiating plasma immunoglobulin from AD patients and control subjects up to the 8<sup>th</sup> (3.91 ppm) and 5<sup>th</sup> plasma concentration (31.25 ppm) for the modified gold electrode and  $\gamma$ -Fe<sub>2</sub>O<sub>3</sub>-Au electrode respectively. The electrodes had a better linear responds to plasma immunoglobulin at high concentration compared to enzyme linked immunosorbent assay (ELISA) technique.

## **Dedication**

This dissertation is dedicated to Jehovah God for his mercies and giving me the strength to carry on this research work and also in memory of my mother Mrs Stella Ketebu who I lost while studying. Mama I missed you so much and I will still love you for a thousand more years.

## **Acknowledgement**

I would like to thank the organization and people who made this dissertation possible. Firstly I want to thank the Petroleum Technology Development Fund (PTDF) in Nigeria for awarding me scholarship to pursue my PhD studies. I want to thank my supervisors Dr Eileen Yu and Dr Lidija Siller for their support specifically Dr Eileen Yu for her constant help and supervision in making this dissertation possible. I also want to thank Dr Elizabeta Mukaetova-Ladinska for her help and assistance and also providing the depleted plasma immunoglobulin used in this thesis work.

## Contents

<b>Abstract</b>	i
<b>Dedication</b>	iii
Acknowledgement	iv
Content	v
Figures	xi
Tables	xix
Nomenclature	xx
<b>Chapter 1- Introduction</b>	1
1.1 Motivation and aims of research	1
1.2 Nanomaterial overview	3
1.3 Nanoparticles	4
1.4 Iron oxide nanoparticles	4
1.5 Magnetic and physical properties	6
1.6 Synthesis of iron oxide magnetic nanoparticles	10
1.6.1 Co-precipitation	10
1.6.2 Thermal decomposition	10
1.6.3 Microemulsion	11
1.6.4 Hydrothermal synthesis	11
1.6.5 Sol-gel Method	11
1.6.6 Flow injection	12
1.6.7 Sonochemical	12
1.7 Applications of iron oxide nanoparticles	12
1.7.1 Magnetic resonance imaging (MRI)	13
1.7.2 Hyperthermia therapy	13
1.7.3 Magnetic recording media	13

1.7.4 Drug delivery	14
1.7.5 Ferrofluids	14
1.7.6 Biosensor application	14
1.8 Gold nanoparticles and its properties	15
1.9 Gold nanoparticles synthesis	16
1.10 Colloid gold technique	16
1.10.1 Turkevish technique	16
1.10.2 Brust Method	17
1.10.3 Perrault Method	17
1.10.4 Martin method	17
1.11 Electrodeposition	18
1.12 Gold nanoparticles functionalization	18
1.13 Biosensors	19
1.14 Immunosensors and immunoassay	20
1.15 Electrochemical immunosensors	22
1.15.1 Potentiometric immunosensors	23
1.15.2 Amperometric immunosensors	23
1.15.3 Conductimetric/capacitive immunosensors	24
1.16 Piezoelectric or acoustic immunosensor	24
1.17 Calorimetric immunosensors	25
1.18 Optical immunosensors	25
1.19 Antibodies	25

1.20 Antibody-Antigen binding	27
1.21 Immobilization of antibody-antigen on substrate	27
1.21.1 Physical immobilization method	27
1.21.2 Chemical immobilization	28
1.22 Research question and hypothesis	28
1.23 Thesis organization	29
<b>Chapter 2 - Physiochemical analytical techniques</b>	31
2.1 Physical characterization techniques	31
2.1.1 X-ray diffraction	31
2.1.2 X-ray photoelectron spectroscopy (XPS)	34
2.1.3 Scanning electron microscopy (SEM)	36
2.1.4 Transmission electron microscopy (TEM)	37
2.1.5 UV-VIS Spectroscopy	39
2.2 Electrochemical techniques	41
2.2.1 Cyclic voltammetry	41
2.2.2 Electrochemical impedance spectroscopy (EIS)	44
<b>Chapter 3 - Nature of Magnetite Nanoparticles Synthesized by Direct Oxidative Alkaline Hydrolysis of Iron II sulphate by varying synthesis parameters</b>	48
3.1 Introduction	48
3.2 Aims	51
3.3 Experimental	51
3.3.1 Materials and chemicals	51

3.3.2 Synthesis of iron oxide core/polyethyleneimine nanoparticles ( $\text{Fe}_3\text{O}_4$ -PEI Nps)	51
3.3.3 Characterization of the iron oxide/PEI nanoparticles	51
3.4 Results and Discussion	52
3.4.1 Physical properties of nanoparticles synthesized by varying iron salt concentration	52
3.4.2 Physical properties of nanoparticles synthesized by varying base (NaOH) concentration	58
3.4.3 Physical properties of nanoparticles synthesized by varying revolution per minute	61
3.4.4 Physical properties of nanoparticles synthesized by varying synthesis temperature	64
Conclusion	65
<b>Chapter 4</b> - The Effect of temperature and agitation on polyethyleneimine adsorption on iron oxide magnetic nanoparticles in the synthesis of iron oxide-Au core-shell nanoparticles	67
4.1 Introduction	67
4.2 Polyethyleneimine	68
4.3 Chitosan	71
4.4 Aims	72
4.5 Experimental	72
4.5.1 Materials and chemicals	72
4.5.2 Synthesis of 50nm oxidized iron oxide nanoparticles ( $\text{Fe}_2\text{O}_3$ Nps)	72
4.5.3 Synthesis of iron oxide core/ gold seed nanoparticles ( $\gamma\text{-Fe}_2\text{O}_3\text{-Au}_{\text{seed}}$ Nps)	73
4.5.4 Synthesis of iron oxide core/gold shell nanoparticles ( $\text{Fe}_2\text{O}_3\text{-Au}_{\text{shell}}$ Nps)	73

4.5.5. Preparation of nanoparticles modified electrodes with chitosan	74
4.5.6 Synthesis of iron oxide nanoparticles ( $\text{Fe}_2\text{O}_3$ /PEI Nps)	75
4.5.7 Preparation of iron oxide-PEI ( $\text{Fe}_2\text{O}_3$ /PEI) modified electrodes	75
4.5.8 Instrumentation and characterization of the nanoparticles	76
4.6 Result and discussion	77
4.7 Physical properties of nanoparticles	77
4.7.1 Paramagnetic effect of iron III oxide ( $\gamma\text{-Fe}_2\text{O}_3$ ), iron oxide/gold shell nanoparticles ( $\gamma\text{-Fe}_2\text{O}_3\text{-Au}$ shell) and their XPS analysis	77
4.8 Electrochemical properties of the nanoparticles	84
4.9 Effect of temperature and agitation on PEI adsorption on iron oxide nanoparticles and gold shell formation	87
4.9.1. Electrochemical analysis on PEI adsorption in iron III oxide/PEI nanoparticle preparation at various heating temperatures	88
4.9.2 Effect of agitation on PEI adsorption	91
4.9.3 UV-VIS Spectroscopy analysis of $\text{Fe}_2\text{O}_3\text{-PEI/Au}$ shell nanoparticles at the different temperatures	93
4.10 Conclusions	94
<b>Chapter 5 – Plasma Ig biomarker immunosensor for Alzheimer’s disease</b>	96
5.1 Introduction	96
5.2 Plasma biomarkers	97
5.3 Aims	98
<b>5.4 Experimental</b>	99
5.4.1 Materials and chemicals	99
5.4.2 Immobilization of polyclonal rabbit Anti-human immunoglobulin and depleted plasma on Gold (Au) electrode	100

5.4.3 Immobilization of polyclonal rabbit Anti-human immunoglobulin and depleted plasma immunoglobulin on iron oxide-gold shell nanoparticles (Fe <sub>2</sub> O <sub>3</sub> -Au Nps) immobilized on Gold electrode	101
5.4.4 Conjugation of depleted plasma immunoglobulin, polyclonal rabbit Anti-human immunoglobulin and polyclonal Goat Anti-rabbit Immunoglobulin/horseradish peroxidase for ELISA detection with UV-Vis spectroscopy reader.	102
5.5 Electrochemical characterization of modified electrodes	103
5.6 Results and discussion	106
5.6.1 Immobilization of MPA, polyclonal rabbit Anti-human immunoglobulin and Marvel on gold electrode	106
5.6.2 Immobilization of MPA, polyclonal rabbit Anti-human immunoglobulin -Marvel and depleted plasma (control) on gold electrode	108
5.6.3 Immobilization of MPA, polyclonal rabbit Anti-human immunoglobulin -Marvel and depleted plasma (severe AD case) on gold electrode	113
5.6.4 ELISA detection of plasma immunoglobulin/polyclonal rabbit Anti-human Ig-polyclonal Goat Anti-rabbit Immunoglobulin/horseradish peroxidase conjugation for severe AD case	119
5.6.5 Immobilization of primary antibody/depleted plasma on Fe <sub>2</sub> O <sub>3</sub> -Au Nps/Gold electrode surface.	122
5.7 Conclusion	128
<b>Chapter 6 – Conclusion and recommendation for future work</b>	130
6.1 Recommendations for Future work	132
<b>References</b>	135
<b>Chapter 7- Appendices</b>	
7.1 List of publications	135

## Figures

Figure 1.1: Crystal structure of magnetite	5
Figure 1.2: Magnetic moment in bulk (a) reduced bulk (b) and single domain materials (c)	6
Figure 1.3: Magnetic moment in bulk (a) absence of magnetic field (b) presence of magnetic field	6
Fig.1.4: Magnetization curve showing M as a function of applied magnetic field H for (A) ferromagnetic (B) super-paramagnetic materials	9
Figure 1.5 Typical immunosensor set up with antigens and antibodies (receptor) immobilized onto solid sensor surface (transducer).	22
Figure 1.6: (A) Generalized structure of immunoglobulin (IgG) and (B) its three dimension structure	26
Figure 2.1: Typical x-ray reflection $2\theta$ and $2\theta'$ resulting from incident ray $1$ and $1'$ on a crystal sample.	32
Figure 2.2: A and B shows the component of a diffractometer and diffractometer beam path $\theta/2\theta$ mode respectively.	33
Figure 2.3: Schematic diagrams showing the major component of XPS equipment	35
Figure 2.4: Energy level diagram for x-ray photoelectron spectroscopy	35
Figure 2.5: Typical SEM equipment operation and components	37
Figure 2.6: Schematic diagrams of the TEM components	39
Figure 2.7: Schematic diagram of the component of UV-Vis spectrometer	40

Figure 2.8: Typical cyclic voltammogram curve showing the cathodic and anodic peak currents and potentials.	42
Figure 2.9: Typical cyclic voltammetry potential wave form.	43
Figure 2.10: Schematic diagram of electrochemical cell with three electrode system.	43
Figure 2.11: (A) Schematic diagram of Nyquist plot (B) Randles circuit showing $R_s$ , $C_{DL}$ , $R_{CT}$ and $Z_w$	44
Figure 3.1: Effect of excess iron II salt on $Fe_3O_4$ synthesis and paramagnetic behaviour and nature before and after magnetic separation (a) and (b) 0.025M (c) and (d) 0.2M (e) and (f) 0.3M (g) and (h) 0.5M	53
Figure 3.2: TEM images of $Fe_3O_4$ nanoparticles synthesized at different $FeSO_4$ concentration (a) 0.0035M $FeSO_4$ , (b) 0.017M $FeSO_4$ (c) 0.025M $FeSO_4$ (d) 0.035M $FeSO_4$ (e) 0.068M $FeSO_4$ (f) 0.2M $FeSO_4$	54
Figure 3.3: Size distribution of $Fe_3O_4$ nanoparticles synthesized at different $FeSO_4$ concentration (a) 0.0035M $FeSO_4$ , (b) 0.017M $FeSO_4$ (c) 0.025M $FeSO_4$ (d) 0.035M $FeSO_4$ (e) 0.068M $FeSO_4$ (f) 0.2M $FeSO_4$	55
Figure 3.4: XRD analysis of $Fe_3O_4$ synthesis by varying iron II sulphate concentration (a) 0.0035M $FeSO_4$ , (b) 0.017M $FeSO_4$ (c) 0.025M $FeSO_4$ (d) 0.035M $FeSO_4$ (e) 0.068M $FeSO_4$ (f) 0.1M (g) 0.2M $FeSO_4$	56
Figure 3.5: $Fe_3O_4$ nanoparticles XPS analysis (a) 2p core electrons (b) 1s core electrons of $O_2$	57

Figure 3.6: TEM images of $\text{Fe}_3\text{O}_4$ nanoparticles synthesized at (a) 0.005M NaOH (b) size distribution of $\text{Fe}_3\text{O}_4$ Nps at 0.005M (c) 0.01M NaOH (d) size distribution for 0.01M NaOH (e) 1M NaOH (f) 1M NaOH size distribution (g) 2M NaOH (h) 2M size distribution.	59
Figure3.7: Images of $\text{Fe}_3\text{O}_4$ nanoparticles synthesized with (A) 0.005M, (B) 0.01M and (C) 1M NaOH respectively	59
Figure3.8: XRD analysis of $\text{Fe}_3\text{O}_4$ synthesis by varying hydroxyl ion concentration (a) 0.005M (b) 0.01M (c) 0.1M (d) 1M and (e) 2M	60
Figure 3.9: XRD analysis of $\text{Fe}_3\text{O}_4$ synthesis at (a) 200, (b) 500 and (c) 1500 revolution per minute	62
Figure 3.10: XPS analysis $\text{Fe}_3\text{O}_4$ synthesis with and without revolution per minute	63
Figure 3.11: XRD analysis $\text{Fe}_3\text{O}_4$ synthesized by varying synthesis temperatures (a) 50°C, (b) 90°C and (c) 150°C	65
Figure 4.1: Chemical structure of linear and branched PEI	69
Figure 4.2: Structures of chitin and chitosan	71
Figure 4.3: Schematic diagram for the synthesis of $\text{Fe}_2\text{O}_3$ -Au shell nanoparticles	74
Figure 4.4 (a) $\text{Fe}_2\text{O}_3$ nanoparticles stabilized in TMAOH before and after magnetic separation (b) $\text{Fe}_2\text{O}_3$ –Au shell before and after magnetic separation	77
Figure 4.5 $\text{Fe}_2\text{O}_3$ nanoparticles XPS analysis (a) 2p core electrons (b) 1s core electrons of $\text{O}_2$	78
Figure 4.6 XPS analysis of Au shell on $\text{Fe}_2\text{O}_3$ nanoparticles (a) 4f core electrons of Au (b) 1s core electrons of $\text{O}_2$	79

Figure 4.7 UV-Vis spectra for Fe <sub>2</sub> O <sub>3</sub> , Au seed, Fe <sub>2</sub> O <sub>3</sub> -Au 5 <sup>th</sup> iteration and Fe <sub>2</sub> O <sub>3</sub> -Au 10 <sup>th</sup> iteration	80
Figure 4.8 UV-Vis spectra for Fe <sub>2</sub> O <sub>3</sub> /Au shell formation showing the 5 iteration step	81
Figure 4.9 (a) Fe <sub>2</sub> O <sub>3</sub> –Au shell 5 iterations (b) Fe <sub>2</sub> O <sub>3</sub> –Au shell 10 iteration (c) TEM of 10 iteration	82
Figure 4.10 XRD analysis of (a) γ-Fe <sub>2</sub> O <sub>3</sub> (b) Fe <sub>2</sub> O <sub>3</sub> -Au shell nanoparticles at 5 iterations (c) Fe <sub>2</sub> O <sub>3</sub> -Au shell nanoparticles at 10 iterations	83
4.11 Cyclic voltammogram of nanoparticles modified electrodes in a 5mM ferrocyanide/ferricyanide [Fe(CN) <sub>6</sub> ] <sup>4-/3-</sup> solution containing 0.1M PBS at a scan rate of 50mV/s	85
Figure 4.12 Nyquist plot of nanoparticles modified electrodes in in 5mM potassium ferrocyanide/ferricyanide ([Fe(CN) <sub>6</sub> ] <sup>4-/3-</sup> ) solution in ratio 1:1 containing 0.1M PBS (pH 7) applying an open circuit potential with amplitude 5mV in frequency range 0.01Hz-10kHz.	86
Figure 4.13 (a) SEM image of Fe <sub>2</sub> O <sub>3</sub> nanoparticles (b) TEM image of Fe <sub>2</sub> O <sub>3</sub> nanoparticles	87
Figure 4.14 Electrochemical characterisation of Fe <sub>2</sub> O <sub>3</sub> -PEI at different temperatures (a) cyclic voltammograms (b) EIS Nyquist plots	88

Figure 4.15 Error bar analysis of average peak current against temperatures	90
Figure 4.16 Effects of agitation: on PEI adsorption on Fe <sub>2</sub> O <sub>3</sub> nanoparticles at room temperatures with and without stirring (a) cyclic voltammograms (b) EIS Nyquist plots	91
Figure 4.17 UV-Vis spectra for Fe <sub>2</sub> O <sub>3</sub> -PEI/Au shell formation after 5 iteration step (a) at different heating temperatures (b) stirred and unstirred process at 25 <sup>0</sup> C	93
Figure 5.1 Schematic diagram showing the stepwise modification of gold electrode with plasma Ig and polyclonal rabbit Anti-human Ig	104
Figure 5.2 Schematic diagrams showing the stepwise modification of gold electrode with plasma/antibody and Fe <sub>2</sub> O <sub>3</sub> - Au nanoparticles	105
Figure 5.3 Cyclic voltammograms of bare Au electrode (a), Au-MPA (b), Au-MPA- Polyclonal rabbit Anti-human Ig (c), Au-MPA- Polyclonal rabbit Anti-human Ig -1% marvel (d)	106
Figure 5.4 EIS (Nyquist plot) of bare Au electrode (light blue line), Au-MPA (dark blue line), Au-MPA- Polyclonal rabbit Anti-human Ig (green line), Au-MPA- Polyclonal rabbit Anti-human Ig -1% marvel (dark red line)	107
Figure 5.5 CV of Au-MPA- Polyclonal rabbit Anti-human Ig -1% marvel –plasma for control patient at dilutions (1:2000), (1:4000), (1:8,000), (1:16,000), (1:32,000), (1:64,000), (1:128,000), (1:256,000)	108
Figure 5.6. EIS (Nyquist plot) of Au-MPA- Polyclonal rabbit Anti-human Ig-1% marvel –plasma for control patient at plasma dilutions (1:2000), (1:4000), (1:8,000), (1:16,000), (1:32,000), (1:64,000), (1:128,000), (1:256,000)	109
Figure 5.7 Error bar analysis for first and second run depleted plasma concentration (control subject) for (A) [1:2000)(500ppm)], (B) [(1:4000) (250 ppm)] (C)[ (1:8000) (125 ppm)], (D) [(1:16,000), (62.5 ppm)], (E) [(1:32,000) (31.25 ppm)], (F) [(1:64,000) (15.62ppm)], (G) [(1:128,000) (7.81ppm)] and (H) [(1:256,000) (3.91ppm)]	110

Figure 5.8 plot of peak currents against plasma immunoglobulin (control) for (A) [1:2000](500ppm), (B) [(1:4000) (250 ppm)] (C)[ (1:8000) (125 ppm)], (D) [(1:16,000), (62.5 ppm)], (E) [(1:32,000) (31.25 ppm)], (F) [(1:64,000) (15.62ppm)], (G) [(1:128,000) (7.81ppm)] and (H) [(1:256,000) (3.91ppm)] 111

Figure 5.9 Calibration plot of peak currents against plasma immunoglobulin dilutions (control) for (A) [1:2000](500ppm), (B) [(1:4000) (250 ppm)] (C)[ (1:8000) (125 ppm)], (D) [(1:16,000), (62.5 ppm)], (E) [(1:32,000) (31.25 ppm)] 112

Figure 5.10 Calibration plot of peak currents against plasma immunoglobulin double dilution (control) for (E) [(1:32,000) (31.25 ppm)], (F) [(1:64,000) (15.62ppm)], (G) [(1:128,000) (7.81ppm)] and (H) [(1:256,000) (3.91ppm)] 113

Figure 5.11 CV of Au-MPA- Polyclonal rabbit Anti-human Ig -1% marvel –plasma for severe AD patient at plasma dilutions (1:2000), (1:4000), (1:8,000), (1:16,000), (1:32,000), (1:64,000), (1:128,000), (1:256,000) 113

Figure 5.12 EIS (Nyquist plot) of Au-MPA- Polyclonal rabbit Anti-human Ig -1% marvel –plasma for severe AD patient at plasma dilution (1:2000), (1:4000), (1:8,000), (1:16,000), (1:32,000), (1:64,000), (1:128,000), (1:256,000) 114

Figure 5.13 Error bar plot of peak currents against plasma immunoglobulin dilution for (A) [1:2000](500ppm), (B) [(1:4000) (250 ppm)] (C)[ (1:8000) (125 ppm)], (D) [(1:16,000), (62.5 ppm)], (E) [(1:32,000) (31.25 ppm)], (F) [(1:64,000) (15.62ppm)], (G) [(1:128,000) (7.81ppm)] and (H) [(1:256,000) (3.91ppm)] 115

Figure 5.14 plot of peak currents against plasma immunoglobulin (Severe) for (A) [1:2000](500ppm), (B) [(1:4000) (250 ppm)] (C)[ (1:8000) (125 ppm)], (D) [(1:16,000), (62.5 ppm)], (E) [(1:32,000) (31.25 ppm)], (F) [(1:64,000) (15.62ppm)], (G) [(1:128,000) (7.81ppm)] and (H) [(1:256,000) (3.91ppm)] 116

Figure 5.15 Calibration plot of peak currents against plasma immunoglobulin double dilution for severe AD patient at (A) [1:2000)(500ppm)], (B) [(1:4000) (250 ppm)] (C)[ (1:8000) (125 ppm)], (D) [(1:16,000), (62.5 ppm)], (E) [(1:32,000) (31.25 ppm)] 117

Figure 5.16 Calibration plot of peak currents against plasma immunoglobulin double dilution for severe AD patient at (E) [(1:32,000) (31.25 ppm)], (F) [(1:64,000) (15.62ppm)], (G) [(1:128,000) (7.81ppm)] and (H) [(1:256,000) (3.91ppm)] 117

Figure 5.17 Comparing peak currents between control and plasma immunoglobulin from severe AD patient at dilutions (A) [1:2000)(500ppm)], (B) [(1:4000) (250 ppm)] (C)[ (1:8000) (125 ppm)], (D) [(1:16,000), (62.5 ppm)], (E) [(1:32,000) (31.25 ppm)] 118

Figure 5.18 Comparing peak currents between control and plasma immunoglobulin from severe AD patient at dilutions (E)[(1:32,000) (31.25 ppm)], (F)[(1:64,000) (15.62ppm)], (G)[(1:128,000) (7.81ppm)], (H)[(1:256,000) (3.91ppm)], 119

Figure 5.19 (a) Plot of Optical densities (OD) against plasma immunoglobulin dilution (b) Error bar plot for A[1:2000)(500ppm)], B[(1:4000) (250 ppm)] C[ (1:8000) (125 ppm)], D[(1:16,000), (62.5 ppm)], E[(1:32,000) (31.25 ppm)], F[(1:64,000) (15.62ppm)], G[(1:128,000) (7.81ppm)], H[(1:256,000) (3.91ppm)], I[(1:512,000) (1.95ppm)], J [(1:1024,000) (0.98ppm)], K [(1:2048,000) (0.49ppm)], L [(1:4096,000) (0.244ppm)] 120

Figure 5.20 Calibration plot of peak currents against plasma immunoglobulin dilution for severe AD patient (a) [High conc. Point A-E], (b) [Point H-L] and (c) logarithmic curve [Low conc. Point F-L] 121

Figure 5.21 CV of bare Au (light blue line), Au-MPA (dark blue), Au-MPA-cysteamine- Fe<sub>2</sub>O<sub>3</sub>-Au Nps- polyclonal rabbit Anti-human Ig (green line), and Au-MPA-cysteamine- Fe<sub>2</sub>O<sub>3</sub>-Au Nps- polyclonal rabbit Anti-human Ig -Marvel (red line) 122

Figure 5.22 EIS of bare Au (light blue line), Au-MPA (dark blue), Au-MPA-cysteamine- Fe<sub>2</sub>O<sub>3</sub>-Au Nps- polyclonal rabbit Anti-human Ig (green line), and Au-MPA-cysteamine- Fe<sub>2</sub>O<sub>3</sub>-Au Nps- polyclonal rabbit Anti-human Ig -Marvel (red line)

123

Figure 5.23 CV of Au-Cys-Fe<sub>2</sub>O<sub>3</sub>-Au Nps- polyclonal rabbit Anti-human Ig -Marvels – Plasma (control) at double dilution (DD) 1:2000 (dark blue line), 1:4000 (sky blue line), 1:8000 (light blue line), 1:16,000 (green line), 1:32,000 (red line)

124

Figure 5.24 CV of Au-Cys-Fe<sub>2</sub>O<sub>3</sub>-Au Nps- polyclonal rabbit Anti-human Ig -Marvels – Plasma (severe AD) at double dilution (DD) 1:2000 (dark blue line), 1:4000 (sky blue line), 1:8000 (light blue line), 1:16,000 (green line), 1:32,000 (red line)

125

Figure 5.25 EIS of Au-Cysteamine-Fe<sub>2</sub>O<sub>3</sub>-Au Nps- polyclonal rabbit Anti-human Ig -Marvels –Plasma (severe AD) at double dilution (DD) 1:2000 (dark blue line), 1:4000 (sky blue line), 1:8000 (light blue line), 1:16,000 (green line), 1:32,000 (red line)

126

Figure 5.26 Error bar analysis for first and second run depleted plasma concentration from severe AD patient at (A) [1:2000)(500ppm)], (B) [(1:4000) (250 ppm)] (C)[(1:8000) (125 ppm)], (D) [(1:16,000), (62.5 ppm)], (E) [(1:32,000) (31.25 ppm)]

127

Figure 5.27 Comparing peak currents between control and plasma from severe AD patient at double dilution (A) [1:2000)(500ppm)], (B) [(1:4000) (250 ppm)] (C)[(1:8000) (125 ppm)], (D) [(1:16,000), (62.5 ppm)], (E) [(1:32,000) (31.25 ppm)]

128

## Tables

Table 1.1 Physical and magnetic property of magnetite and maghemite	9
Table 3.1 Fe <sub>3</sub> O <sub>4</sub> nanoparticles synthesized by varying iron II sulphate concentration	52
Table 3.2 Fe <sub>3</sub> O <sub>4</sub> nanoparticles synthesized by varying base concentration	58
Table 3.3 Fe <sub>3</sub> O <sub>4</sub> nanoparticles synthesized by varying revolution per minute	61
Table 3.4 Fe <sub>3</sub> O <sub>4</sub> nanoparticles synthesized by varying synthesis temperature	64
Table 4.1 Fe <sub>2</sub> O <sub>3</sub> -PEI nanoparticles at room temperature ohmic and charge transfer resistance	89
Table 4.2 Fe <sub>2</sub> O <sub>3</sub> -PEI nanoparticles at room temperature ohmic and charge transfer resistance	92
Table 5.1 Symbols for immobilization diagram	102

## Nomenclature

$\alpha$ -Fe <sub>2</sub> O <sub>3</sub>	Hematite
$\gamma$ -Fe <sub>2</sub> O <sub>3</sub>	Iron III oxide (maghemite)
$\beta$ -FeOOH	Beta iron oxy hydroxide (alkaganeite)
$\gamma$ -FeOOH	Gamma iron oxy hydroxide (lepidocrocite)
a	Activity of ions
AC	Alternating current
AD	Alzheimer's disease
Au	Gold
A $\beta$ 40	Amyloid beta protein (40 amino acids)
A $\beta$ 42	Amyloid beta protein (42 amino acids)
B	Magnetic induction
c	Concentration
C <sub>H</sub>	Constant heavy chain
CHIT	Chitosan
C <sub>L</sub>	Constant light chain
CSF	Cerebrospinal fluid
Cu	Copper
Cu (K $\alpha$ )	Copper alpha radiation
CV	Cyclic voltammetry
Cys	Cysteamine
d <sub>c</sub>	Characteristics size of domains
DA	Deacetylation
DD	Double dilution
E	Electrode potential
E <sub>o</sub>	Standard electrode potential
EDC	N-(3-Dimethylaminopropyl)-N-ethylcarbodiimide hydrochloride
EIS	Electrochemical impedance spectroscopy
ELISA	Enzyme linked immunosorbent assay
ESEM	Environmental scanning electron microscopy

eV	Electron volt
F	Faraday constant
F <sup>II</sup>	Iron (II) cation
F <sup>III</sup>	Iron (III) cation
F <sub>ab</sub>	Antigen binding site in antibody
F <sub>c</sub>	Antigen non-binding site
Fe <sub>3</sub> O <sub>4</sub>	Triiron tetraoxide (magnetite)
Fe(CN) <sub>6</sub> <sup>-3</sup>	Potassium ferricyanide
Fe(CN) <sub>6</sub> <sup>-4</sup>	Potassium ferrocyanide
FeSO <sub>4</sub>	Iron II sulphate
GCE	Glassy carbon electrode
H	Magnetic field strength
HAuCl <sub>4</sub>	Hydrogen tetrachloroauric acid
H <sub>c</sub>	Coercive force field
HCl	Hydrochloric acid
HNO <sub>3</sub>	Nitric acid
KCl	Potassium chloride
m/m	Mass per mass concentration
M	Magnetisation
MHz	Megahertz
MPa	Mega Pascal (unit for pressure)
M <sub>R</sub>	Remnant magnetisation
MRI	Magnetic resonance imaging
M <sub>s</sub>	Saturation magnetization
n	No of moles of electrons
NaBH <sub>4</sub>	Sodium borohydride
NaOH	Sodium hydroxide
NHS	N-Hydroxylsulfosuccinimide sodium salt
N <sub>ps</sub>	Nanoparticles
Ox	Oxidation
PBS	Phosphate buffer solution

PBST	Phosphate buffer solution tween 20
PEI	Polyethyleneimine
Red	Reduction
R <sub>ct</sub>	Charge transfer resistance
RPM	Revolution per minute
R <sub>s</sub>	Solution resistance
SAM	Self-assembly monolayer
SEM	Scanning electron microscopy
TAOB	Tetraoctylammonium bromide
TMAOH	Tetramethylammonium hydroxide pentahydrate
V <sub>L</sub>	Variable light chain
V <sub>H</sub>	Variable heavy chain
w/v	Weight per volume concentration
XPS	X-ray photoelectron spectroscopy
XRD	X-ray diffraction
y	Activity coefficient

# Chapter 1

## Introduction

### 1.1 Motivation and aims of the research

The advances in nanotechnology and nanoscience have made possible the use of nanomaterials with exceptional properties in studying, monitoring and treatment of most biomedical related diseases. Specifically the use of biocompatible nanoparticles (1-100 nm) to interact between cells and molecules in our body has helped in the fabrication of sensors and implantable devices to regulate body functions and disease control. Biocompatible nanoparticles such as iron oxide and gold nanoparticles with unique properties have been of great interest to researchers in environmental, biomedical and medical fields.

The magnetic properties of iron oxide nanoparticles, their stability when functionalized and their robust surface area combined with their biocompatibility, ligands affinity and electron transfer ability of gold nanoparticles has led to the fabrication of iron oxide core-gold shell nanoparticles and their application in biomedical fields such as biosensors fabrication, drug delivery, contrast agent in magnetic imaging, cell separation, disease monitoring and treatment. Iron oxide core-gold shell nanoparticles has been used as drug delivery carriers (Barnett *et al.*, 2013), imaging (Menichetti *et al.*, 2013), biomedical platforms(Hoskins *et al.*, 2012) protein immobilization (Liang *et al.*, 2009) and for disease treatment (Guo *et al.*, 2013)

The use of iron oxide core-gold shell nanoparticles in the monitoring, control and treatment of diseases has being a focal point for researchers to improve on the drawback experienced in most clinical and analytical diagnosis of diseases. Specifically the diagnosis, detection and monitoring of the progression of dementia especially Alzheimer's disease (AD) in ageing people has been of great challenge since there are no standard reliable diagnostic test and cure for the diseases. The disease is a disease of the brain that often causes memory loss, confusion, inability to speak properly and cope

with everyday activities. It is a progressive disease that gets worse over time and eventually leads to death.

The available clinical diagnostic technique such as the use of radio tracers and lumbar puncture are very expensive and challenging. The uses of biomarkers as a supportive measure to aid the diagnosis and monitoring of AD diseases have been encouraged by the National Institute of Ageing and Alzheimer's Association (McKhann *et al.*, 2011). Biomarkers for the detection of cerebrospinal fluids (CSF) proteins such as increase in levels of amyloid beta proteins ( $A\beta$  40) and ( $A\beta$  42) observed in AD patients has been developed (Sunderland *et al.*, 2005), although the CSF biomarkers still faces the problem of extracting the fluid from the brain which is challenging.

The use of blood plasma proteins such as immunoglobulin (Ig), as biomarker for monitoring AD has been encouraging and also has removed the difficulties experience in extracting fluids from the brain for analysis since blood plasma can easily be extracted from the body and use. Plasma immunoglobulin have been used as a biomarker in enzyme linked immunosorbent assay (ELISA) for monitoring AD and also plasma amyloid beta proteins and tau proteins have been used as biomarkers too for AD (Hye *et al.*, 2006; Mukaetova-Ladinska *et al.*, 2012). Although this method shows increase in immunoglobulin or amyloid protein levels in AD compared to normal subjects, the method is still complicated and takes long time for sampling and result analysis.

This dissertation seeks to use gold electrode, iron oxide core-gold shell nanoparticles in developing electrochemical immunosensors electrodes using plasma immunoglobulin as biomarker for the monitoring of AD in patients. This will help in solving the setback experienced in the ELISA method and CSF biomarkers techniques, since immunosensors are easy to handle, highly sensitive and can run many samples within short time intervals.

The specific goal of this PhD dissertation is:

1. Synthesize iron oxide nanoparticles through oxidative alkaline hydrolysis of ferrous salt and the effect of synthesis parameters on the nanoparticles and their possible side products or impurities.

2. Synthesize iron oxide core-gold shell nanoparticles and the effect of temperature and agitation on polyethyleneimine (polymer) adsorption on iron oxide nanoparticles during iron oxide-gold shell formation.
3. The use of gold electrode as an immobilizing platform for depleted plasma immunoglobulin as biomarker for AD immunosensor.
4. The use of iron oxide core-gold shell nanoparticles as immobilizing substrate for depleted plasma immunoglobulin as biomarker for AD immunosensor.

## 1.2 Nanomaterial Overview

Nanomaterials are materials with nano-scale dimension (1-100 nm) or materials with at least one dimension in nanoscale and the others in microscopic scale. These materials possess novel properties due to their unique size and shape that are advantageous compared to their bulky nature (Kreyling *et al.*, 2010). Nanomaterials are the motivating factor in nanotechnology which deals with the use of the nanoscale properties of materials to design, characterize and produce devices. Nanomaterials are often prepared from materials such as are polymers, metals, oxides, carbon, semiconductors and magnetic materials. They can be shaped into different forms based on their application such nanoparticles, nanowires (diameters  $10^{-9}$  metres), nano-crystals (single crystalline structure with at least one  $\leq 100$  nm) and clusters (quantum dots), nanotubes (carbon materials) and dendrimers (nano-size polymers) (Luo *et al.*, 2006).

Nanomaterials has been of great interest in biomedical applications and in biosensor/immunosensor fabrication, by taking advantage of their unique properties such as their surface structures, optical, electronic, catalytic, magnetic, thermal, biocompatibility and chemical properties (Welch and Compton, 2006). These materials improve the biocompatibility, stability, sensitivity and reproducibility of biosensors and immunosensors. Among the different nanomaterial used for biosensor/immunosensor applications, nanoparticles of metal are of great interest. This is due to their biocompatibility to biomolecules which allows biomolecules to regenerate, their ability to act as catalyst in electrochemical reactions, ability to enhance electron transfer between biomolecules and electrode surfaces and their ability to act as labels for biomolecules and also as reactants (Welch and Compton, 2006).

### 1.3 Nanoparticles

Nanoparticles are particles in nanoscale forms or particles with at least one dimension less than 100 nm (Kreyling *et al.*, 2010). They are of great interest due to their wide variety of potential applications in biomedical, optical, and electronic/bioelectronics fields. Nanoparticles for sensor applications can be formed from metals, semiconductor, polymer and oxide materials and each play different roles in different sensing systems. Metal nanoparticles such as gold, silver and platinum are often used as an electronic wire to aid electron transfer in biosensor applications, oxides nanoparticles such as iron oxide are used for biomolecules immobilization due to their biocompatibility and large surface area while semiconductor nanoparticles are often used as labels or tracers (Luo *et al.*, 2006). Among the numerous nanoparticles used for biosensor/immunosensor fabrication iron oxide nanoparticles and gold nanoparticles have received great interest due to their intriguing properties.

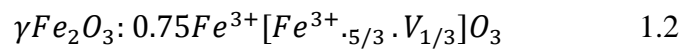
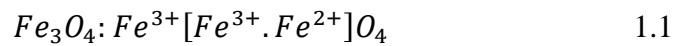
### 1.4 Iron oxide nanoparticles

Iron oxide nanoparticles are nanoscale magnetite ( $\text{Fe}_3\text{O}_4$ ) or maghemite ( $\text{Fe}_2\text{O}_3$ ) particles often referred to as magnetic nanoparticles due to their magnetic properties. They are cost-effective and possess unique properties such as chemical stability, biocompatibility, non-toxicity, effective specific power absorption rate and ability to be chemically functionalized and stable in solution of physiological pH (pH 7.3-7.4). These properties and their strong magnetic properties, high separation efficiency, and high specific surface area makes them useful in the fabrication of DNA and protein biosensors ((Li *et al.*, 2011c) and for other biomedical applications such as magnetic resonance imaging, drug delivery, hyperthermia therapy and cell separations.

Magnetite ( $\text{Fe}_3\text{O}_4$ ) also referred to as tri-iron tetraoxide is the most widely used form of magnetic nanoparticles because of its biocompatibility and high magnetization values. It is an unstable iron oxide that is sensitive to oxidation and also ferrimagnetic at room temperature. Its structure is composed of oxygen anion and iron cation in octahedral or tetrahedral interstitial sites forming a cubic closed packed arrangement (Teja and Koh, 2009) as shown in Figure 1.1. Magnetite contains both iron II ions ( $\text{Fe}^{\text{II}}$ ) and iron III ions ( $\text{Fe}^{\text{III}}$ ) in an inverse cubic spinel structure with the  $\text{Fe}^{\text{II}}$  ions in the octahedral site and half  $\text{Fe}^{\text{III}}$  ions in octahedral and half in tetrahedral site (Goon *et al.*, 2010). The

stoichiometric ratio of  $Fe^{2+}$  and  $Fe^{3+}$  cation in magnetite is 1:2 under a non-oxidizing free oxygen environment (Goon *et al.*, 2010).

Maghemite ( $\gamma$ - $Fe_2O_3$ ) also referred to as iron III oxide is the completely oxidized form of magnetite or iron II deficient magnetite. It is a ferrimagnetic iron oxide at room temperature, unstable at high temperature and loses its magnetization with time (Dronskowski, 2001). It contains three quarter of iron III cation in the tetrahedral site and the rest in the octahedral site. It has similar cubic close packed arrangement with oxygen anions like magnetite. The tetrahedral sites of maghemite are filled while cationic vacancies appear on the octahedral site. The occurrence of the vacancies is due to the migration of cations through the lattice frame work of magnetite during oxidation and in turn maintains the charge balance in the formation of maghemite (Jolivet *et al.*, 2004). The two forms of iron oxide can be represented mathematically as:



The brackets represent the octahedral sites and the V denotes vacancies that occurred in the octahedral sites. .

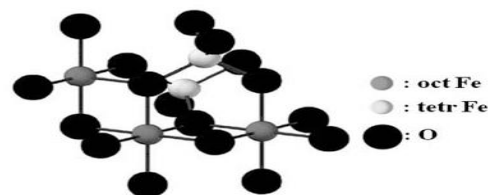


**Figure 1.1 Crystal structure of magnetite**

Although the two major forms of iron oxide in magnetic nanoparticles are magnetite and maghemite, iron oxides also exist in other forms due to its polymorphic nature. The two polymorphs forms of iron oxide are the anhydrous (oxides) which includes maghemite ( $\gamma$ -  $Fe_2O_3$ ), magnetite ( $Fe_3O_4$ ), hematite ( $\alpha$ - $Fe_2O_3$ ), wustite ( $FeO$ ) with magnetite or with both ferrous and ferric iron , and the hydrous form (oxy hydroxides) which often contain excess water e.g. goethite ( $\alpha$ - $FeOOH$ ), lepidocrocite ( $\gamma$ - $FeOOH$ )

and akaganeite ( $\beta$ -FeOOH), of which the goethite is the most stable of the iron oxy hydroxides polymorphs (Snow *et al.*, 2011).

### 1.5 Magnetic and physical properties

The magnetic properties of iron oxide nanoparticles are determined by factors such as their size, shape, temperature, pressure composition and chemical phase present. Most materials including magnetic iron oxide nanoparticles experience magnetic induction  $B$  in the presence of an external magnetic field of strength  $H$  as shown in equation 1. 3

$$B = \mu_0 (H + M) \quad 1.3$$

Where  $\mu_0$  the permeability of free space and  $M$  is the magnetization of the material. Magnetization ( $M$ ) is the magnetic moment per unit volume of the material. Bulk magnetic materials consist of domains with different magnetization and the number of domains decreases as the material becomes smaller resulting to single domain at a characteristic size ( $d_c$ ) as shown in Figure 1.2. The net magnetization of the domains is usually less compared to when all the atomic moment in the individual domains are aligned. But often the magnetization of all the domains may not be aligned in the presence of a magnetic field and this leads to decrease in the net magnetization as shown in Figure 1.3

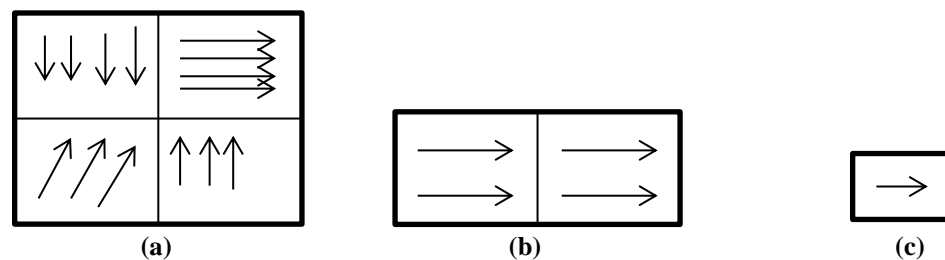


Figure 1.2 Magnetic moment in bulk (a) reduced bulk (b) and single domain materials (c)

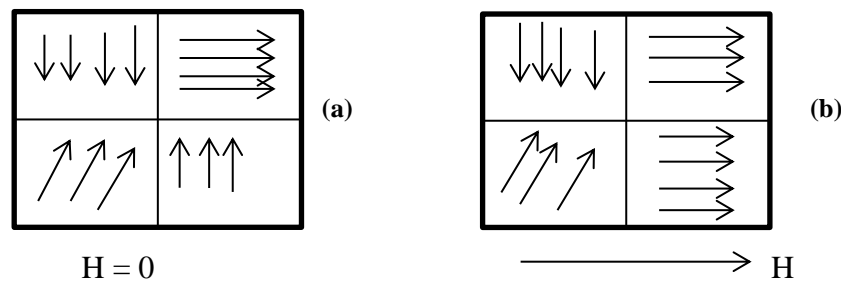


Figure 1.3 Magnetic moment in bulk (a) absence of magnetic field (b) presence of magnetic field

The volumetric susceptibility ( $\chi$ ) of the domains to an external magnetic field of strength H is a dimensionless number as shown in equation 1.4 and varies from one magnetic material to another.

$$M = \chi H \quad 1.4$$

Based on the arrangement and composition of atoms in the domains, magnetic nanoparticles or materials can exhibit different forms of magnetism such as diamagnetism, paramagnetism, ferromagnetism and super-paramagnetism.

Iron oxide nanoparticles orbital have 4 unpaired electrons from its 3d orbitals ( $1s^2 2s^2 2p^6 3s^2 3p^6 3d^6 4s^2$ ) that can move freely and are capable of aligning in direction that result in net dipole moment (magnetic field) in the presence of external magnetic field.

If the alignments of the unpaired electrons in the nanoparticles are parallel to the magnetic field, they are referred to as paramagnetic particles. This type of particles or materials show small repulsion from an external magnet with positive susceptibility and their magnetic properties ceases upon the removal of the external magnet.

The disappearance of the magnetic properties in paramagnetic materials or nanoparticles in the absence of a magnetic field is due to thermal motions which make the electrons to align randomly or fluctuate yielding a net magnet dipole moment of zero. The transition temperature beyond which the material due to thermal motion becomes weak and losses its magnetization is called Curie temperature  $T_C$  for ferromagnetic and ferrimagnetic materials and Neel temperature  $T_N$  for antiferromagnetic materials.

When particles or materials exhibit permanent magnetic dipole in the presence or absence of a magnetic field or have spins moving in the same direction and contributing to the net magnetization, they are referred to as ferrimagnetic or ferromagnetic materials. Ferromagnetic particles shows large and positive susceptibility to magnetic fields and the magnetic properties of the particles are stable upon removal of the external magnet and are also referred to as magnet. Situations where the atoms in the different sub-lattice of the material point in different directions to yield a net magnetic moment of zero, they are referred to as anti-ferrimagnetic particles. The ordering of atoms in anti-ferrimagnetic material disappears at the Neel temperature above which the material is paramagnetic.

Diamagnetism occurs when the velocity of paired electrons around the atomic nuclei of materials changes and creates a dipole moment in the presence of an external magnetic field. Diamagnetic materials have weak repulsion in the presence of an external magnetic field with a negative susceptibility, and their magnetic properties cease upon removal of the field. All materials undergoes diamagnetic effect but the effect are less in the presence of paramagnetic or ferrimagnetic effect.

Materials or particles with size less than 10 nm exhibit super-paramagnetic behaviour which occurs when the materials randomly flip direction during magnetization under the influence of temperature and in the absence of a magnetic field, it takes a longer time more than the Neel relaxation time (time between two flips) to measure the magnetization of the nanoparticles thus, their magnetization appears to be in average zero. The thermal fluctuations that occurs on the average length of time between random flips in the direction of magnetization is described by Neel-Arrhenius equation 1.5

$$\tau_N = \tau_0 \exp\left(\frac{KV}{k_B T}\right) \quad 1.5$$

where  $\tau_N$  is the average length of time between each flip,  $\tau_0$  is the length of time or attempted time (typically between  $10^{-9}$  and  $10^{-10}$  seconds) characteristics of the material,  $K$  is the magnetic anisotropy density of the nanoparticle,  $V$  is the nanoparticle volume,  $k_B$  is the Boltzmann constant,  $KV$  is the energy barrier associated with magnetization and  $T$  is the temperature. In situation where  $\tau_0$  is shorter than  $\tau_N$ , the nanoparticles will become ferrimagnetic even though the material is below its Neel temperature. Super-paramagnetic nanoparticles have significant thermal energy even though the material is below the Neel temperature. They are single domain particles with no hysteresis loop during magnetization as shown in Figure 1.4 (B).

Hysteresis loop are observed in ferromagnetic materials with magnetic strength  $M$  when an external magnetic field of strength  $H$  is applied as shown in Figure 1.4 (A). The magnetization  $M$  of ferromagnetic material increases with  $H$  until a saturation value  $M_s$ . Ferromagnetic materials forms hysteresis loop because the different domains that makes up the bulk ferromagnetic material do not return to their initial orientation upon decrease of the magnetic field after attaining saturation magnetization (Teja and Koh, 2009). Thus, at the point where  $H$  reaches zero, remnant magnetization ( $M_R$ ) is observed

and requires coercive force field ( $H_C$ ) in the opposite direction of the applied magnetic field to remove.

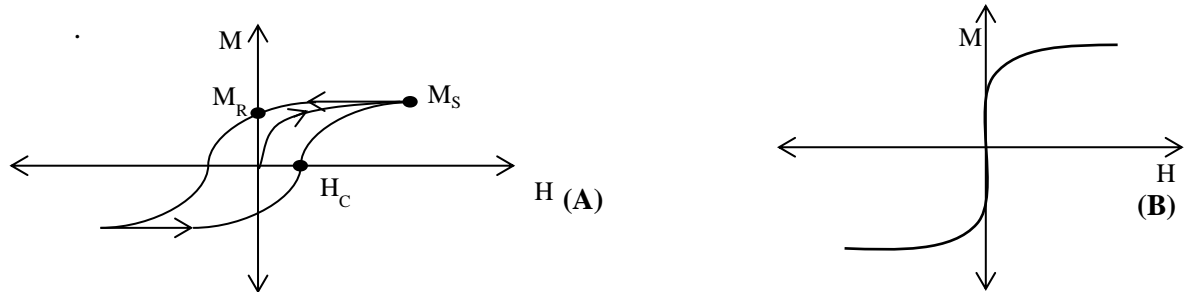


**Figure 1.4 Magnetization curve showing  $M$  as a function of applied magnetic field  $H$  for (A) ferromagnetic (B) super-paramagnetic materials**

The magnetic and physical properties of magnetite and maghemite are summarized in table 1.1 (Teja and Koh, 2009).

Property	Magnetite	Maghemite
Molecular formula	$Fe_3O_4$	$\gamma-Fe_2O_3$
Density ( $g/cm^3$ )	5.18	4.87
Melting point ( $^{\circ}C$ )	1583-1597	-
Hardness	5.5	5.0
Type of magnetism	Ferromagnetic	Ferrimagnetic
Curie temperature (K)	850	820-986
$M_s$ at 300K ( $A\cdot m^2/kg$ )	92-100	60-80
$\Delta G_f^{\circ}$ (KJ/mol)	-1012.6	-711.1
Crystallographic system	Cubic	Cubic or tetrahedral
Structural type	Inverse spinel	Defect spinel
Space group	Fd3m	$P4_332$ (cubic); $P4_12_12$ (tetragonal)
Lattice parameter (nm)	$a = 0.8396$	$a = 0.83474$ (cubic); $0.8347, c = 2.501$ (tetragonal)

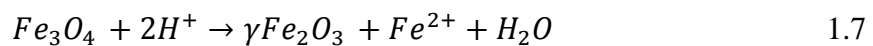
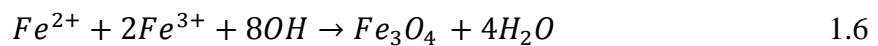
**Table 1.1 Physical and magnetic property of magnetite and maghemite**

## 1.6 Synthesis of iron oxide magnetic nanoparticles

Iron oxide magnetic nanoparticles can be synthesized through various synthetic methods with each method producing nanoparticles with different sizes, morphology, chemical composition and magnetic properties. The common routes for synthesizing iron oxide nanoparticles are co-precipitation, thermal decomposition, sol gel, hydrothermal reactions, microemulsions, flow injection and sonochemical methods.

### 1.6.1 Co-precipitation

This is the simplest and most common method of synthesizing super-paramagnetic and paramagnetic iron oxide nanoparticles ( $Fe_3O_4$  or  $\gamma$ - $Fe_2O_3$ ). It involves ageing mixtures of iron salts (ferric and ferrous chloride) in an aqueous medium based on stoichiometric ratio 2:1 ( $Fe^{3+}/Fe^{2+}$ ) in the absence of oxidizing oxygen. This result in the formation of  $Fe_3O_4$  nanoparticles at higher pH values 8 and 14 (Jolivet *et al.*, 2004) and further undergoes oxidation in the presence of oxygen to form maghemite ( $\gamma$ - $Fe_2O_3$ ). The reaction can be written as:



### 1.6.2 Thermal decomposition

This method produces iron oxide nanoparticles through the decomposition of organic iron salt such as iron acetylacetonate [ $Fe(acac)_3$ ], iron pentacarbonyl  $Fe(CO)_5$  and iron carboxylates at high temperature (250-350°C) (Sharma and Jeevanandam, 2013) in an organic solution. The process sometimes requires the use of complicated iron salts, ligands and inert conditions (argon and nitrogen atmosphere). Iron oxide nanoparticles (super-paramagnetic or paramagnetic) synthesized through this method are highly monodispersed with narrow size distribution. The disadvantage with this method is that the synthesized nanoparticles can only dissolve in nonpolar solvent making its biomedical applications limited.

### ***1.6.3 Microemulsion***

This is a thermodynamically stable method of synthesizing nanoparticles. It involves the thermodynamic dispersion of two immiscible liquids usually water and oil in the presence of a surfactant. This results in the formation of droplets of water in oil (w/o) or oil in water (o/w) stabilized by the surfactant when small amount of oil or water are used respectively. The nano-droplets can take different shapes such as spherical (inverted), cylindrical micelles to lamellar phases coexisting with the predominant oil or aqueous phase. The size of the droplets can be controlled by changing the water or oil to surfactant ratio in the nanometre range. These nano-droplets can be used to obtain size and shape controlled iron oxide nanoparticles (super-paramagnetic or paramagnetic). Water in oil microemulsion technique has been used to synthesize mono-dispersed spherical maghemite nanoparticles with higher saturation magnetization (Vidal-Vidal *et al.*, 2006; Chin and Yaacob, 2007). The disadvantage with this method is the aggregation of the nanoparticles that requires several washing process and stabilization despite the use of surfactant.

### ***1.6.4 Hydrothermal synthesis***

This method is used to grow highly crystalline iron oxide nanoparticles in a sealed medium. It involves crystallization of nanoparticles from high temperature (130-250°C) aqueous solution at high vapour (0.3-04 MPa) in a sealed container by applying wet chemical synthesis routes (e.g. sol-gel, co-precipitation etc.) that meets these conditions. It is also a convenient way of synthesizing iron oxide nanostructures such as iron oxide hollow spheres or iron oxide nanocubes. It is also more advantageous compared to the microemulsion and thermal decomposition methods

### ***1.6.5 Sol gel-method***

This is a wet chemical technique that is used to synthesize nanostructured metal oxides. It involves the introduction of hydroxyl groups and subsequent condensation of molecular precursors into colloidal solution (sol) or nanometric particles that act as the precursor for the formation of a gel of either discrete particles or network polymer. This process is often carried out at room temperature thus further heat treatment is required to obtain the desired crystalline state of the particles. The particles growths are

determined by concentration of the salt precursors (iron salt), agitation, pH, temperature and solvent. This technique is advantageous in that particles with specified structures can be synthesized and the particles sizes can easily be controlled. It also allows for the synthesis of pure amorphous phases of the particles, monodispersed particles and the formation of core-shell.

#### ***1.6.6 Flow injection***

This is a reactor based route for the synthesis of iron oxide nanoparticles under laminar or plug flow conditions. The process involves continuous or segmented mixing of reactants and iron precursor in a capillary reactor under plug flow or laminar flow conditions to form iron oxide nanoparticles. The method allows for the synthesis of reproducible narrow size nanoparticles due to the flow conditions, and better control of the process. This method has been used to synthesize narrow size super-paramagnetic magnetite nanoparticles of sizes 2-7nm (Salazar-Alvarez *et al.*, 2006).

#### ***1.6.7 Sonochemical***

This method uses the chemical effect of ultrasound to synthesize iron oxide nanoparticles from organic iron salts. The process involves the formation, growth and rapid collapse of bubbles (cavities) in liquid during ultrasound (sonolysis). The rapid collapse of the cavities results in the formation of localized hot spots at high temperatures (5000K) (Suslick, 1990) which allows for the conversion of iron salt into nanoparticles. The nanoparticles growth is controlled through the use of organic capping agents either polymers or structural.

### **1.7 Applications of iron oxide nanoparticles**

Iron oxide nanoparticles are widely used in biomedical applications such as magnetic resonance imaging (MRI), Hyperthermia therapy, drug delivery, magnetic recording media, ferrofluids and biosensors fabrication. The application of the nanoparticles for biomedical and other bioengineering largely depends on the nanoparticles specific size with narrow particle size distribution that allows for their uniform physical and chemical properties, shape, characteristics and magnetic properties.

### ***1.7.1 Magnetic resonance imaging (MRI)***

MRI is a medical imaging technique that makes use of a magnetic field and pulses of radio wave energy to picture organs and structures inside the body. Super-paramagnetic iron oxide nanoparticles ( $\text{Fe}_3\text{O}_4$ ) core coated with polymer for colloidal stabilization are used as contrast agent for in vivo MRI. The nanoparticles differentiate between healthy and disease tissue when a strong magnetic field and radio waves are applied. The biocompatibility and stability of the iron oxide nanoparticles over time during MRI, makes MRI a better medical imaging technique compared to X-ray computer tomography (CT) where there is an exposure to ionizing radiation. Super-paramagnetic and paramagnetic iron oxide nanoparticles have been used in magnetic resonance imaging of cancer, tissues and tumours (Ris *et al.*, 2010; Zou *et al.*, 2010; Chung *et al.*, 2011; Ishigami *et al.*, 2011; Lee *et al.*, 2012; Yoo *et al.*, 2012).

### ***1.7.2 Hyperthermia therapy***

Hyperthermia therapy is the application of slight higher temperatures to body tissues in order to damage or kill cancer cells. Super-paramagnetic iron oxide nanoparticles are used as therapeutic agents for cancer treatment. During the treatment, the nanoparticles are exposed to alternating magnetic field and are used to heat tumour cells to temperatures ( $41\text{-}45^\circ\text{C}$ ) that completely damages the tumour cells while the normal tissue cell can be regenerated. Super-paramagnetic iron oxide nanoparticles has been used in hyperthermia analysis and treatment (Kobayashi, 2011; Silva *et al.*, 2011; Bae *et al.*, 2012; Amarjargal *et al.*, 2013).

### ***1.7.3 Magnetic recording media***

Mono-dispersed small size maghemite nanoparticle doped with cobalt to improve its coercivity and storage are the most common material in recording and data storage applications such as magnetic disc, video tapes and high bias audio tapes. The data storage application takes advantage of the chemical and physical stability and switchable magnetic state of maghemite nanoparticles, while for recording data, the doped quality of maghemite and cobalt such as resistance to corrosion, resistance to temperature changes, high coercivity and high remanence are advantageous.

#### **1.7.4 Drug delivery**

Super-paramagnetic iron oxide nanoparticle with special surface coatings that are biocompatible and non-toxic can be used for in vivo drugs delivery to specific site in the body with the aid of an external magnetic field without damaging cells or tissues. The drugs can be covalently attached to functional groups on surface of the iron oxide nanoparticles and delivered with the appropriate local concentration with minimal overall dosage and side effect. Magnetite iron oxide nanoparticles has been used to aid delivery of cancer drugs (Marcu *et al.*, 2013; Omidirad *et al.*, 2013; Zhang *et al.*, 2013).

#### **1.7.5 Ferrofluids**

Ferrofluids are small size magnetic particles suspended in a fluid either water or organic solvent. The small size nature of the particles allows for the stability of the fluids and also reduces the effect of precipitation, charge and surface chemistry that may occur. Ferrofluids have no net magnetic moment but are strongly magnetized in the presence of a magnet. Super-paramagnetic iron oxide ( $\text{Fe}_3\text{O}_4$ ) nanoparticles ferrofluids has been used as seals in space applications and also for sealing computer disk unit (Teja and Koh, 2009).

#### **1.7.6 Biosensor application**

Iron oxide nanoparticles have found great interest in biosensor application. The biocompatibility of iron oxide nanoparticles, its low toxicity, and large surface-to-volume ratio coupled with strong super-paramagnetic properties aids the delivery, effective immobilization and regeneration of bioactive molecules such as enzymes. Various glucose base enzyme biosensors has been developed and other enzyme biosensors using iron oxide nanoparticles as immobilization matrix (Kaushik *et al.*, 2008; Chauhan and Pundir, 2011; Li *et al.*, 2011b).

## 1.8 Gold nanoparticles and its properties

Gold generally is a metal with a shiny metallic yellow colour and standard atomic weight of  $196.9665\text{g mol}^{-1}$ , an electronic configuration of  $[\text{Xe}]4f^{14}5d^{10}6s^1$  and electron per shell of 2, 8, 18, 32, 18, 1 (Yates, 2000). The most common gold compounds are auric chloride ( $\text{AuCl}_3$ ) and chloroauric acid ( $\text{HAuCl}_4$ ). Gold nanoparticles or nanospheres are basically colloid gold of 2 nm to 100 nm in diameter created when gold ions ( $\text{Au}^{3+}$ ) are turned into neutral atoms ( $\text{A}^0$ ). There are different synthetic routes for the synthesis of gold nanoparticles such as citrate-induced reduction of boiling aqueous  $\text{Au}^{3+}$  (Hien Pham *et al.*, 2008; Nguyen *et al.*, 2010; Li *et al.*, 2011a), colloidal Au surface-catalysed reduction of  $\text{Au}^{3+}$  by hydroxylamine (Brown and Natan, 1998; Lyon *et al.*, 2004), sonolysis (Zhang *et al.*, 2006; Zhang *et al.*, 2010), electrodeposition of gold nanoparticles in electrolytic solution containing gold salt or acid (Mohanty, 2011) and block polymer mediated growth of gold nanoparticles (Sakai and Alexandridis, 2005). The sizes and colour of the nanoparticles is determined by the type of synthesis route and variations in concentration of synthesis parameters. The nanoparticles colour depends on the size of particles formed, with deep red colour for nanoparticles less than 100nm and blue/purple colour for larger particles. .

Gold nanoparticles also exist in other forms such as nano-shells, nano-rods and nano-cage based on their sizes, shape and physical properties. The synthesis of these forms of gold nanoparticles depends on their need for specific applications. Gold nanoparticles or other gold forms do not react with air, acids and most reagents but dissolve in aqua regia (mixture of freshly prepared concentrated nitric acid and hydrochloric acid in ratio 1:3), mercury and alkaline solution of cyanide.

Gold shell nanoparticles are non-toxic in nature, biocompatible and have excellent conductivity which enables them to act as electron pathways or mediators between proteins and electrode surfaces in biosensor and immunosensor applications. The high surface area and biocompatible nature of gold nanoparticles enables them to facilitate high enzyme loading and also to retain their bioactivity (Saxena *et al.*, 2011). Gold nanoparticles have strongly enhanced optical properties which makes them suitable for cancer therapy (Huang and El-Sayed, 2010).

The optical properties of gold nanoparticles result from their ability to absorb and scatter light orders of magnitude which is a characteristic mostly found in noble metals. This strong light absorption is due to coherent oscillation of conduction band electrons also known as surface plasmon oscillation caused by interaction with an electromagnetic field (El-Brolosy *et al.*, 2008; Huang and El-Sayed, 2010). The optimal point of the amplitude of the oscillation at a specific frequency is referred to as surface plasmon resonance (SPR). The nature of the surface plasmon resonance and the width of the plasmon absorption band depends on the nanoparticles sizes. Gold nanoparticles have surface plasmon resonance band in the visible region around 520 nm (Huang and El-Sayed, 2010). Nanoparticles with very small size (e.g. 2 nm) do not show surface plasmon bands and damp surface plasmon resonance is observed when particles are less than 10nm. Increasing nanoparticles sizes forces the surface plasmon resonance wavelength to red shift with increased intensity and band broadening occurs when the nanoparticle are greater than 100 nm. The band broadening is due to the dominant contributions from higher order electron oscillations.

## **1.9 Gold nanoparticles synthesis**

Gold nanoparticles can be synthesized through different synthetic routes but the most common method applied in biomedical and biosensor applications are the colloid and electrodeposition techniques.

### **1.10 Colloid gold technique**

Colloidal gold are nanometer size gold particles suspended in fluids such as water or organic liquids. Different methods can be applied in the synthesis of colloidal gold and the resulting gold particle size and properties depends greatly on the method of preparation .This in turn determine the gold nanoparticles colour, their mode of functionalization and applications in various field. The most common colloidal gold synthesis techniques are the Turkevish, Brust, Perrault and Martin methods.

#### ***1.10.1 Turkevish technique***

This is a simple technique that was pioneered by John Turkevish and his co-workers in 1951 (Kimling *et al.*, 2006) before being modified by various researchers . The method

simply involves reacting small amounts of sodium citrate solution in boiling chloroauric acid solution. The method is used to synthesized mono-dispersed spherical gold nanoparticles with size range 10-20 nm. The citrate acts as reducing, stabilizing and capping agent for the gold nanoparticles and is responsible for the gold colloid surface negative charge. Altering the amount of citrate ions in this method i.e. using smaller amount of citrate in the solution results in the formation of large gold nanoparticles size up to 190 nm (Kimling *et al.*, 2006) with less mono-dispersity.

### ***1.10.2 Brust Method***

This is an organic route for the synthesis of gold colloid that was first used by Mathias Brust and co-worker (Brust *et al.*, 1994). The method involves reacting chloroauric acid solution with organic solution that are immiscible with water such as toluene solution containing tetraoctylammonium bromide (TOAB) and sodium borohydride ( $\text{NaBH}_4$ ). The toluenes act as reducing agent and the  $\text{NaBH}_4$  act as anti-coagulant agents. TOAB functions as a stabilizing agent and also as transfer catalyst between the liquid-liquid phases in the system. TOAB is known to have poor binding affinity to gold and often leads to the aggregation of the colloid gold nanoparticles with time. Therefore modification of this method with stronger covalent binding and stabilizing agent such as thiol has been used to in synthesizing gold nanoparticles within the range 5-6 nm in organic liquids (Manna *et al.*, 2003).

### ***1.10.3 Perrault Method***

This is an organic method of synthesizing colloid gold nanoparticles through the use of hydroquinone (benzene-1,4-diol or quinol) as reducing agent. The method involves synthesizing gold seeds through citrate reduction and forming aqueous solution with the gold seed and chloroauric acid ( $\text{HAuCl}_4$ ) and then using hydroquinone as the reducing agent in forming gold nanoparticles. This method produces gold nanoparticles of size range 30-250 nm (Perrault and Chan, 2009).

### ***1.10.4 Martin Method***

This method produces gold nanoparticles by simply reducing chloroauric acid in water with sodium borohydride without the need for a stabilizing agent. Gold nanoparticles

synthesized through this method are stable, nearly mono-dispersed with size distribution of 3.2-5.2 nm (Martin *et al.*, 2010).

### **1.11 Electrodeposition method**

This is an electrochemical technique of synthesizing gold nanoparticles and the most promising methods compared to the other techniques. It is a binder free, simple, less expensive and easy to carry out method of synthesizing gold nanoparticles. It involves the application of electrical potential between a conducting electrode and a counter electrode in an electrolytic solution of gold salt or acid (HAuCl<sub>4</sub>). This results in the formation or deposition of gold nanoparticles on the surface of the working electrode and sometimes the liberation of gas due to the type of redox reaction taking place. It produces gold nanoparticles with controlled morphology, size and composition and this properties can easily be manipulated by simply adjusting the operating conditions (Mohanty and Koucianos, 2006).

### **1.12 Gold nanoparticles functionalization**

Functionalization of nanoparticles plays important role in the stability, functionality, use and biocompatibility of the nanoparticles. This in turn preserves the nanoparticles properties and any bound biological molecules on it. Functionalized gold nanoparticles can be used as building blocks for the attachment of biomolecules, catalysis, core-shell nanoparticles synthesis, surface engineering, bioelectronics sensors and for in-vivo therapeutic applications. Gold nanoparticles are strongly covalently bound to self-assembled monolayer (SAM) surfaces through functional groups such as thiol (-SH), amines (-NH<sub>2</sub>), cyanide (-CN) or polymers

Gold nanoparticles well functionalized have been used in different biosensor and electrochemical sensors applications. High sensitive and stable glucose biosensors has been fabricated for blood glucose detection using gold nanoparticles as the immobilizing substrate due to its biocompatibility and as an electron pathway for the flow of electron between redox solution and proteins (German *et al.*, 2010; Chen *et al.*, 2011; Wang *et al.*, 2011). Electrochemical sensors and immunosensors for antibody/antigen conjugation has been fabricated using gold nanocomposite electrodes (Chen *et al.*; Che *et al.*, 2009; Yang *et al.*, 2009; Jaganathan and Ivanisevic, 2011). The

effectiveness and efficiency of these sensors comes from the biocompatibility and electron transfer ability of gold nanoparticles.

### **1.13 Biosensors**

Biosensors are devices that make use of biological sensing materials (proteins, enzymes, micro-organisms, tissues etc.) to monitor, detect and transmit biological information through a transducer into signals. The two basic component of a biosensor is the biological sensing materials or bioreceptor which monitor and detect molecular changes and a transducer which transform the changes observed by the bioreceptor into signals. The changes from the bioreceptor transformed into signal might be due to changes in pH, heat transfer, electron transfer etc. Sometimes a signal amplifier or processor is used to amplify the signal and read as result. The basic characteristics of biosensors that determine how effective the biosensor can predict physical events taking place are the biosensor sensitivity, response time, selectivity, linearity, detection limit, repeatability and reproducibility.

Biosensor sensitivity is the ability of a biosensor to response to the change when a material is been investigated. It also determines the usefulness of the biosensor in specific applications and is often expressed as the ratio of the output signal to the input signal. The response time of a biosensor is the time it takes the biosensor to attain a steady state position when carrying out measurement from the onset of change in the analyte concentration. It is often referred to as the time it takes a biosensor to reach 95% response during investigation (Wang et al., 2006). The selectivity of the biosensor is the ability of the biosensor to minimally detect interferences from chemicals during measurements. The interference determines the selectivity of the biosensor and if the interference is minimal during measurement, the biosensor is said to be more selective and the result more accurately measured. Biosensors selectivity depends solely on applied bio-receptor and transducers.

The point where the biosensor attains maximum linear value in its calibration curve is referred to as the linearity of the biosensor. This is normally achieved by measuring the increasing or decreasing response when the concentration of the analyte is varied during measurement. When no significant change in the response of the biosensor is observed

during analyte investigation, the biosensor is said to have reached its detection limit or limit of the linear range at low concentration. The repeatability of a biosensor deals with the ability of the biosensor to repeat the same result when a sample is re-run or repeat results that will be closely related to a similar result from a different run. The reproducibility of the biosensor determines how effective the biosensor can reproduce its previous result if re-run in another laboratory operated by different workers. It also determines the commercial viability of the biosensor. These characteristics are also applicable in the different types of biosensors.

Biosensors are classified either by their detection mode or the type of biological recognition elements used. In terms of the detection mode or transduction, they are classified as electrochemical, calorimetric, piezoelectric and photometric biosensors. In terms of the type of bioreceptors, they are classified as enzyme electrodes biosensors for enzymes, Immunosensors for antibody and antigen detection, DNA sensors (DNA), and microbial sensors for organelles or microbial cell.

#### **1.14 Immunosensors and immunoassay**

Immunoassays uses antibody as specific recognition reagent to detect analyte (antigens). The specific binding of an antibody to an antigen are classified into two formats, homogenous immunoassay and the heterogeneous immunoassay. The homogeneous immunoassay assay format does not require physical separation of the antibody-antigen bound complexes from unbound antigen molecules. The heterogeneous immunoassay requires separation of the unbound immune reagent (antigen) from the antibody-antigen bound complexes by washing them out of the system. In this immunoassay format, antibody-antigen bound complexes are bound to a solid substrate which allows for the retention of the molecule of interest as the unbound once are washed off. The heterogeneous assays are more reliable, versatile, sensitive and more specific (Ju *et al.*, 2011).

Solid substrates for the heterogeneous immunoassay are made of biocompatible materials and are often prepared with excess immunological elements (antigen or antibodies). Immobilization of the antigen or antibodies on the substrate vary from substrate to substrate, and the orientation of the antibodies and its optimum density

plays important role in achieving optimal antigen-antibodies reaction and minimal destruction of the paratope on the substrate (Luppa *et al.*, 2001). Immobilization techniques such as physical adsorption, covalent bonding and embedding are often used on heterogeneous immunoassay format. The two most common heterogeneous immunoassay strategies are competitive and sandwich methods.

In competitive immunoassay sample antigens and labelled antigens compete for limited binding site of the antibody immobilized onto a substrate and the bound label signal detected after washing off the unbound antigens. The detected signal is inversely proportional to the antigen concentration in the sample (Ju *et al.*, 2011). In sandwich immunoassay the antigens are captured by a highly specific primary antibody immobilized onto a substrate followed by the binding of the captured antigen with a labelled secondary antibody which acts as tracer and provide a signal that is directly proportional to antigen concentration in the sample after washing off excess tracer. The antigen in sandwich immunoassay must have at least two antigenic epitope capable of binding to the two different antibodies. Monoclonal or polyclonal antibodies are either used as capture or detection antibodies in Sandwich systems. But the polyclonal antibody is most preferable in order to bind as much of the antigen as possible.

Immunosensor is a type of biosensor that detects antibody-antigen interaction and relay these complementary interactions between the antibody and antigen through a transducer as signal. The working principle of immunosensor is the same as the working principles applied in solid phase immunoassay, where antibody or antigens are immobilized on the sensor surface. The sensitivity and specificity of the immunosensors are determined by the affinity and specificity of the antibody- antigen and the level of background noise from the transducer (Morgan *et al.*, 1996). The use of immunosensors to analyse extensive range of samples such as drugs, hormones, pollutants and diseases with quick and highly sensitive immunological response have led to increased interest in its manufacture. A typical immunosensor set up is shown in Figure 1.5.

There are two categories of immunosensors based on their mode of detection, direct and indirect immunosensors. Direct immunosensors detects directly the antibody-antigen interactions without the use of labels while the indirect immunosensors uses a separate

labelled species such as enzymes or fluorescent to aid the detection of the antibody-antigen interactions. Indirect immunosensors are less affected by non-specific binding phenomena, but direct immunosensors have advantage over the indirect once because of its simplicity and ability to carry out real time monitoring of samples (Rahman *et al.*, 2007).

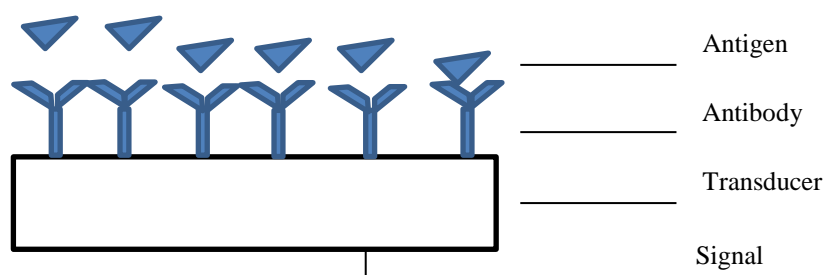


**Figure 1.5 Typical immunosensor set up with antigens and antibodies (receptor) immobilized onto solid sensor surface (transducer).**

Immunosensors can also be classified into four different types based on the type of transducer applied and signal result. The four basic types of immunosensors are: electrochemical (potentiometric, amperometric, or conductimetric), mass (piezoelectric or acoustic), heat (calorimetric) and optical immunosensors. All these type of immunosensors can be run as direct or indirect immunosensors. Among these different types of immunosensors, the electrochemical immunosensor is known for its high sensitivity, high detection speed, easy handling and fabrication (Sun *et al.*, 2011).

### **1.15 Electrochemical immunosensors**

Electrochemical immunosensors uses electrochemical transducer to detect and measure the immunochemical reaction between an antibody and a specific antigen. The immunochemical reactions results in the generating or depleting of electrons or ions on the surface of an electrode. These types of immunosensors are highly sensitive, less expensive, easy to operate and have a high selectivity which makes them easily acceptable and applicable compared to other types of immunosensors. Electrochemical immunosensors can be classified into three categories namely: potentiometric, amperometric and conductimetic based on their operating principles.

### **1.15.1 Potentiometric immunosensors**

This type of immunosensor measures the potential resulting from the selective binding of ions to an electrode or sensing surface due to changes in the ionophoric properties resulting from antibody-antigen conjugation. The potentials generated are measured by a working and reference electrode both in contact with a solution and it is proportional to the activity of ions present in the solution but logarithmic with concentration as shown in Nerst equation in equation 1.8 and 1.9. This forms the basis for the fabrication of the ion-selective electrodes (ISE), in which ions present in a sample are selectively bound to electrode surface and a charge separation occurs between the sample and the electrode surface which is then measured.

$$E = E_0 + \frac{RT}{nF} \ln \frac{[Ox]}{[Red]} \quad 1.8$$

Where E is the electrode potential,  $E_0$  is the standard electrode potential, [Ox] and [Red] are the concentration of the oxidized and reduced forms of the system, F is faraday constant and n is the number of moles of electron transferred in the cell reaction. For the case of ionic concentration, the concentration (c) is replaced by the activity of ions (a);

$$a = \gamma c \quad 1.9$$

Where,  $\gamma$  represents the activity coefficients.

Sometimes field effect transistor (FET) which allows for the detection and conversion of any charges that are built up on the electrode surface into measurable response without depleting the current or electrode are incorporated with the ISE (Morgan *et al.*, 1996). This has led to the fabrication of an advance ion sensitive field effect transistor (ISFET) which is more sensitive and selective with minimal interference of signal.

### **1.15.2 Amperometric immunosensors**

Amperometric immunosensors measure the intensity of current flow generated when antibody-antigen electrochemical reactions occurs at a forced or constant potentials. The intensity of the current measured is proportional to the concentration of the antibody-

antigen immune-complex being investigated (Morgan *et al.*, 1996). This immunosensor makes use of a working electrode either as anode or cathode and reference electrodes for the detection of the redox reaction or immunochemical reaction taking place due to antibody- antigen conjugation.

Most available amperometric immunosensors uses electrochemical active labels directly or product from an enzymatic reaction to facilitate the electrochemical reaction of analyte at the electrode surface. This makes it difficult for the fabrication of direct amperometric immunosensor since most proteins analyte for amperometric detection cannot act as redox couples in electrochemical reactions (Luppa *et al.*, 2001). Despite this disadvantage, this type of immunosensors have linear analyte sampling range which results in its excellent sensitivity compared to the logarithmic relationship found in the potentiometric system (Luppa *et al.*, 2001).

### ***1.15.3 Conductimetric/capacitive immunosensors***

This type of immunosensor measures changes observed in electrical conductivity or capacitance in a solution at constant voltage due to biochemical reaction which produces or consumes ions. The production or consumption of ions changes the overall conductivity of the solution which is then measured. This type of sensors is designed with the bioactive materials e.g. enzymes, antibodies, proteins attached to a noble metal surface or electrodes such as gold, or platinum and changes in conductance that occur in the solution containing the samples are measured by applying an electric field.

### **1.16 Piezoelectric or acoustic immunosensor**

This type of immunosensors generates acoustic wave through the oscillation of piezoelectric crystals at high frequency (30-200 MHz) when an alternating voltage is applied across inter-digital electrodes. The immobilization of biological recognition element on the crystal produces a change in the resonance frequency or a decrease of the acoustic wave and the change in the velocity of the acoustic wave is recorded by a second inter-digital electrode as signal. The change in velocity recorded is proportional to the concentration of the analyte of interest. This type of immunosensors is limited in their applications because of the effect of factors such as temperature, pressure and surface conductivities which can alter the acoustic wave properties.

### **1.17 Calorimetric immunosensors**

This type of immunosensors also referred to as thermal immunosensors makes use of heat sensing transducer or thermistors to detect the changes in temperature of a biological analyte immobilized on it or biological analyte in solution. The biological analyte in solution might be due to enzymatic catalysed reaction giving out heat or antibody action in detecting specific antigen. The results are often read as analyte concentration in the solution. This type of immunosensors is widely used in determining analyte concentrations in fermentation and environmental analysis.

### **1.18 Optical immunosensors**

Optical immunosensor uses optical transducer to detect the change in the intensity of light absorbed by certain materials which might be reactants or products from biological and chemical systems. The materials are capable of absorbing fluorescence, luminescence, bioluminescence and chemiluminescence light depending on their surface. Optical immunosensor can be direct sensing without the use of labels such as ellipsometry, surface plasmon resonance or indirect sensing which makes use of enzymes, antibodies or other biological materials to generate light absorbing products.

### **1.19 Antibodies**

Antibodies also referred to as immunoglobulin (Ig) are glycoprotein produced by plasma cells (B cells) that bind specifically to foreign molecules (antigen) or immunogen. Antibodies can be polyclonal or monoclonal. Polyclonal means that the antibodies come from clones of separate B-cells and different antibodies in this group react with different antigen determinant. Monoclonal antibodies are from one clone of B-cells and reacts with one specific antigen. The monoclonal antibodies are highly specific and has better sensitivity compared to the polyclonal antibodies

Structurally antibodies are composed of two identical light chains and two identical heavy chains linked together by disulphide bonds. The heavy and light chains are further divided into two regions based on the variability of the amino acid sequence in the chains into variable light chains ( $V_L$ ), constant light chains ( $C_L$ ), variable heavy chains ( $V_H$ ) and constant heavy chains ( $C_H$ ) as shown in the Figure 1.6 (Kumagai *et al.*,

2010). The antibody has a hinge region which allows for its flexibility therefore forming a Y shape molecule. The structure is also divided into two fragments, the Fab (fragment antigen-binding) fragment which is the antigen combining site of the antibody and the Fc (fragment crystallisable) fragments which has the ability to fix to cell surface and are easily crystallized. They contain the heavy chains CH<sub>2</sub> and CH<sub>3</sub> domains and carbohydrates are attached to the CH<sub>2</sub> domains in most immunoglobulin and sometimes in other regions.

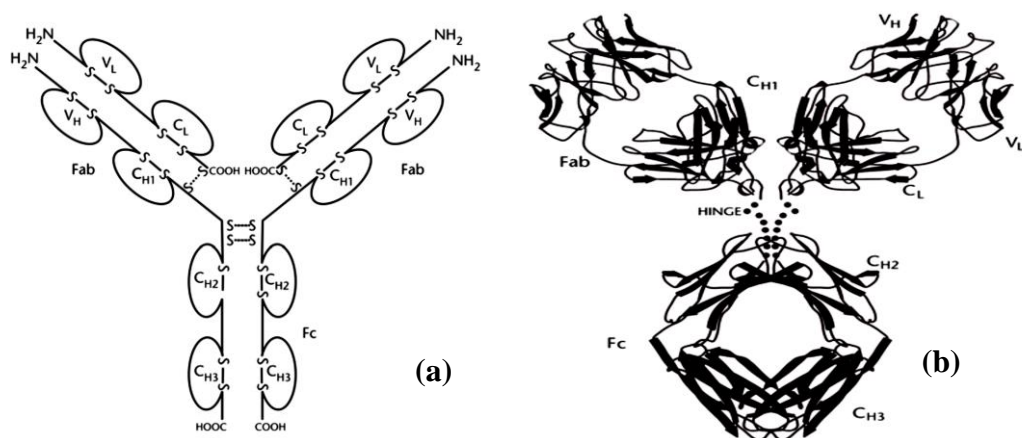


**Figure 1.6 (a) Generalized structure of immunoglobulin (IgG) and (b) its three dimensional structure**

Immunoglobulin are divided into five classes based on the differences in their amino acid sequence and the number of domains in the constant regions of the heavy chains namely: IgG (gamma heavy chains), IgM (mu heavy chains), IgA (alpha heavy chains), IgD (delta heavy chains) and IgE (Epsilon heavy chains). The IgM and IgG antibodies primary functions is to respond to invading foreign substance, IgA protects mucous membranes, IgE protects against parasites while no specific function of IgD is known.

Among the classes of immunoglobulin, the IgG is the most versatile and extensively studied because of its ability to carry out all the functions of immunoglobulin.

Immunoglobulin can also be classified into subtypes based on the differences in amino acid sequence in the constant region of the light chain as Kappa light chains ( $\kappa$ ) and Lambda light chains ( $\lambda$ ).

## **1.20 Antibody-Antigen binding**

The main function of antibody is the binding of an antigen and protecting of the host. The binding of an antigen to antibody is highly specific and antigen binds to an antibody through its antigenic determinant (epitope). The epitope binds the antigen binding site in antibody (paratope) located in the Fab fragment section of the antibody which contains the  $V_L$  and  $V_H$  chains. The binding of antigen epitope and antibody paratope occurs only when they both have the same combination of  $V_L$  and  $V_H$  chains. This also determines the binding strength of the epitope and paratope (affinity). Specific binding of an antibody and antigen is held together by non-covalent bonds including electrostatic force, hydrophobic attraction, hydrogen bonding and Van der Waals interaction between the antigen and the amino acids of the binding site (Ju *et al.*, 2011).

## **1.21 Immobilization of antibody-antigen on substrate**

The type of immobilization technique employed for antibody/antigen conjugation plays important role in determining the sensitivity, stability, reproducibility and effectiveness of an immunosensor or immunoassay. The orientation of the antibody on the solid substrate is of great importance because it determines the availability of antigen binding sites (paratope) for antigen conjugation which in turn affects the effectiveness of the immunosensor. Antibody is said to be properly oriented when the Fc region with no antigen binding site is immobilized onto a solid surface (Lee *et al.*, 2013). Random orientation of the antibody or the binding of antibody active site Fab on solid substrate result in lower antigen binding capacity. Antibody binding or immobilization technique can be divided into two namely: physical and chemical immobilizations.

### ***1.21.1 Physical immobilization method***

Physical immobilization of antibody onto a solid substrate is a cheaper and simple way of immobilizing antibodies to an insoluble matrix. The antibodies are directly adsorbed onto the surface of water insoluble carriers or substrate. This method results in the denaturation and random immobilization of the antibody which in turn lowers the availability of the antibody active site for antigen conjugation. Physical immobilization results in the fabrication of immunosensors with low sensitivity and stability due to weak binding force involved such as Van der Waal's force, hydrogen bond etc.

### ***1.21.2 Chemical immobilization***

Chemical immobilization involves binding proteins or antibody onto a solid substrate through the formation of covalent bonds. This method allows for the specific orientation of the antibody on a solid substrate which increases the antigen binding ability. This in turn increases the sensitivity, stability and effectiveness of the immunosensor or immunoassay. Functional groups such as amino, hydroxyl, thiol, carboxyl groups etc. are used as chemical cross-linkers to create strong covalent bond with the antibody onto solid substrate. Despite the advantages of the chemical immobilization technique compared to the physical method, the chemical immobilization technique also has some setback. The immobilization method is a complex procedure and can damage the proteins or antibody active site through induced crosslinking of antibodies to antibodies. This reduces the availability of antigen binding sites and leads to loss of antibody activities.

### **1.22 Research question and hypothesis**

How can we improve on the sensitivity, reproducibility, stability and selectivity of AD biomarkers as a supportive measure in the clinical diagnosis of AD, specifically the use of plasma immunoglobulin as biomarkers?

Research has shown that the use of biomarkers from cerebrospinal fluids or plasma can detect changes in the concentration of amyloid beta proteins (A $\beta$  40 and 42) and neuronal cell line proteins such as tau and phospho-tau proteins in AD patient compared to non-AD patient. The use of plasma immunoglobulin as biomarker in ELISA technique for AD monitoring has also shown changes in the concentration of plasma immunoglobulin in AD patient compared to AD patients treated with cholinesterase inhibitor. Despite this developments these biomarkers still faces the problem of controlling repeat sampling, technically challenge, complex analysis, high cost and still not proven to effectively detect and monitor the progression of AD.

The development of direct immunosensor electrode that will detect directly the conjugation of plasma immunoglobulin (antigen) with specific antibody immobilized on the surface of gold electrode and the use of iron oxide core-gold shell nanoparticles as immobilizing substrate, will be a cheaper, faster, sensitive, reproducible and more

reliable way of detecting and monitoring AD progression. The immunosensor when developed can also be incorporated into portable devices for online measurement of the early onset and late onset monitoring of AD progression.

### **1.23 Thesis organization**

There are three project chapters in this thesis work with the exception of chapter one, two, six and seven. Each project chapters have different goals and focus, but the nanoparticles synthesized from the first two project chapters were used to achieve the goal of the last project chapter.

Chapter one of this dissertation gives background knowledge of immunosensors, immunoassay, nanomaterials specifically iron oxide-gold shell nanoparticles, their synthesis, properties and applications in biomedical fields. It also looks into the problem faced with the diagnosis and monitoring of the progression of Alzheimer's disease in patients through the use of CSF biomarkers, plasma biomarkers and plasma ELISA methods. It also looks at the question and hypothesis of existing AD biomarkers and gives the reason why plasma immunoglobulin biomarker immunosensor will be a better and reliable option compared to the other methods.

Chapter two of this thesis looks into the state of art equipment used in the characterization of iron oxide nanoparticles and gold nanoparticles synthesized and also for the fabricated depleted plasma immunosensor electrode. Physical characterization and electrochemical characterization of the nanoparticles were carried out. The physical characterization techniques include X-ray diffraction (XRD), X-ray photoelectron spectroscopy (XPS), scanning electron microscopy (SEM), transmission electron microscopy (TEM) and UV-Vis spectroscopy. The electrochemical characterization technique of the nanoparticles and immunosensor electrode was carried out through the use of cyclic voltammetry (CV) and electrochemical impedance spectroscopy (EIS).

The project in chapter three describe the synthesis of magnetite iron oxide nanoparticles ( $\text{Fe}_3\text{O}_4$ ) through oxidative alkaline hydrolysis of ferrous salt (iron II sulphate) and the effect of synthesis parameters such as temperature, salt concentration, hydroxyl concentration and synthesizing under the influence of revolution per minute on the

nanoparticles. It also looks at the type of impurity or by-products that accompany the synthesized iron oxide nanoparticles by altering these parameters.

The project in chapter four looks at the formation of iron oxide core-gold shell nanoparticles ( $\text{Fe}_2\text{O}_3$ -Au Nps) by synthesizing maghemite iron oxide nanoparticles ( $\gamma$ - $\text{Fe}_2\text{O}_3$ ) from the oxidation of  $\text{Fe}_3\text{O}_4$ . Gold shell nanoparticles were subsequently formed on the  $\text{Fe}_2\text{O}_3$ -Au Nps through the iterative reduction of chloroauric acid with hydroxylamine as reducing agent. This chapter also look at the role of polyethyleneimine (PEI) a polycation used in stabilizing and capping of the nanoparticles. Specifically the effect of temperature and agitation on polyethyleneimine (PEI) adsorption on iron oxide nanoparticles and how it affects the formation or attachment of gold nanoparticles on the surface of the iron oxide nanoparticles in the formation of iron oxide core-gold shell nanoparticles.

Project chapter five looks at the fabrication of depleted plasma immunoglobulin immunosensor electrode for AD detection and monitoring. The plasma immunoglobulin (Ig) was used as the antigen while anti-human immunoglobulin (polyclonal rabbit Anti-human IgA, IgG, IgM) as the specific antibody to the antigen. Firstly the plasma immunoglobulin biomarker immunosensor electrode was developed using gold electrode surface as the immobilizing platform and secondly iron oxide-gold shell nanoparticles synthesized in chapter four was used as immobilization substrate for the antibody/antigen conjugation on the gold electrode. Depleted plasma samples containing immunoglobulin as the major constituent from AD patient and control subjects where used for the analysis. The two different immunosensor for AD was compared with similar samples carried out through the use of ELISA method with UV-Vis spectroscopy analysis.

Chapter six of this thesis work looks at the general conclusion obtained from the results and analysis of the three project chapters (3, 4 and 5) and possible recommendations to improve on the results. Chapter seven is the appendices section of this thesis work.

## Chapter 2

### Physiochemical analytical techniques

This chapter looks at the state of art equipment used in the characterization of the nanoparticles ( $\text{Fe}_3\text{O}_4$ ,  $\text{Fe}_2\text{O}_3\text{-Au}$ ) and immunosensor electrode and their basic principle, uses and mode of operation. The characterization of the nanoparticles is based on both physical and electrochemical techniques. The physical technique looks at the composition, structure, crystallography, conductivity and optical properties of the nanoparticles. The electrochemical technique looks at the electrochemical properties of the nanoparticles such as electron transfer ability, resistance to charge transfer, reaction kinetics, surface modification and double layer capacitance.

#### 2.1 Physical characterization techniques

##### 2.1.1 X-ray diffraction

This is an analytical technique in crystallography widely used in measuring the molecular structure, atomic structure, chemical bonds and defects found in crystals. This technique is often used in biochemistry, chemistry, chemical engineering etc. to determine the structure of DNA, protein, inorganic compounds and variety of molecules. Its working principle is based on the use of x-ray beams to bombard crystal sample at suitable angles resulting in reflected or diffracted beams from the crystalline atoms in different directions. The combination of the angle of diffraction beam and their intensities are then used as a measure to determine the composition of the crystal or their lattice spacing.

Crystalline materials have atoms arranged in regular patterns and each unit cell of the crystals contains smallest volume element that describe the crystals. When an x-ray electromagnetic beam is bombarded through the closely spaced lattice in crystal samples, the electrons surrounding the atoms of the crystals oscillates at the same frequency with the incident beam resulting in reflected or diffracted beam composed of scattered rays that is characteristic of the atoms in the crystal ('Fundamentals of Diffraction,' 2009) as shown in Figure 2.1.

Incident ray 1 and 1' reaches the crystals and makes an angle theta with the crystal plane resulting in reflected rays 2 and 2' which comes from series of parallel planes inside the crystals and their orientation and interplaner spacing are defined by the integers or miller indices h, K, l (notations used to identify planes in crystal lattice) at angle 2 theta. The difference in path length 1 to 1' and 2 to 2' is an integral number of wavelengths ( $\lambda$ ). The spacing of the crystal is determined by using the Bragg's law as shown in equation 2.1

$$n\lambda = 2d\sin\theta \quad 2.1$$

Where  $\lambda$  is the wavelength of incident ray beam, n is an integer and d is the distance between atomic layers in a crystal.

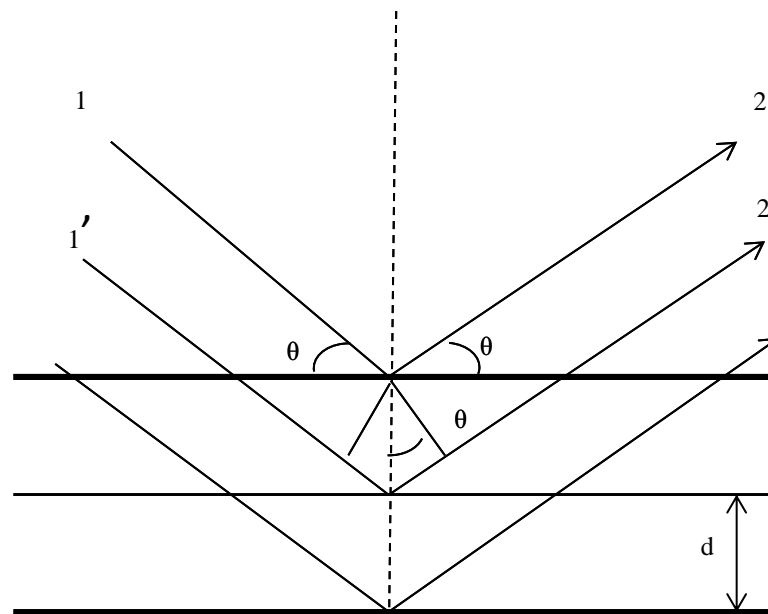


**Figure 2.1 Typical x-ray reflection 2 and 2' resulting from incident ray 1 and 1' on a crystal sample.**

The size of the crystallite is related with the broadening of peak in the diffraction patterns and can be determined by using the shape factor in Scherrer equation as shown below;

$$\tau = \frac{K\lambda}{\beta \cos\theta} \quad 2.2$$

where  $K$  is the shape factor,  $\lambda$  is the x-ray wavelength,  $\beta$  is the line broadening at half

the maximum intensity in radians,  $\theta$  is the Bragg's angle and  $\tau$  is the mean size of the crystalline in ordered domains.

The equipment used for x-ray diffraction analysis is called the x-ray diffractometer and its basic components includes an x-ray tube, detector, sample holder, goniometer circle or measuring circle, scatter slit, receiving slit, soller slit,  $\theta$  and  $2\theta$  indicator, and a filter or monochromator as shown in Figure 2.2A and B (Connolly, 2007).

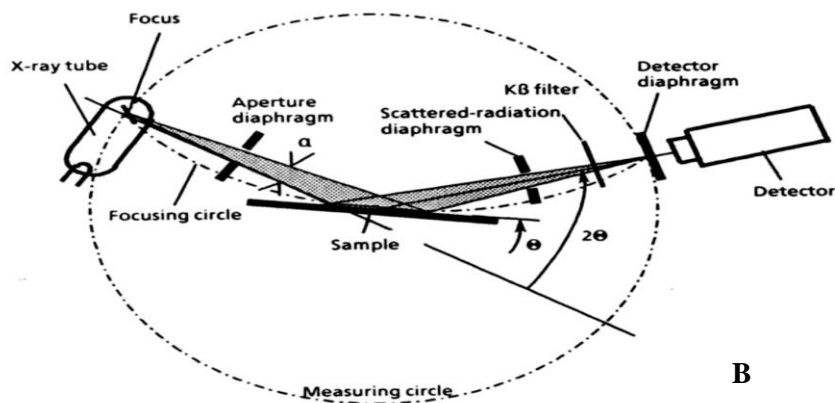
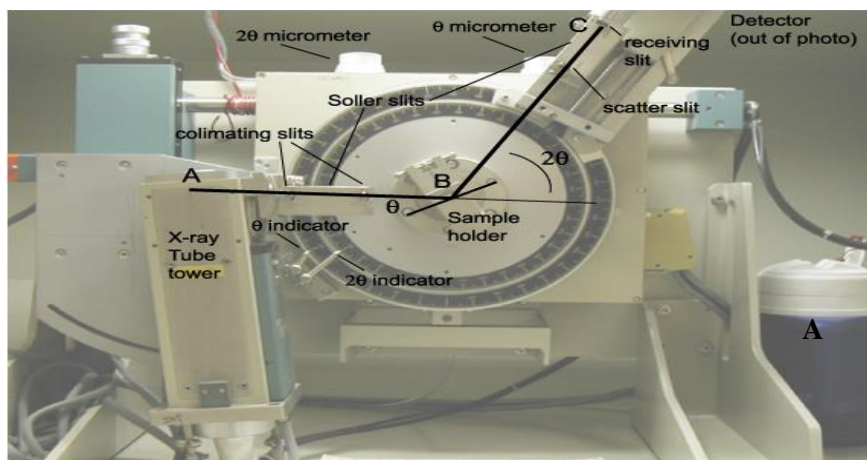


Figure 2.2 A and B shows the component of a diffractometer and diffractometer beam path  $\theta/2\theta$  mode respectively.

The x-ray diffractometer works in scanning range of  $\theta$ - $2\theta$  or  $\theta$ - $\theta$  where the incident and diffracted beam both form the same angle  $\theta$  with the surface of a flat sample while the diffracted beam forms an angle  $2\theta$  with the incident beam. The x-ray radiation is produced in a sealed vacuum tube when high energy electrons strike the anode of a pure metal. Often used is Copper (Cu) x-ray tubes and this generates cu radiations with different wavelength of which Cu ( $K\alpha$ ) is the strongest with wavelength approximately

1.54 angstroms (Å). The Cu (K $\alpha$ ) radiation goes to the goniometer circle where the sample is placed in a holder, and where series of parallel plates (collimating slit, soller slit) arranged parallel to the plane of goniometer circle combined with scattered slit, receiving slit arranged perpendicular to the goniometer circle creates parallel incident beam of x-rays that strikes the sample. The resulting diffracted beam from the sample passes through receiving slit located at the same distance from the sample and the detector end and through the scattered slit which reduces the background before being filtered off copper radiation (K $\beta$ ) by a filter of monochromator.

The beam then passes through a soller slit before entering the detector where data on the sample are recorded. The quality of the data from the x-ray depends on the nature and energy of the radiation, resolution of the instrument, sample preparation and the physical and chemical composition of the sample ('Powder Diffractometry,' 2009).

### ***2.1.2 X-ray photoelectron spectroscopy (XPS)***

X-ray photoelectron spectroscopy is a surface chemical analysis technique that determines the elemental composition, empirical formula, chemical state, core electrons and corresponding binding energy of materials. Materials are known to have atoms in their surfaces with characteristic binding energy that is not necessarily equal to the ionization energy of their electron. During an x-ray photoelectron spectroscopy analysis, x-ray beam are used to bombards sample surface and the energy of the x-ray photon is completely adsorbed by the core electron of atoms in the sample. At larger photon energy ( $h_\nu$ ), the core electrons will escape from the atom and out of the top 0 to 10 nm surface of the materials (Hofmann, 2013). The emitted electrons possess kinetic energy  $E_k$  called photoelectron and the corresponding binding energy of these core electrons is mathematically expressed by Einstein in equation 2.3 and 2.4. Equation 2.5 indicates the absence of work function which can be compensated artificially.

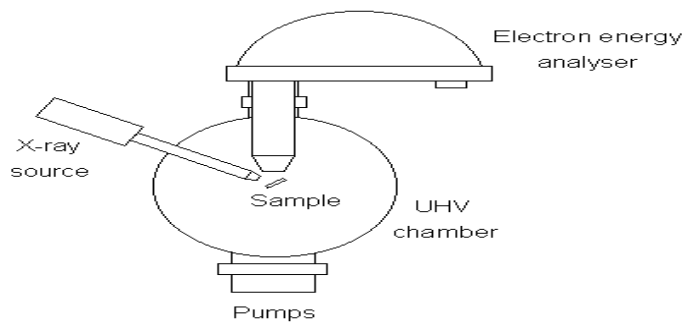
$$h_\nu = E_b + E_k + \phi \quad 2.3$$

$$E_b = h_\nu - E_k - \phi \quad 2.4$$

$$E_b = h_\nu - E_k \quad 2.5$$

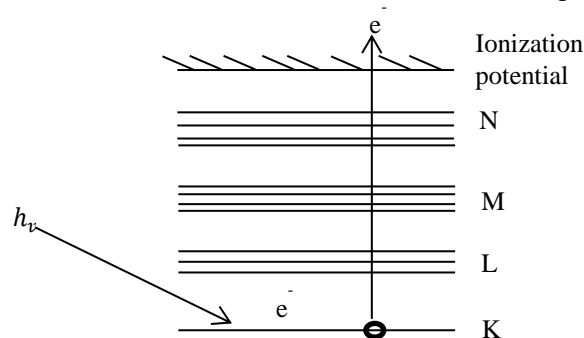
Where  $h_\nu$  is the x-ray photon energy,  $E_k$  is the kinetic energy of photoelectron which can be measured by the energy analyser and  $\phi$  is the work function induced by the analyser or spectrometer about 4~5eV.

Figure 2.2 shows a schematic diagram of typical x-ray photon electron equipment which consists of a fixed x-ray radiation source, an energy electron analyser and a high vacuum chamber. X-ray beams are emitted from the x-ray radiation source and directed towards the sample in the high vacuum chamber. The radiation causes the emission of photoelectrons on the surface of the sample when bombarded and the vacuum chamber allows the emitted photoelectrons to be analysed without interference from gas phase collision. The emitted electrons are then dispersed inside the electron analyser based on their kinetic energy through the use of an electric field between two hemispherical surfaces. This in turn measures the flux of emitted electrons of a particular energy which can be used to identify the sample. The most common x-ray radiation source used in XPS analysis are magnesium ( $Mg K_{\alpha}$  radiation) with photon energy ( $h\nu$ ) of 1253.6 eV and aluminium ( $Al K_{\alpha}$  radiation) with photon energy of 1486.6 eV.



**Figure 2.3 Schematic diagrams showing the major component of XPS equipment**

The energy level diagram for x-ray photoelectron spectroscopy analysis is shown in Figure 2.4. It shows how the emitted electrons due to the photon energy moves through the different electron shells or principal energy levels (K, L, M and N) from K closest to the atom nucleus to the outer N and out of the material being analysed.



**Figure 2.4 Energy level diagrams for x-ray photoelectron spectroscopy**

### **2.1.3 Scanning electron microscopy (SEM)**

This is an electron scanning technique that uses directed beams of electrons to produce images of an analyte at the surface. It is used to analyse the composition, surface topography and electrical conductivities of sample at high vacuum, low vacuum and in wet conditions. It operates by scanning the surface of the sample with high energy beam of electrons in a raster scan pattern, and the electrons interacts with atoms of the sample producing signals that gives information about the sample shape, composition and electrical conductivities.

Samples in scanning electron microscopy are detected in three different basic modes based on the emitted electrons from the atoms of the sample when strike by electron beams. The modes are: (a) the emission of secondary electrons from the surface of atoms and the number of secondary electron emitted is a function of the angle between the surface and the beam which allows for the imaging of tilt in the sample, (b) the emission of back scattered electrons which is the reflection of the electrons back to the direction they came from. The back scattered electron mode allows for the gathering of information about the distribution of element in the sample and (c) the emission of characteristics X-ray from the atoms surface due to the striking electron beam and this gives information about the composition and abundance of element in the sample.

Figure 2.5 shows a schematic diagram of SEM equipment, the equipment is composed of an electron gun, two or more electromagnetic lens, vacuum system, scanning system which includes fine probe and scan coil, a detector and electronic control (TV or computer). The electron gun generates and accelerates electrons at energies around 0.1-30keV (Goldstein *et al.*, 2003). The electron beam passes through the lenses which creates a small focused electron probe on the sample placed in a vacuum. The focused probe of electrons is scanned across the sample surface in a raster pattern with the aid of the scanning coil. The electrons strike the sample surface and up to a depth of approximately 1 $\mu$ M at different points generating electromagnetic radiations as signals.

Selected portion of the generated electromagnetic radiation which includes the secondary or back scattered electrons are picked up by the detector system and amplified as signal on a TV or computer screen. The image produced on the screen or

cathode ray monitor is directly related to each point the electron beam strikes on the sample (Egerton, 2011) and give rise to the linear magnification in SEM. The linear magnification is mathematically related to the raster length of the screen or cathode ray tube and the raster length on the sample as shown in equation 2.6.

$$M = \frac{L}{I} \quad 2.6$$

Where M is the magnification, L is the raster's length of the monitor and I the raster's length on the sample surface. Samples are analysed in SEM either at low magnification or high magnification depending on the information needed.

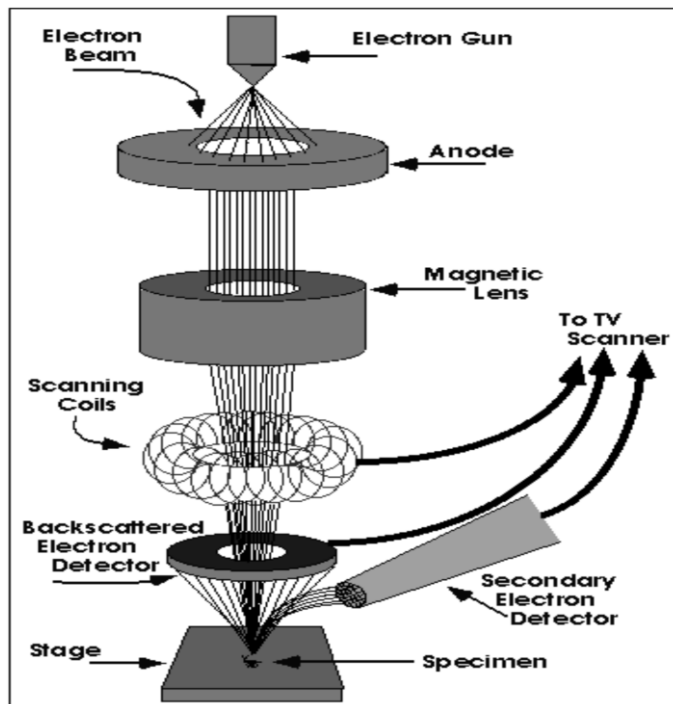


Figure 2.5 Typical SEM equipment operation and components

#### 2.1.4 Transmission electron microscopy (TEM)

Transmission electron microscopy is an electron microscopy technique that is used to characterize samples structure, defects, composition and crystallographic nature. Samples are analysed in TEM when beam of electrons are emitted from an electron source at low wavelength which interacts with the sample and forms an image of the sample. The sample is then magnified with lenses and projected to an imaging detector.

TEM working principles is the same as that of light microscopy but is a thousand times better than the light microscopy due to the lower wavelength of electrons which allows for detailed analysis of samples compared to the use of light in the light microscopy. The principle involves the release of electron from an electron source when the cathode of the source is heated up by current and the electrons accelerated by a high voltage (50-150kV) at the anode up through vacuum. The electrons are confined by passing through two condenser lenses which also determines their brightness and through the condenser aperture before hitting the sample surface in vacuum. The electrons pass through the sample forming elastically scattered beam (transmitted beam) which then passes through the objective lens and objective aperture. The objective lens forms the sample image display and with selected area of the aperture the elastically scattered electrons are collected to form image on the microscope. The electron beams from the objective aperture then passes through sets of magnifying lens consisting of first and second intermediate lenses which control the magnification of the image and a projector lens which projects the image on a screen or monitor as shown in Figure 2.6 (Williams and Carter, 2009b).

Different type of images can be formed in TEM based on the selected aperture and type of electrons selected. Dark field images are formed when the objective aperture selects diffracted beam due to scattered electrons and bright field images are formed when the objective aperture selects unscattered electrons. The wavelength of the electrons determines the resolution of the TEM, thus the shorter the electron waves the higher the power of resolution. The power of resolution is also a function of the quality of lens in the system, specifically the objective lens ability to manage the image (Williams and Carter, 2009a) and the sample preparation method. Other microscopic analytical techniques such as energy diffractive X-ray (EDX), electron energy loss spectrum (EELS) and energy filtered transmission electron microscopy (EFTEM) can also be carried out with the TEM.

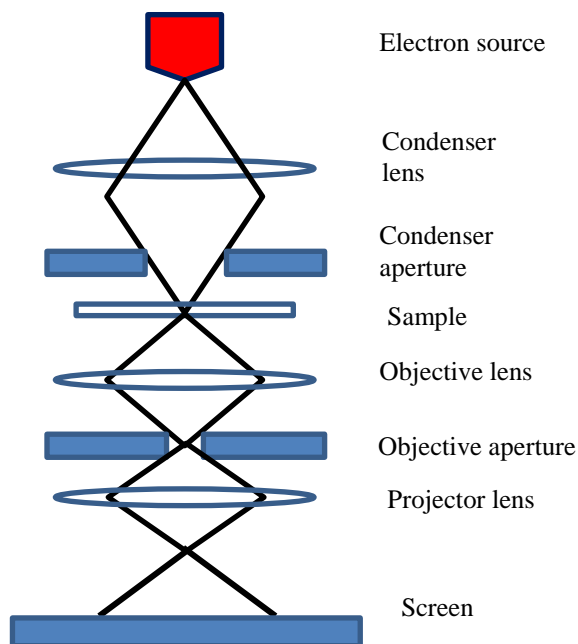


**Figure 2.6 Schematic diagrams of the TEM components**

### ***2.1.5 UV-VIS Spectroscopy***

This is a chemical analytical technique that is used to determine quantitatively the presence of different analytes in solution. Analytes such as metal ions (noble or transition), biomolecules, organic compounds with high degree of conjugations or charge transfer complex compounds in solution can be analysed with UV-spectroscopy. UV-Vis spectroscopy deals with the absorbance of light wavelength by the atoms of a molecule which result in the excitation of electrons in the atoms from the ground state to the excited state within the ultraviolet and visible region of an electromagnetic spectrum. When light wavelength is absorbed by the atoms, some of the light are reflected or transmitted and these result in the change in the colour observed during sample analysis. The more the absorbed light wavelength, the more concentrated the solution and the darker the colour.

For metal ions in solution it involves the excitation of the d electrons from the ground state to the excited state when visible light is absorbed and the resulting colour of the solution also depends on the type of ligands or anions present. Organic compounds can absorb either ultraviolet or visible electromagnetic radiations lights depending on their

degree of conjugation. The absorbance of light in the solution can be used to quantitatively determine the concentration of the absorbing species in solution according to Beer Lambert Law. The law states that the absorbance of a solution is directly proportional to the concentration of the absorbing species in the solution and the path length (Rodger, 2013) as shown in equation 2.7. The law does not hold a universal relationship for the concentration and absorbance of all substances.

$$A = -\log T = \log \frac{I_0}{I} = \epsilon bc \quad 2.7$$

Where A is the absorbance measured,  $I_0$  is the intensity of incident light at a given wavelength, I is the intensity transmitted, b is the path length through the sample, c the concentration of the absorbing species,  $\epsilon$  is the molar absorptivity or extinct coefficient and T is the transmittance.

UV-Spectroscopy analysis focuses on the absorption from the ultraviolet (200-380 nm), visible (280-780 nm) and infrared radiation (0.78-300  $\mu\text{m}$ ) regions of the electromagnetic radiation spectrum. The electromagnetic radiation spectrum is made up of gamma rays, x-ray, ultraviolet, visible, near infrared, infrared, microwave and radio wave each having different wavelength and affects the electronic configuration of atoms in different ways when absorbed. UV-Spectroscopy equipment is called a spectrophotometer and it works by measuring the intensity of light passing through a sample I and compares it to the intensity of light before it passes through the sample  $I_0$ . It is basically composed of five basic parts, light source, sample holder (transparent cuvette), monochromator (prism or grating), and a detector as shown in Figure 2.7.

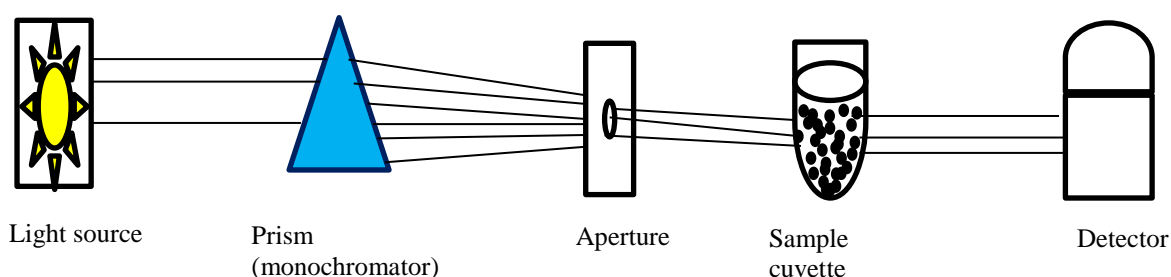


**Figure 2.7 Schematic diagram of the component of UV-Vis spectrometer**

The light source (e.g. tungsten filaments (300-2500 nm)) generates lights which passes through a monochromator (prism) and then separated into different wavelengths. The

light separated into different wavelength then passes through the aperture which selects a single wavelength that goes through the sample (liquid) in a cuvette. The light passes through the sample and some are absorbed by species and also transmitted which is detected by a detector (photodiode or photomultiplier tubes) that allows the intensity of light reaching it to be measured as a function of wavelength. The result is then amplified by a processor and recorded.

## **2.2 Electrochemical techniques**

The electrochemical techniques used in this thesis work for the characterization of the nanoparticles are cyclic voltammetry (CV) and electrochemical impedance spectroscopy (EIS)

### ***2.2.1 Cyclic voltammetry***

Cyclic voltammetry is a potentiodynamic electrochemical technique used in studying and analysing the electrochemical properties of analyte in a solution and their redox potentials. It is often the first electrochemical technique carried out in the study of the electrochemical properties of analyte in solution. It involves the application of potential between a working electrode and a reference electrode in a solution (electrolytic) containing analyte and then measuring the current between the working and a counter electrode. The current of the working electrode is then plotted against the applied potential forming a cyclic voltammogram trace as shown in Figure 2.8.

The cyclic voltammogram trace shows the reduction of analyte due to the application of a negative initial potential resulting in cathodic peak current scan ( $I_{pc}$ ) and a corresponding cathodic peak potential ( $E_{pc}$ ) at point C. The potential reaches a switching potential (D) which has enough voltage that causes the oxidation of the analyte to an anodic peak current ( $I_{pa}$ ) and corresponding anodic peak potential ( $E_{pa}$ ) at point F. The anodic peak current is attained when all the analyte at the surface of the working electrode is completely oxidized. The oxidation and reduction of analyte on the electrode surface results from the movement of electrons across the electrode surface (Stojek, 2010). The redox potential ( $E^0$ ) of the analyte represents the potential where the reduced analyte or species equals the oxidized species and is obtained at half the height

of the cathodic peak and anodic peaks (Scholz, 2010) as shown in equation in equation 2.8.

$$E^o = \frac{(E_{pa} + E_{pc})}{2} \quad 2.8$$

Cyclic voltammetry analysis also ramps time (scan rate) against the working electrode potential measured against a reference electrode forming a reversible wave form as shown in Figure 2.9. The waveform is scanned forward negatively with greater potential at point (a) and the current keeps increasing as the potential reaches the analyte reduction potential ends at lower potential point (d) where the analyte is depleted. Point d is the switch potential and the reverse scan which is the re-oxidation of the analyte starts and ends at point (g). The forward scan of the waveform produces current peak for analyte reduction within scanned potential range and the reverse shows the analyte oxidation and the scan direction can be changed depending the type of analyte, thus for analyte that undergoes oxidation first, the scan potential will be positive first before reduction.

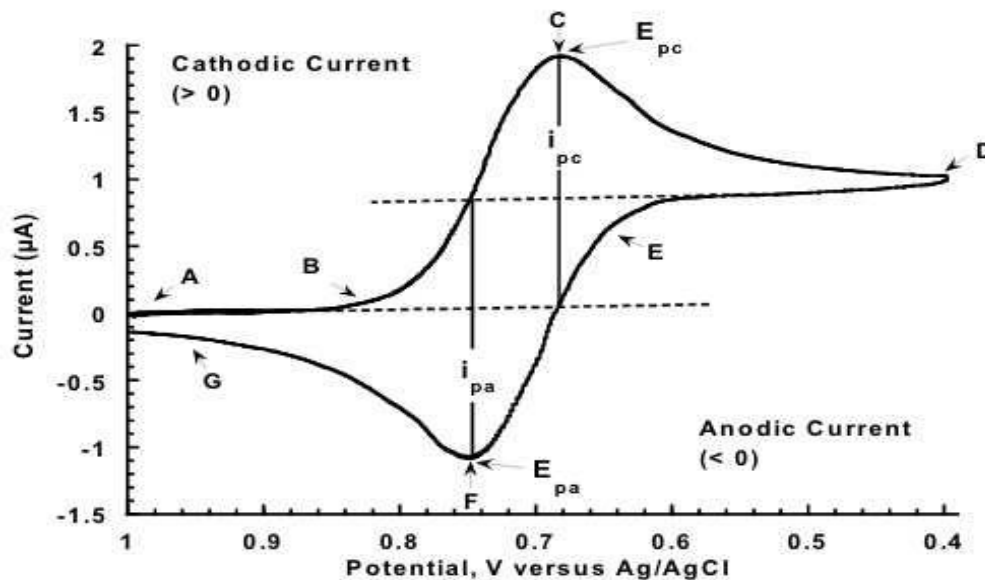
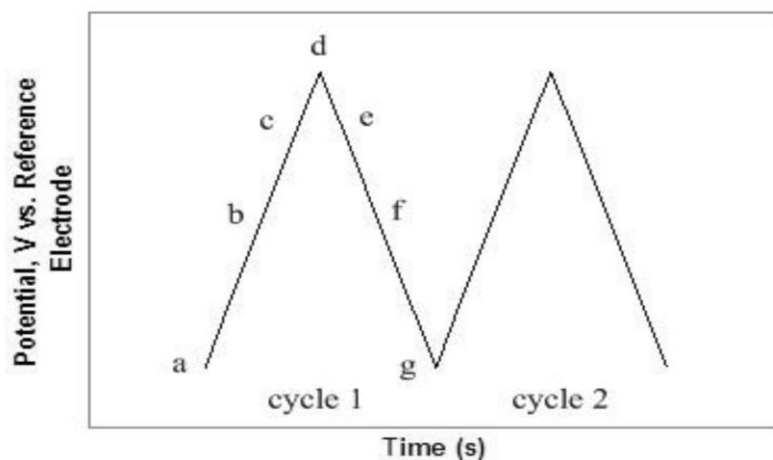
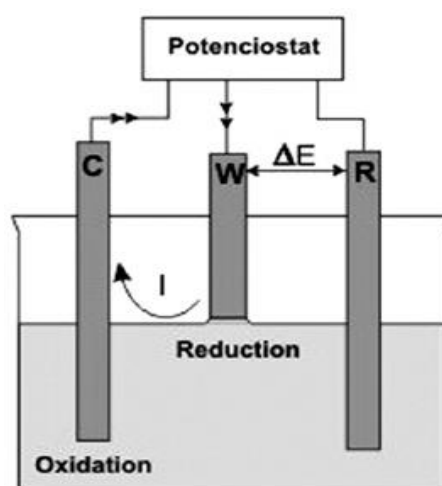


Figure 2.8 Typical cyclic voltammogram curve showing the cathodic and anodic peak currents and potentials.



**Figure 2.9 Typical cyclic voltammetry potential wave form.**

Cyclic voltammetry equipment is composed of a three electrode system made up of working electrode, a reference electrode (calomel or Ag/AgCl) and a counter electrode (platinum), a potentiostat, measurement cell and a recording device (computer system). The operation simply involves the placement of analyte in an electrolytic solution in cell with three electrode set up and then applying a potential between the reference electrode and the working electrode with the aid of a potentiostat. The corresponding current is automatically measured between the working electrode and the reference electrode as shown in Figure 2.10 (Rico *et al.*, 2009).



**Figure 2.10 Schematic diagram of electrochemical cell with three electrode system**

### 2.2.2 Electrochemical impedance spectroscopy (EIS)

Electrochemical impedance spectroscopy is used to measure a system response to varying frequencies. This allows for the characterization of electrode processes, complex interface, charge transfer resistance determination, double layer capacitance and ohmic resistance (electrolyte resistance) of the system. Also information on the general electrochemical processes and reaction kinetic involved in the processes can be obtained. The EIS principle is based on the opposition or resistance of alternating current (impedance) flowing in a system under investigation over range of frequencies and the result is plotted on a Nyquist plot or Bode plot.

The Nyquist plot displays the real component of the impedance against the imaginary component of the impedance in EIS experiment. In the Nyquist plot a semi-circle arc is formed on the real axis at high frequencies (high kHz range) which shows the resistive displacement caused by electrolyte impedance (Yeu *et al.*, 1991). The plot is dominated by processes occurring at or very close to an electrode surface. When an electrode is modified with a layer of nanoparticles or film, the film resistance ( $R_F$ ) is in series with the charge transfer resistance ( $R_{CT}$ ) at high frequencies at the real axis. The impedance of the film is the difference between when film is present on the electrode surface and the absence of film on the electrode surface (Yeu *et al.*, 1991). In the absence of any major difference, the electrolyte is said to have effectively penetrated the film and the film resistance can be considered negligible (Armstrong *et al.*, 1986).

The semi-circle arc can also be formed at lower frequencies due to the parallel effect of the charge transfer resistance of the redox process and double layer capacitance at the electrode surface (Deslouis *et al.*, 1989).

Figure 2.11 (A) shows typical Nyquist plot for an electrode modified with a layer of film. It shows the real ( $Z'$ ) and imaginary parts ( $Z''$ ) component of the impedance, electrolyte resistance ( $R_S$ ), immobilized film resistance ( $R_F$ ), resistance to charge transfer ( $R_{CT}$ ), low frequency capacitance ( $C_{LF}$ ) and frequency  $\omega$ .

The semi-circular arc appearance in the Nyquist plot can be explained through the use of Randles equivalent circuit in Figure 2.11 (B) for simple charge transfer as shown in the reaction in equation 2.9

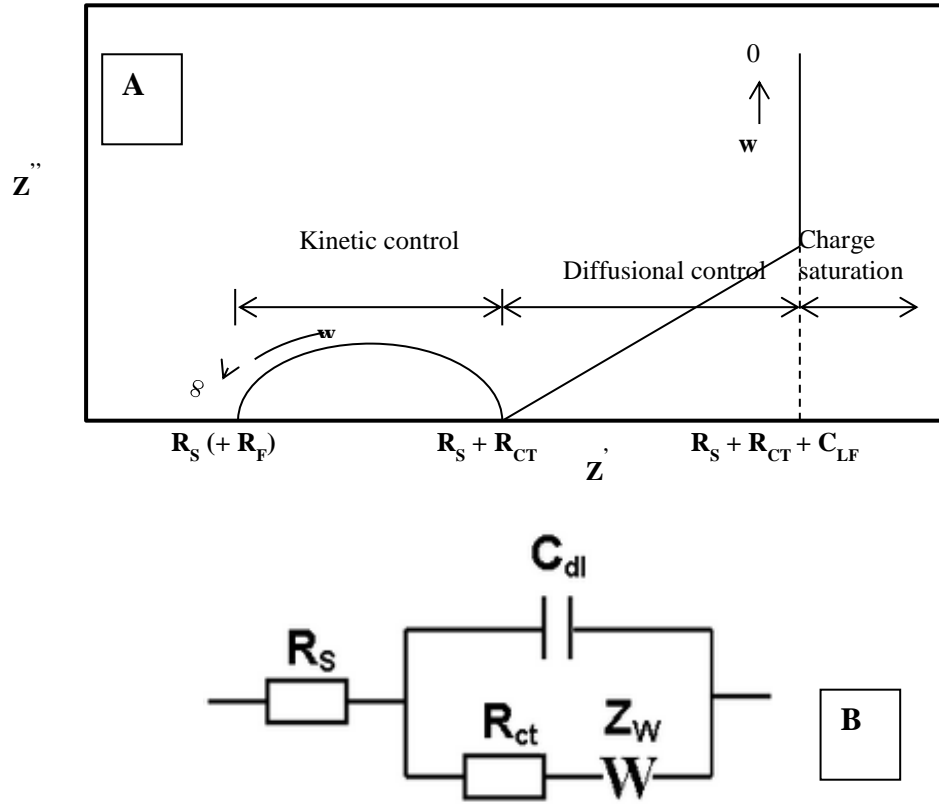


Figure 2.11 (A) Schematic diagram of Nyquist plot (B) Randles circuit showing  $R_S$ ,  $C_{DL}$ ,  $R_{CT}$  and  $Z_W$



separating the in phase and out of phase component of impedance, gives:

$$Z' = R_S + \frac{R_{CT} + \sigma W^{-\frac{1}{2}}}{(\sigma W^{\frac{1}{2}} C_{DL} + 1)^2 + W^2 C_{DL}^2 (R_{CT} + \sigma W^{-\frac{1}{2}})^2} \quad 2.10$$

$$Z'' = R_S + \frac{W C_{DL} (R_{CT} + \sigma W^{-\frac{1}{2}})^2 + \sigma^2 C_{DL} + \sigma W^{-\frac{1}{2}}}{(\sigma W^{\frac{1}{2}} C_{DL} + 1)^2 + W^2 C_{DL}^2 (R_{CT} + \sigma W^{-\frac{1}{2}})^2} \quad 2.11$$

$\sigma$  is given as:

$$\sigma = \frac{RT}{n^2 F^2 A \sqrt{2}} \left( \frac{1}{D_O^{\frac{1}{2}} [O]_{Bulk}} + \frac{1}{D_R^{\frac{1}{2}} [R]_{Bulk}} \right) \quad 2.12$$

Where R is gas constant, T is temperature, F is faraday constant, n is the number of electron involved, A is the electrode area, W is the frequency of applied perturbation and  $\sigma$  is the warburg coefficient. For a limiting situation where W moves towards zero ( $W \rightarrow 0$ ), the real and imaginary part of the impedance is writing as:

$$Z' = R_S + R_{CT} + \sigma W^{-\frac{1}{2}} \quad 2.13$$

$$Z'' = -\sigma W^{-\frac{1}{2}} - 2\sigma^2 C_{DL} \quad 2.14$$

When W moves towards infinity ( $W \rightarrow \infty$ ), the real and imaginary component of the impedance becomes:

$$Z' = R_S + \frac{R_{CT}}{1+W^2 C_{DL} R_{CT}^2} \quad 2.15$$

$$Z'' = -\frac{W C_{DL} R_{CT}^2}{1+W^2 C_{DL} R_{CT}^2} \quad 2.16$$

Therefore at high frequencies, the imaginary impedance displayed in the y axis of the Nyquist plot becomes very small but gradually increases as the frequency diminishes. Further decrease in frequency causes more current to flow through the charge transfer ( $R_{CT}$ ) component of the equivalent circuit and the contribution from  $C_{DL}$  decreases gradually to a minimum point corresponding to the second intercept of the semicircle in the x axis as shown in Figure 2.10 (A). This intercept at a lower frequency of the semicircle arc is the sum of the charge transfer resistance ( $R_{CT}$ ) and solution resistance  $R_S$ . The charge transfer resistance can be calculated by subtracting the solution resistance obtained from the high frequency intercept from the low frequency intercept.

The EIS experimental procedure involves placing a three electrode system comprising of the working electrode (electrode of interest), reference electrode and a counter electrode in an electrolyte solution. Applying a voltage through a potentiostat to the working electrode with a small sinusoidal amplitude e.g. 10 mV waveform, and this AC (alternating current) potential perturbation drives the redox processes (if any) at the electrode surface. The resulting amplitude and phase angle from the AC current are then measured and used in calculating the real and imaginary components of the impedance displayed in the Nyquist plot (Martin *et al.*, 1989). The impedance is calculated as the ratio of the applied sinusoidal voltage to the sinusoidal current that flows between the counter and working electrodes as a result of the applied voltage (Ehret *et al.*, 1997).

The Randle circuit which is an equivalent circuit of resistors and capacitors that passes current with the same amplitude and phase angle that the real cell does under a given excitation as shown in Figure 2.10 (B) is used to predict the performance of the electrochemical cell or EIS experimental set up. It also describes the recorded impedance spectrum at high to medium frequencies when the EIS experiment is run at the formal potential of redox couple present (Lindholm, 1990). In the Randle circuit  $R_s$  is the electrolyte resistance,  $C_{DL}$  is the double layer capacitance,  $R_{CT}$  is the charge transfer resistance and  $Z_W$  is the Warburg impedance.

The  $C_{DL}$  results from a separation of charge in space due to the asymmetry that occurs when a metal-solution interphase is formed.  $Z_W$  is the Warburg impedance ( $Z_W$ ) caused by mass transport limitation by diffusion and it gives rise to a constant phase angle of  $45^\circ$  ( $\pi/4$ ) as shown in the Nyquist plot Figure 2.10 (A). The  $Z_W$  occurs in EIS experiment if the reaction is dominated by partial or complete mass transport control by diffusion. The  $C_{DL}$ ,  $R_{CT}$  and  $Z_W$  are placed in parallel positions in the circuit because the current passing through the working electrode is the sum of the individual contributions from these processes. The  $R_s$  is placed in series position in the equivalent circuit since all the current must pass through the uncompensated solution resistance (Ehret *et al.*, 1997).  $R_s$  and  $C_{DL}$  are nearly ideal circuit elements but  $R_{CT}$  and  $Z_W$  which are components of the faradaic impedance changes with frequency because they are not ideal (Ehret *et al.*, 1997). Therefore in real experiment a much more complex behaviour is expected due to coupling between faradaic and double layer charging processes.

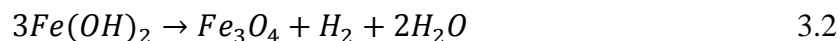
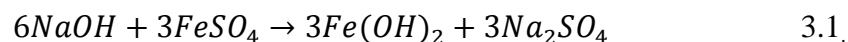
## Chapter 3

### Nature of Magnetite Nanoparticles Synthesized by Direct Oxidative Alkaline Hydrolysis of Iron II sulphate by varying synthesis parameters

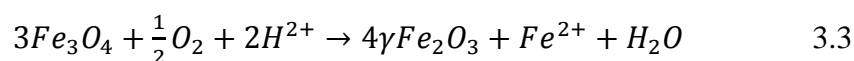
#### 3.1 Introduction

Iron oxide nanoparticles magnetite ( $\text{Fe}_3\text{O}_4$ ) or maghemite ( $\gamma\text{-Fe}_2\text{O}_3$ ) are widely used in medical and biomedical applications such as in hyperthermia therapy, drug delivery and magnetic resonance imaging (Gupta and Gupta, 2005; Gupta *et al.*, 2007; Jain *et al.*, 2008). Their use depends on their sizes, nature, stability and purity which are influenced by their mode of synthesis. This in turn affects their magnetic properties, potency and sensitivity in their applications e.g. resonance imaging. There are different synthetic routes for the synthesis of iron oxide nanoparticles, such as sol gel, sonochemical reactions, hydrothermal reactions, co-precipitation, microemulsions, flow injection and electro spray method (Laurent *et al.*, 2008). It is important that the method chosen for the nanoparticles synthesis leads to mono-dispersed particles domains which are easy to characterize with controllable properties. These types of particles are mostly desirable in biomedical applications compared to the poly-dispersed domain. The type of synthesis route also affects the nanoparticle sizes, shape, structural defects and degree of impurities. The method also should be reproducible and industrially scalable without complex purification processes.

Magnetite nanoparticles ( $\text{Fe}_3\text{O}_4$ ) in this dissertation were synthesized through direct oxidative alkaline hydrolysis of iron II sulphate salt. The process simply involves reacting iron II salt with a strong base (e.g. sodium hydroxide) in the presence of a mild reducing agent (potassium nitrate) to form iron (II) hydroxide. The iron (II) hydroxide formed is heated and undergoes anaerobic oxidation by the protons of water to form magnetite and molecular hydrogen (Schikorr reaction). The chemical reaction for the synthesis of magnetite and Schikorr reaction are shown in equation 3.1 and 3.2.



Magnetite ( $Fe_3O_4$ ) is known to be an unstable iron oxide and easily undergoes oxidation in the presence of oxygen to form maghemite ( $\gamma$ - $Fe_2O_3$ ) as shown in equation 3.3 (Rebodos and Vikesland, 2010). The process of oxidation involves the iron II cation ( $Fe^{2+}$ ) in the octahedral site of magnetite being oxidized to iron III cation ( $Fe^{3+}$ ) creating cationic vacancies which helps to maintain the charge balance in maghemite.



Most often stabilizers are used during magnetite nanoparticles synthesis to improve the mono-dispersity and stability of the particles. This section of the dissertation will be based on the synthesis and characterization of magnetite using polyethyleneimine (PEI) a polycation as stabilizing agent.

Within the past decade and recently, authors have published works on the synthesis of iron oxide nanoparticles ( $Fe_3O_4$ ) through oxidative alkaline hydrolysis of iron II sulphate salt. Most attention has been focussed on the synthesis of desired  $Fe_3O_4$  nanoparticles sizes, stabilization and application of the nanoparticles in various fields. But not much work has been done on the type of likely side products (iron oxides) or impurities that may accompany the formation of iron oxide nanoparticles by varying synthesis parameters using this method.

Recently 50 nm cubic shaped average size iron oxide nanoparticles ( $Fe_3O_4$ ) were successfully synthesized using the oxidative alkaline hydrolysis of ferrous ions at 90°C (Goon *et al.*, 2010). Murbe and co-workers (Mürbe *et al.*, 2008) showed that oxidative alkaline hydrolysis of ferrous ion at 90°C allowed the synthesis of large size magnetite nanoparticles with cubo-octahedral morphologies. They also showed that complete oxidation of the nanoparticles was achieved at temperatures 300°C and the degree of oxidation depends on the particle sizes.

Hexagonal  $Fe_3O_4$  nano-plates of thickness 10-15 nm with side length of 150-200 nm were successfully synthesized through oxidative alkaline hydrolysis of ferrous ion at

90°C (Ma *et al.*, 2013). Their research was focused on how ethylene glycol affects the size and shape of the nano-plates. Verges and co-workers synthesized Fe<sub>3</sub>O<sub>4</sub> nanoparticles with different sizes by varying synthesis parameters (salt concentration, hydroxyl concentration and ethanol concentration) at 90°C using oxidative alkaline hydrolysis of ferrous ion. They showed that increasing salt concentration increases the nanoparticles sizes and shape with maximum particle size of 300 nm. Changes in hydroxyl iron concentration and the presence of ethanol results in the formation of smaller particles. No other iron oxide phase was detected during synthesis. The effect of temperature changes and synthesis under the influence of revolution per minute on the sizes and shape of the nanoparticles were not studied.

Oxidative alkaline hydrolysis of ferrous ion was also used by Sugimoto and co-worker, who showed that dramatic change in particle size and morphology, was determined by the iron salt concentration. Sharp pH change from iron II salt concentration and hydroxyl ion affects the formation mechanism of the particles (Sugimoto and Matijević, 1980). They also reported that synthesizing the particles at 80°C is much slower than 90°C, but gave crystals with same modal diameters with broader size distribution than the system aged at 90°C. No analysis was carried out by the group on the effect of higher temperatures and synthesis under the influence revolution per minutes on the nature of nanoparticles.

### **3.2 Aims**

The aims of this work is to synthesis magnetite (Fe<sub>3</sub>O<sub>4</sub>) nanoparticles through oxidative alkaline hydrolysis of iron II sulphate salt and explore the effect of synthesis temperature, iron salt concentration, hydroxyl concentration and revolution per minute on the nature and purity of iron oxide nanoparticles (Fe<sub>3</sub>O<sub>4</sub> Nps). Polyethyleneimine (PEI) was used as a stabilizing agent and X-ray diffraction, X-ray photoelectron spectroscopy and transmission electron microscopy were used in characterizing the nanoparticles.

### **3.3 Experimental**

#### ***3.3.1 Materials and chemicals***

Polyethyleneimine (branched 25000mw), iron II sulphate heptahydrate >99%, were purchased from Sigma Aldrich (Dorset UK), sodium hydroxide 97%, and potassium nitrate 99% were from Alfa Aesar (Lancashire UK). All chemicals were used as received without further purification. Solutions were prepared using Millipore deionised water.

#### ***3.3.2 Synthesis of iron oxide core/polyethyleneimine nanoparticles ( $Fe_3O_4$ -PEI NPs)***

Iron oxide nanoparticles ( $Fe_3O_4$  Np) were synthesized following a method by Goon and co-workers with some modification (Goon *et al.*, 2009). Different concentration of iron (II) sulphate heptahydrate (0.0035-0.2M) were added into 80ml of deionized water containing PEI (500mg $l^{-1}$ ) in a 250ml round bottom flask after sparging for 20 minutes. Potassium nitrate (10ml, 2M) was added followed by the addition of sodium hydroxide (10ml, 1M). This results in the formation of iron (II) hydroxide which was heated for 2 hours at 90<sup>0</sup>C while constantly sparging the system with nitrogen. Black precipitate of iron oxide nanoparticles was formed and washed several times with deionised water. The nanoparticles were finally suspended in 80ml of deionised water at pH 6-7. The procedure was repeated but by varying the heating temperature (50<sup>0</sup>C, 90<sup>0</sup>C and 150<sup>0</sup>C), heating at 90<sup>0</sup>C with different revolution per minute (200, 500 and 1500) and varying hydroxyl ion concentrations (0.001M, 0.01M, 0.1M, 1.0M and 2.0M).

#### ***3.3.3 Characterization of the iron oxide/PEI nanoparticles***

X-ray diffraction pattern of nanoparticles were obtained using PANalytical X'pert Pro MPD, powered by Philips PW 3040/60 x-ray generator fitted with X'celerator and using Cu K $\alpha$  radiation with wavelength of 1.54180Å to determine the crystalline structure of the nanoparticles. The nature and core electrons of the  $Fe_3O_4$  nanoparticles were obtained by x-ray photoelectron spectroscopy (XPS) with Thermo Scientific K- $\alpha$  monochromated small spot x-ray Photoelectron Spectrometer system. Transmission electron microscopy analysis (TEM) was carried out with Philips CM200 FEGTEM field emission gun TEM/STEM with supertwin objective lens.

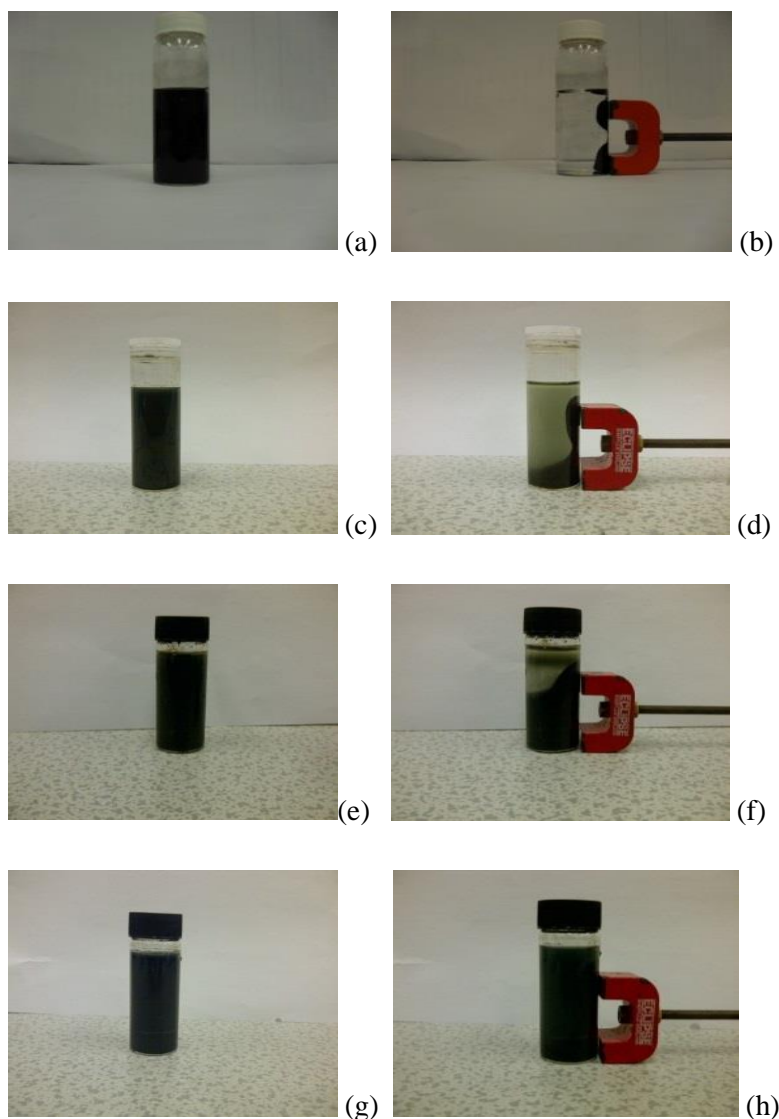
### 3.4 Results and Discussion

#### 3.4.1 Physical properties of nanoparticles synthesized by varying iron salt concentration

FeSO <sub>4</sub> (M)	KNO <sub>3</sub> (M)	NaOH (M)	Temp °C	PEI mg l <sup>-1</sup>	XRD (nm)	TEM (nm)	Shape
0.0035	2.0	1.0	90	500	57	58	cubic
0.017	2.0	1.0	90	500	62	66	cubic
0.025	2.0	1.0	90	500	50	50	cubic
0.035	2.0	1.0	90	500	70	72	cubic
0.068	2.0	1.0	90	500	216	565	hexagonal
0.1	2.0	1.0	90	500	192	-	-
0.2	2.0	1.0	90	500	76	78	shapeless

**Table 3.1 Fe<sub>3</sub>O<sub>4</sub> nanoparticles synthesized by varying iron II sulphate concentration**

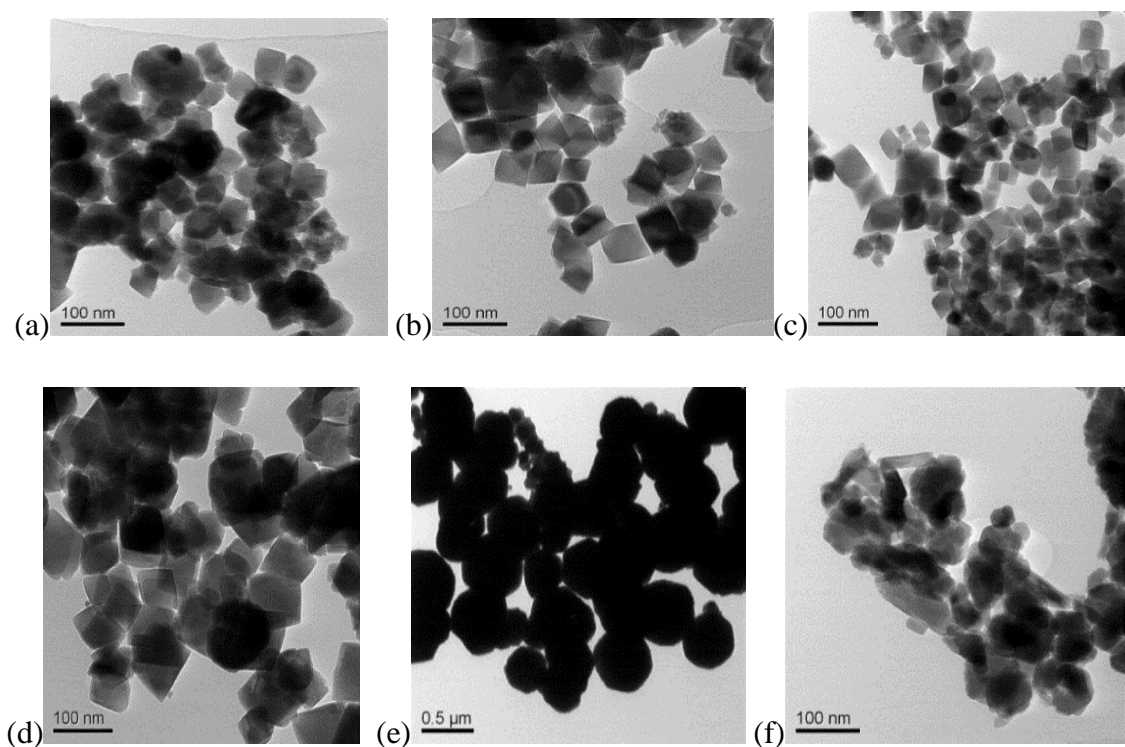
Synthesizing Iron oxide (Fe<sub>3</sub>O<sub>4</sub>) nanoparticles by varying the salt concentration as shown in table 3.1, showed that the nanoparticles changes in sizes and shape as the salt concentration varies. This might be due to the fluctuations in the pH (5-6) of the system caused by large changes in salt concentration. Slight changes in the pH of the reacting system are known to affect the nanoparticles sizes and shapes (Sugimoto and Matijević, 1980; Vergés *et al.*, 2008). The largest nanoparticles sizes was observed when the salt concentration was increased to 0.068M and the nanoparticles sizes start decreasing with further increase in salt concentration. Although there is a large difference between the crystallite nanoparticles sizes as analysed by the XRD compared to the TEM results for the large particles formed at 0.068M FeSO<sub>4</sub>. This might be due to aggregation of the nanoparticles over the length of time it took for the TEM analysis to be carried out. It might also result from poor stabilizing effect of polyethyleneimine on larger nanoparticles during synthesis.



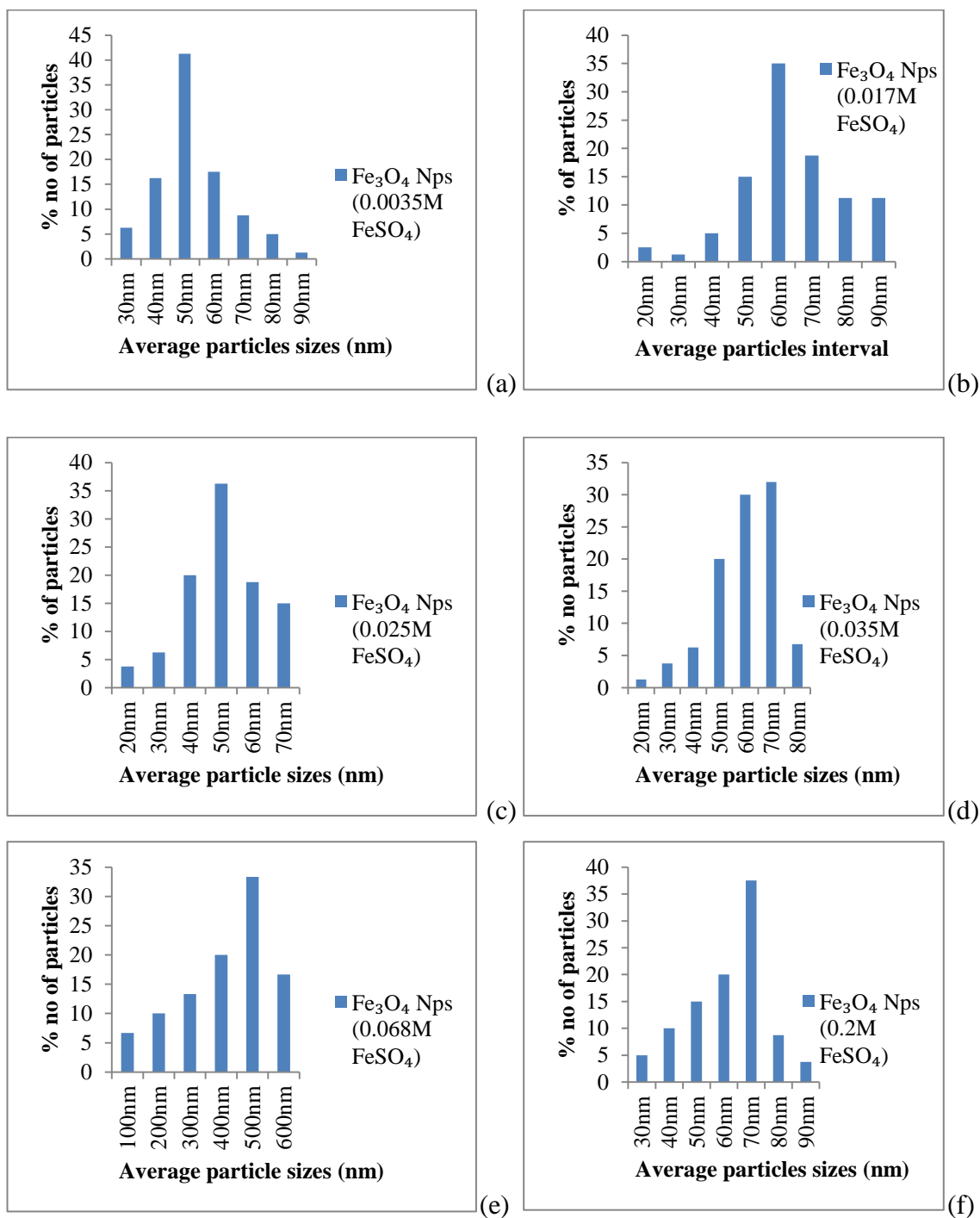
**Figure 3.1 Effect of excess iron II salt on  $\text{Fe}_3\text{O}_4$  synthesis and paramagnetic behaviour and nature before and after magnetic separation (a) and (b) 0.025M, (c) and (d) 0.2M, (e) and (f) 0.3M, (g) and (h) 0.5M**

Figure 3.1 showed that increasing the salt concentration to 0.2M and above (0.3M and 0.5M) results in less paramagnetic effect or no visible paramagnetic effect of the nanoparticles at room temperature. Paramagnetism is the ability of a material to be attracted to an external magnet and losing the magnetic property upon removal of the external magnet. The observed less or no visible paramagnetic effect at higher salt concentration is as a result of the presence of  $\beta$ -iron oxy hydroxide nano-rods also known as alkaganeite ( $\beta\text{-FeOOH}$ ) mixed with the formed iron oxide nanoparticles. The  $\beta\text{-FeOOH}$  nano-rods are brownish in colour and have Neel temperatures that lie close to

room temperature thus making them less paramagnetic or antiferrimagnetic under ambient conditions. The antiferromagnetic behaviour of  $\beta$ -FeOOH nano-rods also increases with increasing iron salt concentration in the mixture. The TEM images in Figure 3.2 shows that the nanoparticles have cubic shape at lower salt concentration, hexagonal shape at 0.068M and not well defined shape 0.2M mixed with  $\beta$ -FeOOH nano-rod. The average size distribution of the nanoparticles from TEM analysis shows that nanoparticles did not have broad size distribution as shown in Figure 3.3.



**Figure 3.2** TEM images of  $\text{Fe}_3\text{O}_4$  nanoparticles synthesized at different  $\text{FeSO}_4$  concentration (a) 0.0035M  $\text{FeSO}_4$ , (b) 0.017M  $\text{FeSO}_4$  (c) 0.025M  $\text{FeSO}_4$  (d) 0.035M  $\text{FeSO}_4$  (e) 0.068M  $\text{FeSO}_4$  (f) 0.2M  $\text{FeSO}_4$



**Figure 3.3** Size distribution of  $\text{Fe}_3\text{O}_4$  nanoparticles synthesized at different  $\text{FeSO}_4$  concentration (a)  $0.0035\text{M FeSO}_4$ , (b)  $0.017\text{M FeSO}_4$  (c)  $0.025\text{M FeSO}_4$  (d)  $0.035\text{M FeSO}_4$  (e)  $0.068\text{M FeSO}_4$  (f)  $0.2\text{M FeSO}_4$

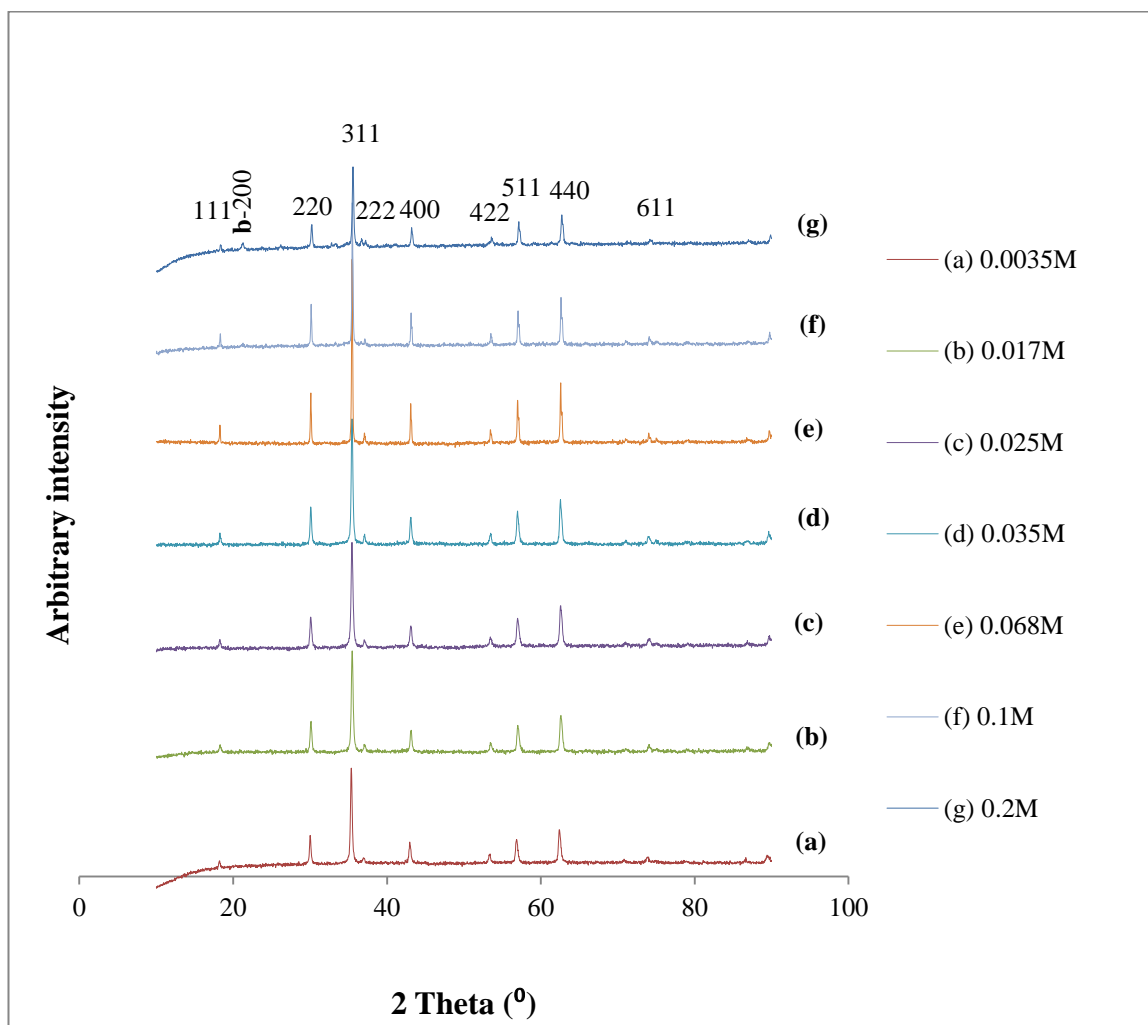


**Figure 3.4 XRD analysis of  $\text{Fe}_3\text{O}_4$  synthesis by varying iron II sulphate concentration (a) 0.0035M  $\text{FeSO}_4$ , (b) 0.017M  $\text{FeSO}_4$  (c) 0.025M  $\text{FeSO}_4$  (d) 0.035M  $\text{FeSO}_4$  (e) 0.068M  $\text{FeSO}_4$  (f) 0.1M (g) 0.2M  $\text{FeSO}_4$**

The XRD analysis in Figure 3.4 shows diffraction peaks of iron oxide ( $\text{Fe}_3\text{O}_4$ ) nanoparticles synthesized at the different iron salt concentrations. The diffraction peaks represented by the miller index (111), (220), (311), (222), (400), (422), (511), (440), and (611) can be indexed to the face-centered cubic structure of magnetite ( $\text{Fe}_3\text{O}_4$ ) according to joint committee of powder diffraction standards (JCPDS) number 00-019-0629. The presence of diffraction peak (b-200) at lower angle for sample (g) prepared with 0.2M  $\text{FeSO}_4$  indicates the presence of  $\beta\text{-FeOOH}$ .

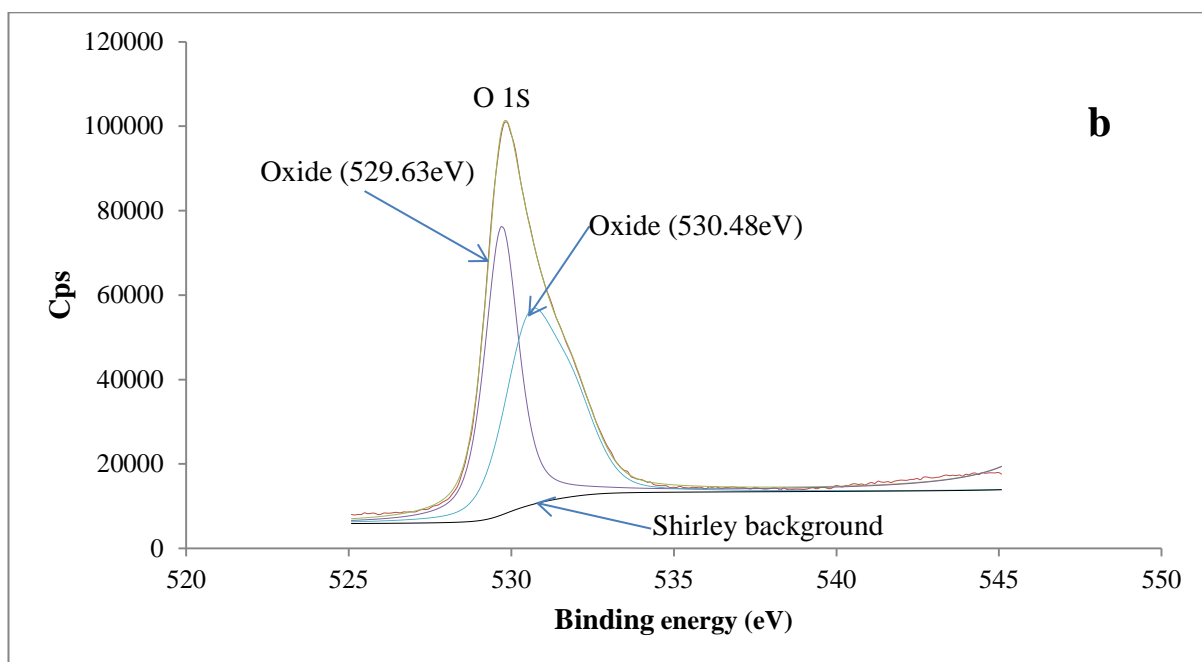
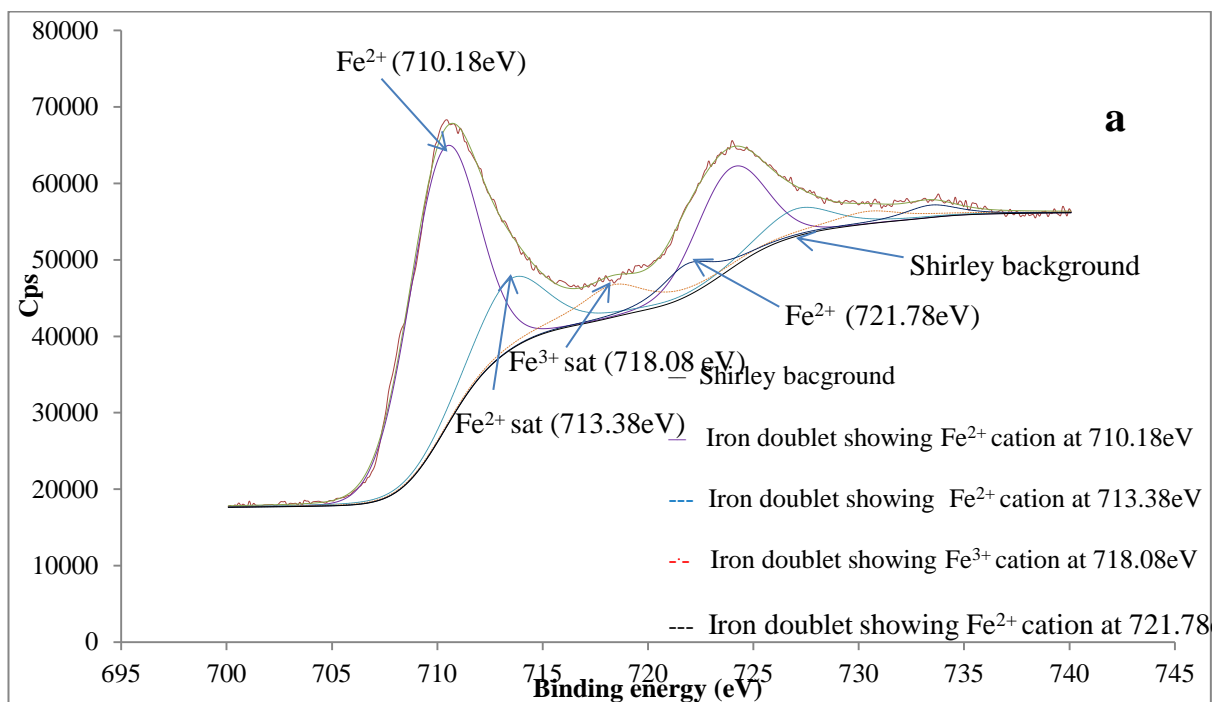


**Figure 3.5**  $\text{Fe}_3\text{O}_4$  nanoparticles XPS analysis (a) 2p core electrons (b) 1s core electrons of  $\text{O}_2$

Figure 3.5a shows the XPS analysis for magnetite nanoparticles synthesized without excess salt concentration (0.025M  $\text{FeSO}_4$ ). It shows the characteristic doublet for iron base compounds indicating the presence of 2p core electrons ( $\text{Fe } 2p_{3/2}$  and  $2p_{1/2}$ ). The arrows shows the presence of iron II cation ( $\text{Fe}^{2+}$ ) at binding energies of 710.18eV, 713.38eV and 721.78eV and iron III cation ( $\text{Fe}^{3+}$ ) at 718.08eV confirming the formation

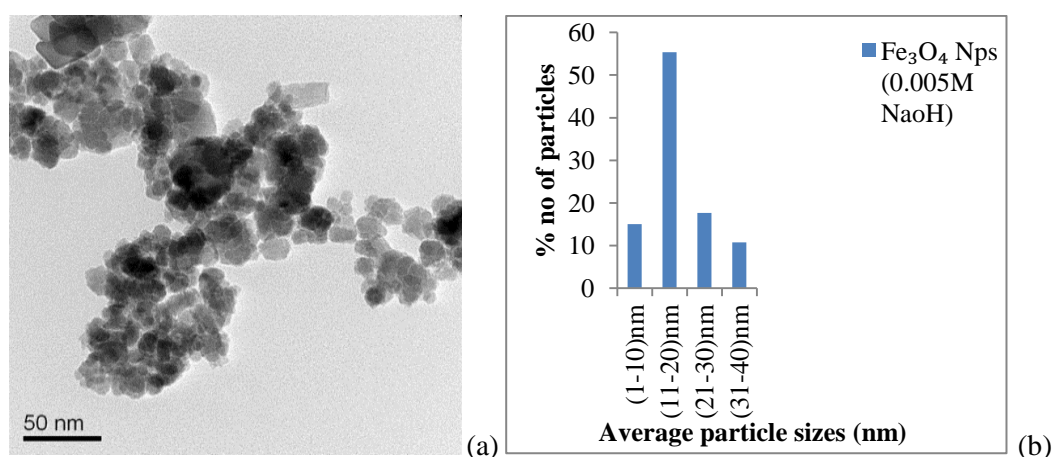
of magnetite ( $\text{Fe}_3\text{O}_4$ ) nanoparticles. Figure 3.5b also shows that the 1s core electron of oxygen in  $\text{Fe}_3\text{O}_4$  nanoparticles results only from oxides in the nanoparticles at lower binding peak of 529.58eV and 530.48eV.

### 3.4.2 Physical properties of nanoparticles synthesized by varying base (NaOH) concentration

FeSO <sub>4</sub> (M)	KNO <sub>3</sub> (M)	NaOH (M)	Temp °C	PEI mg l <sup>-1</sup>	XRD (nm)	TEM (nm)	Shape
0.025	2.0	0.005	90	500	19	20	shapeless
0.025	2.0	0.01	90	500	26	26	s/spherical
0.025	2.0	0.1	90	500	40	44	cubic
0.025	2.0	1.0	90	500	50	51	cubic
0.025	2.0	2.0	90	500	60	64	cubic

**Table 3.2**  $\text{Fe}_3\text{O}_4$  nanoparticles synthesized by varying base concentration

Iron oxide nanoparticles synthesized by varying the  $\text{OH}^-$  concentration results in the formation of smaller nanoparticles (super-paramagnetic and paramagnetic) with broader size distribution at lower  $\text{OH}^-$  concentrations. The nanoparticles sizes increases with lesser size distribution and the shape changes from shapeless form to cubic as the  $\text{OH}^-$  concentration increases as shown in table 3.2.



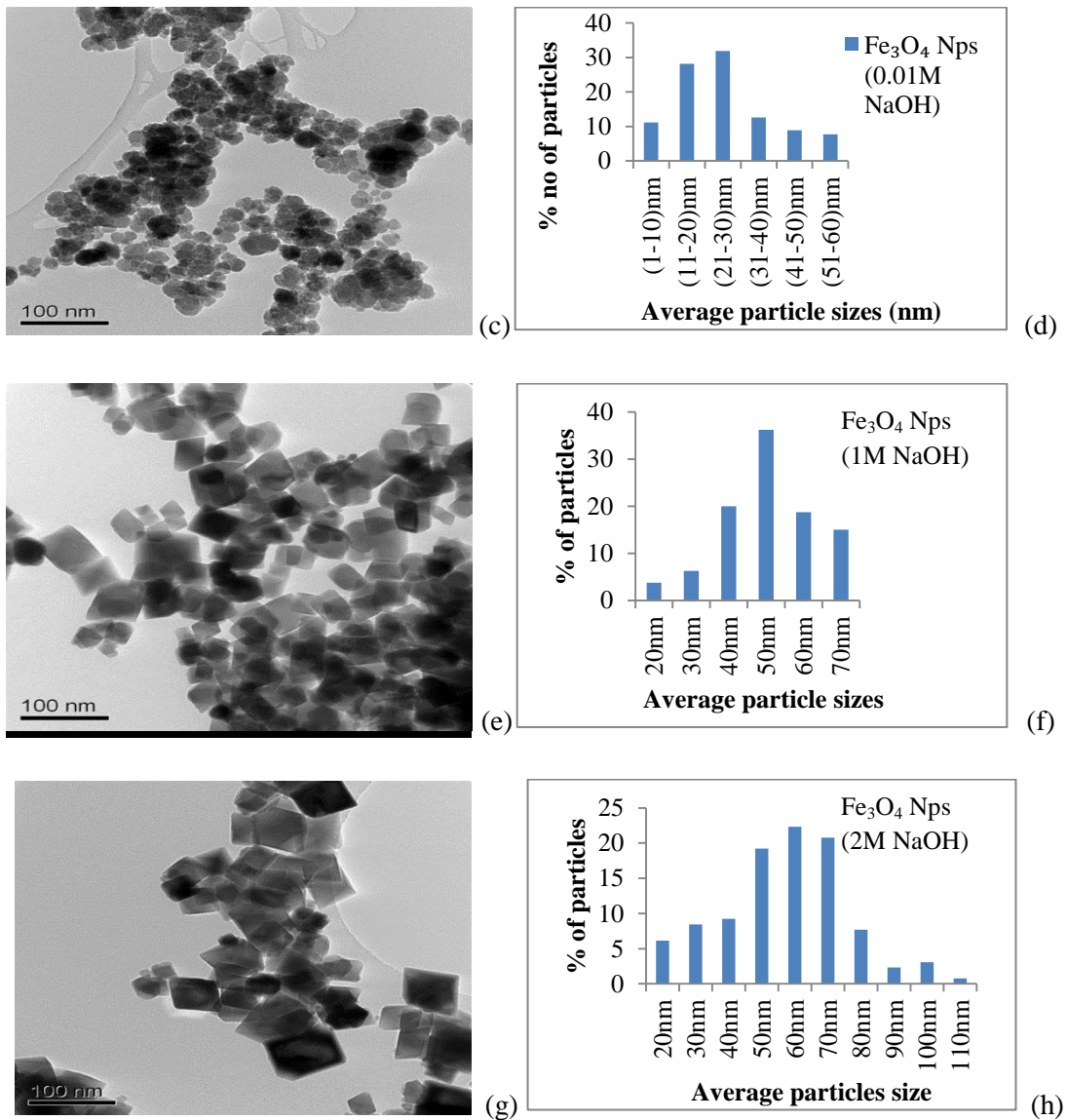


Figure 3.6 TEM images of  $\text{Fe}_3\text{O}_4$  nanoparticles synthesized at (a) 0.005M NaOH (b) size distribution of  $\text{Fe}_3\text{O}_4$  Nps at 0.005M (c) 0.01M NaOH (d) size distribution for 0.01M NaOH (e) 1M NaOH (f) 1M NaOH size distribution (g) 2M NaOH (h) 2M size distribution.

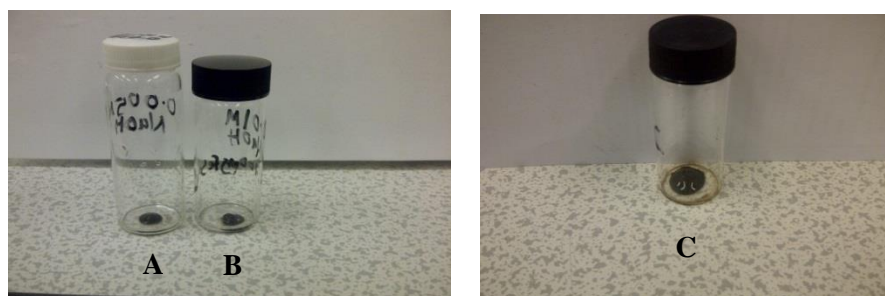


Figure 3.7 Images of  $\text{Fe}_3\text{O}_4$  nanoparticles synthesized with (A) 0.005M, (B) 0.01M and (C) 1M NaOH respectively

Figure 3.6 shows the TEM images of nanoparticles synthesized with the different base concentrations and their size distribution. Nanoparticles synthesized with 0.005M and 0.01M NaOH have broader size distribution (1-40 nm) and 1-50 nm respectively. The average particle size is 20 nm for 0.005M NaOH with no preferred particles shape and 26 nm for 0.01M NaOH with spherical shape. Nanoparticles synthesized with 0.1M, 1M and 2M NaOH had cubic shape with less size distribution. The average particle size is 44 nm, 51nm and 64 nm respectively from the TEM images. Figure 3.7 A, B and C after magnetic separation and removal of supernatant shows that only small quantity of iron oxide nanoparticles can be synthesized in the presence of lower hydroxyl concentrations (0.005M and 0.01M) compared to higher concentration (C). This can be attributed to the insufficient hydroxyl groups present that can convert the iron salt to iron oxide nanoparticles. This phenomenon can be explained from the stoichiometric relationship between iron salt to NaOH concentration in the formation of iron oxide nanoparticles in equation 3.1. The equation shows that two moles of NaOH is needed to react with one mole of iron salt to form magnetite nanoparticles.

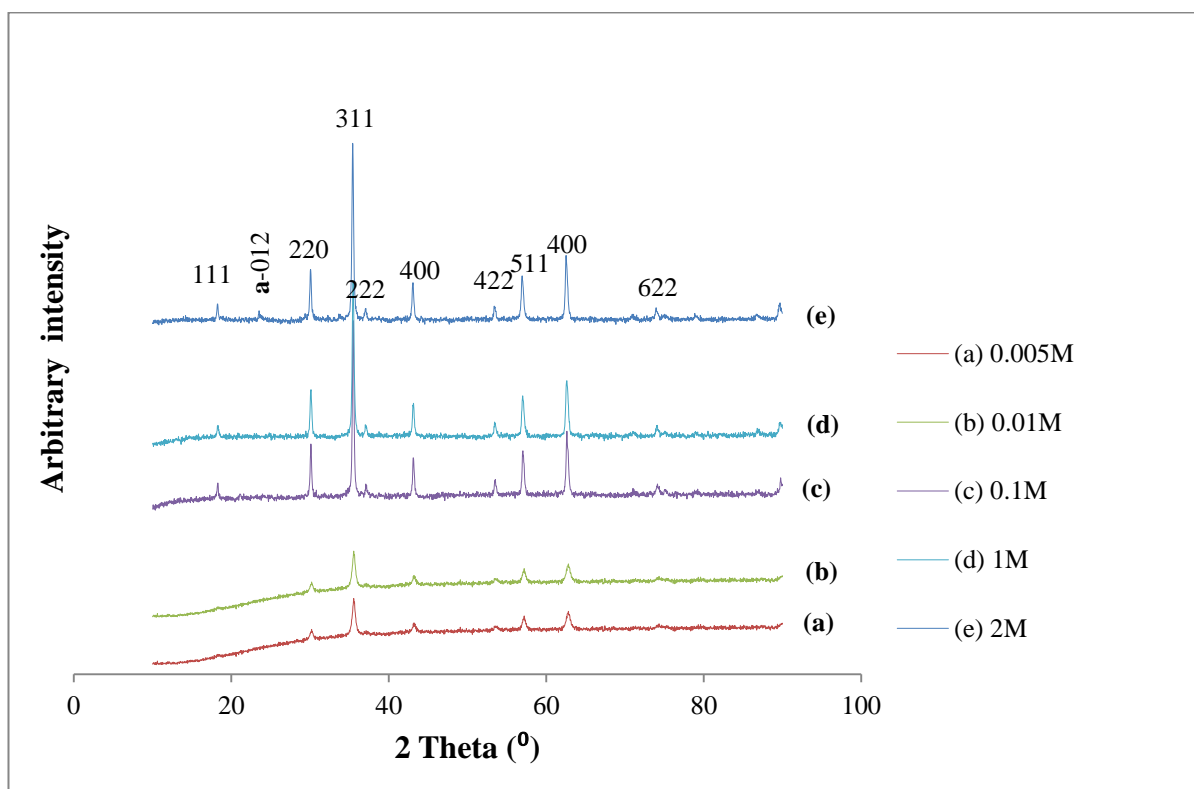


Figure 3.8 XRD analysis of  $\text{Fe}_3\text{O}_4$  synthesis by varying hydroxyl ion concentration (a) 0.005M (b) 0.01M (c) 0.1M (d) 1M and (e) 2M

Figure 3.8 shows the XRD analysis of iron oxide nanoparticles synthesized with the different NaOH concentrations. The diffraction peaks for samples a, b, c, d, and e can be indexed to the face centred cubic structure of magnetite except for peak (**a**-012). It was observed from the XRD diffraction spectra the disappearance of the miller index 111 peaks at 0.005M (a) and 0.01M (b) concentrations. This indicates the absence of large size crystals nanoparticles at these concentrations. The 111 diffraction peaks are used in identify the presence of large-size crystal in samples, it can also result from the preferred orientation effects of the nano-crystal during preparation.

The presence of diffraction peaks (**a**-012) for iron nanoparticles synthesized with 2M NaOH shows that other form of iron oxide hematite ( $\alpha$ -Fe<sub>2</sub>O<sub>3</sub>) in trace amount was formed. The small letter **a** attached to the miller index is used to differentiate this peak from the magnetite peaks.

### ***3.4.3 Physical properties of nanoparticles synthesized by varying revolution per minute***

<b>FeSO<sub>4</sub></b> <b>(M)</b>	<b>KNO<sub>3</sub></b> <b>(M)</b>	<b>NaOH</b> <b>(M)</b>	<b>Temp</b> <b>°C</b>	<b>PEI</b> <b>mg l<sup>-1</sup></b>	<b>RPM</b> <b>(rmin<sup>-1</sup>)</b>	<b>XRD</b> <b>(nm)</b>
0.025	2.0	1.0	90	500	200	74
0.025	2.0	1.0	90	500	500	65
0.025	2.0	1.0	90	500	1500	50

**Table 3.3 Fe<sub>3</sub>O<sub>4</sub> nanoparticles synthesized by varying revolution per minute**

Iron oxide nanoparticles synthesized by varying the revolution per minute showed that the nanoparticles crystallite sizes increased with decrease in revolution per minute as shown in table3.3. It was observed that XRD spectrum for Fe<sub>3</sub>O<sub>4</sub> at 500 and 1500 revolution per minutes contains some diffraction peaks that shows the presence of small amount of  $\alpha$ -Fe<sub>2</sub>O<sub>3</sub> and iron oxy hydroxide ( $\gamma$ -FeOOH) also known as Lepidocrocite present in the nanoparticles as shown in Figure 3.9. The presence of Lepidocrocite at diffraction peak 011 denoted by **L**-011 is due to the oxidation of iron II hydroxide

(Fe(OH)<sub>2</sub>) leading to mixed ferric and ferrous ions in solution and the formation of magnetite (Snow *et al.*, 2011). Lepidocrocite is known to be paramagnetic at room temperature and antiferromagnetic at its Neel temperature of 77K with slightly smaller band gap than goethite at 2.2eV (Hall *et al.*, 1995). The formation of small amount of  $\alpha$ -Fe<sub>2</sub>O<sub>3</sub> (hematite) at the lower angle might be as a result of larger multiplet splitting of the high spin state 2p<sub>3/2</sub> core electrons during synthesis of Fe<sub>3</sub>O<sub>4</sub> nanoparticles caused by higher revolution per minute.

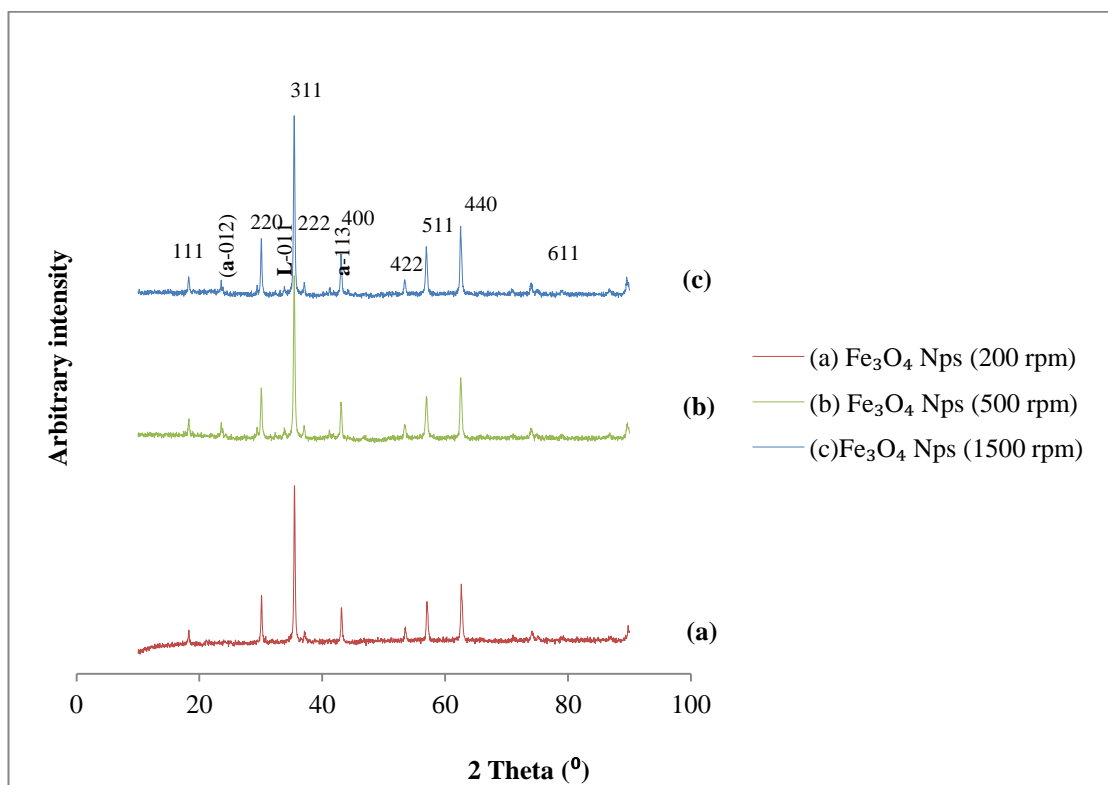
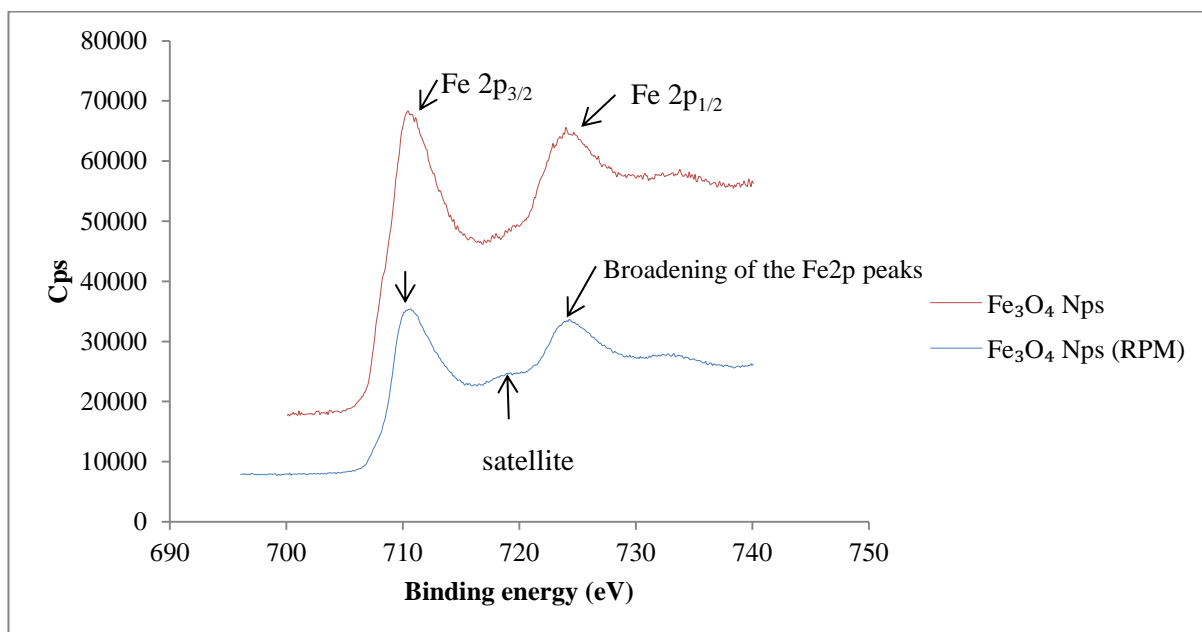


Figure 3.9 XRD analysis of Fe<sub>3</sub>O<sub>4</sub> synthesis at (a) 200, (b) 500 and (c) 1500 revolution per minute



**Figure 3.10 XPS analysis  $\text{Fe}_3\text{O}_4$  synthesis with and without revolution per minute**

Figure 3.10 shows the XPS analysis of the nanoparticles synthesized at higher revolution per minute compared to magnetite nanoparticles synthesized without revolution per minute. It corroborates the result from the XRD analysis that the  $\alpha\text{-Fe}_2\text{O}_3$  (hematite) formed is as a result of multiplet splitting of the high spin core electrons causing the broadening of the Fe2p peaks as indicated by arrow for magnetite synthesized with revolution per minute.

The Multiplet splitting of high spin state core electrons is known to be a characteristics step for  $\alpha\text{-Fe}_2\text{O}_3$  formation. (Mills and Sullivan, 1983; Nasibulin *et al.*, 2009). It is a phenomenon associated with photoelectron peaks caused by an unpaired valence electrons present giving rise to exchange interactions which affect differently the remaining spin-up or spin-down core electrons. In the case of the high spin states the phenomenon is heightened, thus for high spin states of  $\text{Fe}^{\text{II}}$  and  $\text{Fe}^{\text{III}}$  a broadening of the Fe2p peaks due to unresolved multiplet splitting is observed.

#### 3.4.4 Physical properties of nanoparticles synthesized by varying synthesis temperature

FeSO <sub>4</sub> (M)	KNO <sub>3</sub> (M)	NaOH (M)	Temp °C	PEI mg <sup>l</sup> <sup>-1</sup>	XRD (nm)
0.025	2.0	1.0	50	500	55
0.025	2.0	1.0	90	500	51
0.025	2.0	1.0	150	500	52

**Table 3.4 Fe<sub>3</sub>O<sub>4</sub> nanoparticles synthesized by varying synthesis temperature**

Synthesizing iron oxide nanoparticles by varying the synthesis temperatures does not really affect the size of the nanoparticles as shown in table 3.4. The XRD diffraction pattern of the nanoparticles in Figure 3.11 showed the nanoparticles peaks can be indexed to the face centred cubic structure of magnetite for samples a, b and c except for the appearance of diffraction peak a-012 at lower angle planes around 24° (Hou *et al.*, 2007) for increased synthesis temperature 150°C. This peak indicates the presence of  $\alpha$ -Fe<sub>2</sub>O<sub>3</sub> (hematite) which is a more stable iron III oxide. This might result from the oxidation of Fe<sub>3</sub>O<sub>4</sub> at higher temperature (150°C).

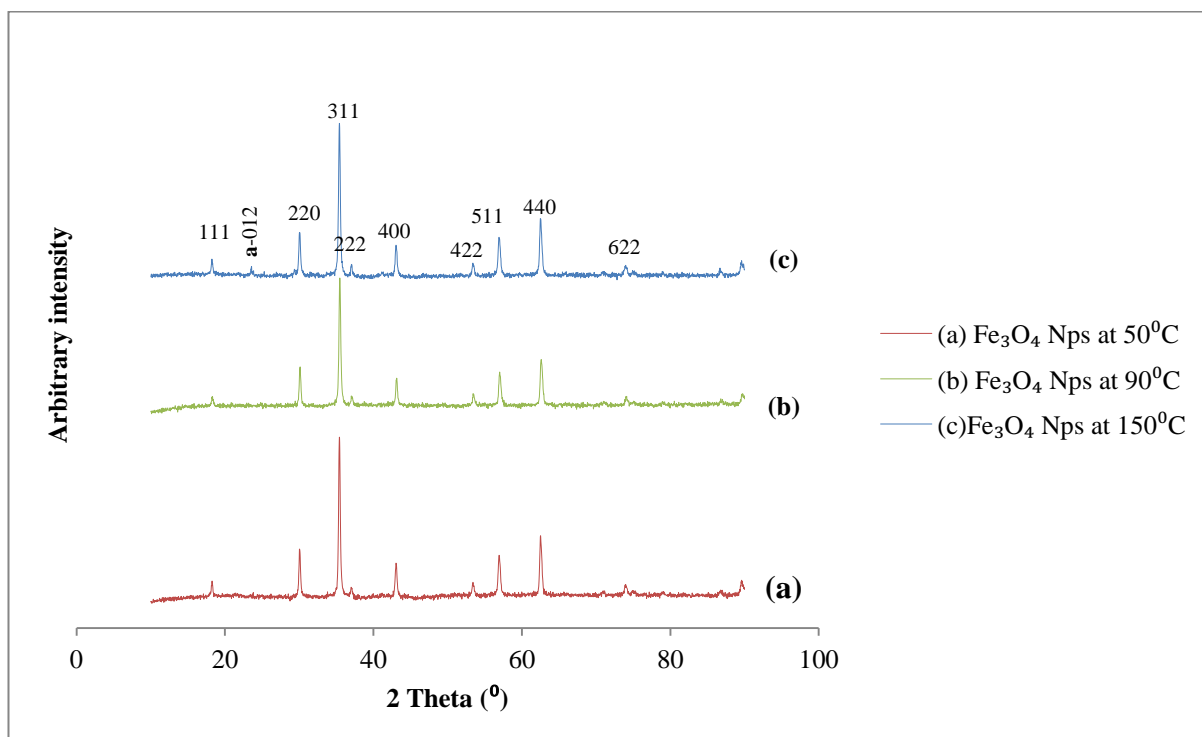


**Figure 3.11** XRD analysis  $\text{Fe}_3\text{O}_4$  synthesized by varying synthesis temperatures (a)  $50^\circ\text{C}$ , (b)  $90^\circ\text{C}$  and (c)  $150^\circ\text{C}$

#### 4.0 Conclusion

This work shows that iron oxide nanoparticles ( $\text{Fe}_3\text{O}_4$ ) were successfully synthesized through oxidative alkaline hydrolysis of ferrous ion and that synthesis parameters affect the nature and purity of the nanoparticles. Changing iron salt concentration affects the size and shape of the nanoparticles and salt concentration up to 0.2M and above results in less paramagnetic effect of the nanoparticles due to the formation of alkaganeite ( $\beta\text{-FeOOH}$ ) nano-rods mixed with iron oxide nanoparticles. Hydroxyl ion concentrations (0.005M and 0.01M) results in lesser conversion of iron salt to nanoparticles with the formation of smaller nanoparticles (super-paramagnetic and paramagnetic) with broad size distribution. Increasing hydroxyl concentration results in the formation of cubic shaped paramagnetic  $\text{Fe}_3\text{O}_4$  nanoparticles with less size distribution and traces of  $\alpha\text{-Fe}_2\text{O}_3$  formed at 2M NaOH.

Synthesis temperature does not affect the  $\text{Fe}_3\text{O}_4$  nanoparticles sizes, but synthesizing the nanoparticles at temperature  $150^\circ\text{C}$  results in the formation of trace amount of hematite ( $\alpha\text{-Fe}_2\text{O}_3$ ) mixed with  $\text{Fe}_3\text{O}_4$  nanoparticles. Iron oxide nanoparticles synthesized

through revolution per minutes (RPM) showed that the  $\text{Fe}_3\text{O}_4$  nanoparticles sizes increases with decreasing RPM, but the nanoparticles synthesized at higher RPM contains small amount of  $\alpha\text{-Fe}_2\text{O}_3$  and lepidocrocite ( $\gamma\text{-FeOOH}$ ) as impurities.

## Chapter 4

# **The Effect of temperature and agitation on polyethyleneimine adsorption on iron oxide magnetic nanoparticles in the synthesis of iron oxide-Au core-shell nanoparticles**

### **4.1 Introduction**

Iron oxide nanoparticles are known for their cost effectiveness and unique properties such as chemical stability, biocompatibility, non-toxicity, effective specific power absorption rate, strong magnetic properties, high separation efficiency and high specific surface area which makes them useful in various field applications. These properties become limited in use due to the aggregation of iron oxide nanoparticles with time during synthesis and applications especially in biomedical and biosensor/immunosensor applications. Biomedical applications such as in vitro magnetic separation (particles sizes >50 nm) and in vivo analysis (particles sizes <50 nm) require the use of iron oxide nanoparticles with narrow size distribution and surface coating with biocompatible materials at physiological pH (pH 7.3 to 7.4 in which body cells can survive and function best). The surface modification of these nanoparticles is necessary for the full utilization of the magnetic property of iron oxide nanoparticles and also to adjust the zeta potential of the ferro fluid to zero at physiological pH.

The use of electrostatic stabilization of nanoparticles through the creation of electrostatic repulsion of similarly charged surfaces due to an electric double layer around the particles (Kim *et al.*, 2003) is one of the most efficient and practical ways for the surface modification of iron oxide nanoparticles.

Magnetic iron oxide nanoparticles are known to be isoelectric at a pH of 7 (Vergés *et al.*, 2008; Daou *et al.*, 2009), indicating that they are only stable at high or low pH values thus requiring surface modification through the use of organic or inorganic stabilizers. In synthesizing Iron oxide nanoparticles organic stabilizers (natural or synthetic) such as dextran, starch, gelatin, chitosan, poly (ethyleneglycol) (PEG), poly(vinyl alcohol) (PVA), poly(lactide acid) (PLA), alginate, polymethylmethacrylate (PMMA),

polyacrylic acid (PAA), and inorganic stabilizers (silica, metal, non-metal, metal oxides and sulphides) have been used to functionalize the nanoparticles. Among the synthetic organic stabilizers used in functionalizing iron oxide nanoparticles, polyethyleneimine (PEI) is known to be effective in stabilizing, preventing aggregation of iron oxide nanoparticles and as capping agent in formation of iron oxide core gold shell nanoparticles for biomedical applications.

In recent years great deal of research has been focused on ways of improving the use and application of Iron oxide nanoparticles in in-vivo and bioelectronics applications. Iron oxide nanoparticles coated with gold shell serve as excellent platform for the construction of biosensors, immunosensors and other biomedical and environmental applications. The presence of gold shell on iron oxide nanoparticles increases the nanoparticles surface area, electrical conductivity and biocompatibility for the conjugation of proteins, enzymes, antibodies and deoxyribonucleic acid (DNA). The magnetic properties of iron oxide nanoparticles allows for the control of the iron oxide-Au shell nanoparticles with external magnetic force to specific targets in in-vivo biomedical applications such as drug delivery and cell separation. Iron oxide-gold shell nanoparticles often used in biomedical or biosensor analysis are either magnetite coated gold shell ( $\text{Fe}_3\text{O}_4\text{-Au}$ ) or maghemite coated gold shell ( $\text{Fe}_2\text{O}_3\text{-Au}$ ).

Research have shown that it is easier to synthesize maghemite coated gold shell ( $\text{Fe}_2\text{O}_3\text{-Au}$ ) compared to magnetite coated gold shell ( $\text{Fe}_3\text{O}_4\text{-Au}$ ) because  $\text{Au}^{3+}$  reduces preferentially onto  $\gamma\text{-Fe}_2\text{O}_3$  surfaces compared to  $\text{Fe}_3\text{O}_4$  (Lyon *et al.*, 2004), although the reasons for the disparity in the deposition is not known since  $\text{Fe}_3\text{O}_4$  and  $\gamma\text{-Fe}_2\text{O}_3$  have very close lattice parameters ( $a=0.840$  and  $0.835\text{nm}$  respectively).

Iron oxide core-Au shell nanoparticles has been successfully used in fabricating DNA sensors (Li *et al.*, 2011c; Loaiza *et al.*, 2011), immobilization of biomolecules (Tamer *et al.*, 2013), enzyme glucose biosensor (Li *et al.*, 2011b), catalysis (Wu *et al.*, 2010), protein immunosensors (Liang *et al.*, 2009) and as contrast agents (Kim *et al.*, 2009).

## 4.2 Polyethyleneimine

PEI also known as polyaziridine is an organic molecule that exists in two forms, linear and branched forms. Linear PEI contains two methyl groups and a secondary amine and

is a solid at room temperature with melting point of 73-75 °C. It is soluble in methanol, chloroform, ethanol at low pH and in hot water. Branched PEI is a polycation with 25% primary, 50% secondary and 25% tertiary amino groups as shown in Figure 4.1. It is water soluble polyamine, a liquid at room temperature with melting and boiling points of 59-60 °C and 250 °C respectively and is normally synthesized from its monomer in the presence of a catalyst.

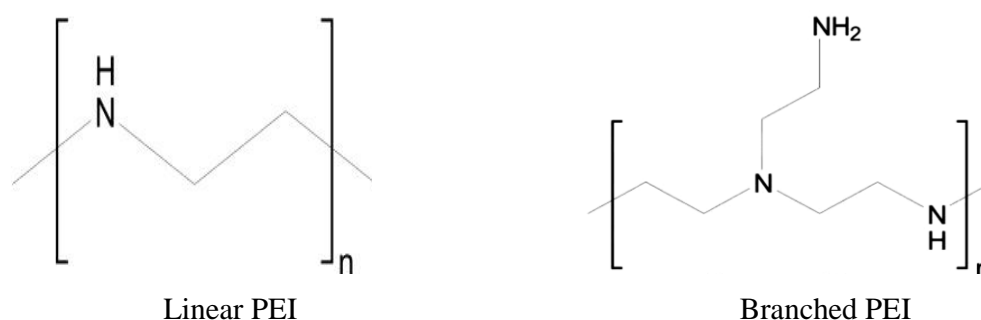


**Figure 4.1 Chemical structure of linear and branched PEI**

Branched PEI is synthesized in different molecular weight suitable for the stabilization of different sizes of iron oxide nanoparticles. In solution during synthesis of iron oxide nanoparticles the negatively charged iron oxide nanoparticles binds electrostatically with the positively charge PEI to form a stabilizing polyelectrolyte layer. This enhances the iron oxide stability due to the steric hindrance and electrostatic repulsion between the iron oxide nanoparticles as a result of PEI coatings (Goon *et al.*, 2010; Zhou *et al.*, 2010).

Polyethyleneimine forms stable complex with metal ions at pH 4-12 due to the high amount of amine-nitrogen it contains that can donate electrons and chelate metal ions (Maketon and Ogden, 2009). The presence of the amine groups also allow for the easy modification of polyethyleneimine to act as coating on inorganic materials, carriers for enzymes immobilization and the neutralization of excess anionic colloidal charges mostly found in acidic and neutral pH conditions .

Researches have been carried out on the use of PEI as stabilizing and capping agent for nanoparticles. Goon and co-workers (Goon *et al.*, 2010) studied the adsorption of PEI on iron oxide nanoparticles (Fe<sub>3</sub>O<sub>4</sub>) by varying PEI concentration from 0-50mg l<sup>-1</sup> at 80 °C. They showed that increased PEI concentration, increases the amount of PEI adsorbed on the surface of iron oxide nanoparticles due to the greater number of PEI

chains present and it also increases the electrophoretic mobility of the particles. The nanoparticles were found to be most stabilized at  $50\text{mg l}^{-1}$  and lower or higher concentrations of PEI results in nanoparticle aggregation. In a separate research, they also found out that by varying PEI concentration from  $0\text{--}4\text{g l}^{-1}$  at  $60^{\circ}\text{C}$ , the maximum amount of PEI adsorbed on iron oxide nanoparticles ( average particles size 50 nm) was  $0.88\mu\text{g PEI per cm}^3$  particles surface by measuring the solution organic carbon content since PEI is the only source of carbon (Goon *et al.*, 2009).

Zhou and co-workers stabilized and coated iron oxide nanoparticles (40 nm) with gold shell using  $5\text{g l}^{-1}$  PEI at  $60^{\circ}\text{C}$  for protein detection (Zhou *et al.*, 2010) although the molecular weight of the PEI used depends on the size of the nanoparticles. Wang et al, controlled the aggregation of iron oxide nanoparticles by agitating the nanoparticles at room temperature with different amount of 5% mass per mass (m/m) PEI solution (Wang *et al.*, 2009). Jin-jun and co-workers coated iron oxide nanoparticles with PEI by stirring the nanoparticles with PEI at room temperature for the selective removal of cadmium ion from blood (Jin *et al.*, 2012). Also Yiu et al., coated iron oxide nanoparticles with PEI by heating the nanoparticles with PEI at  $130^{\circ}\text{C}$  for possible neutral cell transplantation therapies (Yiu *et al.*, 2012).

PEI was used to improve the stability and sensitivity of glucose biosensor up to 200% by reacting PEI and glucose oxidase at room temperature (Qian *et al.*, 2004). The result showed that the response of the glucose biosensor increases as PEI concentration increases up to 2.5% (w/v) PEI before decreasing. The biosensor stability was dramatically increased with reduced detection limit due to PEI ability to prevent the oxidation of the enzyme's sulfidic groups.

Although many studies have been carried out on iron oxide magnetic nanoparticles synthesis, there have not been systematic studies on the effect of heating temperature on PEI coating. Temperature is a crucial factor for the amount of PEI adsorption on nanoparticle surface and therefore will affect the stability and capping effect of PEI in gold coating process when preparing gold shell iron oxide core magnetic nanoparticles. The more PEI adsorbed on the surface of the iron oxide nanoparticles, the higher the electrostatic attachment of gold shell nanoparticles which in turn improves the electron transfer properties of the nanoparticles when used for biosensor/immunosensor fabrication.

In this thesis work biopolymer chitosan was used as a coating film for the immobilization of the nanoparticles (iron oxide core-gold shell) on to the surface of an electrode for the electrochemical characterization of the nanoparticles.

### 4.3 Chitosan

Chitosan is a natural linear polysaccharide derived by deacetylation (DA) of chitin found in the shells of crustacea such as crab, shrimp, and crawfish. Chitin is associated with proteins and therefore, high in protein contents. The deacetylation of chitin involves removing the acetyl groups found in the molecular chain of chitin, resulting in the formation of chitosan with a high degree chemical reactive amino group ( $-\text{NH}_2$ ). Chitin and chitosan have similar chemical structures but the difference is the absence of the acetyl groups ( $\text{CH}_3\text{-CO}$ ) found in chitin. Chitosan is composed of randomly distributed  $\beta$ -(1-4)-linked D-glucosamine (deacetylated unit) and N-acetyl-D-glucosamine (acetylated unit). The structure of chitin and chitosan are shown in Figure 4.2.

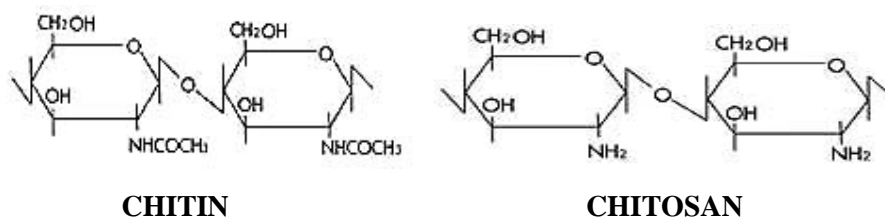


Figure 4.2 Structures of chitin and chitosan

Chitosan is non-toxic, biodegradable and biocompatible polymer which has made its application widely accepted in field such as pharmaceutical and biomedical industries for enzyme immobilization and purification, wastewater treatment in chemical plants and in food industries for food formulations as binding, gelling, thickening and stabilizing agent (Knorr, 1984). Chitosan possesses unique properties including the ability to form films, optical structural characteristics and much more. Chitosan also possesses a positive ionic charge, which gives it the ability to chemically bind with negatively charged fats, lipids and bile acids (Sandford, 1992).

## 4.4 Aims

The aim of this chapter is to synthesize iron oxide core-gold shell nanoparticles and to study the effect of different heating temperatures (25 °C, 40 °C, 60 °C, 80 °C and 100 °C) and agitation on polyethyleneimine adsorption on magnetic iron oxide nanoparticles (50 nm) and in the formation of gold shell nanoparticles. Comparisons between different temperatures were based on electrochemical techniques using cyclic voltammetry (CV) and electrochemical impedance spectroscopy (EIS). It demonstrates a simple electrochemical method on characterization of the effect of temperature and PEI adsorption in nanoparticles synthesis. Physical characterization of iron oxide core-gold shell nanoparticles were carried out with x-ray diffraction, x-ray photoelectron spectroscopy, scanning electron microscopy and transmission electron microscopy. Electrochemical characterizations were carried out using cyclic voltammetry and electrochemical impedance spectroscopy after immobilizing the iron oxide core-gold shell nanoparticles with chitosan on an electrode surface.

## 4.5 Experimental

### 4.5.1 Materials and chemicals

Polyethyleneimine (branched 25000 mw), iron II sulphate heptahydrate >99%, Chitosan powder (deacetylated chitin) were purchased from Sigma Aldrich (Dorset UK), sodium hydroxide 97%, sodium citrate 100%, hydrogen tetrachloroauric acid 100% (HAuCl<sub>4</sub>), Sodium borohydride powder 98% (NaBH<sub>4</sub>) and Hydroxylamine hydrochloride (99%), tetramethylammonium hydroxide pentahydrate (TMAOH) and potassium nitrate 99% were from Alfa Aesar (Lancashire UK). All chemicals were used as received without further purification. Solutions were prepared using Millipore deionised water.

### 4.5.2 Synthesis of 50nm average size oxidized iron oxide nanoparticles ( $\gamma$ -Fe<sub>2</sub>O<sub>3</sub>Nps)

0.025M FeSO<sub>4</sub> was added to 80ml of deionized water in 250ml round bottom flask after sparging for 20 minutes. Potassium nitrate (10ml, 2M) was added followed by the addition of sodium hydroxide (10ml, 1M). The mixture was sparged constantly and heated for 2 hours at 90 °C. The black precipitate of iron oxide nanoparticles formed was washed several times with deionised water and dispersed in 80ml deionised water with concentration 2.4gl<sup>-1</sup> at pH 6-7. The precipitate was separated with magnet and washed

once with 250ml of TMAOH (0.1M) solution and separated with a magnet. The precipitate was further washed with 250ml of HNO<sub>3</sub> (0.01M) and separated with magnet. Finally the precipitate was dispersed in 250ml of HNO<sub>3</sub> (0.01M) and heated at 90-100°C with stirring until the colour turns brown (Hien Pham *et al.*, 2008). The oxidized particles were separated with magnet and washed twice with deionised water and dispersed in 250ml of TMAOH (0.1M).

#### **4.5.3 Synthesis of iron oxide core/ gold seed nanoparticles ( $\gamma$ -Fe<sub>2</sub>O<sub>3</sub>-Au<sub>seed</sub> NPs)**

Gold seed (3 nm) nanoparticles were deposited on the oxidized iron oxide by a modified method from Zhou and co-workers (Zhou *et al.*, 2010). 5ml of TMAOH stabilized  $\gamma$ -Fe<sub>2</sub>O<sub>3</sub> nanoparticles were stirred for 30 minutes in 50ml of 5gl<sup>-1</sup> PEI to exchange absorbed OH<sup>-</sup> ions with PEI ions and separated with an external magnet. The particles were rinsed with deionised water to pH 6-7 and dispersed in 50ml of 5gl<sup>-1</sup> PEI by sonicating for 5 minutes before heating for 1 hour at 60°C. The nanoparticles were separated with magnet and the supernatant discarded and washed severally with deionised water to pH 6-7.

The nanoparticles were then dispersed in 90ml of deionised water and sonicated for 5 minutes followed by the addition of 1ml of 1% HAuCl<sub>4</sub> acid and stirred for another 5 minutes. 2ml of sodium citrate (38.8mM) solution was added and stirred for 2 minutes. Finally 1ml of freshly prepared 0.075 wt. % of sodium borohydride (NaBH<sub>4</sub>) in 1ml of 38.8mM sodium citrate was added and the system stirred for 2 hours. This allows for the direct deposition of gold seeds on the surface of the iron oxide nanoparticles.

The iron oxide-gold seed nanoparticles ( $\gamma$ -Fe<sub>2</sub>O<sub>3</sub>-Au<sub>seed</sub> NPs) formed were separated with magnet and washed to a pH of 6-7 with deionised water to remove excess gold seed. The nanoparticles were then dispersed in 50ml of 5gl<sup>-1</sup>PEI solution and heated at 60°C for 1 hour to form Fe<sub>2</sub>O<sub>3</sub>- Au seed-PEI nanoparticles (Fe<sub>2</sub>O<sub>3</sub>- Au seed-PEI). After heating, the nanoparticles were separated with magnet and rinsed to a pH of 6-7 with deionised water.

#### **4.5.4 Synthesis of iron oxide core/gold shell nanoparticles (Fe<sub>2</sub>O<sub>3</sub>-Au<sub>shell</sub> NPs)**

Gold shells were formed on the iron oxide gold seeds nanoparticles through iterative reduction of chloroauric acid with hydroxylamine chloride as the mild reducing agent.

Iron oxide-Au seed nanoparticles with PEI layers ( $\text{Fe}_2\text{O}_3$ - Au seed-PEI) were dispersed in 110ml of NaOH (0.01M) and agitated for 5 minutes followed by the addition of 0.5ml of 1% chloroauric acid and 0.75ml of hydroxylamine with vigorous stirring. The reaction was allowed to proceed for ten minutes followed by subsequent iteration of 0.5ml chloroauric acid and 0.25ml of hydroxylamine for the 2<sup>nd</sup>, 3<sup>rd</sup>, 4<sup>th</sup>, and 5<sup>th</sup> iterations with ten minutes intervals between iterations (Goon *et al.*, 2009; Zhou *et al.*, 2010). The process was repeated twice for a total of ten iterations and the iron oxide gold shell nanoparticles ( $\text{Fe}_2\text{O}_3$ - Au shell) were then washed twice with water, once with HCl (1M) and rinse with water. Figure 4.3 shows a schematic diagram for the iron oxide core-gold shell nanoparticles synthesis process. The concentration of the gold shell formed is  $0.000254\text{mol}^{-1}$  and thickness 24 nm based on calculation from the absorbance peaks.

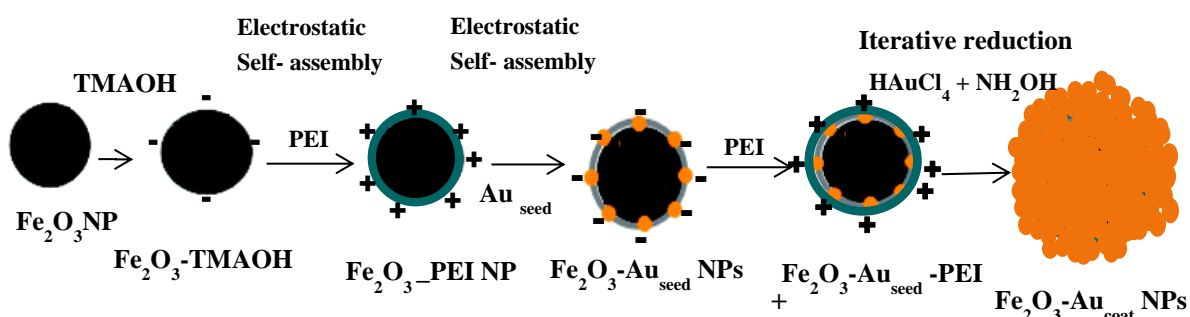


Figure 4.3 Schematic diagrams for the synthesis of  $\text{Fe}_2\text{O}_3$ -Au shell nanoparticles

#### 4.5.5. Preparation of nanoparticles modified electrodes with chitosan

Chitosan glassy carbon electrode (GC-CHIT) was formed by dropping 10 micro-litres ( $\mu\text{L}$ ) of 0.2wt.% of chitosan solution on a polished glassy carbon electrode ( $0.071\text{cm}^2$ ) and allowed to dry in air. The 0.2 wt. % Chitosan solution was prepared by dissolving 0.2g of deacetylated chitosan powder in 100ml of acetic acid (0.05M) and the mixture stirred for three hours. Iron oxide-TMAOH-chitosan modified glassy carbon electrode (GC- $\text{Fe}_2\text{O}_3$ -TMAOH-CHIT) was prepared by first adding 1ml of TMAOH stabilized  $\text{Fe}_2\text{O}_3$  nanoparticles in 2ml of chitosan (0.2wt.%) solution and sonicated for 3 minutes to form a mixture. Then 10  $\mu\text{L}$  of the mixture was deposited on a cleaned glassy carbon electrode and allowed to dry in air.

Iron oxide-PEI-chitosan modified electrodes (GC- Fe<sub>2</sub>O<sub>3</sub>-PEI-CHIT) was prepared by adding 1ml of iron oxide PEI nanoparticles obtained from stirring TMAOH stabilized iron oxide nanoparticles with PEI and then heating the nanoparticles in the presence of 5gl<sup>-1</sup>PEI at 60°C as described in section 4.5.3., in 2ml of 0.2wt% chitosan solution and sonicated for 3 minutes. Then 10 µL of the mixture was deposited on a cleaned glassy carbon electrode and allowed to dry in air. Finally iron oxide core-gold shell modified electrode (GC- Fe<sub>2</sub>O<sub>3</sub>-PEI-Au-CHIT) was prepared by adding 1ml of iron oxide-gold shell nanoparticles in 2ml chitosan solution and sonicated for 3 minutes. 10 µL of the mixture was then deposited on a clean glassy carbon electrode and allowed to dry in air.

#### ***4.5.6 Synthesis of iron oxide nanoparticles (Fe<sub>2</sub>O<sub>3</sub> /PEI NPs) at different temperatures***

2.4gl<sup>-1</sup> Fe<sub>3</sub>O<sub>4</sub> solution at pH 6-7 prepared in section 4.5.2 was separated with a magnet and the precipitate washed with 250ml of HNO<sub>3</sub> (0.01M). The precipitate was dispersed in 250ml of 0.01M HNO<sub>3</sub> and heated at 90-100°C until the solution colour turned to brown (Hien Pham *et al.*, 2008). The oxidized nanoparticles were separated with magnet and washed twice with deionised water and dispersed in 250ml tetramethylammonium hydroxide (TMAOH). Then 5ml of TMAOH stabilized Fe<sub>2</sub>O<sub>3</sub> nanoparticles were stirred for 30 minutes in 50ml of 5gl<sup>-1</sup> PEI to exchange absorbed OH<sup>-</sup> ions with PEI ions and separated with an external magnet. The particles were rinsed to pH 6-7 with deionised water and dispersed in 50ml of 5gl<sup>-1</sup> PEI by sonicating for 3 minutes. For synthesis at 25°C, the particles were allowed to stabilize in the PEI solution for 1 hour without stirring and the others were heated for 1 hour at 40°C, 60°C, 80°C and 100°C respectively.

#### ***4.5.7 Preparation of iron oxide-PEI (Fe<sub>2</sub>O<sub>3</sub> /PEI) modified electrodes at different temperatures***

Iron oxide/polyethyleneimine modified glassy carbon electrodes (GC- Fe<sub>2</sub>O<sub>3</sub>-PEI-CHIT) were prepared by adding 1ml of iron oxide/PEI nanoparticles in 2 ml of 0.2 wt.% chitosan (CHIT) solution and sonicated for 5 minutes. 10µl of the mixture was pipetted on a clean glassy carbon electrode and allowed to dry in air. This process was repeated for iron oxide-PEI nanoparticles synthesized at the different temperatures (25 °C, 40 °C, 60 °C, 80 °C and 100 °C).

#### ***4.5.8 Instrumentation and characterization of the nanoparticles***

The synthesized nanoparticles were characterized using physical and electrochemical characterization techniques. Physical characterization of the nanoparticles were carried out using Philips XL 30 environmental scanning electron microscopy (ESEM) operated at 20kV to determine the surface morphology of the particles. X-ray diffraction pattern of the nanoparticles were obtained using PANalytical X'pert Pro MPD, powered by Philips PW 3040/60 X-ray generator fitted with X'celerator and using Cu K $\alpha$  radiation with wavelength of 1.54180Å to determine the crystalline structure of the nanoparticles. UV-Vis spectroscopy analysis of nanoparticles was carried out using Jenway 6705 model UV-VIS Spectrometer to detect the presence of gold shell nanoparticles on the iron oxide core-Au shell composite nanoparticles and their surface Plasmon resonance and band. Transmission electron microscopy (TEM) was carried out with Philips CM200 FEGTEM field emission gun TEM/STEM with supertwin objective lens. The TEM was used in analysing the shape, size and morphology of the iron oxide core-Au shell nanoparticles.

Electrochemical characterizations of the nanoparticles electrode were carried out using cyclic voltammetry (CV) and electrochemical impedance spectroscopy (EIS). CV analysis was obtained with Ecochemie BV PGSTAT 302 Autolab (Netherland) in 0.1M phosphate buffer (pH 7.4) containing 5mM ferrocyanide/ferricyanide [Fe (CN) $_6$ ] $^{4-/3-}$  at a scan rate of 50mV/s. The cyclic voltammetry (CV) allows for the determination of changes on the electrode behaviour after modification with nanoparticles and the ability of the nanoparticles to allow the flow of electrons between the probe solution and electrode surface.

EIS analysis was carried out with Ecochemie BV PGSTAT 302 Autolab (Netherland) in 0.1M phosphate buffer (pH 7.4) containing 5mM ferrocyanide/ferricyanide [Fe (CN) $_6$ ] $^{4-/3-}$  in ratio 1:1 by applying an open circuit potential with amplitude 5mV in frequency range 0.01Hz-10kHz. EIS analysis was carried out on the modified electrodes to obtain information on the opposition or resistance (impedance) to alternating current of the electrodes modified with the different stages of the nanoparticles. The resistance determines the movement of electrons of the redox probe (ferrocyanide/ferricyanide) at the electrode interface. A three electrode cell with a 3mm diameter (area 0.07cm $^2$ )

glassy carbon electrode (GCE) as working electrode, Ag/AgCl (3M NaCl, 0.208V vs SHE) as the reference electrode and a platinum wire as the counter electrode was used for the analysis.

## 4.6 Result and discussion

### 4.7 Physical properties of nanoparticles

#### 4.7.1 Paramagnetic effect of iron III oxide ( $\gamma\text{-Fe}_2\text{O}_3$ ), iron oxide/gold shell nanoparticles ( $\gamma\text{-Fe}_2\text{O}_3\text{-Au shell}$ ) and their XPS analysis

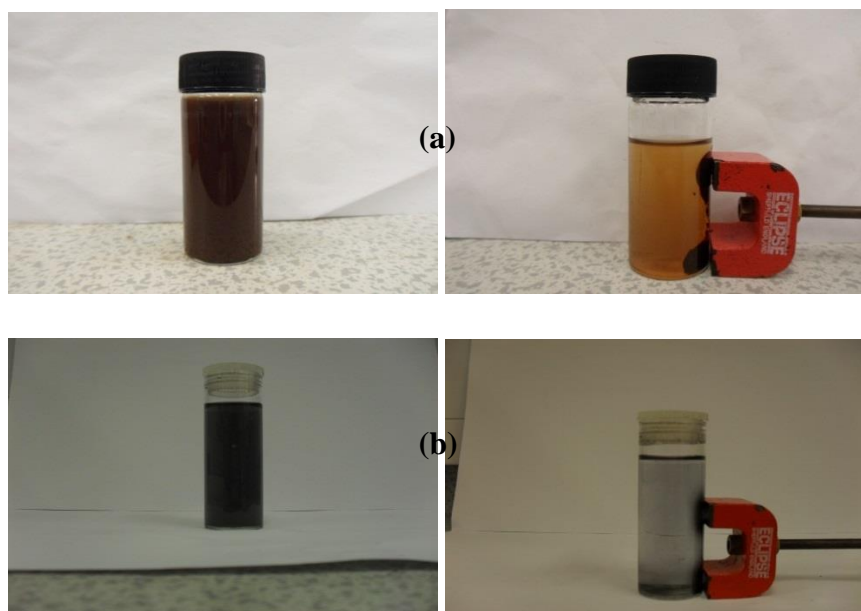


**Figure 4.4 (a)  $\text{Fe}_2\text{O}_3$  nanoparticles stabilized in TMAOH before and after magnetic separation (b)  $\text{Fe}_2\text{O}_3\text{-Au shell}$  before and after magnetic separation**

Figure 4.4a shows that iron III oxide (maghemite) displayed paramagnetic behaviour in the presence of an external magnetic field and gradually re-disperse back in solution in the absence of the magnet. It was also observed in Figure 4.4b that despite coating the iron oxide with gold shell, the nanoparticles still maintained paramagnetic effect. This indicates that the magnetic property of the iron oxide nanoparticles is not affected by the formation of gold shell on its surface, and the combined properties of the iron oxide-gold shell nanoparticles can effectively be applied.

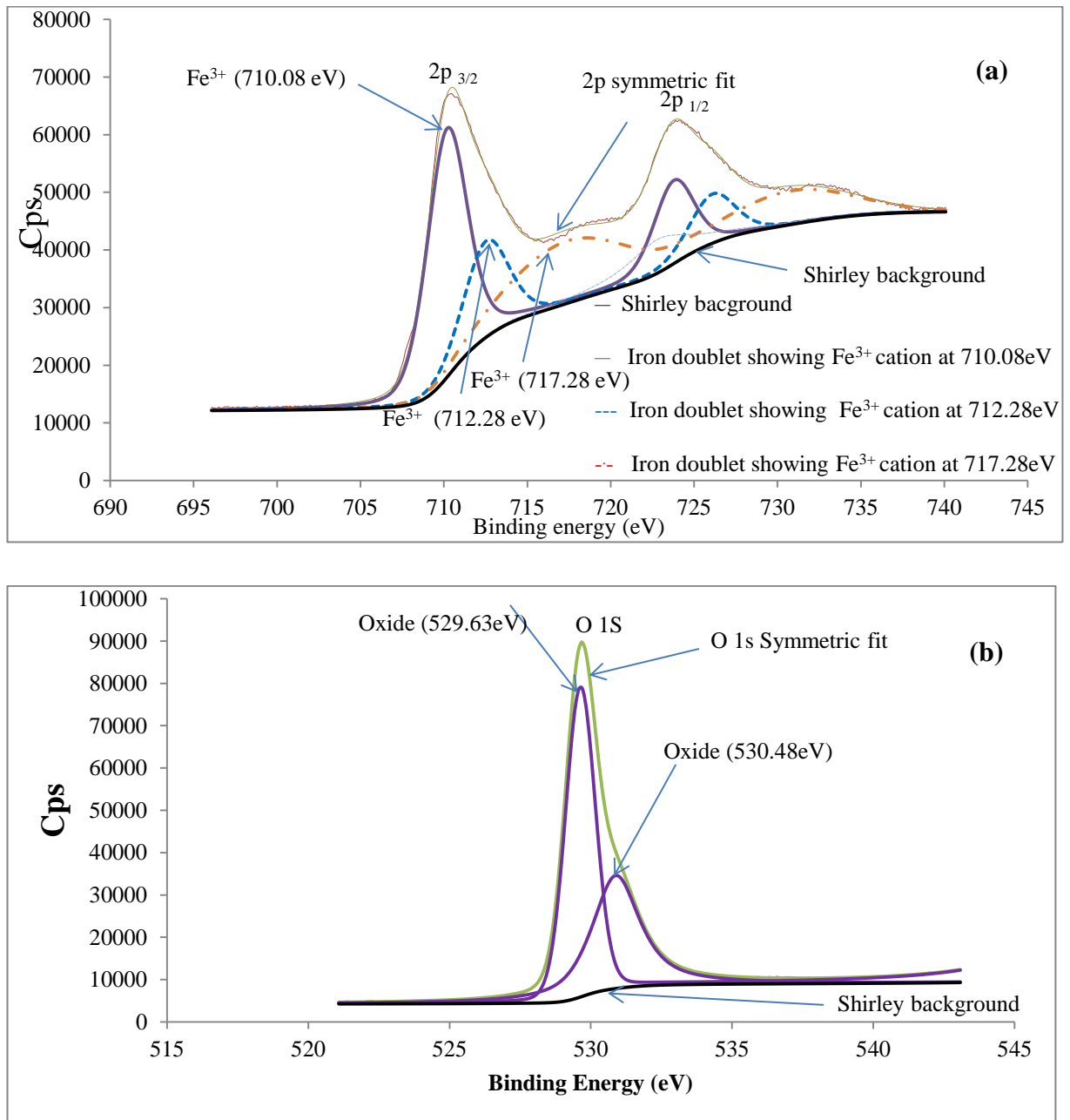


**Figure 4.5** Fe<sub>2</sub>O<sub>3</sub> nanoparticles XPS analysis (a) 2p core electrons (b) 1s core electrons of O<sub>2</sub>

Figure 4.5a shows the characteristic doublet of iron based compounds showing the 2p core electrons for maghemite ( $\gamma$ -Fe<sub>2</sub>O<sub>3</sub>). The doublets shows peaks indicated by the arrows which can be assigned to iron III cation (Fe<sup>3+</sup>) at 710.08eV, 712.28eV and a characteristic satellite peak at 717.28eV. These peaks are characteristics of maghemite which contains only iron III oxidation states (Goon *et al.*, 2010). The appearance of satellite peaks at 717.28eV in the oxidized samples as shown in Figure 4.5a indicates the presence of iron III. The satellite peak results from an incident x-ray photon which

gives up a discrete portion of its energy to the excitation of a second electron rather than imparting its quantum of energy to the primary (Mills and Sullivan, 1983; Yamashita and Hayes, 2008). Figure 4.5b shows the XPS spectra for oxygen 1s core electron present in the nanoparticles. The scan shows characteristics oxide peaks at 529.63eV and 530.48eV confirming the presence of only oxides in the iron oxide nanoparticles sample ( $\gamma$ -Fe<sub>2</sub>O<sub>3</sub>) and no hydroxyl species (iron oxy- hydroxide).

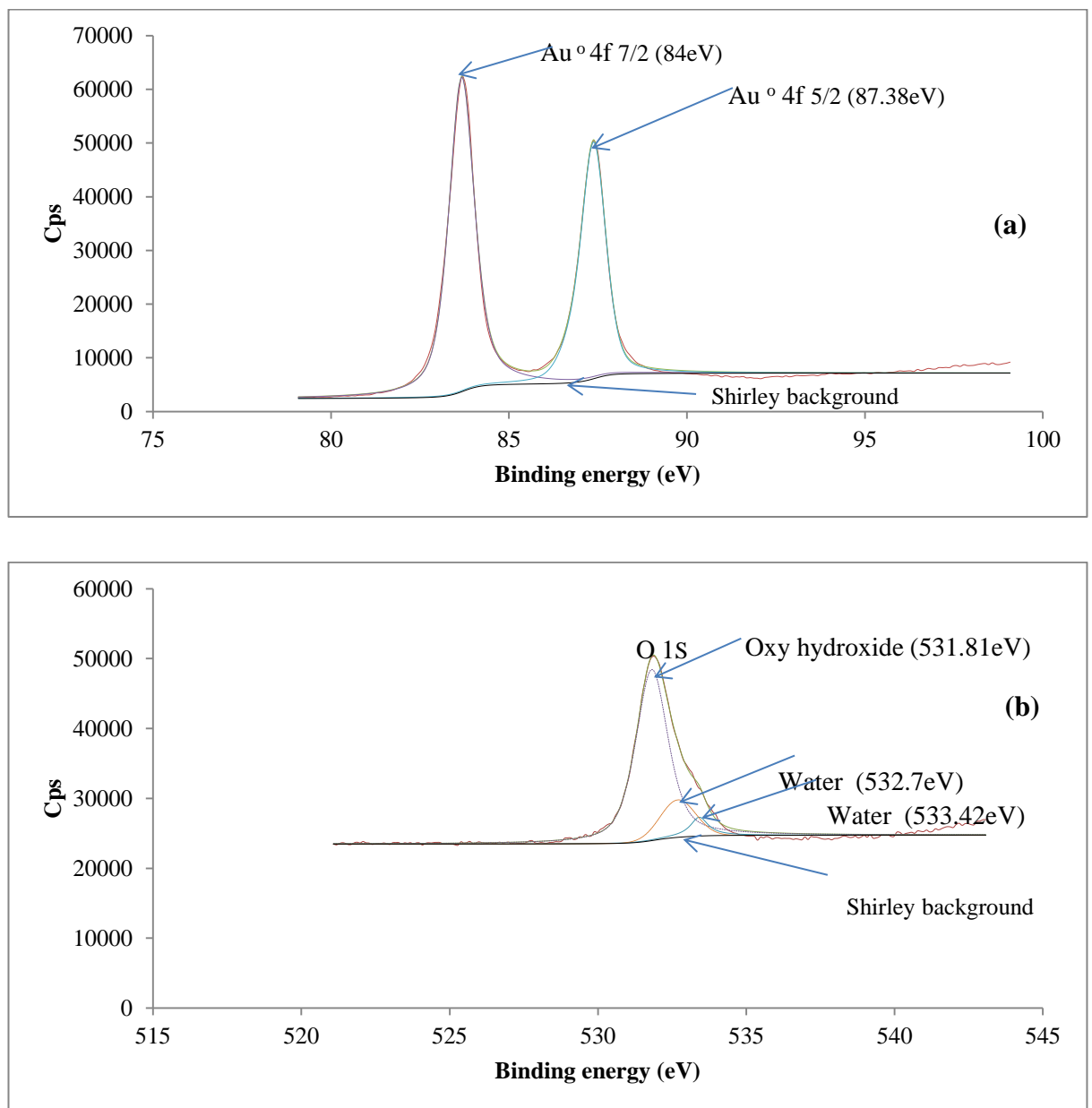


**Figure 4.6 XPS analysis of Au shell on Fe<sub>2</sub>O<sub>3</sub> nanoparticles (a) 4f core electrons of Au (b) 1s core electrons of O<sub>2</sub>**

Figure 4.6a shows the XPS analysis of  $\text{Fe}_2\text{O}_3$ -Au shell nanoparticles indicating the presence of 4f core electrons of Au resulting from the formation of Au shell on the iron oxide nanoparticles. The 4f core electrons of Au was observed at binding energies of 84eV and 87.38eV corresponding to  $4f_{7/2}$  and  $4f_{5/2}$  core electrons respectively. The presence of the 4f peaks indicates that gold shell was deposited on the iron oxide nanoparticles. The 1s core electron of oxygen in the  $\text{Fe}_2\text{O}_3$ -Au shell nanoparticles observed at binding energy 531.81eV, might be attributed to the presence of iron oxy hydroxide resulting from chemisorption of water on the air exposed surfaces of the nanoparticles or the presence of non-stoichiometric surface oxygen atom which can still be observed in samples not exposed to air (Rodríguez Nieto *et al.*, 2009). The higher binding energy peaks at 532.7eV and 533.42eV can be attributed to the presence of water on the nanoparticles during gold shell formation or the sample not completely dried before XPS analysis. The XPS analysis in Figures 4.5 and 4.6 confirms the presence of the components that make up iron oxide core and gold shell nanoparticles, indicating that iron oxide core-gold shell were formed during synthesis.

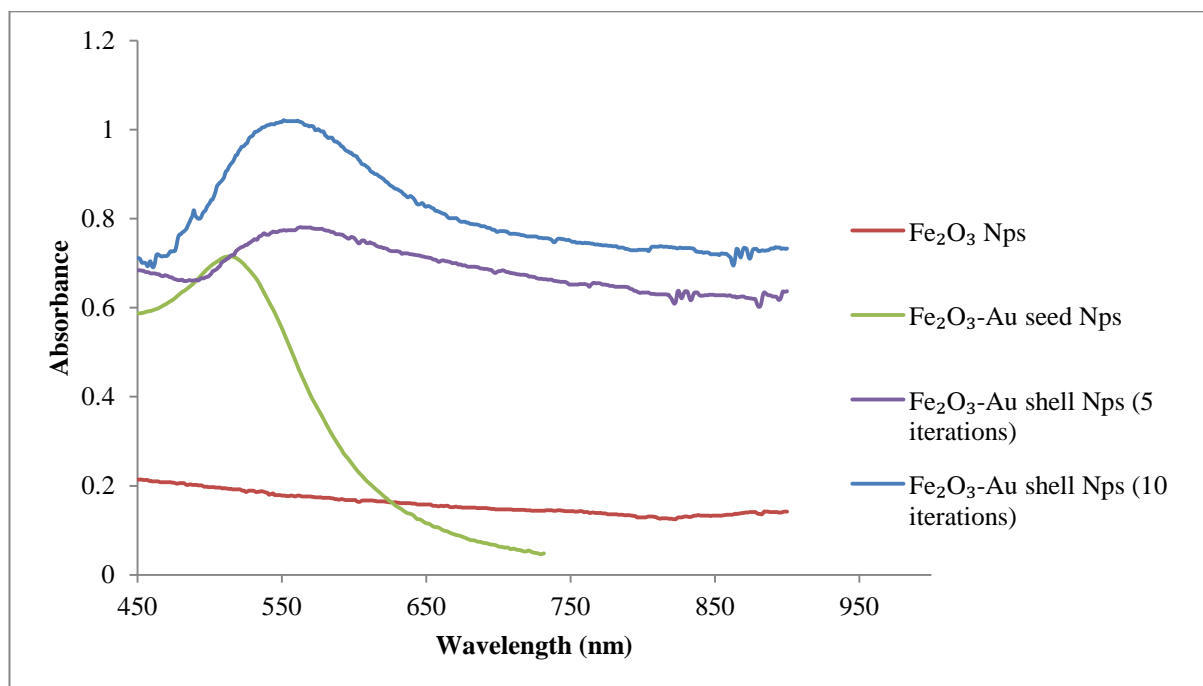
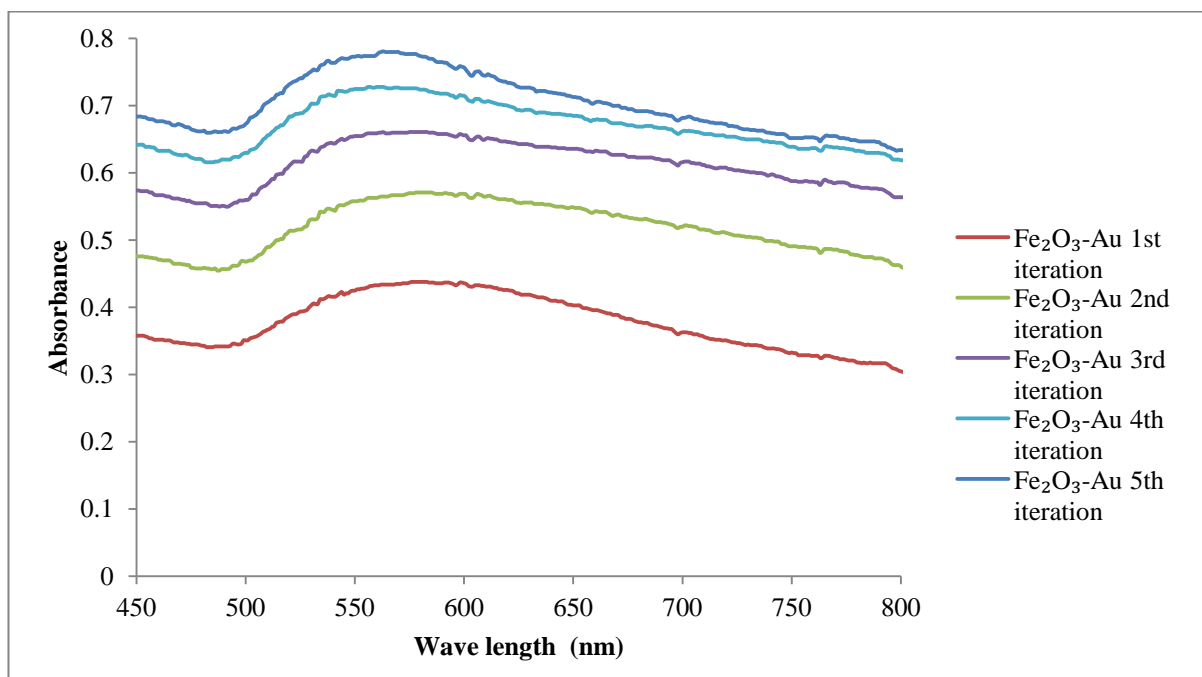


Figure 4.7 UV-Vis spectra for  $\text{Fe}_2\text{O}_3$ , Au seed,  $\text{Fe}_2\text{O}_3$ -Au 5<sup>th</sup> iteration and  $\text{Fe}_2\text{O}_3$ -Au 10<sup>th</sup> iteration



**Figure 4.8 UV-Vis spectra for Fe<sub>2</sub>O<sub>3</sub>/Au shell formation showing the 5 iteration steps**

The optical properties of the as-prepared nanoparticles ( $\gamma$ -Fe<sub>2</sub>O<sub>3</sub>, Fe<sub>2</sub>O<sub>3</sub> –Au<sub>shell</sub>) was analysed with the aid of UV- Vis spectroscopy. In Figure 4.7 a featureless spectra was observed for iron oxide (Fe<sub>2</sub>O<sub>3</sub>) nanoparticles indicating the absence of surface plasmon resonance. The gold seed nanoparticles showed the presence of surface plasmon resonance peak at 512 nm indicating the formation of approximately 3 nm gold seed nanoparticle. The sizes of the gold seed nanoparticles were determined based on UV- Vis spectra analysis following a method as reported by Haiss and co-workers (Haiss *et al.*, 2007).

The formation of Fe<sub>2</sub>O<sub>3</sub>-Au<sub>shell</sub> nanoparticles using the iterative reduction of chloroauric acid with hydroxylamine was done for both 5 iteration and 10 iteration steps. It was observed that during the 5 iterative steps, the amount of the gold shell on the iron oxide nanoparticles increases resulting to a blue shift of the surface plasmon resonance in the UV-Vis spectra to 556 nm wavelength. Increasing the iteration process to 10 iterations, result in further blue shift in the UV-Vis spectra to 546 nm. The 10 iteration steps allows for the almost 100% coverage of the iron oxide nanoparticles with gold shell compared to the 5 iteration process as shown in ESEM results in Figure 4.9.

Figure 4.8 shows that the surface plasmon resonance peaks wavelength decreases as the iteration steps increases from 578 nm, 574 nm, 565 nm 558 nm and 556 nm for 1<sup>st</sup>, 2<sup>nd</sup>, 3<sup>rd</sup>, 4<sup>th</sup> and 5<sup>th</sup> iterations respectively, thus increasing the amount of gold nanoparticles on the iron oxide core nanoparticles surface. The size of the Au shell nanoparticles on the iron oxide was estimated to be approximately 25 nm after the 10<sup>th</sup> iteration based on UV-Vis spectra analysis which was further corroborated with the XRD results of 24 nm in Figure 4.10.

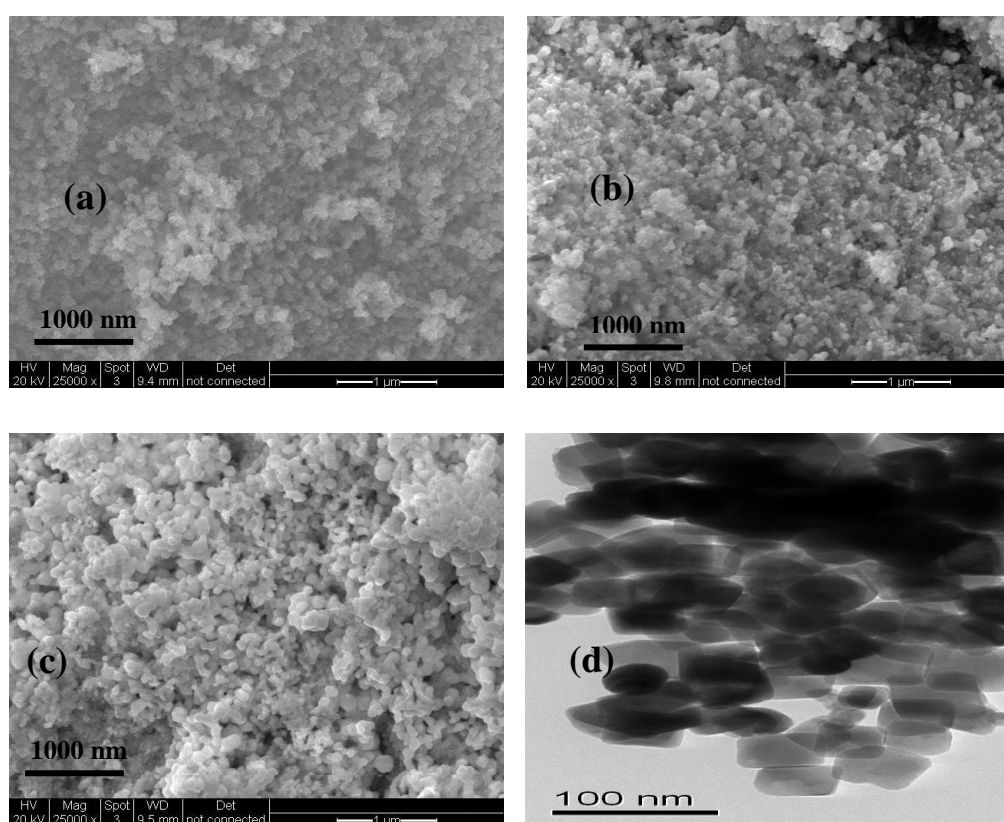


**Figure 4.9 (a) Fe<sub>2</sub>O<sub>3</sub> (b) Fe<sub>2</sub>O<sub>3</sub> –Au shell 5 iterations (c) Fe<sub>2</sub>O<sub>3</sub> –Au shell 10 iteration (d) TEM of 10 iteration**

Figure 4.9 (a), (b) and (c) shows the ESEM analysis of the Fe<sub>2</sub>O<sub>3</sub>, Fe<sub>2</sub>O<sub>3</sub> –Au shell gold shell nanoparticles after 5 iterations, Fe<sub>2</sub>O<sub>3</sub> –Au shell gold shell nanoparticles after 10 iterations and TEM image of Fe<sub>2</sub>O<sub>3</sub> –Au shell gold shell nanoparticles after 10 iterations respectively. Figure 4.9a shows the iron oxide nanoparticles with no gold shell formed as control and Fig, 4.9b shows that the nanoparticles were partially coated with gold shell after 5 iterations as reflected in the bright image due to the conductive property of gold compared to Fig 4.9a. Figure 4.9c shows that the nanoparticles were fully covered

with gold shell. Although the  $\text{Fe}_2\text{O}_3$ -Au shell nanoparticles after 10 iterations looks clustered together, this might be as a result of the nanoparticles not finely grounded before ESEM analysis and also due to low magnification of the ESEM during analysis. Figure 4.9d shows the TEM images of the iron oxide-Au shell nanoparticles showing the presence of gold shell on the iron oxide nanoparticles. The TEM resolution is different from the ESEM because of its detail analysis. The gold shell nanoparticles are the dark spots particles on the iron oxide nanoparticles as shown in the TEM analysis, although the TEM could not show how the gold shell is placed on the iron oxide nanoparticles surface. The TEM analysis also shows little fraction of the iron oxide nanoparticles not covered with gold shell, but the XRD result in Figure 4.10 indicates that the iron oxide nanoparticles were almost 100% covered with gold shell.

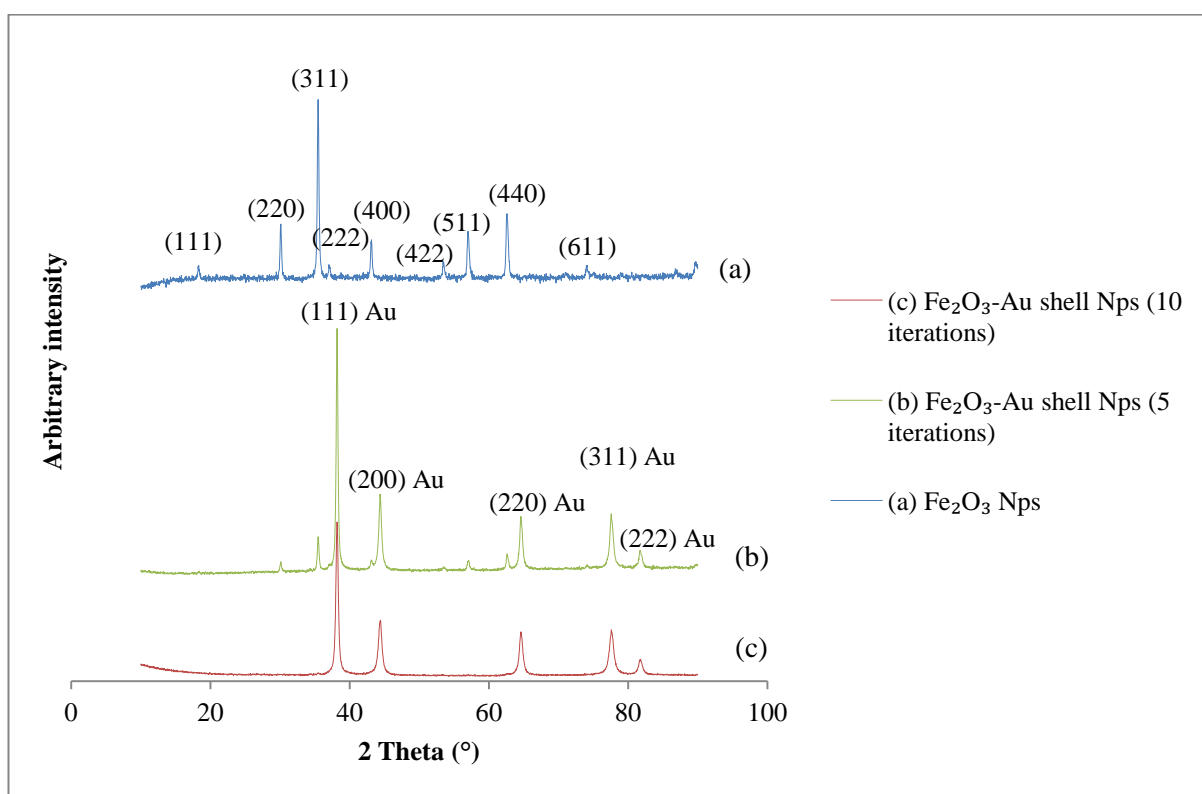


**Figure 4.10 XRD analysis of (a)  $\gamma\text{-Fe}_2\text{O}_3$  (b)  $\text{Fe}_2\text{O}_3$ -Au shell nanoparticles at 5 iterations (c)  $\text{Fe}_2\text{O}_3$ -Au shell nanoparticles at 10 iterations**

Figure 4.10a shows the X-ray diffraction patterns for maghemite ( $\gamma\text{-Fe}_2\text{O}_3$ ) nanoparticles synthesized using 0.025M  $\text{FeSO}_4$ . The diffraction peaks (111), (220), (311), (222), (400), (422), (511), (440) and (622) can be indexed to the face centre cubic

structure of maghemite which has similar crystallographic nature as magnetite ( $\text{Fe}_3\text{O}_4$ ). The average particle size of  $\gamma\text{-Fe}_2\text{O}_3$  NPs was calculated to be approximately 50 nm using peaks (311), (440), (222) and (511) with the Scherrer equation.

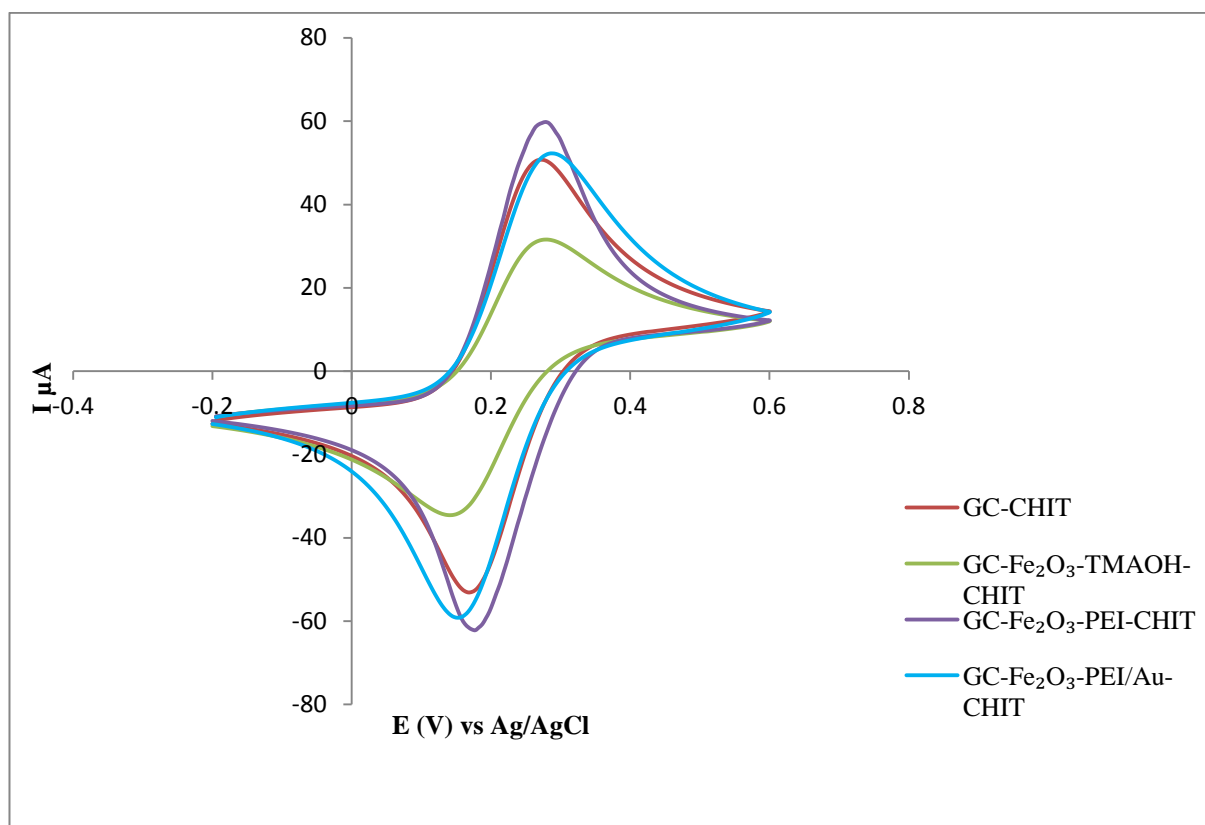
Figure 4.10b and c shows the  $\text{Fe}_2\text{O}_3$ -Au shell nanoparticles synthesized from 5 and 10 iteration processes respectively. The diffraction peaks at  $2\theta = 38.2^\circ, 44.4^\circ, 64.6^\circ, 77.5^\circ$  and  $81.7^\circ$  denoted with Au, can be indexed to (111), (200), (220), (311), and (222) of gold in a cubic phase. It was observed that after 5 iteration steps, diffraction peaks for maghemite were still present in the sample (b) with reduced intensity. This indicates that the maghemite nanoparticles were not fully covered with gold shell. Figure 4.10c shows that after 10 iteration processes in repeated sequence, the maghemite nanoparticles were fully covered with gold shell indicated by the disappearance of the maghemite peaks. The gold nanoparticles after 10 iterations have an average particles size of 24 nm and the total particle size for the iron oxide core- gold shell nanoparticles is 74 nm.

#### **4.8 Electrochemical properties of the nanoparticles**

Electrochemical characterization of the nanoparticles was carried out to determine the electrochemical properties of the nanoparticles when modified on an electrode. This shows how good the nanoparticles at different stages of modification can allow the flow of electrons between the probe solution and the surface of a modified electrode, and their biocompatibility to biomolecules.

Figure 4.11 shows the cyclic voltammogram trace of the nanoparticles at different stages modified on a glassy carbon electrode (GCE). The cyclic voltammogram trace is the plot of the working electrode current against applied potential in a cyclic voltammetry (CV) analysis. The results shows a well-defined oxidation and reduction peaks caused by the  $\text{Fe}^{3+}/\text{Fe}^{2+}$  redox couple for all the modified electrodes for both forward and reverse scans. The highest oxidation and reduction peaks of the  $\text{Fe}^{3+}/\text{Fe}^{2+}$  redox couple was observed when the glassy carbon electrode was modified with  $\text{Fe}_2\text{O}_3$ -PEI-CHIT nanoparticles at 0.27V and 0.18V respectively. This is attributed to the synergy between iron oxide and PEI and the ability of PEI to reduce electron transfer resistance in solutions due to its polycationic nature (Tan *et al.*, 2007).

The electrode modified with Fe<sub>2</sub>O<sub>3</sub>-PEI-Au-CHIT nanoparticles showed the second highest oxidation and reduction peaks at 0.28V and 0.15V respectively compared to Fe<sub>2</sub>O<sub>3</sub>-TMAOH-CHIT and CHIT modified electrodes.



**4.11 Cyclic voltammogram of nanoparticles modified electrodes in a 5mM ferrocyanide/ferricyanide [Fe(CN)<sub>6</sub>]<sup>4-/3-</sup> solution containing 0.1M PBS at a scan rate of 50mV/s**

This can be attributed to the ability of gold nanoparticle to act as an electron path way allowing the flow of electrons between the redox couple and the surface of the electrodes and also due to the synergetic effect of the composite film formed with iron oxide/PEI. The electrode modified with chitosan (CHIT) also showed a well-defined oxidation and reduction peaks lower than that of Fe<sub>2</sub>O<sub>3</sub>-PEI-CHIT and Fe<sub>2</sub>O<sub>3</sub>-PEI-Au-CHIT nanoparticles, but higher than Fe<sub>2</sub>O<sub>3</sub>-TMAOH-CHIT modified electrodes. This indicates that a layer of chitosan was formed on the GCE and that chitosan blocked the movement of electrons to the electrode surface. The reason why the chitosan modified electrode has higher oxidation and reduction peaks compared to Fe<sub>2</sub>O<sub>3</sub>-TMAOH-CHIT

modified electrode is because of the OH<sup>-</sup> ion present in TMAOH which further blocks the flow of electrons between redox couple and electrode surface.

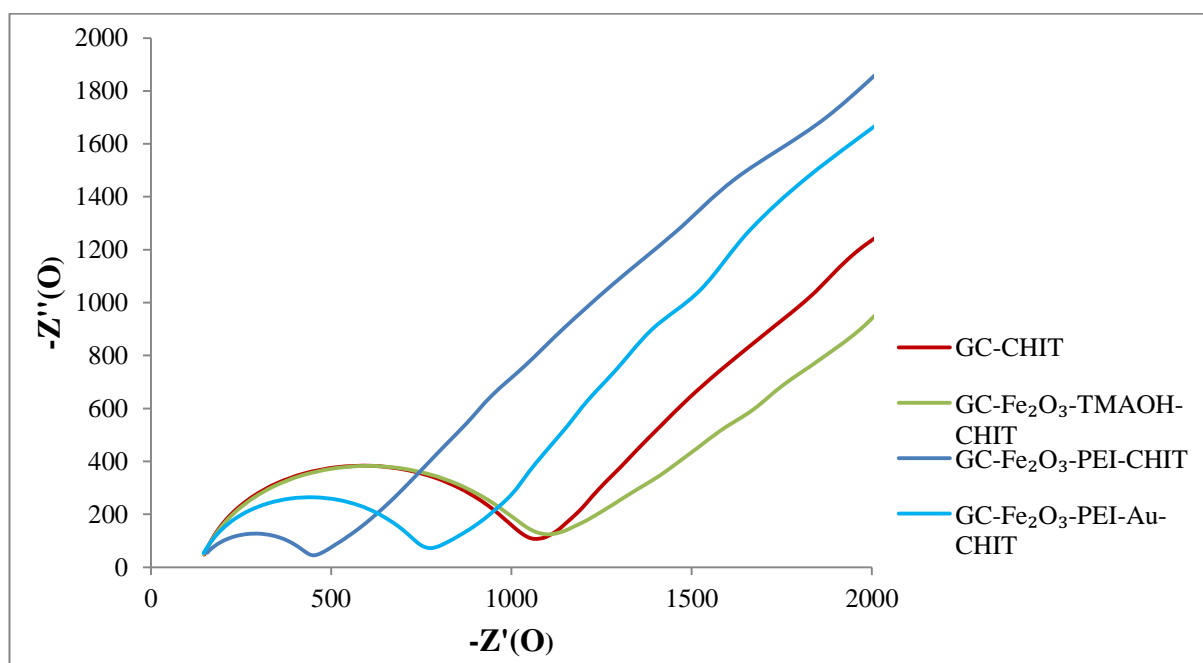


**Figure 4.12 Nyquist plot of nanoparticles modified electrodes in 5mM potassium ferrocyanide/ferricyanide ( $[\text{Fe}(\text{CN})_6]^{4-/3-}$ ) solution in ratio 1:1 containing 0.1M PBS (pH 7.4) applying an open circuit potential with amplitude 5mV in frequency range 0.01Hz-10kHz.**

Figure 4.12 shows the Nyquist plot of the nanoparticles modified electrodes in an EIS analysis. The plot shows the real component of impedance plotted against the imaginary component. The semicircle portion in the Nyquist plot represents the electron transfer limiting process at higher frequencies while the linear portion represents the diffusion limited process.

The result showed that the glassy carbon electrode modified with Fe<sub>2</sub>O<sub>3</sub>-PEI-CHIT nanoparticles had the lowest charge or electron transfer resistance ( $R_{ct}$ ) of 268Ω which can be attributed to the presence of PEI in the composite. PEI is known to reduce charge transfer resistances due to its polycationic nature that neutralizes any negative charges developed by composite (Tan *et al.*, 2007). This is followed next by the electrode modified with Fe<sub>2</sub>O<sub>3</sub>-PEI-Au-CHIT with resistance to charge transfer of 584Ω. This is lower compared to the electron transfer resistance of CHIT (881Ω) and Fe<sub>2</sub>O<sub>3</sub>-TMAOH-CHIT (900Ω) modified electrodes. This shows the presence of gold shell on

the iron oxide/PEI nanoparticles and also the decrease in resistance can be attributed to the ability of gold nanoparticles in the composite to act as a conducting pathway between the electrode and electrolyte promoting electron transfer of the redox probe towards the electrode surface.

The modified electrode with chitosan (CHIT) shows a high interfacial resistance (an increase in the diameter of the semicircle) towards electron transfer of about  $881\Omega$ . This shows the composite film blocked the electron transfer of the electrochemical probe caused by the presence of non-conducting chitosan. The resistance to electron transfer was further increased when the glassy carbon electrode was modified with  $\text{Fe}_2\text{O}_3$ -TMAOH-CHIT to  $900\Omega$ . This is attributed to the presence of the negative charge hydroxyl group ( $\text{OH}^-$ ) in the TMAOH which further increases the charge transfer resistance and prevents the flow of electrons. There was no difference observed in the solution resistance  $R_s$  ( $152\Omega$ ) for the modified electrodes at their formal potentials.

#### 4.9 Effect of temperature and agitation on PEI adsorption on iron oxide nanoparticles and gold shell formation

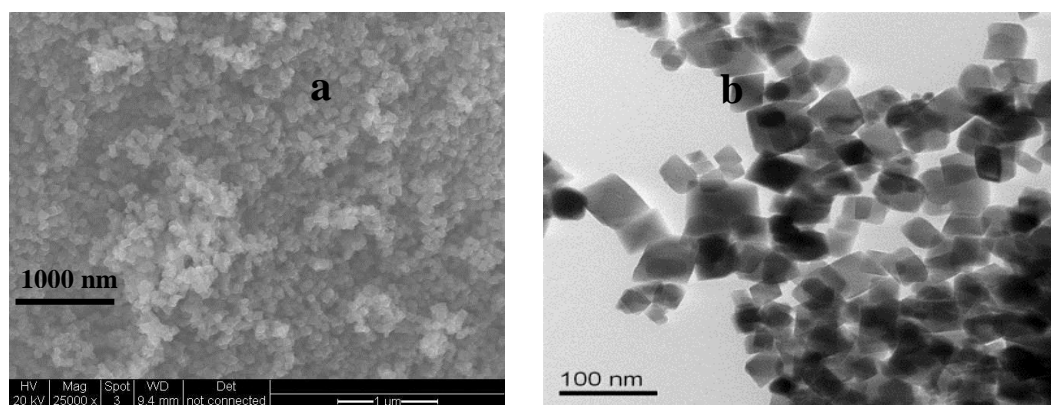


**Figure 4.13 (a) ESEM image of  $\text{Fe}_2\text{O}_3$  nanoparticles (b) TEM image of  $\text{Fe}_2\text{O}_3$  nanoparticles**

The ESEM and TEM images of ( $\gamma\text{-Fe}_2\text{O}_3$ ) nanoparticles are shown in Figure 4.13. The ESEM image in Figure 4.13a showed the as-prepared  $\gamma\text{-Fe}_2\text{O}_3$  nanoparticles and the TEM in Figure 4.13b indicated that the nanoparticles are cubic in shape with average particle size of 50 nm.

**4.9.1. Electrochemical analysis on PEI adsorption in iron III oxide/PEI nanoparticle preparation at various heating temperatures**

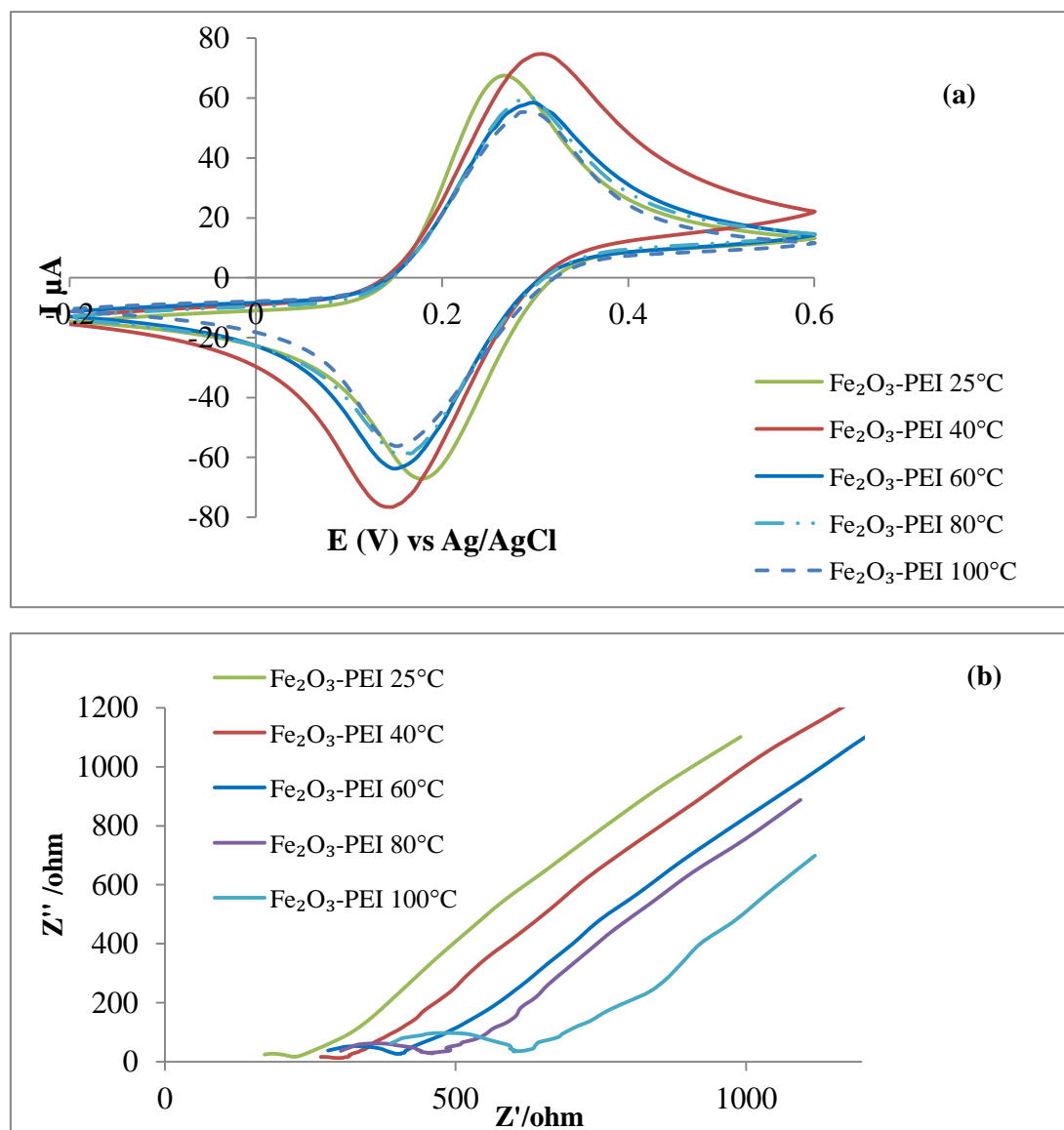


**Figure 4.14 Electrochemical characterisation of Fe<sub>2</sub>O<sub>3</sub>-PEI at different temperatures (a) cyclic voltammograms (b) EIS Nyquist plots**

Figure 4.14a shows the cyclic voltammogram of the modified electrodes with PEI at different temperatures. The result showed that PEI is well adhered to the surface of  $\gamma$ -Fe<sub>2</sub>O<sub>3</sub> nanoparticles at 40°C compared to 25°C and heating at 60, 80 and 100 for 1 hour. The nanoparticles heated with PEI at 40°C had the highest oxidation and

reduction peaks at 0.3V and 0.15V respectively as shown in the cyclic voltammograms (Fig.4.14a) followed by 25 °C, 60 °C and the lowest at 100 °C when the solution turned oily. This is an indication that more of the PEI is adhered or adsorbed electrostatically onto the surface of the Fe<sub>2</sub>O<sub>3</sub> nanoparticles at 40 °C compared to the other temperatures.

The high increase in the oxidation and reduction current of the modified electrode with Fe<sub>2</sub>O<sub>3</sub>-PEI at 40 °C is due to the presence of more PEI molecules attached to the surface of the iron oxide nanoparticles, which reduces the electron transfer charges between the probe solution and the electrode surface thus, increasing the oxidation and reduction peaks. This result is further verified with the electrochemical impedance spectroscopy (EIS) results shown in Figure 4.14b showing the ohmic resistance (Rs) which includes the ohmic resistance of solution and the coating layer, and the charge transfer resistance (Rct). It was observed that the lowest ohmic resistance was obtained at 25 °C followed by 40 °C which had the lowest charge transfer resistance. The temperatures and their corresponding ohmic and charge transfer resistance are shown in Table 4.1

<b>Fe<sub>2</sub>O<sub>3</sub>-PEI nanoparticles heating temp. (°C)</b>	<b>Charge transfer resistance (Ohm)</b>	<b>Ohmic resistance (Ohm)</b>
25	76	177
40	38	268
60	104	280
80	128	302
100	207	388

**Table 4.1 Fe<sub>2</sub>O<sub>3</sub>-PEI nanoparticles at different temperature ohmic and charge transfer resistance**

The result shows that change in temperatures affects the ohmic resistance and as the heating temperature of PEI on iron oxide nanoparticles increases, the charge transfer resistance increases. This also indicates that the polycationic nature of PEI which

neutralizes any negative charge that tends to increase charge transfer resistance diminishes with increasing temperatures on the surface of the iron oxide nanoparticles. A repeat of the experiment carried out showed similar result with 40 °C showing better PEI adsorption on iron oxide nanoparticles compared to the other temperatures. The reason for this observation might be that 40 °C favoured the electrostatic interaction between positively charges PEI molecule and negatively charged iron oxide nanoparticles. Error bar analysis carried out as shown in Figure 4.15 for the first and second run experiment showed minimal errors from the average peak current data as indicated by the vertical upper and lower error bars for the different temperatures. This indicates that the experiment is reproducible.

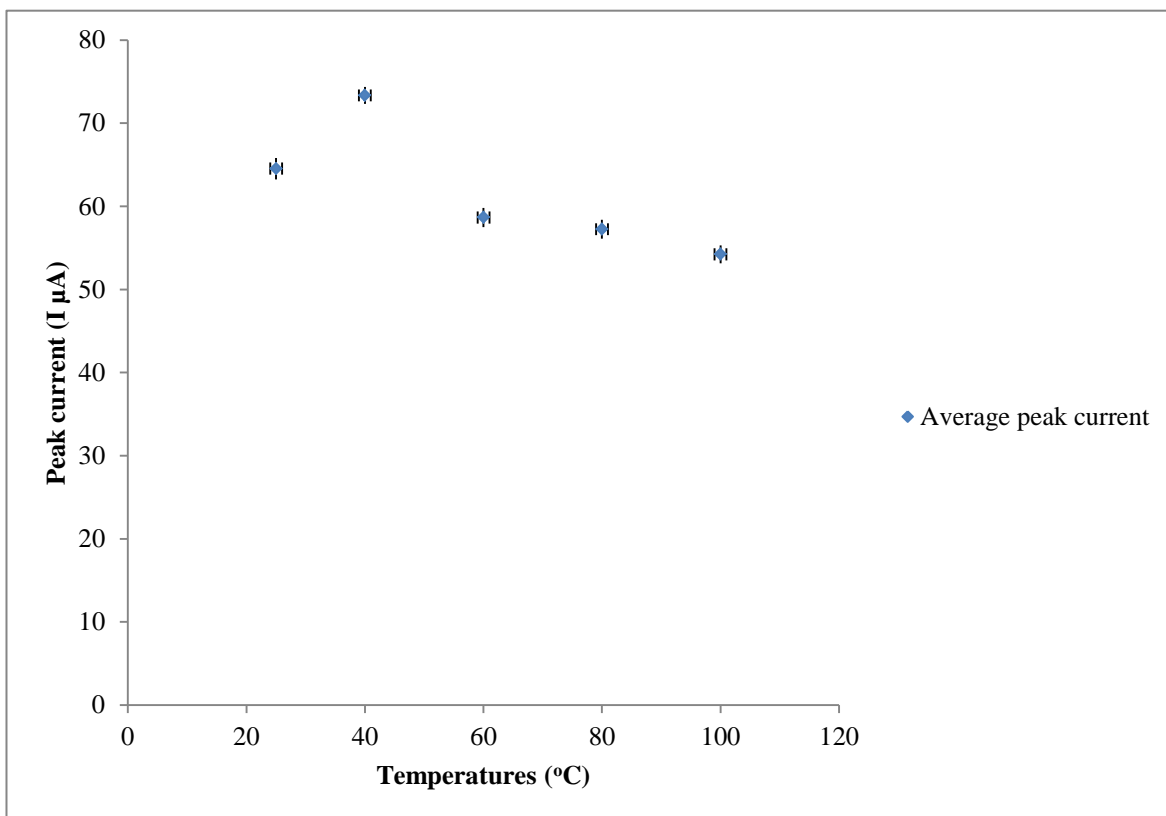


**Figure 4.15 Error bar analysis of average peak current against temperatures**

#### 4.9.2 Effect of agitation on PEI adsorption

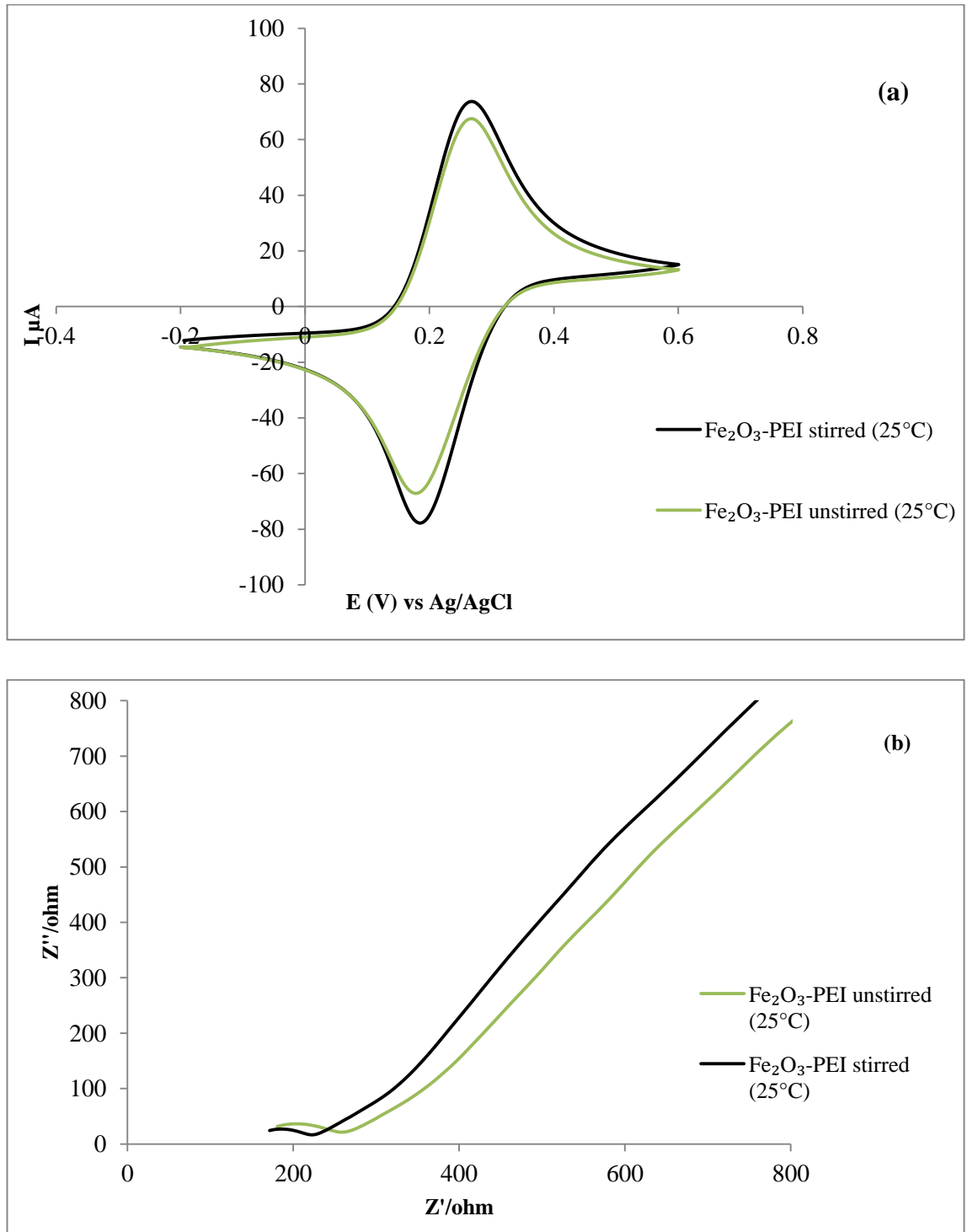


**Figure 4.16** Effects of agitation: on PEI adsorption on Fe<sub>2</sub>O<sub>3</sub> nanoparticles at room temperatures with and without stirring (a) cyclic voltammograms (b) EIS Nyquist plots

Comparison was made between stirring iron oxide nanoparticles with PEI at room temperature for 1 hour and the unstirred process at room temperature. It was observed from the cyclic voltammetry results shown in Figure 4.16a that the nanoparticles ( $\text{Fe}_2\text{O}_3\text{-PEI}$ ) obtained by stirring PEI with iron oxide had the higher oxidation and reduction peaks at 0.25V and 0.19V respectively for the redox couple compared to the unstirred process. This result is corroborated with the EIS analysis shown in Figure 4.16b and the results in Table 4.2 which showed that the stirred nanoparticles had lower charge transfer resistance compared to the unstirred synthesis.

This can be attributed to the stirring process which enables the random mixing of the iron oxide nanoparticles with PEI molecules, resulting in an increased PEI ion attached on the surface of iron oxide nanoparticles due to increased electrostatic attraction between the negatively charged iron oxide and positively charged PEI.

The EIS results (Figure 4.16b) also showed that the ohmic resistance ( $R_s$ ) is slightly affected at room temperature compared to large variation observed when the particles were heated at increased temperatures as shown in Table 4.1. This indicates that PEI synthesized at room temperature and at  $40^\circ\text{C}$  had less opposition to the flow of electrons of a probe solution due to increased polycationic nature of PEI at this temperatures on the iron oxide nanoparticles. Higher heating temperatures results in opposition to flow of electrons as the PEI polycationic nature diminishes and the solution turns oily.

<b><math>\text{Fe}_2\text{O}_3\text{-PEI}</math> nanoparticles at room temp. (<math>^\circ\text{C}</math>)</b>	<b>Charge transfer resistance (Ohm)</b>	<b>Ohmic resistance (Ohm)</b>
25 (stirred)	44	171
25 (not stirred)	76	177

**Table 4.2  $\text{Fe}_2\text{O}_3\text{-PEI}$  nanoparticles at room temperature ohmic and charge transfer resistance**

### 4.9.3 UV-VIS Spectroscopy analysis of Fe<sub>2</sub>O<sub>3</sub>-PEI/Au shell nanoparticles at the different temperatures

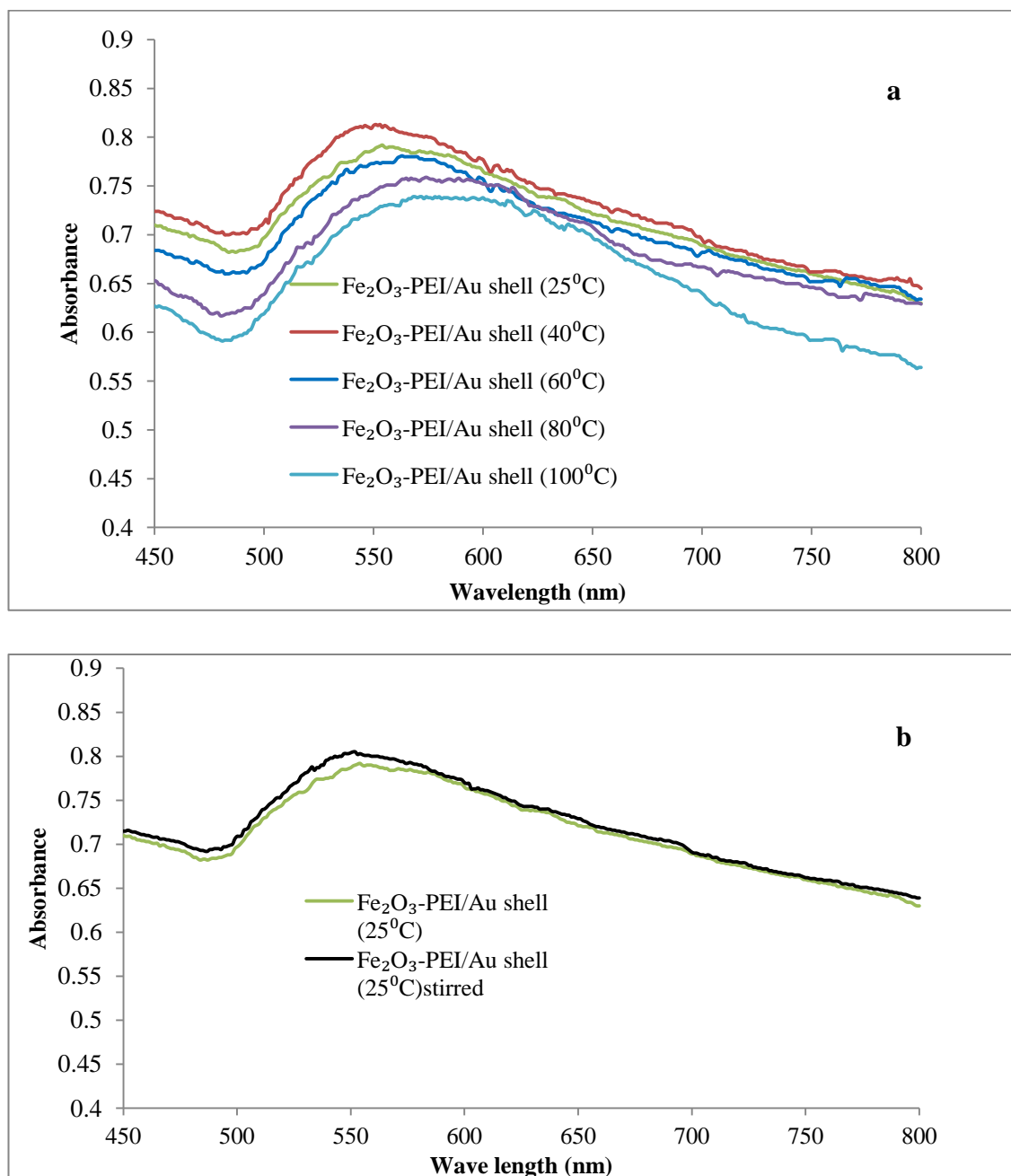


**Figure 4.17** UV-Vis spectra for Fe<sub>2</sub>O<sub>3</sub>-PEI/Au shell formation after 5 iteration step (a) at different heating temperatures (b) stirred and unstirred process at 25°C

The optical properties of the Fe<sub>2</sub>O<sub>3</sub>-PEI nanoparticles at the different temperatures coated with gold shell was analysed with the aid of UV- Vis spectroscopy and the results is shown in Figure 4.17. The formation of Fe<sub>2</sub>O<sub>3</sub>-PEI–Au shell nanoparticles was

achieved after five iterations through the iterative reduction of chloroauric acid with hydroxyl amine (Lyon *et al.*, 2004), (Goon *et al.*, 2009). The results in Figure 4.17a shows that after 5 iteration steps for each temperature, the size and amount of gold shell on the surface of the iron oxide nanoparticles increases resulting to a blue shift of the surface plasmon resonance in the UV-Vis spectra. The blue shift indicates an increase in gold shell formation to the iron oxide nanoparticles. The shift in surface plasmon resonance is most observed at 40°C as the ratio of gold to iron oxide increases with peak wavelength of 548 nm followed by 25°C (553 nm), 60°C (562 nm) and the lowest at 100°C (584 nm). This result indicates the presence of more positively charged PEI ions on the iron oxide nanoparticles at 40°C that can act as capping agents for gold shell formation.

The UV- spectra (Figure 4.17b) showed that stirred nanoparticles at 25 °C had higher absorbance and surface plasmon resonance peak at 550 nm compared to the unstirred nanoparticles 553 nm. This indicates that agitating PEI with iron oxide nanoparticles at room temperature favoured capping capability of the PEI in the attachment of gold shell nanoparticles.

A paper has been published by me on this topic the effect of temperature and agitation on polyethyleneimine adsorption on iron oxide magnetic nanoparticles in the synthesis of iron oxide-Au core-shell nanoparticles in the journal of Advance Science, Engineering and Medicine, volume 6, number 5 (pp 531-537) (2014). The copy of the paper is shown in the appendices in chapter seven.

#### **4.10 Conclusions**

In conclusion iron oxide core-gold shell nanoparticles were successfully synthesized. The gold nanoparticles after 10 iterations have an average particles size of 24 nm and the total particle size for the iron oxide core- gold shell nanoparticles is 74 nm. The nanoparticles showed good electro-catalytic properties towards redox probe with Fe<sub>2</sub>O<sub>3</sub>-PEI having the highest oxidation and reduction peaks and least charge transfer resistance followed by the gold coated iron oxide nanoparticles due to the electron transfer ability of gold. It was also found that temperature places a major role in the

adsorption of PEI on iron oxide nanoparticles and the ability of PEI to act as capping agents in the formation of gold shell on the iron oxide nanoparticles.

The result showed that 40°C is most favourable for PEI adsorption on iron oxide nanoparticles and favours the capping properties of PEI in the formation of iron oxide core/gold shell nanoparticles. The result also indicates that the polycationic nature of PEI on iron oxide nanoparticles diminishes as the heating temperature increases which is reflected in the reduced electrochemical properties observed at 100°C compared to 40°C. Also the ohmic resistance of iron oxide/PEI nano-composite is affected with increased heating temperatures above 40°C. At room temperature synthesis, the stirred iron oxide/PEI nanoparticles showed better electrochemical properties compared to the unstirred process due to the agitation which encouraged better electrostatic attraction between the negatively charge iron oxide nanoparticles and positively charged PEI ions.

## Chapter 5

### Plasma immunoglobulin biomarker immunosensor for Alzheimer's disease

#### 5.1 Introduction

Alzheimer disease (AD) is a physical disease of the brain and the major cause of dementia which is a group of symptoms such as loss of memory, confusion, problems with speech and understanding that occur when the brain is affected by diseases in ageing people. The disease result in the death of nerve cells in particular regions of the brain, and shrinking of the brain as gaps develop in the temporal lobe and hippocampus, which are responsible for storing and retrieving new information. It also affects the production of acetylcholine which is an important chemical in the brain. AD is a progressive disease that gets worse over time and leads to death if not properly managed. The level of progress of the symptoms depends on the affected individual. The diagnosis of Alzheimer's disease has been of great challenge since there is no reliable diagnostic test and cure for the disease, but drugs such acetylcholinesterase inhibitors (donepezil hydrochloride, galantamine and rivastigmine) has been used to temporarily alleviate some of the symptoms (Mukaetova-Ladinska *et al.*, 2012). The diagnosis of AD is often based on clinical ground and neuropsychological assessment of dementia (Dubois *et al.*, 2007). Clinical analysis of the disease detects treatable conditions which might have similar symptoms to dementia such as depression, chest and urinary infections, severe constipation, vitamin and thyroid deficiencies and brain tumors. It identifies possible causes of confusion in patients, such as poor sight or hearing; emotional changes and upsets, such as moving or bereavement; or the side-effects of certain drugs or combinations of drugs. It also gives patient time to access advice, information and support (emotional, practical and financial) from social services, voluntary agencies and support groups and plan and make arrangements for the future.

To improve on the clinical diagnosis accuracy of AD the use of one or more biomarker as supportive measures for structural or molecular neuroimaging of AD, particularly analysis of cerebrospinal fluid (CSF) such as amyloid- $\beta$  ( $A\beta$ ) or tau proteins was recommended by the National Institute of Ageing and Alzheimer's Association

guidelines (McKhann *et al.*, 2011). Most studies on AD markers have been focused in CSF (fluid that bathes the brain) which reflects more of the metabolic state of the brain (Sunderland *et al.*, 2005). CSF contains amyloid beta proteins (A $\beta$  1-40) and hydrophobic (A $\beta$  1-42) which are peptide produced from amyloid  $\beta$ -protein precursor ( $\beta$ APP) through successive cleavage from proteolytic enzymes  $\beta$  and  $\gamma$  secretases. Amyloid beta proteins are the main focus of AD pathology especially (A $\beta$  40) and (A $\beta$  42). CSF biomarkers have shown reproduced decreases in (A $\beta$  42) levels in CSF and increased in tau and phospho-tau in AD patients and other dementias (Sunderland *et al.*, 2005; Hansson *et al.*, 2006; Kasuga *et al.*, 2010; Mulder *et al.*, 2010). Despite the promising outcome from the CSF biomarkers, their applications have not successfully shown that AD diagnosis and progression can be monitored with these biomarkers. The CSF biomarkers are also expensive, rarely available and difficult to control repeated sampling for regular monitoring of AD. This makes peripheral source such as plasma and serum better biomarker options.

## **5.2 Plasma biomarkers**

Biomarkers in blood are good diagnostic marker which allows for disease monitoring and therapy initiation at the early stages of the disease. Biomarker molecules in blood such as plasma are less challenging and readily applicable. Blood Plasma contains lots of dissolved proteins such as albumin, immunoglobulin, fibrinogen and other neuronal cell line proteins such as tau protein, amyloid beta protein (Hye *et al.*, 2006). These proteins or groups of proteins undergo changes in concentration or structural composition as a result of the physiological state in normal or diseased conditions. Blood plasma is also a rich source of CSF since CSF is readily adsorbed in the blood and can also be used as biomarker for CSF monitoring. The presence of amyloid beta proteins (A $\beta$  40 and 42) in plasma, makes plasma a good diagnostic marker for monitoring AD progression compared to the relatively invasive lumbar puncture procedure involve in CSF biomarker procedures or the use of radio tracers which are technically challenging.

The use of plasma as biomarkers also faces some challenges due to the wide range in protein concentration in plasma, making diagnosis assays for the very low concentration proteins difficult. Research has shown that as blood circulates around the brain, small hydrophobic and lipophilic molecules from the CSF and large amount of specific

molecules and metabolites are absorbed in the blood (Bell and Zlokovic, 2009). This is due to the activity of the blood brain barrier (BBB) which restricts diffusion of macroscopic pathogens to the brain. This indicates that relevant markers in the plasma which reflects what is happening in the brain will be in low concentration in normal humans (Bell and Zlokovic, 2009).

These have led to the removal of uninformative or non-diagnostic proteins in the plasma through depletion processes in order to enhance the detection of low abundant proteins as biomarkers. The process also has disadvantages in that it removes some proteins that might be potential biomarkers for AD (Yocum *et al.*, 2005; Zolotarjova *et al.*, 2005). Despite the disadvantage, depleted or non-depleted plasma can yield potential biomarkers (Hye *et al.*, 2006).

Depleted and non-depleted forms of plasma has been used for AD diagnostic assays and the result has shown increases in the A $\beta$  42 levels for plasma obtained from AD patients at early onset and late onset compared to normal control subjects (Scheuner *et al.*, 1996; Hye *et al.*, 2006; Ertekin-Taner *et al.*, 2008). Resent research on plasma biomarker for AD has been focused on antibody based detection through the use of enzyme link immunosorbent assay (ELISA).

ELISA method detects the proteins in plasma using antibodies and colour change. Increases in plasma A $\beta$  40 and A $\beta$  42 levels with ageing for AD patients have been reported by Van and co-workers (van Oijen *et al.*, 2006; Ertekin-Taner *et al.*, 2008) using ELISA method. Detecting plasma and platelet immunoglobulin (Ig) levels in patients instead of amyloid beta proteins (A $\beta$  40 or A $\beta$  42) have shown to be a useful way for diagnosing and monitoring AD. Mukaetova-Ladinska and co-workers, reported an increase in plasma and platelet immunoglobulin in AD patient not treated with cholinesterase inhibitor compared to control subjects using indirect ELISA method (Mukaetova-Ladinska *et al.*, 2012). Their method used polyclonal rabbit Anti-human IgA, IgG, IgM as primary antibody specific to platelet or plasma immunoglobulin to bind the immunoglobulin (Ig) deposited in microliter plates and polyclonal Goat Anti-rabbit Immunoglobulin/horseradish peroxidase (HRP) as secondary antibody bound to the primary antibody to amplify the detection of the immunoglobulin. The concentrations of the plasma immunoglobulin were detected through the formation of colour read by a UV-Vis spectroscopy reader.

ELISA method despite its sensitivity and ability to detect plasma proteins for AD diagnosis is found to be time consuming, expensive and a complex process that might give false result due to light sensitive chemicals applied during analysis. This makes electrochemical detection of plasma proteins as biomarkers for AD better option. Electrochemical immunoassays are highly sensitive, less time consuming, easy to handle and also easily integrated into portable devices. Currently there is no electrochemical detection of plasma immunoglobulin as biomarker for AD.

### **5.3 Aims**

The aim of this chapter is to develop a direct immunosensor electrode for detecting plasma immunoglobulin as a biomarker for AD patients and control subjects. The sensor will make use of depleted plasma immunoglobulin as antigen conjugated to polyclonal rabbit Anti-human IgA, IgG, IgM, as the specific antibody on the surface of a gold electrode. Also iron oxide core-Au shell nanoparticles will be used as immobilization substrate for the polyclonal rabbit Anti-human IgA, IgG, IgM/plasma Ig conjugation to enhance plasma detection. Secondary antibody (Goat Anti-rabbit Immunoglobulin/horseradish peroxidase) will not be used in the development of the electrode because of the immobilization technique employed which is different from the ELISA technique, and also due to the non-conducting properties of HRP which obstruct electron transfer of the redox solution. Electrochemical techniques (CV and EIS) will be used for the detection of changes in the immuno-complex in AD and control subjects.

## **5.4 Experimental**

### **5.4.1 Materials and chemicals**

3-mercaptopropionic acid (MPA), cysteamine hydrochloride (cys) >97%, N-(3-Dimethylaminopropyl)-N-ethylcarbodiimide hydrochloride (EDC), N-Hydroxysulfosuccinimide sodium salt (NHS), Tween 20, TNB (3,3',5,5'-tetramethylbenzadene) and potassium chloride (KCl) were purchased from Sigma Aldrich (Dorset UK), Polyclonal rabbit Anti-human IgA, IgG, IgM, and Polyclonal Goat Anti-rabbit Immunoglobulin/horseradish peroxidase (HRP) were purchased from Dako (Denmark), Depleted plasma immunoglobulin (1000 ppm ) were obtained from Institute for Ageing and health Newcastle University, hydrogen peroxide 30% were purchased from VWR (Leicestershire UK). Skimmed milk (marvel) was purchased

from Lidl (UK). All chemicals were used as received without further purification. Solutions were prepared using Millipore deionised water.

#### ***5.4.2 Immobilization of polyclonal rabbit Anti-human immunoglobulin and depleted plasma immunoglobulin on Gold (Au) electrode.***

Gold electrode (1.6mm diameter) was polished in 0.05 and 0.3 microns polish kit and rinse with distilled water. The electrode was further cleaned by running cyclic voltammetry in 0.1M H<sub>2</sub>SO<sub>4</sub> at potential 0-1.5V, at scan rate 100mV/s for 20 cycles. The electrode was dipped in 200 µl ethanolic solution of 3-mercaptopropionic acid (40mM) for 2hr 30minutes sealed with parafilm for self-assembly monolayer (SAM) of thiol functional groups on the electrode. The electrode was drop washed immediately with 200µl of ethanol. The gold electrode was immediately dipped into 200 µl mixture of NHS (0.05M) and EDC (0.2M) for 30minutes to activate the carboxylic group of the MPA. Immediately electrode was dipped in 50µl polyclonal rabbit Anti-human immunoglobulin with constant concentration (1000 ppm) in 2ml eppendorf tube, sealed with parafilm and stored at 4°C overnight.

The gold electrode immobilized with primary antibody was rinsed with 200µl phosphate buffer (pH 6.26) containing 0.05% of tween 20 (PBST) and dipped in 200µl of 1% marvel (skimmed milk) in an eppendorf tube and seal with parafilm and heated in water bath or oven at 37 °C for 1hr. The electrode was drop washed with 200µl of PBST and dipped in 50µl of depleted plasma Ig (500 ppm or 1:2000 dilution) prepared from stock plasma Ig solution (1000 ppm or 1:1000 diluted) in an eppendorf tube sealed and stored at 4°C in fridge for 1hr. The electrode was finally rinsed with 100µl of PBST. The process was repeated for depleted plasma Ig double dilutions 1:4000, 1:8000, 1:16,000, 1:32,000, 1:64,000.00, 1:128,000, and 1:256,000 respectively. The dilutions were made by first placing 100µl depleted plasma immunoglobulin stock solution (1000 ppm or 1:1000 diluted) in the first cell of a 96 cell micro-plate, and pipetting 50µl of the 100µl stock into the second cell and then diluting the stock in the second cell with 50µl PBST to get 1:2000 dilutions. The process was then repeated with the second cell to get the third cell (1:4000 dilutions) etc.

#### ***5.4.3 Immobilization of polyclonal rabbit Anti-human immunoglobulin and depleted plasma immunoglobulin on iron oxide-gold shell nanoparticles ( $Fe_2O_3$ -Au Nps) immobilized on Gold electrode.***

The immobilization of polyclonal rabbit Anti-human IgA, IgG, IgM and depleted plasma Ig on  $Fe_2O_3$ -Au nanoparticles follows similar immobilization process carried out by Sharma and co-workers for the detection of aflatoxin B1 (Sharma *et al.*, 2010) with some modifications. 2000 $\mu$ l of  $Fe_2O_3$ -Au nanoparticles average particle size 74 nm synthesized in chapter four was dispersed in 3000 $\mu$ l PBS (pH 6.28) and agitated to mix. 200 $\mu$ l of the mixed  $Fe_2O_3$ -Au nanoparticles in PBS was added to 800 $\mu$ l of 10mM of cysteamine solution (Cys) in 2ml eppendorf tube covered with kitchen foil and agitated overnight for SAM of thiol functional group on the  $Fe_2O_3$ -Au nanoparticles. The nanoparticles were separated from the cysteamine solution after overnight agitation with magnet and rinsed with 1000 $\mu$ l of distilled water. The nanoparticles were then dispersed in 50 $\mu$ l of polyclonal rabbit Anti-human IgA, IgG, IgM by agitation followed by the addition of 100 $\mu$ l mixture of NHS (0.05M) and EDC (0.2M) in ratio 1:1 to activate the carboxylic group in the antibody for amine binding with the SAM  $Fe_2O_3$ -Au nanoparticles. The mixture was agitated for 2 hours. The  $Fe_2O_3$ -Au-polyclonal rabbit Anti-human IgA, IgG, IgM formed was separated with magnet and rinsed with PBS (pH 6.28) and then dispersed in 50 $\mu$ l of PBS.

Prior to immobilization of polyclonal rabbit Anti-human IgA, IgG, IgM on  $Fe_2O_3$ -Au nanoparticles, gold electrode (2mm diameter) was polished in 0.05 and 0.3 microns polish kit and rinse with distilled water. The electrode was cleaned by running cyclic voltammetry in 0.1M  $H_2SO_4$  at potential 0-1.5V, at scan rate 100mV/s for 20 cycles. The Au electrode was dipped into 200 $\mu$ l of MPA (40mM) in 2ml eppendorf tube sealed and left for 2.30 hours for SAM of thiol on the electrode. The electrode was drop washed with 500 $\mu$ l of ethanol and dipped in 100 $\mu$ l mixture of NHS (0.05M) and EDC (0.2M) for 30 minutes. The electrode was then removed from the NHS and EDC solution after 30 minutes and immediately 20 $\mu$ l of  $Fe_2O_3$ -Au nanoparticles-polyclonal rabbit Anti-human IgA, IgG, IgM solution was dropped on the surface of the electrode and stored at 4 $^{\circ}$ C for 4 hours for amide bond formation between the activated carboxylic end terminal of the electrode and the amine end of the polyclonal rabbit Anti-human IgA, IgG, IgM. The non-binding site of the polyclonal rabbit Anti-human IgA, IgG,

IgM was blocked by dropping 20µl of 1% marvel on the modified electrode and incubating at 37°C for 1hour. The electrode was rinsed with 100µl of PBST and dipped in 50µl depleted plasma Ig (500 ppm or 1:2000 dilutions) and left overnight at 4°C before measurement. The process was repeated for plasma immunoglobulin dilutions 1:4000, 1:8000, 1:16,000 and 1:32,000 respectively. Figure 5.1 and 5.2 shows the schematic diagrams for the gold electrode and Fe<sub>2</sub>O<sub>3</sub>-Au nanoparticles gold electrode modification steps with polyclonal rabbit Anti-human IgA, IgG, IgM and plasma immunoglobulin respectively.

***5.4.4 Conjugation of depleted plasma immunoglobulin, polyclonal rabbit Anti-human immunoglobulin and polyclonal Goat Anti-rabbit Immunoglobulin/horseradish peroxidase for ELISA detection with UV-Vis spectroscopy reader.***

The conjugation of depleted plasma Ig, polyclonal rabbit Anti-human immunoglobulin and Goat Anti-rabbit immunoglobulin/horseradish peroxidase was carried out by following similar method used by Mukaetova and co-workers (Mukaetova-Ladinska *et al.*, 2012). First 50µl of 50mM ammonium bicarbonate buffer (pH 9.6) was added to the 12 cells of the first and second rows (experiment 1 and 2) of a 96 cell microliter plate as diluent for coating microliter plates. Then 50µl of depleted plasma immunoglobulin (1000 ppm) was added to the first cells of the two rows and mix twice with pipette and 50 µl removed and added to the next cell and the process repeated to the 12th cell to obtain 1:2000, 1:4000, 1:8000, 1:16,000, 1:32,000, 1:64,000, 1:128,000, 1:256,000, 1:512,000, 1:1024,000, 1:2048,000, 1:4096,000 dilutions. The microplate was then covered and incubated overnight at 4°C. The plates were then washed twice with PBS containing 0.05% tween 20 and blocked with 1% of marvel at 37°C for another 1 hour. After blocking for 1 hour the solution in the plates was poured out and washed thrice with PBS containing 0.05% tween 20 by turning the cells upside down to pour off the liquids and the cells dried with hand cleaning tissue. 50µl of 1000 ppm (1:1000 dilutions) polyclonal rabbit Anti-human immunoglobulin was then added to all the 12 cells of the first two rows (24 cells) of the microliter plate and incubated for 1 hour. The plates were then washed three times with PBS containing 0.05% tween 20 and dried by hand cleaning tissue.

After drying, 50 $\mu$ l of 1000 ppm (1:1000 dilutions) Goat Anti-rabbit immunoglobulin/horseradish peroxidase prepared by adding 1 $\mu$ l of Goat Anti-rabbit immunoglobulin/horseradish peroxidase solution in 999 $\mu$ l PBST was then added to the 12 cells of the 2 rows and incubated for 1 hour at 37°C. After incubating the plates were washed three times with PBST and soak in water for 5 minutes and dried using hand cleaning tissue. Next 50  $\mu$ l of freshly prepared substrate reagent for ELISA was added to the cells and the reaction allowed to progress for 10 minutes. As the colour of the reaction starts changing to blue, the reaction was quenched with the addition of 50 $\mu$ l of H<sub>2</sub>SO<sub>4</sub> (2N) to the cells which results in the formation of yellow colour indicating the concentration of antigens that has reacted with antibodies. The colours were read in a UV-Vis spectroscopy reader at 450 nm wavelength. The substrate reagent for the ELISA was prepared by adding 90ml of distilled water in a tube, followed by the addition of 10ml of 0.5M sodium acetate (pH 5.0) and swirl to mix, then 1ml of dimethyl sulphoxide containing 0.01g TNB (3,3',5,5'-tetramethylbenzidine) was added and swirl to mix. Finally 10  $\mu$ l of 30% hydrogen peroxide was added and swirl to mix before use.

### **5.5 Electrochemical characterization of modified electrodes**

Cyclic voltammetry (CV) and electrochemical impedance spectroscopy (EIS) were used for the electrode characterization. The CV was obtained in 10mM of phosphate buffer (pH 6.26) containing 5mM of ferrocyanide/ferricyanide [Fe (CN)<sub>6</sub>]<sup>4-/3-</sup> at a scan rate of 50mV/s. EIS analysis were carried out in 10mM of phosphate buffer (pH 6.26) containing 5mM of ferrocyanide/ferricyanide [Fe (CN)<sub>6</sub>]<sup>4-/3-</sup> in ratio 1:1 by applying an open circuit potential with amplitude 1mV in frequency range 0.01Hz-10kHz. Three electrode cell with modified gold electrode as working electrode, Ag/AgCl (3M NaCl, 0.208V vs. SHE) as the reference electrode and a platinum wire as the counter electrode was used for the analysis.

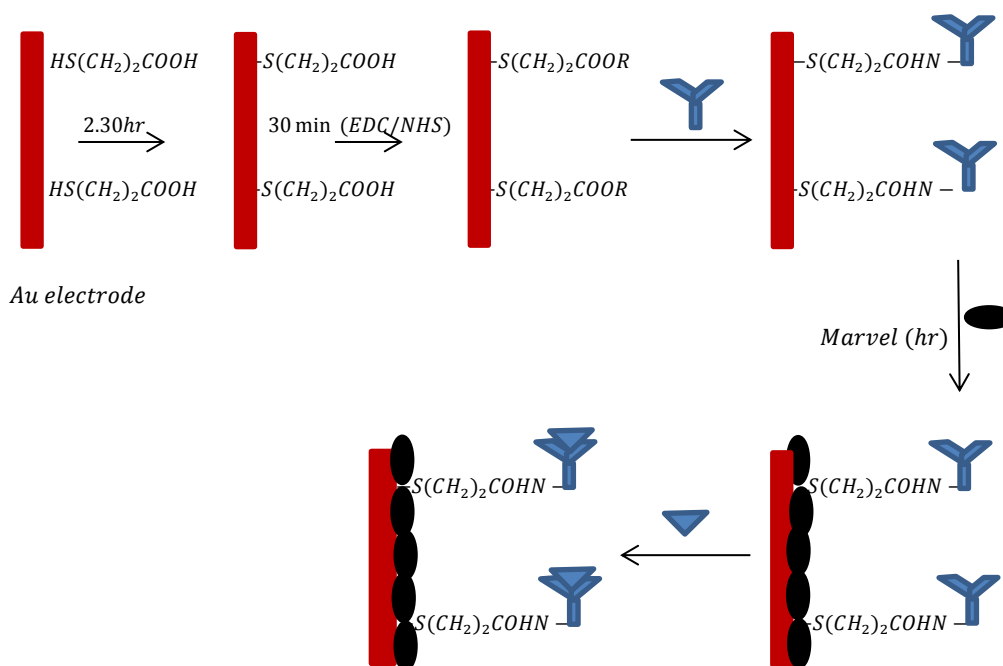


**Figure 5.1** Schematic diagram showing the stepwise modification of gold electrode with plasma Ig and polyclonal rabbit Anti-human Ig

The schematic diagrams in Figure 5.1 shows the polished gold electrode treated with MPA (40mM) for two and half hour then followed by treating with a mixture of EDC and NHS for thirty minutes to activate the carboxylic group in the MPA attached to the gold electrode. Polyclonal rabbit Anti-human Ig (antibody) was then immobilized on the electrode overnight. After the immobilization the electrode was blocked with marvel followed by the immobilization of depleted plasma Ig (antigen) before experimentation as explained in section 5.4.2. Table shows the symbols and what they represent.

Symbols	Meaning
	Polyclonal rabbit Anti-human Ig (antibody)
	Depleted plasma Ig (antigen)
	Iron oxide-gold shell nanoparticles
	Marvel
	Gold electrode

**Table 5.1** symbols for immobilization diagrams

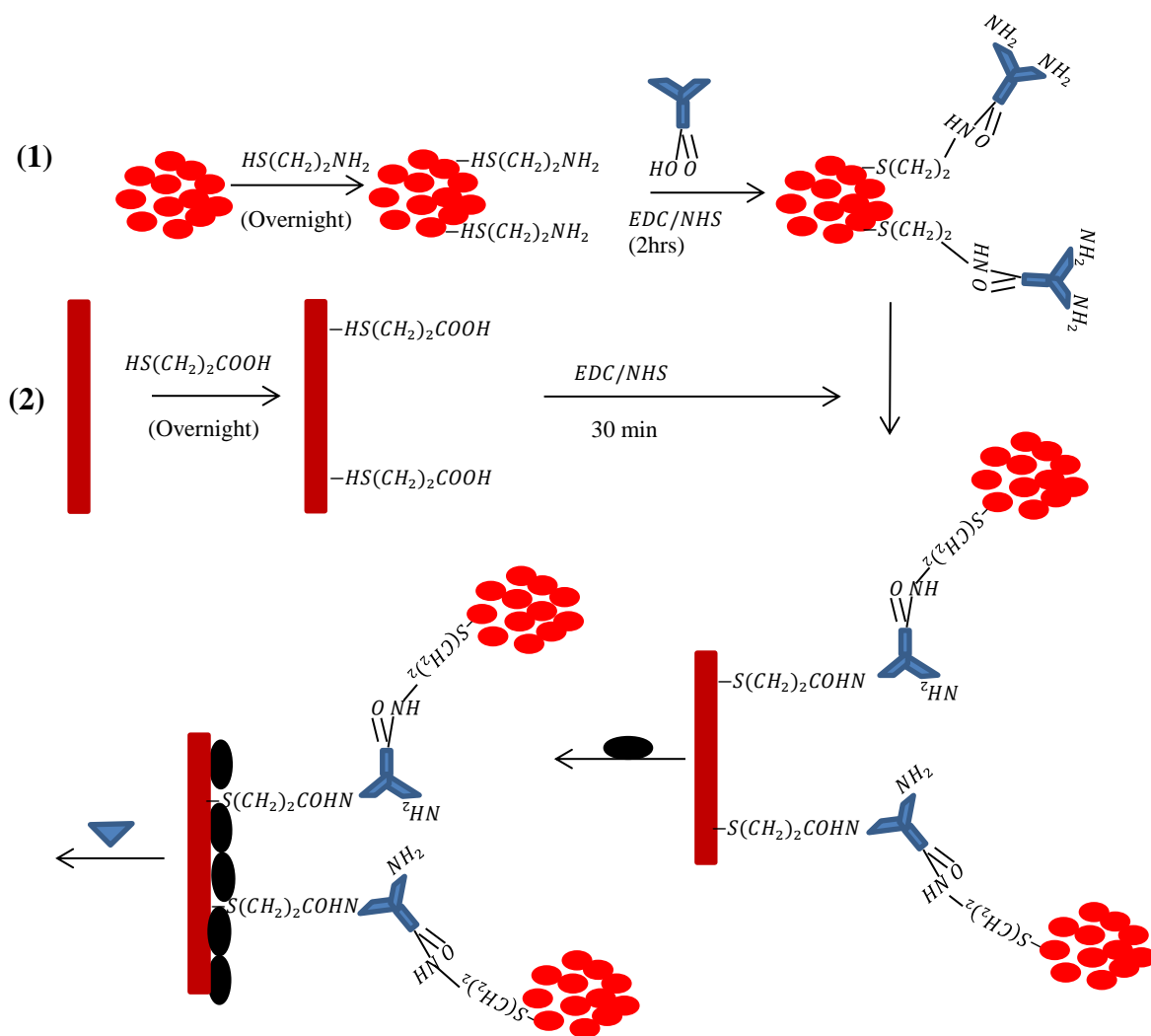


**Figure 5.2 Schematic diagrams showing the stepwise modification of gold electrode with depleted plasma/antibody and Fe<sub>2</sub>O<sub>3</sub>- Au nanoparticles**

The schematic diagram in Figure 5.2 shows the stepwise functionalization of the iron oxide –Au shell nanoparticles and its subsequent immobilization on gold electrode. Step 1 is the formation of the iron oxide gold shell nanoparticles-Polyclonal rabbit Anti-human Ig (antibody) composite and the step 2 is the immobilization of this composite on the surface of a gold electrode for depleted plasma immunoglobulin conjugation. In step 1 iron oxide gold shell nanoparticles was treated with cysteamine (10mM) overnight to attach thiol groups on the electrode, followed by dispersing the electrode in Polyclonal rabbit Anti-human Ig (antibody) solution and treating with EDC and NHS for two hours to form iron oxide-Au shell- Polyclonal rabbit Anti-human Ig composite. Step 2 shows the cleaned gold electrode treated with MPA followed by mixture of EDC and NHS and the immobilization of iron oxide-Au shell- Polyclonal rabbit Anti-human

Ig composite on the electrode and blocking the non-binding site of the antibody with marvel before immobilization of depleted plasma Ig as explained in section 5.4.3.

## 5.6 Results and discussion

### 5.6.1 Immobilization of MPA, polyclonal rabbit Anti-human immunoglobulin and Marvel on gold electrode

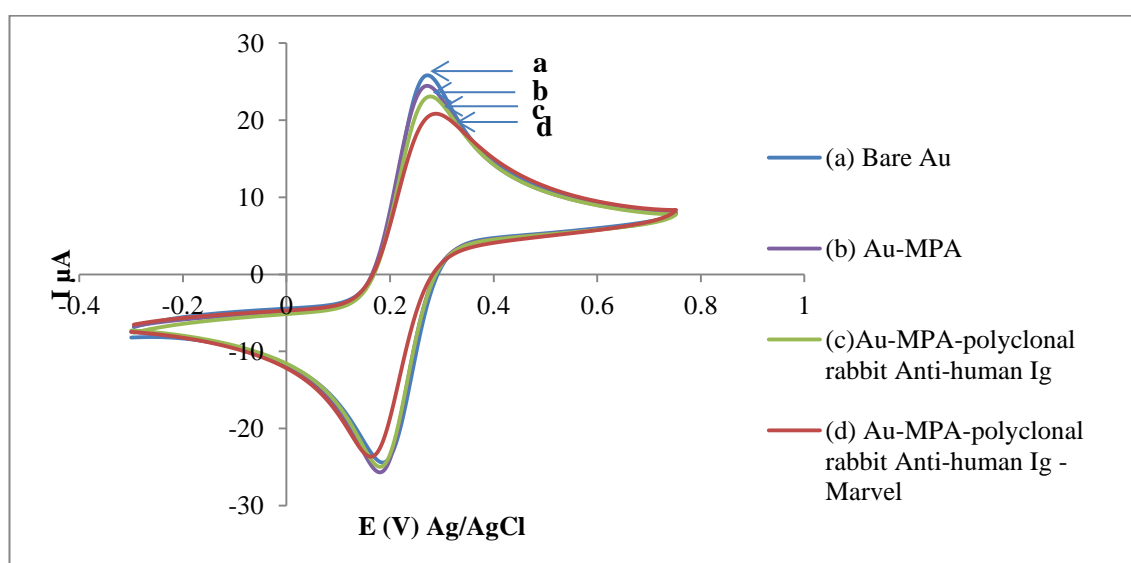


**Figure 5.3** Cyclic voltammograms of bare Au electrode (a), Au-MPA (b), Au-MPA-Polyclonal rabbit Anti-human Ig (c), Au-MPA- Polyclonal rabbit Anti-human Ig -1% marvel (d)

Figure 5.3 shows the stepwise assembly of polyclonal rabbit Anti-human immunoglobulin (antibody) and depleted plasma Ig (antigen) on gold electrode using cyclic voltammetry (CV). The cyclic voltammogram shows well-defined oxidation and reduction peaks of redox probe ( $[\text{Fe}(\text{CN})_6]^{4/3-}$ ) observed at the bare gold electrode (a), gold electrode with SAM of MPA (b), gold electrode with MPA-polyclonal rabbit Anti-human Ig (c) and gold electrode modified with MPA-polyclonal rabbit Anti-human Ig and blocked with 1% marvel (d). The peak current decreases after coating the gold electrode surface with 3-mercaptopropionic acid (MPA). This indicates that the surface of the gold electrode was covered with SAM of MPA which in turn resulted in the decrease in the peak current observed. Further decreases in the peak current were observed when the electrode was modified with polyclonal rabbit Anti-human Ig (Fig.5.3c), and polyclonal rabbit Anti-human Ig blocked with 1% of marvel (Fig.5.3d). The large decrease in peak current observed in Fig.5.3d is attributed to the blocking

property of marvel which prevents the flow of electrons between the redox probe and electrode surface.

The result further shows that increased immobilization on the bare gold electrode blocked the flow of electrons between the surface of the electrode and the redox solution. The bare gold electrode had the highest oxidation and reduction peaks at 0.27V and 0.17V, followed by gold electrode modified with SAM of MPA. The lowest oxidation and reduction peaks at 0.29V and 0.16V were observed when the electrode was blocked with 1% marvel (skimmed milk).

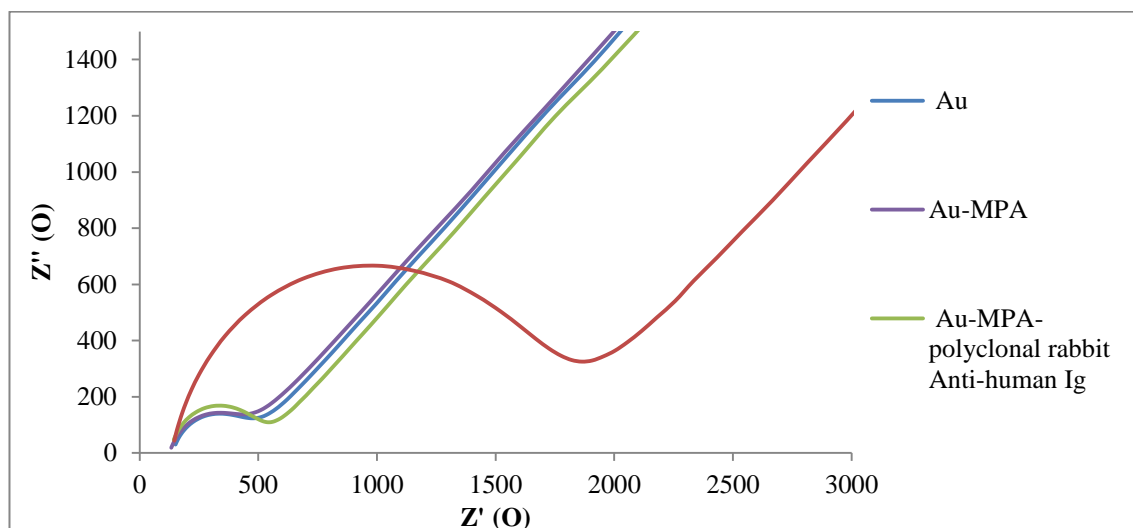


**Figure 5.4** EIS (Nyquist plot) of bare Au electrode (light blue line), Au-MPA (dark blue line), Au-MPA- Polyclonal rabbit Anti-human Ig (green line), Au-MPA- Polyclonal rabbit Anti-human Ig - 1% marvel (dark red line)

These results were further verified with the electrochemical impedance spectroscopy analysis for the modified electrodes in PBS (10mM, pH 6.26) containing 0.1M potassium chloride and 5mM  $\text{Fe}(\text{CN})_6^{3-}/\text{Fe}(\text{CN})_6^{4-}$  (ferric/ferrocyanide solution) ratio 1:1 by applying an open circuit potential with amplitude 1mV at frequency range 0.01Hz-10kHz shown in Figure 5.4.

The Nyquist plot shows that bare gold electrode (light blue line) had the lowest charge transfer resistance of  $240\Omega$  indicating that the gold electrode acted as an electron pathway for the flow of electrons between the redox probes. The charge transfer resistance increased with each modification step with the highest resistance at ( $1820\Omega$ ) for

electrode modified with MPA-polyclonal rabbit Anti-human Ig and blocked with 1% marvel (dark red line) because of the blocking property of marvel.

### 5.6.2 Immobilization of MPA, polyclonal rabbit Anti-human immunoglobulin - Marvel and depleted plasma immunoglobulin (control) on gold electrode

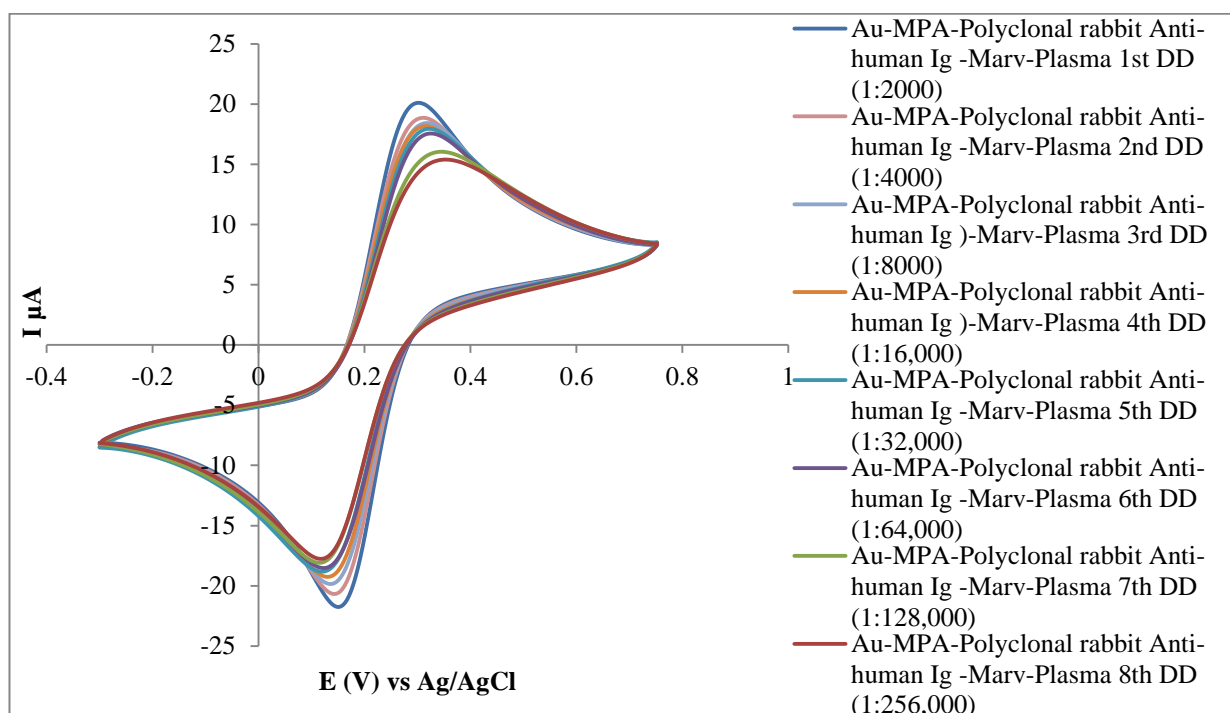
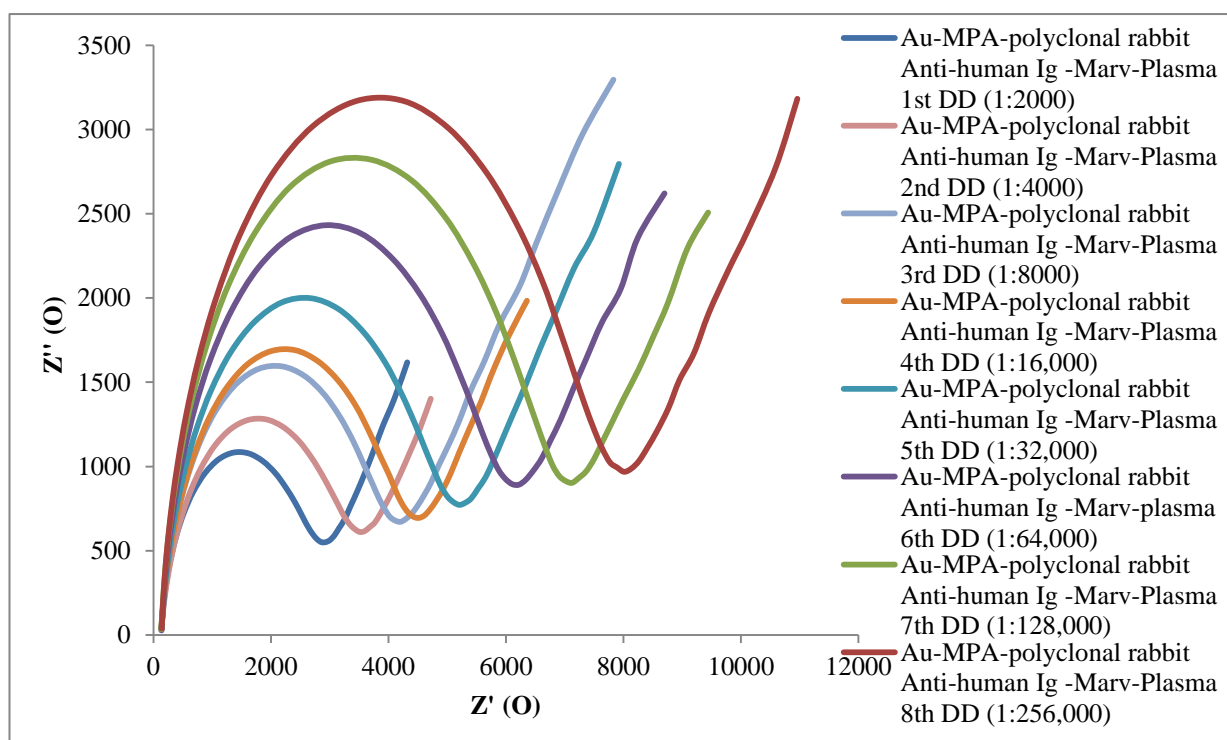


**Figure 5.5 CV of Au-MPA- Polyclonal rabbit Anti-human Ig -1% marvel –plasma for control patient at dilutions (1:2000), (1:4000), (1:8,000), (1:16,000), (1:32,000), (1:64,000), (1:128,000), (1:256,000)**

Figure 5.5 shows the cyclic voltammogram for the immobilization of constant concentration (1000 ppm) of polyclonal rabbit Anti-human Ig with double diluted depleted plasma immunoglobulin (control) samples (1:2000, 1:4000, 1:8000, 1:16,000, 1:32,000, 1:64,000, 1:128,000, 1:256,000 ) with corresponding concentrations 500, 250, 125, 62.5, 31.25, 15.62, 7.81 and 3.91 in parts per million respectively on gold electrode. The method in which the dilutions were carried out is described in section 5.2.4.

The CV was carried out in PBS (10mM, pH 6.26) containing KCl (0.1M) and 5mM of ferric/ferrocyanide solution  $[\text{Fe}(\text{CN})_6^{3-}/\text{Fe}(\text{CN})_6^{4-}]$  at scan rate 50mV/s. The result shows a well-defined redox peaks for each double dilutions. Increased dilution

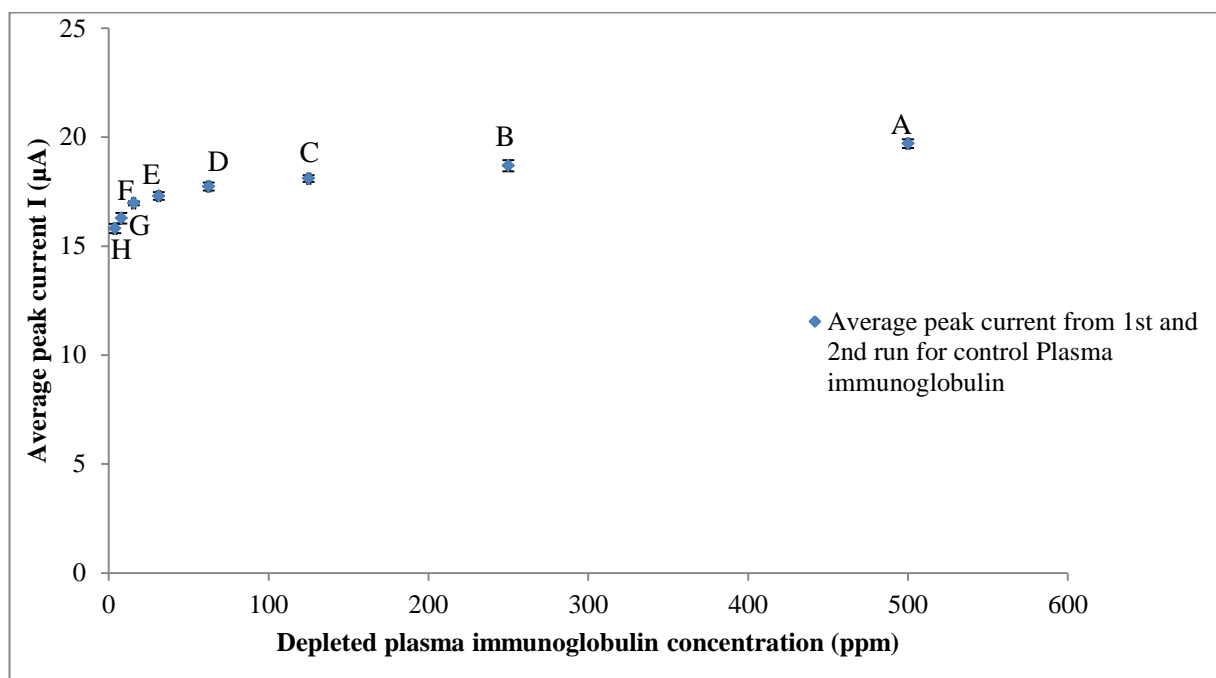
decreases the plasma immunoglobulin concentration and results in decreasing peak currents observed in Figure 5.5. The highest peak current  $19.95\mu\text{A}$  was observed at  $0.31\text{V}$  for plasma Ig dilution 1:2000 (500 ppm) (dark blue line) and the lowest peak current  $14.82\mu\text{A}$  was observed for dilution 1:256,000 (3.91 ppm) (dark red line).



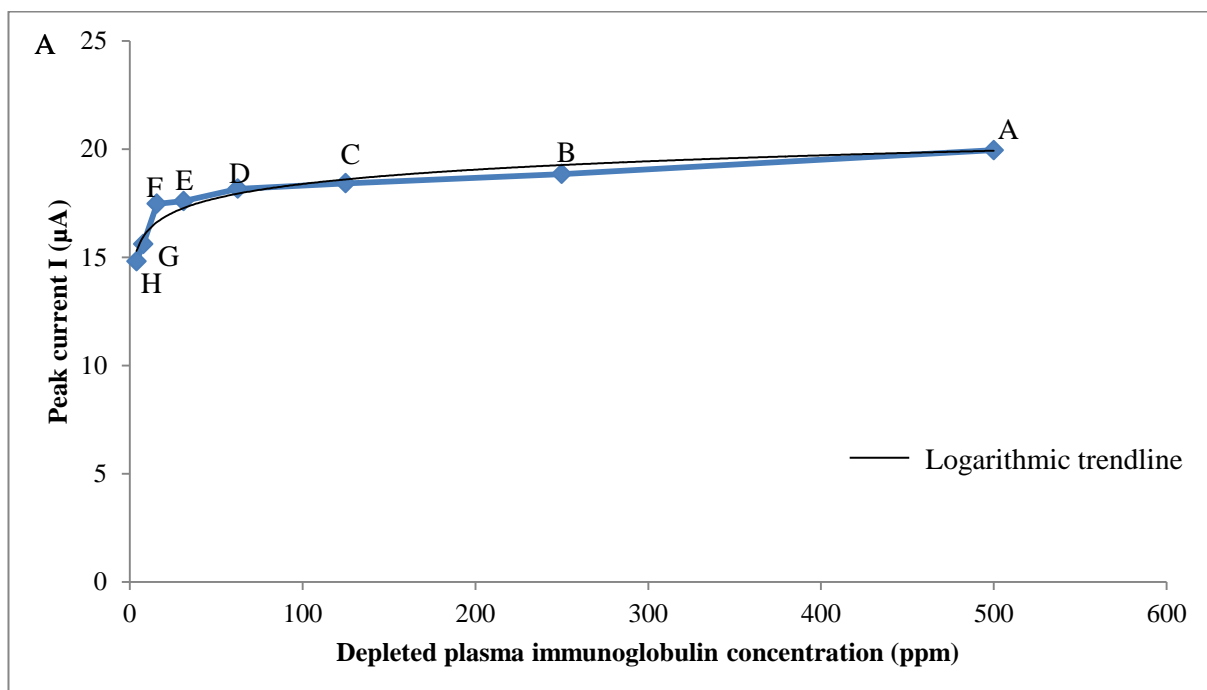
**Figure 5.6. EIS (Nyquist plot) of Au-MPA- Polyclonal rabbit Anti-human Ig-1% marvel –plasma for control patient at plasma dilutions (1:2000), (1:4000), (1:8,000), (1:16,000), (1:32,000), (1:64,000), (1:128,000), (1:256,000)**

The result from the CV analysis was corroborated with the EIS analysis carried out on the samples as shown in the Nyquist plot in Figure 5.6. The Nyquist plot showed that plasma Ig dilution 1:2000 (500 ppm) with high plasma immunoglobulin concentration had the lowest charge transfer resistance ( $R_s$ ) of  $2648\Omega$  indicating that high concentration of polyclonal rabbit Anti-human Ig/plasma immunoglobulin conjugate on the surface of the gold electrode acts as an electron accelerator (Sharma *et al.*, 2010). The charge transfer resistance increases with increasing plasma Ig dilutions and the highest charge transfer resistance of  $7751\Omega$  was observed for plasma Ig at the 8<sup>th</sup> dilution (1:256,000) with low plasma Ig concentration (3.91 ppm).

This result also confirms the findings from the CV that less diluted plasma (high concentration) conjugated with polyclonal rabbit Anti-human Ig increases the electron accelerating capabilities of the polyclonal rabbit Anti-human Ig /plasma conjugates resulting in the reduced charge transfer resistance observed for the high concentrations. The CV and EIS analysis could not detect plasma immunoglobulin concentration beyond the 8<sup>th</sup> dilution (1:256,000) (3.91 ppm). The reason for this might be due to the constant concentration of polyclonal rabbit Anti-human Ig (1000 ppm) used for conjugating the different plasma Ig dilutions. The concentration of the polyclonal rabbit Anti-human Ig might not be sufficient enough to bind the very low concentrations of plasma Ig and results in no further electrochemical response beyond the 8<sup>th</sup> dilution. A repeat experiment for the control plasma showed similar findings and error bars where plotted as shown in Figure 5.7. The error bar analysis showed minimal errors in the experiment as indicated by the appearance of small upper and lower error bars away from the average peak current data for the 1<sup>st</sup> and 2<sup>nd</sup> runs. This indicates that the experiment is reproducible if repeated. .

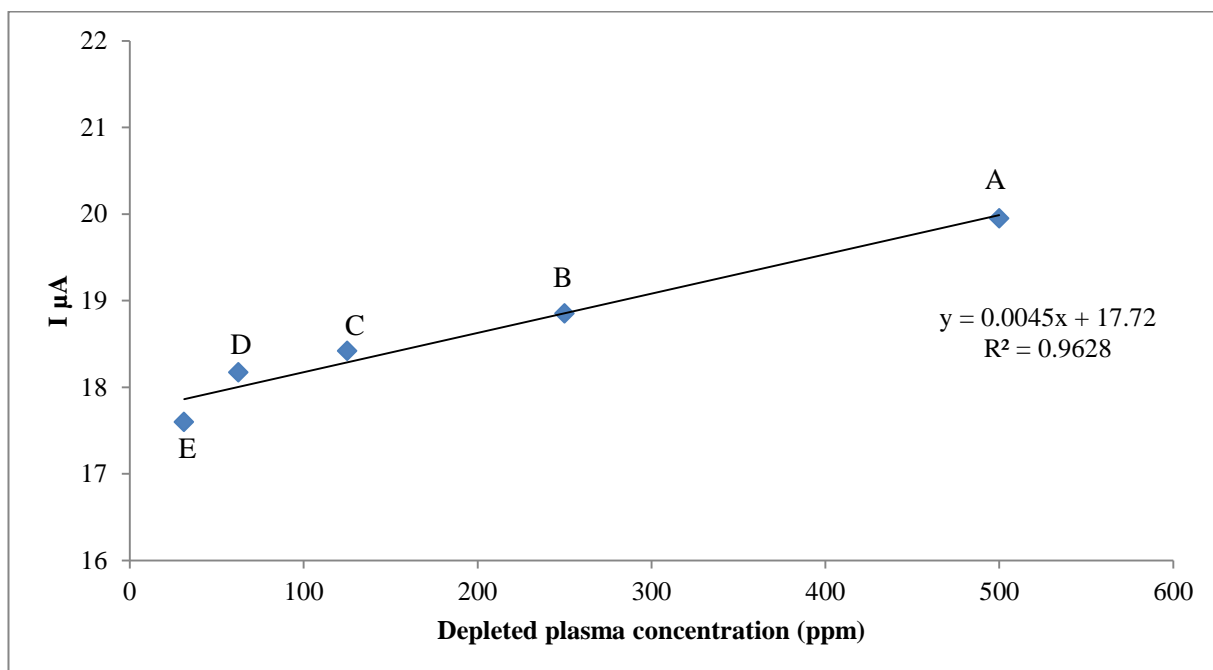


**Figure 5.7** Error bar analysis for first and second run depleted plasma concentration (control subject) for (A) [1:2000](500ppm), (B) [(1:4000) (250 ppm)] (C)[ (1:8000) (125 ppm)], (D) [(1:16,000), (62.5 ppm)], (E) [(1:32,000) (31.25 ppm)], (F) [(1:64,000) (15.62ppm)], (G) [(1:128,000) (7.81ppm)] and (H) [(1:256,000) (3.91ppm)]



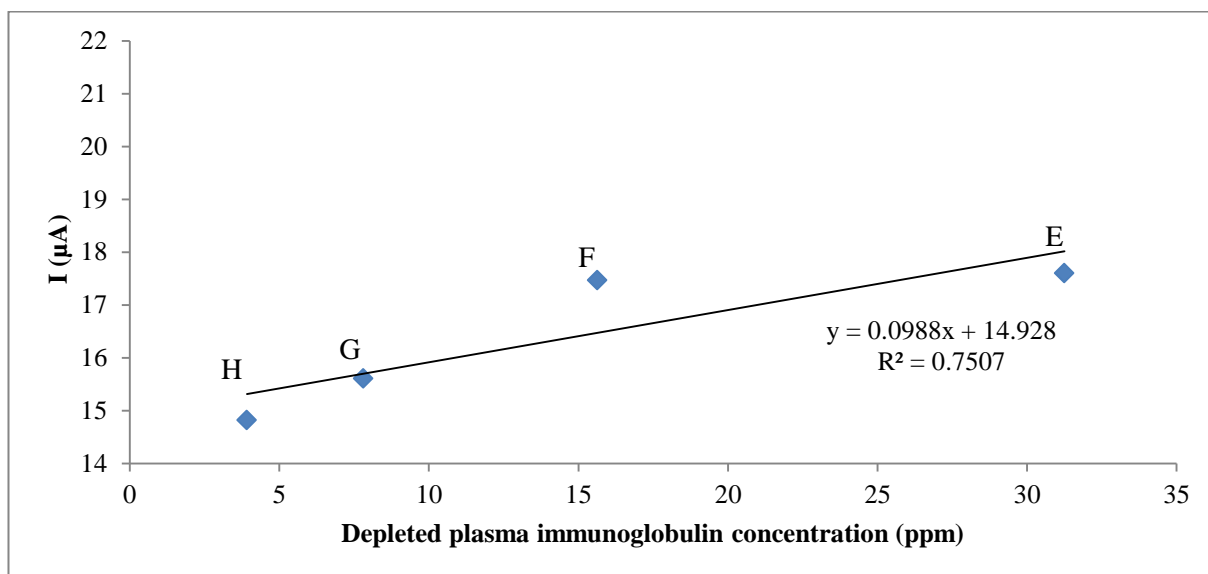
**Figure 5.8** plot of peak currents against plasma immunoglobulin (control) for (A) [1:2000](500ppm), (B) [(1:4000) (250 ppm)] (C)[ (1:8000) (125 ppm)], (D) [(1:16,000), (62.5 ppm)], (E) [(1:32,000) (31.25 ppm)], (F) [(1:64,000) (15.62ppm)], (G) [(1:128,000) (7.81ppm)] and (H) [(1:256,000) (3.91ppm)]

The relationship between the different plasma Ig dilutions and its effect on the peak current when conjugated with constant concentration of polyclonal rabbit Anti-human Ig was plotted as shown in Fig. 5.8. The plot shows that the peak current decreases in a logarithmic pattern as indicated by the logarithmic trend line (black line) with increasing plasma Ig dilutions. The increasing plasma Ig dilution decreases the concentration of the plasma immunoglobulin available for conjugation with polyclonal rabbit Anti-human Ig. The result in Fig. 5.8 shows that two linear trend were observed, one at higher plasma concentration (31.25 to 500 ppm) indicated by point A to E with level off point at E (31.25 ppm ) and the other at lower concentrations points (H to E).



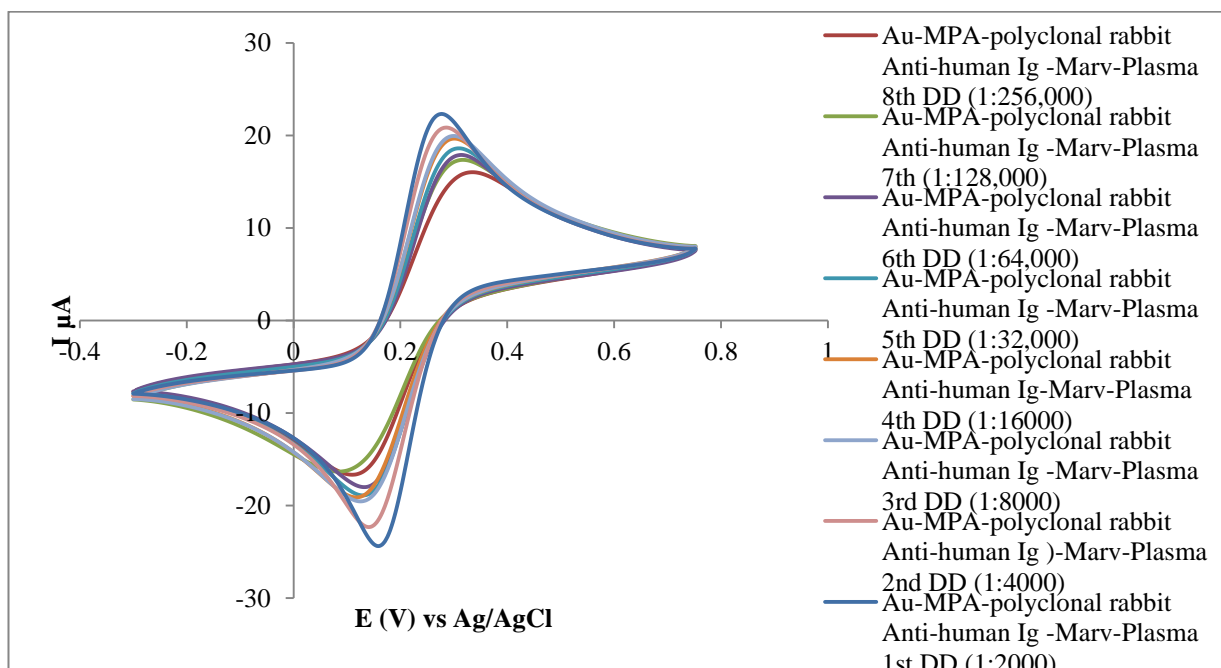
**Figure 5.9 Calibration plot of peak currents against plasma immunoglobulin dilutions (control) for (A) [1:2000](500ppm), (B) [(1:4000) (250 ppm)] (C)[ (1:8000) (125 ppm)], (D) [(1:16,000), (62.5 ppm)], (E) [(1:32,000) (31.25 ppm)]**

Figure 5.9 shows the calibration curve for the depleted plasma Ig at high concentration (500-31.25 ppm) with a linear regression equation  $I_p (\mu A) = 0.0045 (\mu A ppm^{-1}) + 17.72$  and sensitivity of  $0.0045 (\mu A ppm^{-1})$ . The calibration curve has a coefficient of determination ( $R^2$ ) of 0.9628 which shows that the data point fit above 95% closely to the calibration line at high plasma immunoglobulin concentrations compared to  $R^2$  of 0.7507 (75%) for the lower concentrations as shown in Figure.5.10. This indicates that the plasma immunoglobulin biomarker electrode is more sensitive to less diluted (high concentrations) of the plasma Ig than the more diluted low concentration (H-E) for the control subjects.



**Figure 5.10** Calibration plot of peak currents against plasma immunoglobulin double dilution (control) for (E) [(1:32,000) (31.25 ppm)], (F) [(1:64,000) (15.62ppm)], (G) [(1:128,000) (7.81ppm)] and (H) [(1:256,000) (3.91ppm)]

### 5.6.3 Immobilization of MPA, polyclonal rabbit Anti-human Ig-Marvel and depleted plasma immunoglobulin (AD case) on gold electrode



**Figure 5.11** CV of Au-MPA- Polyclonal rabbit Anti-human Ig -1% marvel –plasma for AD patient at plasma dilutions (1:2000), (1:4000), (1:8,000), (1:16,000), (1:32,000), (1:64,000), (1:128,000), (1:256,000)

Figure 5.11 shows the cyclic voltammogram of depleted plasma immunoglobulin obtained from AD patient. A well-defined oxidation and reduction peaks of the redox probe was also observed as compared to the control samples in Figure 5.5. Highest peak current of  $20.39\mu\text{A}$  was observed for plasma immunoglobulin for the first double dilution 1:2000 (500 ppm) (dark blue line) obtained from the plasma stock solution and the lowest peak current of  $15.75\mu\text{A}$  was observed at the 8<sup>th</sup> double dilution 1:256,000 (dark red line). This follows similar trend observed for the control subjects in Fig.5.5 in which the higher the concentration of plasma immunoglobulin the more plasma Ig available for polyclonal rabbit Anti-human Ig conjugation which in turn acts as an electron accelerator between the redox probe and the electrode surface.

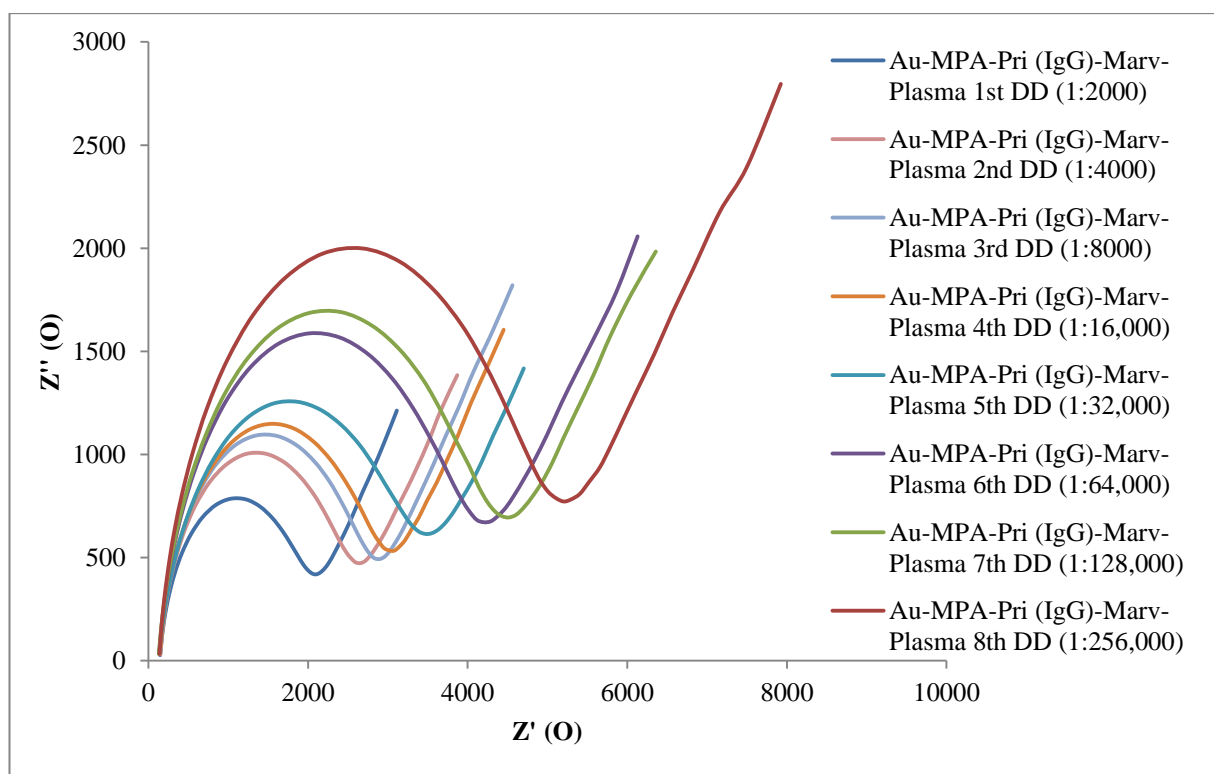


**Figure 5.12 EIS (Nyquist plot) of Au-MPA- Polyclonal rabbit Anti-human Ig -1% marvel –plasma for AD patient at plasma dilution (1:2000), (1:4000), (1:8,000), (1:16,000), (1:32,000), (1:64,000), (1:128,000), (1:256,000)**

The result is further corroborated with the Nyquist plot obtained from EIS experiment shown in Figure 5.12. The result shows that 1<sup>st</sup> double dilution (1:2000) with concentration (500 ppm) of the depleted plasma Ig had the lowest charge transfer resistance of  $1961\Omega$ . This indicates that high concentration of the antibody/plasma Ig

conjugate on the electrode acts as an electron accelerator, which in turn reduces the charge transfer resistance ( $R_s$ ). As the double dilution increases the charge transfer resistance increased with the highest charge transfer resistance of  $5069\Omega$  observed for the 8<sup>th</sup> plasma immunoglobulin dilution (1:256,000). This also indicates that increase in plasma immunoglobulin dilution decreases the electron accelerating capabilities of the polyclonal rabbit Anti-human Ig (antibody)/plasma Ig conjugate for the AD case which gives rise to increased charge transfer resistance observed at the 8<sup>th</sup> dilution.

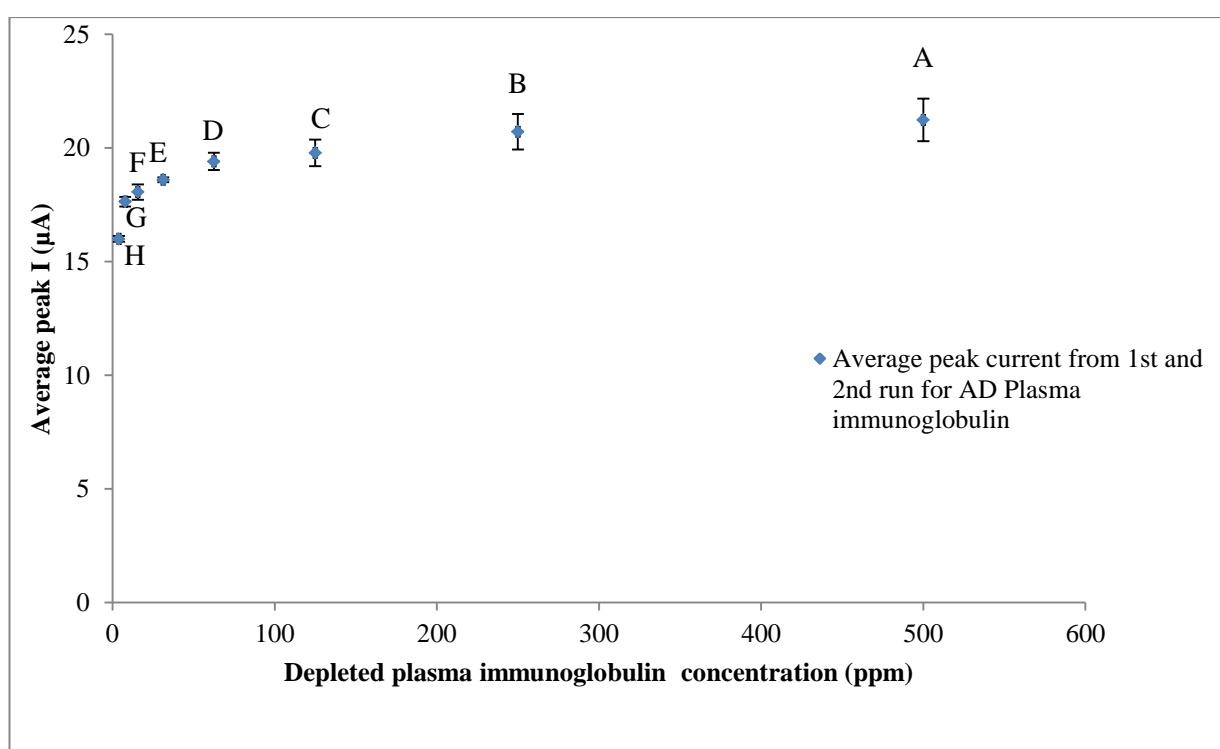


**Figure 5.13 Error bar plot of peak currents against plasma immunoglobulin dilution for (A) [1:2000](500ppm), (B) [(1:4000) (250 ppm)] (C)[ (1:8000) (125 ppm)], (D) [(1:16,000), (62.5 ppm)], (E) [(1:32,000) (31.25 ppm)], (F) [(1:64,000) (15.62ppm)], (G) [(1:128,000) (7.81ppm)] and (H) [(1:256,000) (3.91ppm)]**

Figure 5.13 shows the error bar analysis of the first and second experimental runs for the plasma immunoglobulin obtained from AD patient. The error bar analysis showed slightly high positive and negative errors in peak currents as indicated by the upper and lower error bars away from the average peak current for the high concentrations of plasma immunoglobulin (point A, B and C). The error bars becomes minimal as dilution

of plasma immunoglobulin increases. This result shows that the experiment is also reproducibility if repeated.

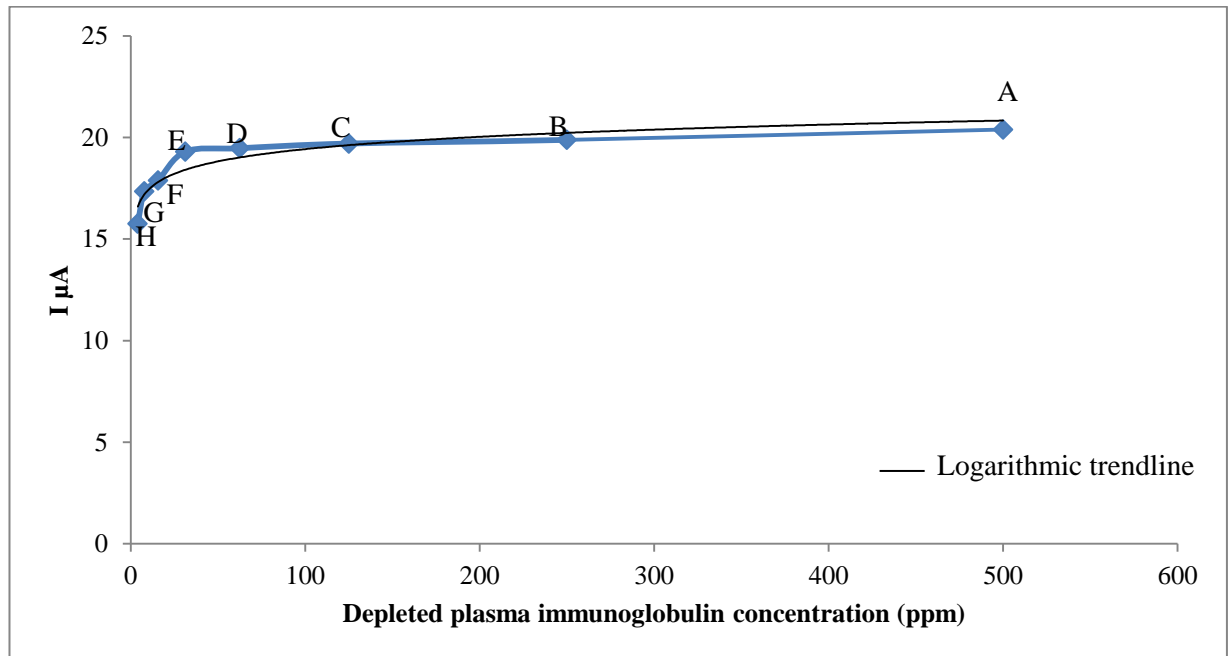
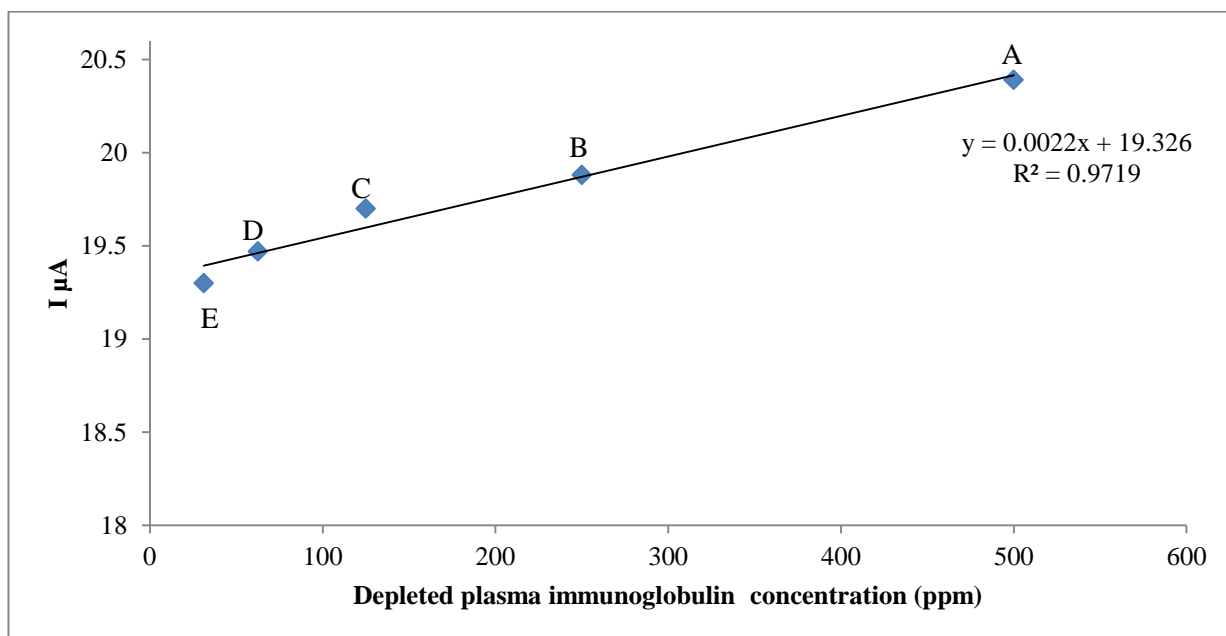


**Figure 5.14** plot of peak currents against plasma immunoglobulin (AD case) for (A) [1:2000](500ppm), (B) [(1:4000) (250 ppm)] (C)[ (1:8000) (125 ppm)], (D) [(1:16,000), (62.5 ppm)], (E) [(1:32,000) (31.25 ppm)], (F) [(1:64,000) (15.62ppm)], (G) [(1:128,000) (7.81ppm)] and (H) [(1:256,000) (3.91ppm)]

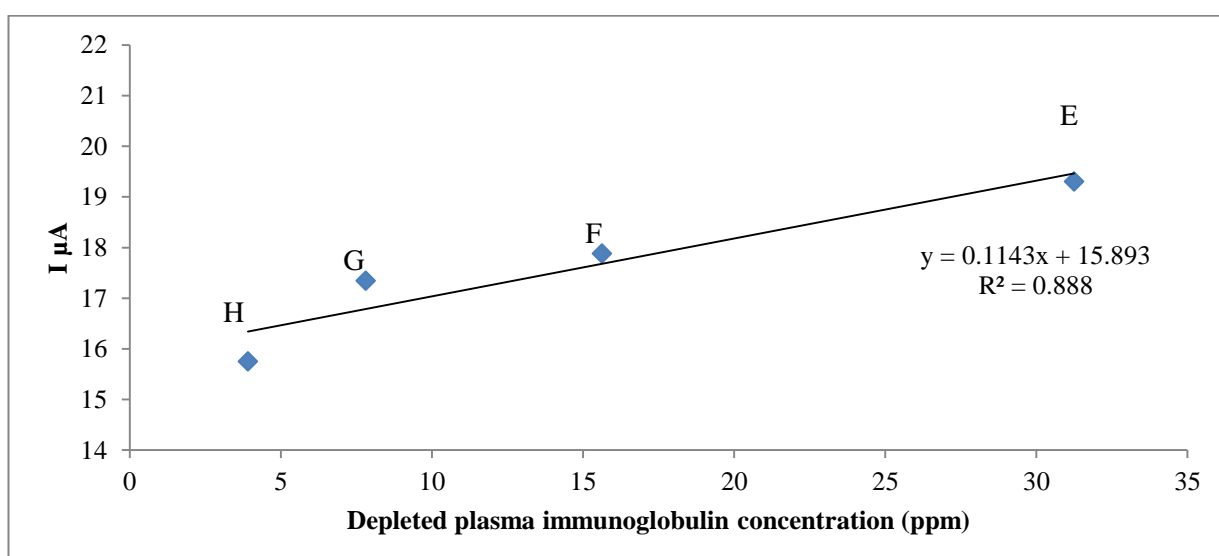
Figure 5.14 shows the plot of peak currents against plasma immunoglobulin dilutions for AD patient. The figure shows similar logarithmic trend (black line) observed for the control subjects in Figure 5.8. It also indicates two linear zones in the graph, first at the high concentration zones (A-E) and the second at the low concentration zone (H-E).

Figure 5.15 shows the calibration plot of the peak currents against the plasma immunoglobulin at high concentrations (31.25-500 ppm) for the AD. The result shows the relationship between the current and plasma has a linear regression equation  $I_p (\mu A) = 0.0022 (\mu A ppm^{-1}) + 19.326$  with sensitivity of  $0.0022 (\mu A ppm^{-1})$ . It also has a coefficient of determination ( $R^2$ ) of 0.9719 which indicate that the data point fit (97 %) closely to the line compared to  $R^2$  of 0.888 (88 %) obtained from the calibration curve for low plasma immunoglobulin concentrations (E-H) as shown in Figure 5.16. This indicates that the plasma immunoglobulin/ polyclonal rabbit Anti-human Ig

electrode can detect the plasma concentration linearly at high concentration better than at low concentration.



**Figure5.15** Calibration plot of peak currents against plasma immunoglobulin double dilution for AD patient at (A) [1:2000](500ppm), (B) [(1:4000) (250 ppm)] (C)[ (1:8000) (125 ppm)], (D) [(1:16,000), (62.5 ppm)], (E) [(1:32,000) (31.25 ppm)]



**Figure5.16** Calibration plot of peak currents against plasma immunoglobulin double dilution for se AD patient at (E) [(1:32,000) (31.25 ppm)], (F) [(1:64,000) (15.62ppm)], (G) [(1:128,000) (7.81ppm)] and (H) [(1:256,000) (3.91ppm)]

Figure 5.17 shows the comparison between the peaks current against plasma Ig at high concentrations point A to E (500-31.25 ppm) for control subject and AD case with error bars for the 1<sup>st</sup> and second run experiment. The result shows that the conjugation between polyclonal rabbit Anti-human Ig and plasma immunoglobulin for AD patient had higher peak current values compared to the control subjects. The high peak current might be due to the availability of large amount of plasma immunoglobulin in AD patients that conjugates with polyclonal rabbit Anti-human Ig and thus acts as an electron accelerator between the probe solution and the surface of the electrode. Research have shown that AD patients not treated with cholinesterase inhibitors have high plasma immunoglobulin in their body than control subjects (Mukaetova-Ladinska *et al.*, 2012). Similar result is obtained for lower plasma immunoglobulin concentration point E to H (31.25-3.91 ppm) shown in Figure 5.18. These results shows the sensitivity of the electrochemical method in detecting changes between control and plasma immunoglobulin from AD patient. The error bars in Figure 5.17 and Figure 5.18 showed minimal upper and lower errors showing that the results are reproducible.

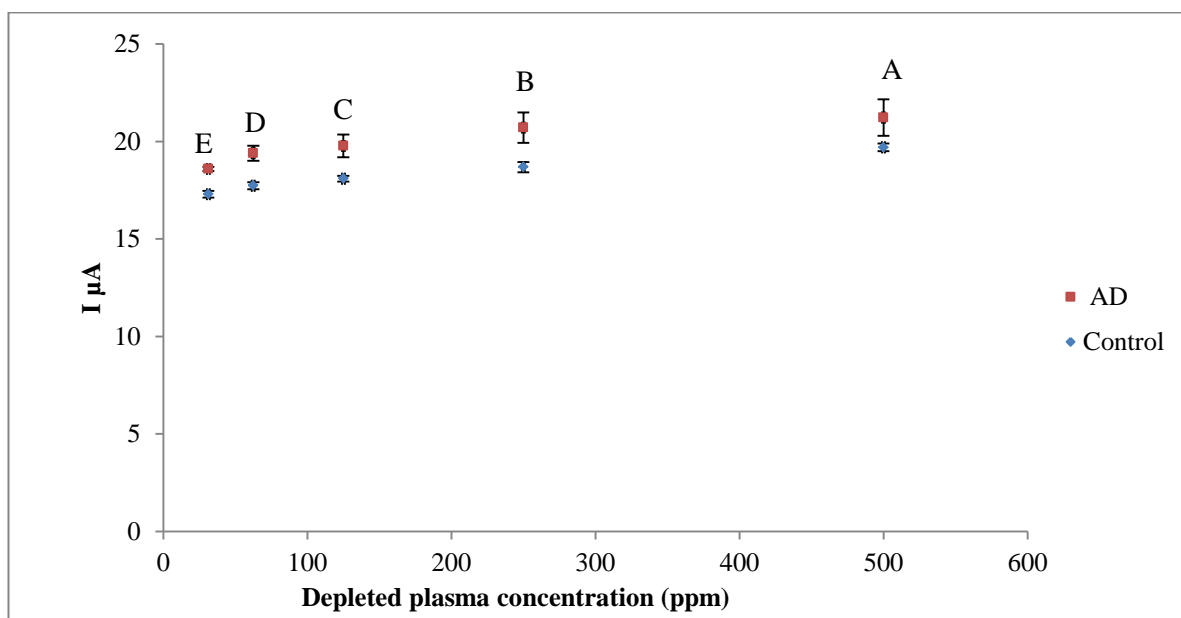


**Figure.5.17 Comparing peak currents between control and plasma immunoglobulin from AD patient at dilutions (A) [1:2000](500ppm)], (B) [(1:4000) (250 ppm)] (C)[ (1:8000) (125 ppm)], (D) [(1:16,000), (62.5 ppm)], (E) [(1:32,000) (31.25 ppm)]**

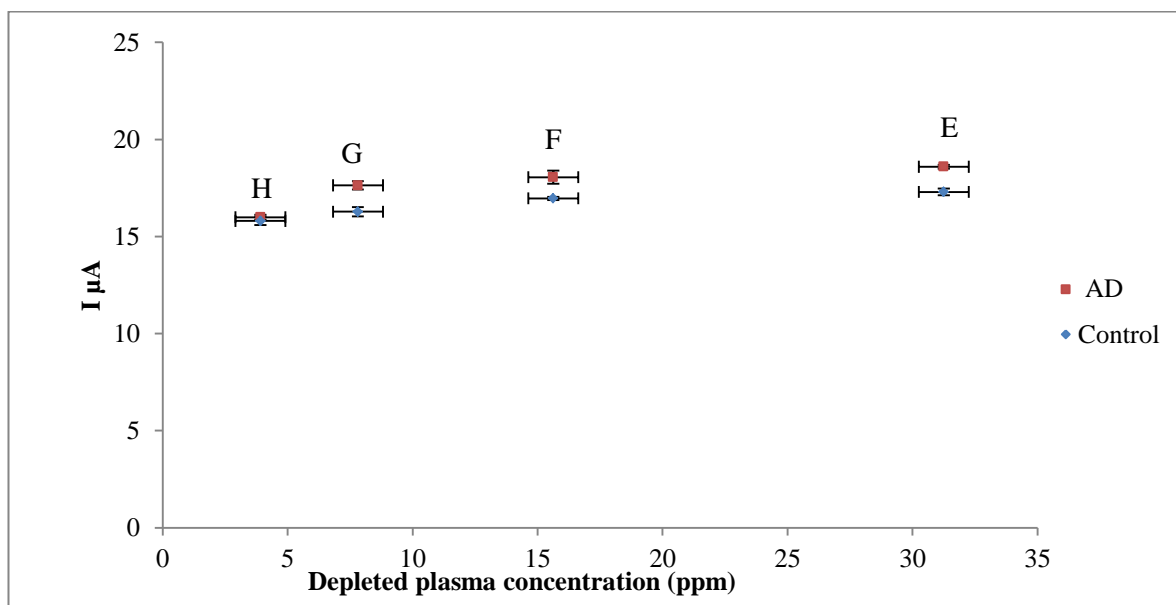


**Figure.5.18** Comparing peak currents between control and plasma immunoglobulin from AD patient at dilutions (E)[(1:32,000) (31.25 ppm)], (F)[(1:64,000) (15.62ppm)], (G)[(1:128,000) (7.81ppm)], (H)[(1:256,000) (3.91ppm)],

#### ***5.6.4 ELISA detection of plasma immunoglobulin/polyclonal rabbit Anti-human Ig-polyclonal Goat Anti-rabbit Immunoglobulin/horseradish peroxidase conjugation for AD case***

Figure 5.19a show the result obtained for the different dilution of plasma immunoglobulin for AD patient using ELISA method. This experiment was carried out in order to compare this result with the electrochemical technique and see which technique is better for detecting plasma immunoglobulin as biomarker for AD. The optical density for the plasma immunoglobulin/ polyclonal rabbit Anti-human Ig/polyclonal Goat Anti-rabbit Immunoglobulin/horseradish peroxidase conjugation was measured using a UV-spectrometer reader.

ELISA incorporates polyclonal Goat Anti-rabbit Immunoglobulin/horseradish peroxidase to amplify the conjugation of plasma immunoglobulin/polyclonal rabbit Anti-human Ig for detection by the UV-Vis reader. Plotting the optical densities against the depleted plasma immunoglobulin concentrations (Fig 5.19a) showed the possibility of two linear segments at low plasma immunoglobulin concentration (3.91-0.244 ppm) points H to L and high plasma concentration (3.91-500 ppm) point E to A. A

logarithmic relationship exists from point F to L at the low concentration region. A repeat of the experiment showed similar findings. Error bar plots of the average optical densities against plasma Ig concentrations as shown in Figure 5.19b, showed negligible errors at high concentration points (A-E) indicated by the presence of small upper and lower error bars. The upper and lower error bars increased for the more diluted plasma concentration at point F to L. The result shows that the optical method is also a reproducible technique for detecting plasma immunoglobulin concentrations.

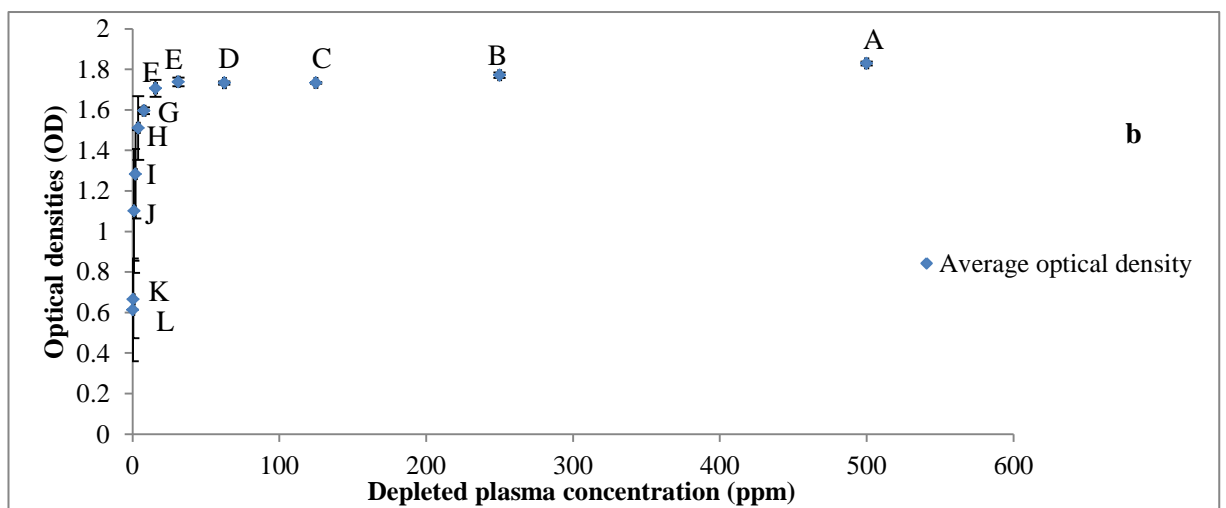
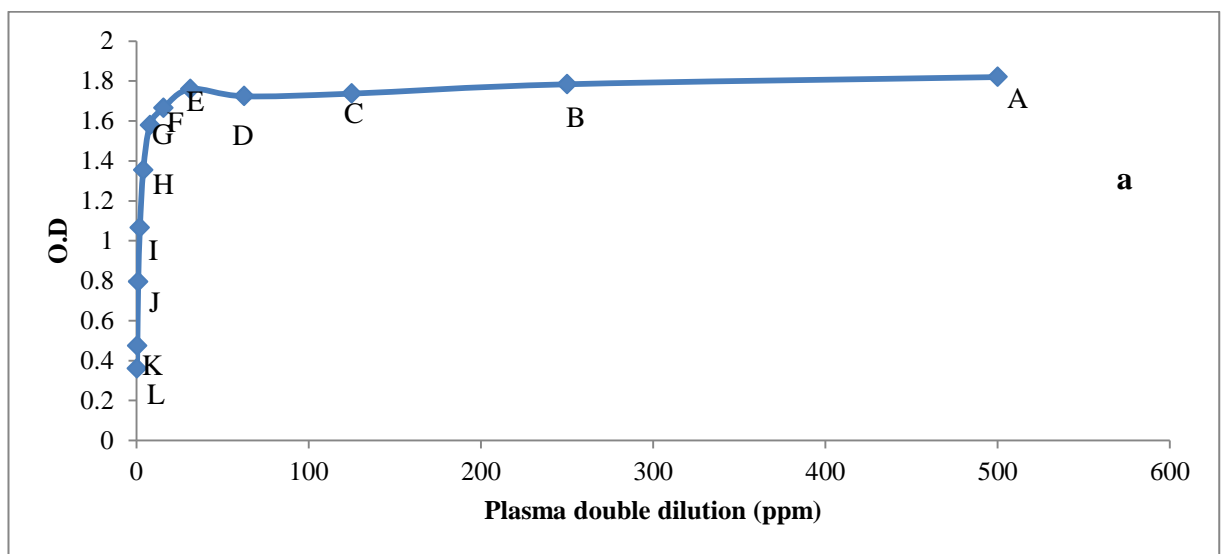


**Figure 5.19 (a) Plot of Optical densities (OD) against plasma immunoglobulin dilution (b) Error bar plot for A[1:2000](500ppm), B[(1:4000) (250 ppm)] C[ (1:8000) (125 ppm)], D[(1:16,000), (62.5 ppm)], E[(1:32,000) (31.25 ppm)], F[(1:64,000) (15.62ppm)], G[(1:128,000) (7.81ppm)], H[(1:256,000) (3.91ppm)], I[(1:512,000) (1.95ppm)], J [(1:1024,000) (0.98ppm)], K [(1:2048,000) (0.49ppm)], L [(1:4096,000) (0.244ppm)]**

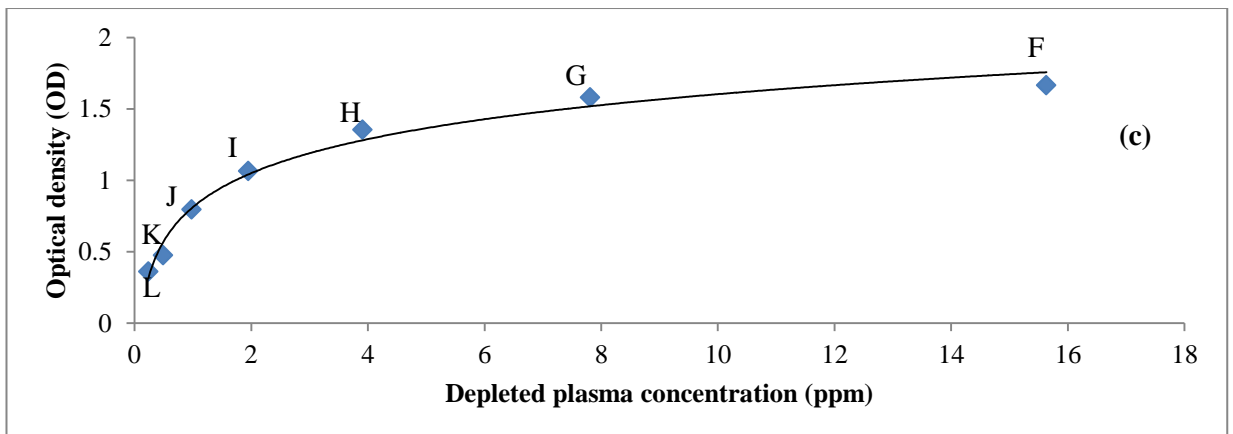
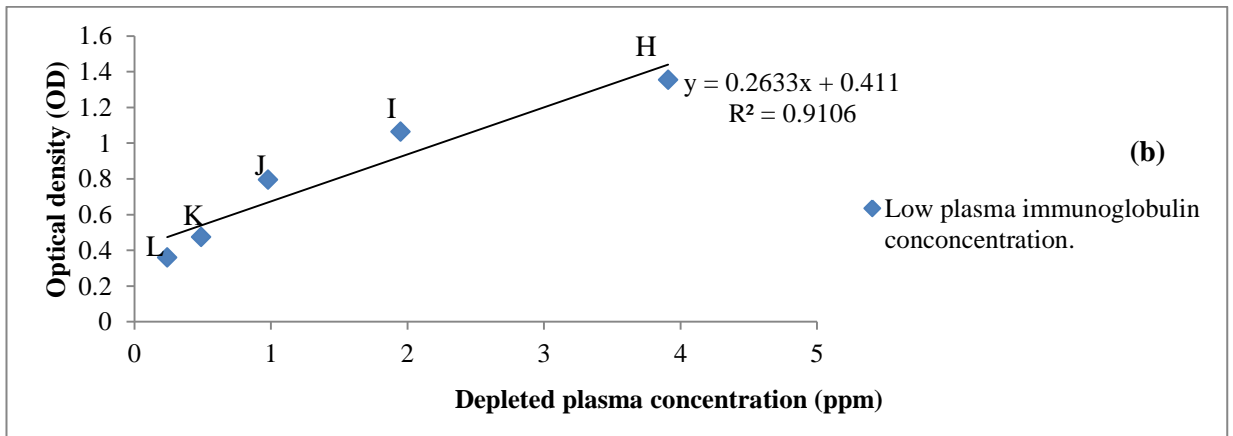
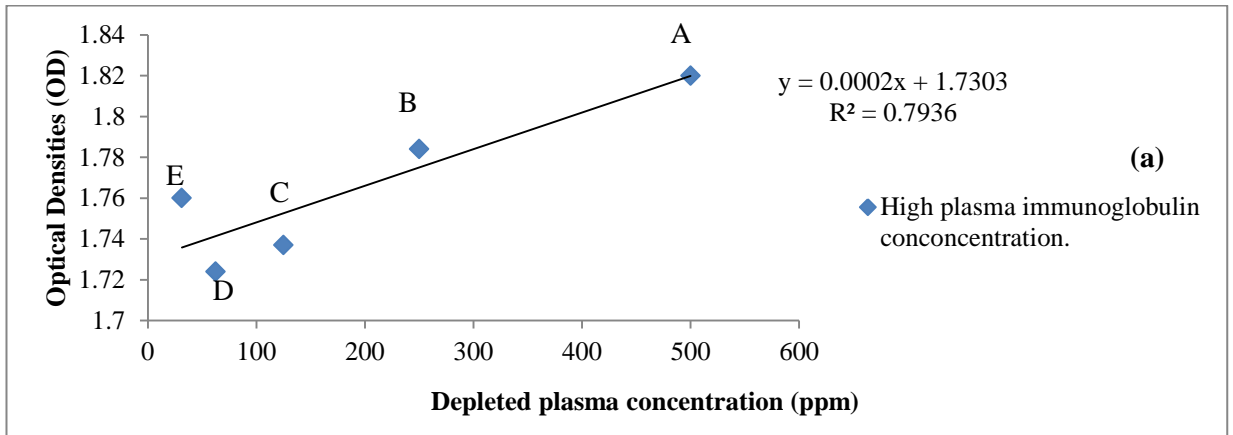


**Figure.5.20 Calibration plot of peak currents against plasma immunoglobulin dilution for AD patient (a) [High conc. Point A-E], (b) [Point H-L] and (c) logarithmic curve [Low conc. Point F-L]**

Plotting calibration curve of the average optical densities against high concentration points (A-E) and low concentration points (H-L) of the plasma immunoglobulin showed that none of the segment fits closely to the calibration line as shown in Figure 5.20a and b. Figure 5.20a has coefficient of determination ( $R^2$ ) of 0.7936 (79 %) and Figure

5.20b of 0.9106 (91 %) which are very low. The coefficient of determination determines the degree of closeness of an experimental data in linear regression analysis. The higher the value of  $R^2$  the closer the experimental data fits linearly. Figure 5.20c shows that logarithmic relationship exist at points F to L indicating that point E (31.25 ppm) is the detection limitation point for linearity at high concentration. Comparing these results with AD case from the electrochemical method in Figure 5.13 and calibration curves in Figure 5.15, shows that both methods has limiting detection point for linearity at high concentration at point E. But the electrochemical method detects better linearly at the high plasma immunoglobulin concentrations than the optical method. The optical method based on the calibration curve analysis in Figure 5.20a and b, can neither detect better linearly at low or high concentration of plasma immunoglobulin.

**5.6.5 Immobilization of polyclonal rabbit Anti-human Ig /depleted plasma immunoglobulin on  $Fe_2O_3$ -Au Nps/Gold electrode surface.**

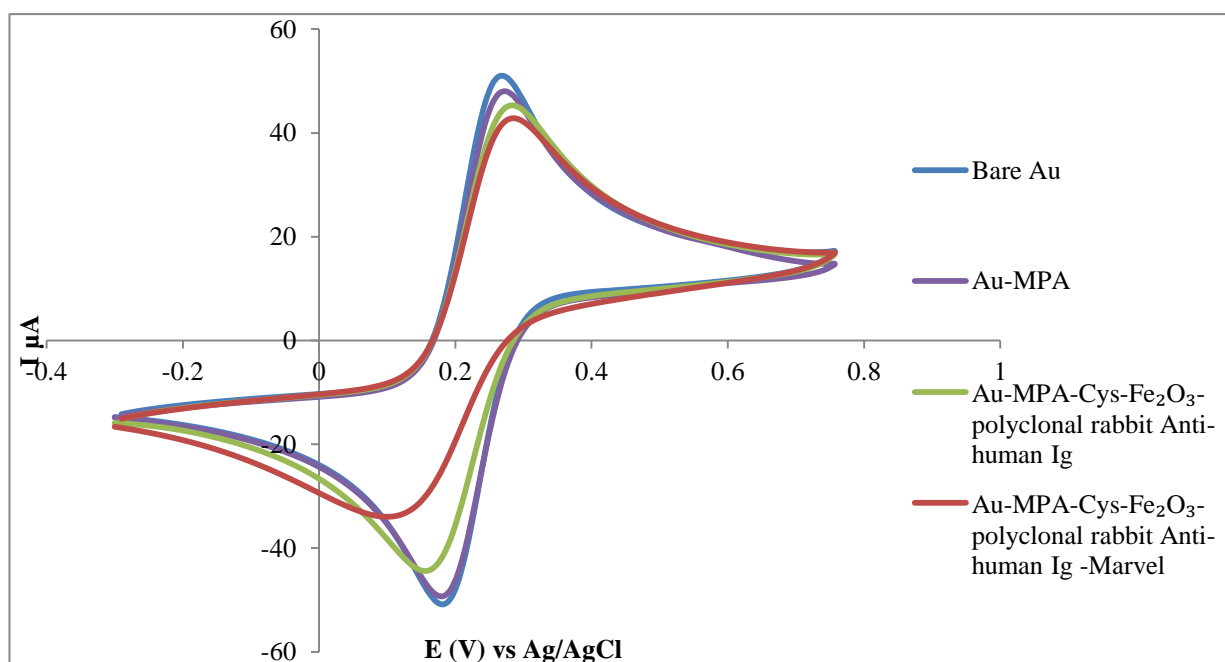


**Figure 5.21 CV of bare Au (light blue line), Au-MPA (dark blue), Au-MPA-cysteamine-  $Fe_2O_3$ -Au Nps-polyclonal rabbit Anti-human Ig (green line), and Au-MPA-cysteamine-  $Fe_2O_3$ -Au Nps-polyclonal rabbit Anti-human Ig -Marvel (red line)**

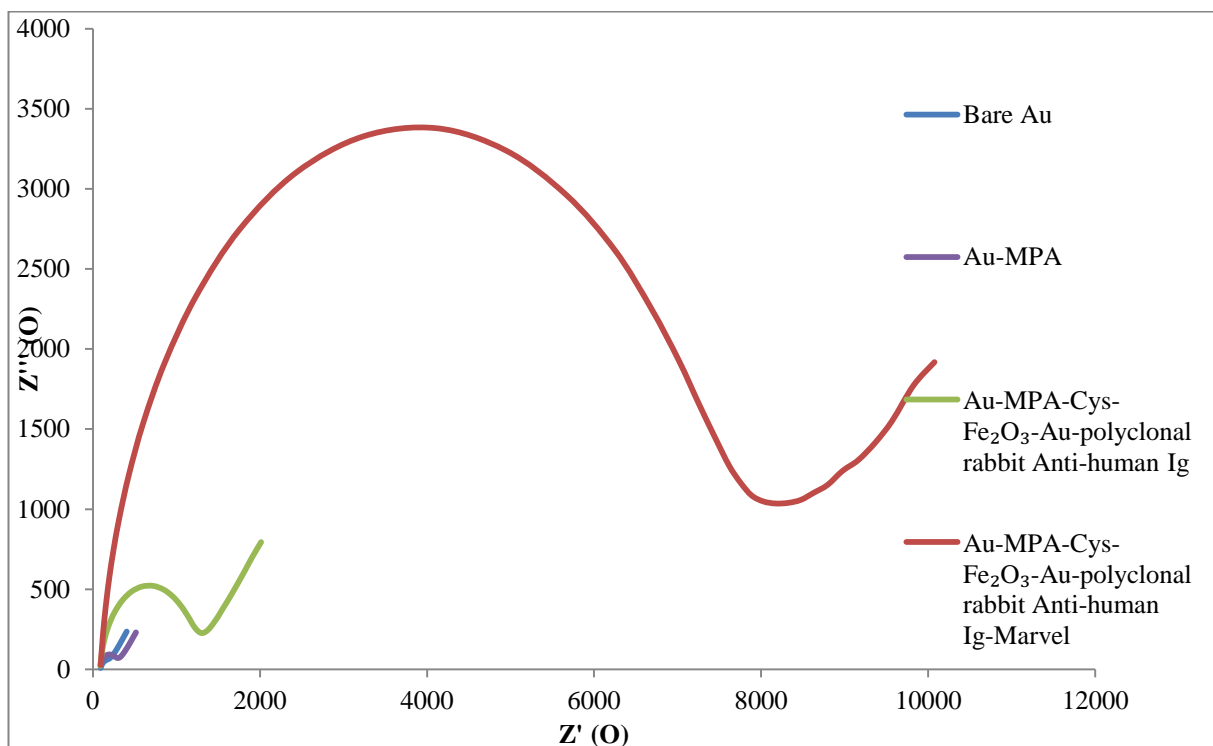
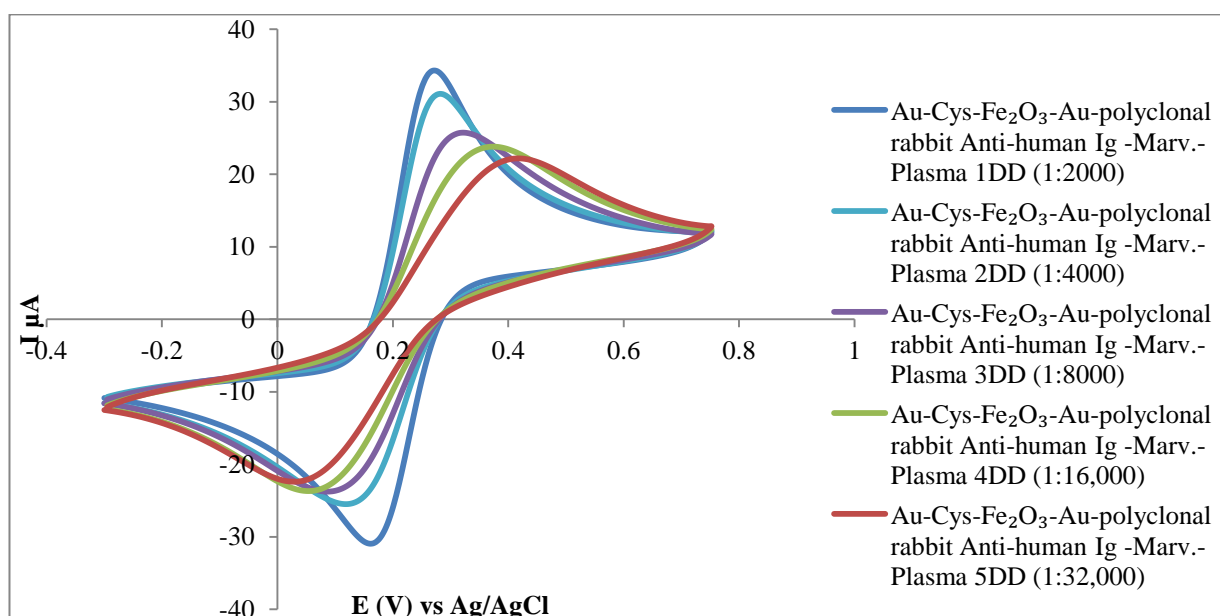


**Figure 5.22** EIS of bare Au (light blue line), Au-MPA (dark blue), Au-MPA-cysteamine-  $\text{Fe}_2\text{O}_3$ -Au Nps-polyclonal rabbit Anti-human Ig (green line), and Au-MPA-cysteamine-  $\text{Fe}_2\text{O}_3$ -Au Nps-polyclonal rabbit Anti-human Ig -Marvel (red line)

Figure 5.21 shows the cyclic voltammogram of bare gold electrode (light blue line), gold electrode modified with MPA (dark blue line), gold electrode modified with  $\text{Fe}_2\text{O}_3$ -Au Nps- polyclonal rabbit Anti-human Ig (green line) and gold electrode modified with  $\text{Fe}_2\text{O}_3$ -Au Nps- polyclonal rabbit Anti-human Ig -marvel (red line). The result shows a gradual decrease in the oxidation and reduction peaks of the redox probe. The bare Au electrode had the highest oxidation and reduction peaks of  $49.25\mu\text{A}$  and  $-49.68\mu\text{A}$  at  $0.25\text{V}$  and  $0.19\text{V}$  respectively. This shows the ability of gold to act as an electron conductor for the flow of electrons between its surface and the redox solution. The oxidation and reduction peaks decreases when SAM of MPA was formed on the surface of the gold electrode. Further decrease in the oxidation and reduction peaks was observed when the gold electrode was modified with  $\text{Fe}_2\text{O}_3$ -Au Nps-polyclonal rabbit Anti-human Ig. The  $\text{Fe}_2\text{O}_3$ -Au nanoparticles act as immobilization substrate for the polyclonal rabbit Anti-human Ig with increased surface area and also aid the acceleration of electron transfer between the probe solution and the electrode surface. The lowest oxidation and reduction peaks of  $42.3\mu\text{A}$  and  $-35.7\mu\text{A}$  were observed at

0.27V and 0.08V respectively when the Fe<sub>2</sub>O<sub>3</sub>-Au Nps-polyclonal rabbit Anti-human Ig was blocked with 1 % of Marvel.

The result is corroborated with the Nyquist plot in Figure 5.22 which shows that gold electrode had the lowest charge transfer resistance of 96.75Ω and the Fe<sub>2</sub>O<sub>3</sub>-Au Nps-polyclonal rabbit Anti-human Ig blocked with Marvel electrode had the highest charge transfer resistance of 1199Ω. This showed that indeed the gold electrode was successfully modified with polyclonal rabbit Anti-human Ig/plasma immunoglobulin immune-complex and that the marvel blocked the flow of electrons.



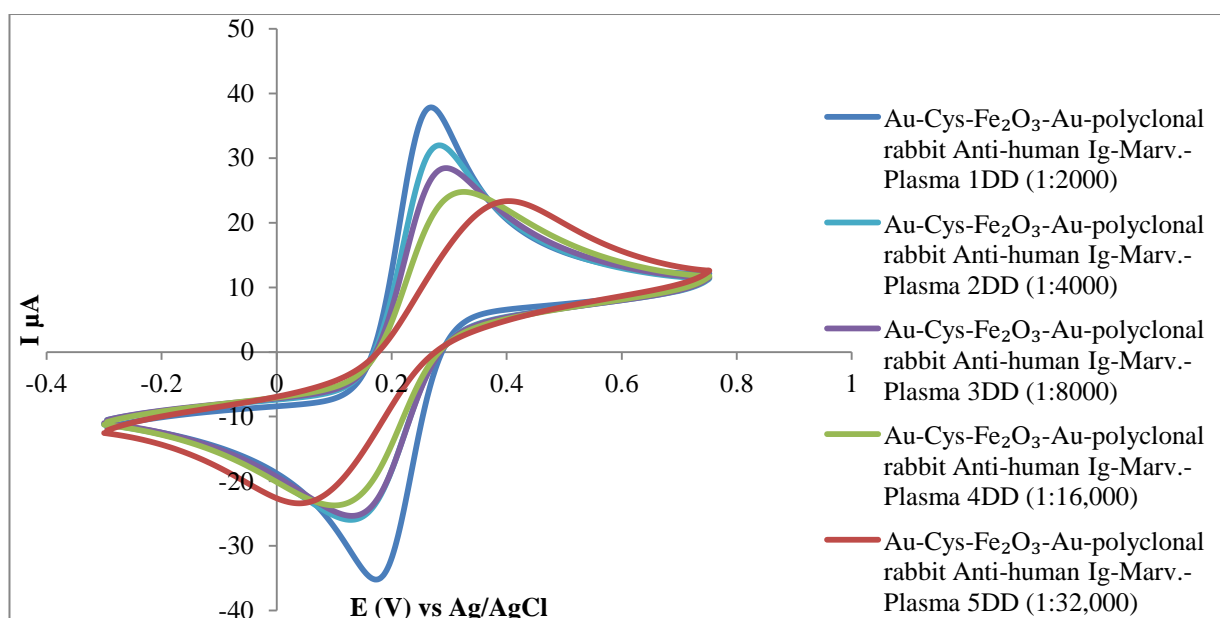
**Figure 5.23 CV of Au-Cys-Fe<sub>2</sub>O<sub>3</sub>-Au Nps- polyclonal rabbit Anti-human Ig -Marvels –Plasma (control) at double dilution (DD) 1:2000 (dark blue line), 1:4000 (sky blue line), 1:8000 (light blue line), 1:16,000 (green line), 1:32,000 (red line)**

Figure 5.23 shows the cyclic voltammogram of gold electrode modified with Fe<sub>2</sub>O<sub>3</sub>-Au Nps-polyclonal rabbit Anti-human Ig-Marvel for depleted plasma Ig (control) for 1:2000,1:4000,1:8000, 1:16000 and 1:32000 dilutions respectively. The result showed that as plasma dilution increases, the oxidation and reduction peaks of the redox solution decreases and shifts towards the right. The decrease in the oxidation and reduction peaks results from low plasma Ig available for polyclonal rabbit Anti-human Ig conjugation due to the increased dilution of the plasma Ig stock. But less dilution results in high amount of plasma Ig available for conjugation with the polyclonal rabbit

Anti-human Ig and thus acts as electron accelerator, resulting in increased oxidation and reduction peaks.

The result in Figure 5.23 showed that gold electrode modified with Fe<sub>2</sub>O<sub>3</sub>-Au Nps-polyclonal rabbit Anti-human Ig-Marvel-Plasma (1:2000 dilution (1DD)) had the highest oxidation and reduction peak current of 34.27μA and -30.83μA at 0.26V and 0.16V respectively (dark blue line). The lowest redox peak of 22.10μA and -22.20μA where observed at 0.41V and 0.040V respectively when the electrode was modified with plasma Ig (1:32,000 (5DD)) (red line). The electrode could not measure further changes in the redox peaks beyond plasma 5<sup>th</sup> double dilution (5DD) due to the shift towards the right as observed in the cyclic voltammogram.

The shift in the redox peaks might be as a result of the depletion of Fe<sub>2</sub>O<sub>3</sub>-Au Np from the surface of the electrode as the Fe<sub>2</sub>O<sub>3</sub>-Au Nps gradually diffuses into the redox solution with time as experimentation proceeds. This might be due to poor bonding of the Fe<sub>2</sub>O<sub>3</sub>-Au nanoparticles on the surface of the electrode, and also due to low plasma immunoglobulin available for conjugation with polyclonal rabbit Anti-human Ig as result of increased dilution of the plasma Ig stock solution.



**Figure 5.24 CV of Au-Cys-Fe<sub>2</sub>O<sub>3</sub>-Au Nps- polyclonal rabbit Anti-human Ig -Marvels –Plasma (AD) at double dilution (DD) 1:2000 (dark blue line), 1:4000 (sky blue line), 1:8000 (light blue line), 1:16,000 (green line), 1:32,000 (red line)**

Figure 5.24 shows the CV of the modified electrode with  $\text{Fe}_2\text{O}_3$ -Au Nps-polyclonal rabbit Anti-human Ig-Marvel-Plasma Ig for AD patient. The result is similar to the one obtained for control subjects in Figure 5.23. The highest oxidation and reduction peak current of  $37.74\mu\text{A}$  and  $-34.76\mu\text{A}$  at  $0.25\text{V}$  and  $0.18\text{V}$  respectively (dark blue line) was observed for the 1<sup>st</sup> double dilution (1:2000) and the lowest redox peak of  $23.35\mu\text{A}$  and  $-23.40\mu\text{A}$  where observed for the 5<sup>th</sup> double dilution (1:32,000) at  $0.41\text{V}$  and  $0.042\text{V}$  respectively (red line). The EIS experiment carried out shown in Figure 5.25 shows the Nyquist plot for the different dilutions.

The result shows that as the plasma Ig dilution increases, the charge transfer increases. The electrode modified with  $\text{Fe}_2\text{O}_3$ -Au Nps-polyclonal rabbit Anti-human Ig-Marvel-Plasma (1:2000 dilution) had the lowest charge transfer resistance of  $8241\Omega$  (dark blue line) and the highest charge transfer resistance of  $10774\Omega$  was observed at the 5<sup>th</sup> plasma Ig dilution (1:32,000). This result further verifies the effect of the different plasma Ig dilutions on the electrochemical response of the  $\text{Fe}_2\text{O}_3$ -Au Nps-polyclonal rabbit Anti-human Ig modified electrode. The experiment was repeated for the AD plasma Ig and similar result with slight variation was obtained.

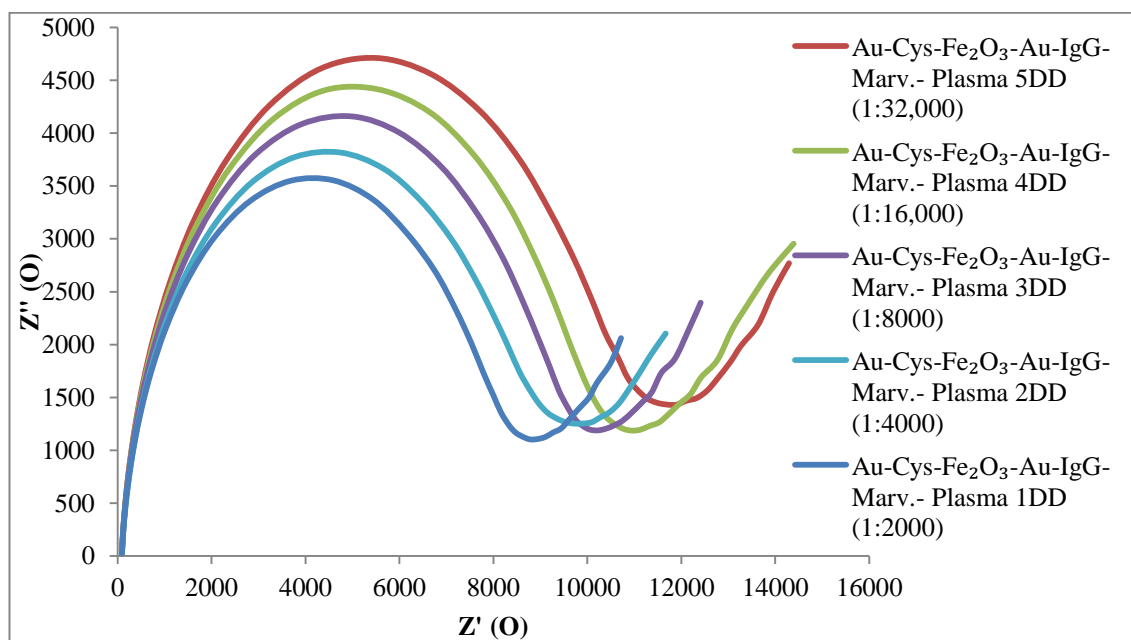


**Figure 5.25 EIS of Au-Cysteamine- $\text{Fe}_2\text{O}_3$ -Au Nps- polyclonal rabbit Anti-human Ig -Marvels – Plasma (AD) at double dilution (DD) 1:2000 (dark blue line), 1:4000 (sky blue line), 1:8000 (light blue line), 1:16,000 (green line), 1:32,000 (red line)**

Error bar analysis was carried out on the first and second run for the AD case as shown in Figure 5.26. The result showed minimal errors as indicated by the upper and lower error bars. Although the error bars are slightly high at high plasma concentrations 500 and 125 ppm (point A and C), the result in general does not show much deviation from the average peak current data indicating that the experiment is reproducible if carried out.

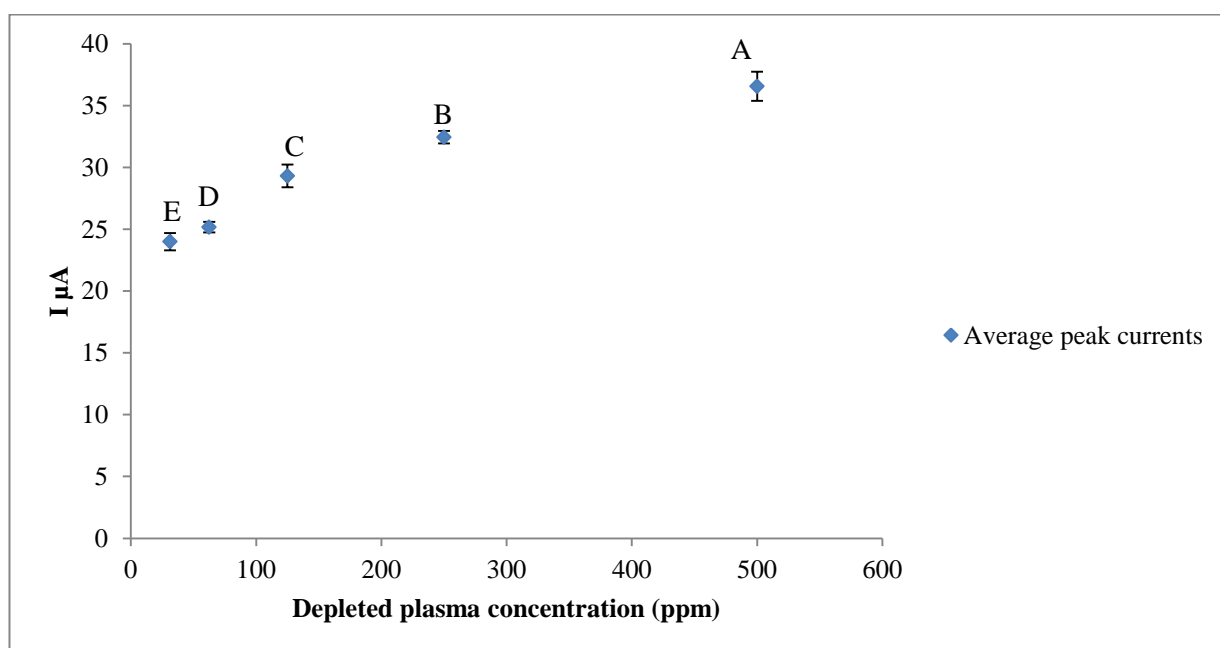


**Figure 5.26 Error bar analysis for first and second run depleted plasma concentration from AD patient at (A) [1:2000](500ppm)], (B) [(1:4000) (250 ppm)] (C)[ (1:8000) (125 ppm)], (D) [(1:16,000), (62.5 ppm)], (E) [(1:32,000) (31.25 ppm)]**

Based on the CV results obtained for the control subjects (Fig.5.23) and AD case (Fig.5.24) using  $\text{Fe}_2\text{O}_3\text{-Au Nps}$ -polyclonal rabbit Anti-human Ig modified electrode, the difference between the AD case and control is that there is an increase in the redox peaks currents in the AD case compared to the control subjects as shown in Figure 5.27. This is true because research have shown that patients with AD have increased plasma immunoglobulin in their blood plasma. Therefore the increase in peaks currents observed for the AD case results from the presence of high amount of plasma Ig that conjugates with polyclonal rabbit Anti-human Ig immobilized on  $\text{Fe}_2\text{O}_3\text{-Au Nps}$  modified gold electrode. This in turn acts as an electron accelerating platform for electrons to flow between the redox probe and the surface of the electrode. The error

indicates minimal errors in the first and second run experiment for the control and AD case respectively as shown by the upper and lower error bars. This shows that the experiment is reproducible.

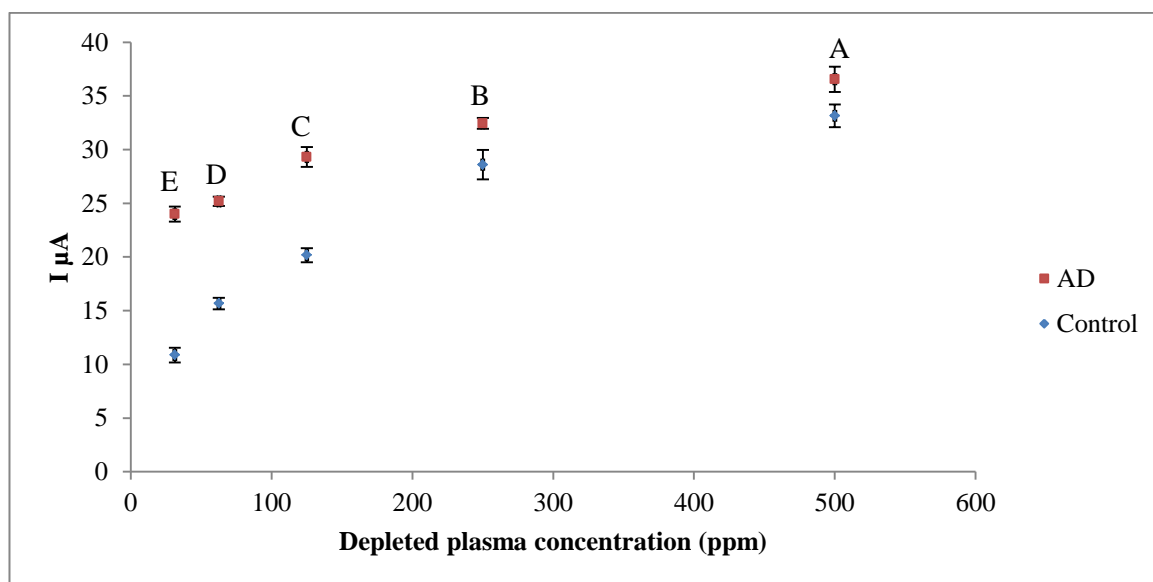


**Figure 5.27 Comparing peak currents between control and plasma from severe AD patient at double dilution (A) [1:2000](500ppm)], (B) [(1:4000) (250 ppm)] (C)[ (1:8000) (125 ppm)], (D) [(1:16,000), (62.5 ppm)], (E) [(1:32,000) (31.25 ppm)]**

The experimental results have shown that it is possible to develop an immunosensor electrode for detecting plasma immunoglobulin as biomarker for AD. The experiment needs further studies and improvements on the immobilization and stabilization of Fe<sub>2</sub>O<sub>3</sub>-Au nanoparticles, and polyclonal rabbit Anti-human Ig on the electrode surface to prevent diffusion of particles in solution during experimentation and also to improve on the sensitivity of the immunosensor electrodes.

## 5.7 Conclusion

In conclusion the result shows that plasma immunoglobulin can be detected directly as a biomarker for AD first by immobilization of the polyclonal rabbit Anti-human Ig and depleted plasma Ig on gold electrode and secondly through the use of Fe<sub>2</sub>O<sub>3</sub>-Au Nps as immobilization substrate . For the immobilization on gold electrode, it was observed that the depleted plasma Ig from AD patient had higher peak currents compared to control subjects indicating that more plasma immunoglobulin was available for

conjugation with polyclonal rabbit Anti-human Ig in AD patient. This in turn increases their tendencies to act as electron accelerator between the redox probe and electrode surface. The modified gold electrode was able to detect plasma concentration up to the 8<sup>th</sup> plasma Ig dilutions (1:256,000) (3.91 ppm) in a combination of linear and logarithmic patterns. The linear detection was observed at high plasma Ig concentrations 31.25-500 ppm (1-5<sup>th</sup> DD) with a level off point at concentration 31.25 ppm. Although linear detection was observed at the lower concentrations, indications from the calibration curve at the lower concentrations show less linearity in detection compared to the higher concentrations. Comparing the result with the ELISA method showed that the electrochemical method is more sensitive and reproducible in detecting plasma Ig concentrations within linear range for the less diluted plasma Ig (high concentrations). Although the ELISA method detected the plasma Ig concentration up to the 12<sup>th</sup> double dilutions (0.244ppm), calibration analysis showed that it had less linearity in detecting plasma Ig both in high and low concentrations.

The results also showed that Fe<sub>2</sub>O<sub>3</sub>-Au Nps can be used as immobilization substrate for the detection of varying plasma Ig concentrations. Higher peak current values were also observed for plasma obtained from AD patients compared to the control subjects. Although the modified electrode could not measure further changes in the redox peaks beyond plasma 5<sup>th</sup> double dilution (31.25 ppm). This is attributed to the shift observed in the cyclic voltammogram which result as the Fe<sub>2</sub>O<sub>3</sub>-Au Np gradually diffuses into the redox solution with time and also low plasma immunoglobulin available for conjugation due to dilution. Both methods still require further studies to improve on their sensitivity, detection of the depleted plasma Ig samples from early and late stages of AD in patients, and stabilization of the nanoparticles on the surface of the electrode for better immobilization.

## Chapter 6 -Conclusions and recommendation for future work

In conclusion the main work of this thesis was to synthesis and characterise iron oxide nanoparticles (magnetite and maghemite), iron oxide core-gold shell nanoparticles and their application in the development of immunosensor electrodes for the detection of depleted plasma immunoglobulin as biomarker for Alzheimer's disease (AD). The iron oxide nanoparticles (magnetite) were successfully synthesized through oxidative alkaline hydrolysis of ferrous salt ( $\text{FeSO}_4$ ) and the effect of synthesis parameters on the morphology and nature of the nanoparticles were analysed. The conclusions drawn from the synthesis of magnetite are as follows:

1. Increasing iron salt concentration affects the nanoparticles sizes and shape and higher salt concentration of up to 2M and above reduces the paramagnetic properties of the magnetite and the formation of rod shape  $\beta$ -iron oxy hydroxide (alkaganeite).
2. Changes in hydroxyl ion concentration affect the nanoparticles size, shape and morphology. Smaller hydroxyl ion concentration (0.005M and 0.01M) results in the formation of super-paramagnetic nanoparticles with broader size distribution. The nanoparticles sizes increases with less size distribution at higher hydroxyl ion concentrations with the formation of hematite ( $\alpha$ - $\text{Fe}_2\text{O}_3$ ) at 2M as impurity.
3. Synthesis temperature did not affect the nanoparticles sizes but higher synthesis temperature up to 150°C results in the formation of hematite ( $\alpha$ - $\text{Fe}_2\text{O}_3$ ) as impurity with the magnetite.
4. Synthesizing the magnetite nanoparticles under the influence of revolution per minutes showed that the nanoparticles sizes decreases with increasing revolution per minute and the formation of small amount of hematite ( $\alpha$ - $\text{Fe}_2\text{O}_3$ ) and iron oxy hydroxide ( $\gamma$ - $\text{FeOOH}$ ) as impurities at 500 rpm and 1500 rpm.

Iron oxide core-gold shell nanoparticles were successfully formed first by oxidizing magnetite to maghemite by heating the magnetite (50 nm) in nitric acid solution while stirring at temperature 90-100°C till solution turns brown. Gold shell 24 nm average particles size was formed as shell on the iron oxide ( $\text{Fe}_2\text{O}_3$ ) nanoparticles through the

iterative reduction of chloroauric acid with hydroxylamine as reducing agents. The total average particles size of the iron oxide core-gold shell nanoparticles formed is 74 nm.

During the formation of iron oxide core-gold shell nanoparticles, the effect of temperature and agitation on PEI adsorption on the nanoparticles were studied and the following conclusions were drawn:

1. Temperature and agitation affects the adsorption of PEI molecules onto the surface of iron oxide nanoparticles which in turn affects the attachment of gold shells on the iron oxide nanoparticles.
2. 40°C was found to be most favourable for the electrostatic attachment of gold shell on iron oxide nanoparticles since more PEI molecules are available. Also the polycationic nature of PEI was observed to diminish as the heating temperature increases which results in the reduced electrochemical properties observed at 100°C compared to 40°C.
3. Agitation also affects the attachment of PEI molecules on iron oxide nanoparticles in the formation of iron oxide core-gold shell nanoparticles. It was found that agitating PEI solution with the iron oxide nanoparticles at room temperature favoured the electrostatic attraction between the positively charged PEI cation and the negatively charged iron oxide nanoparticles. This also favours the electrostatic attachment of gold shell on the nanoparticle indicative of the better electrochemical properties observed compared to the unstirred process at room temperature.

The iron oxide core-gold shell nanoparticle (74 nm) was used in the development of an immunosensor electrode for the detection depleted plasma Ig as biomarker for Alzheimer's diseases. Firstly the immunosensor electrode was developed with gold electrode as the immobilizing and sensing surface for the depleted plasma immunoglobulin biomarker and antibody (polyclonal rabbit Anti-human IgA, IgG, IgM). The immunosensor electrode was able to detect depleted plasma Ig concentration for both control subject and severe AD case up to the 8<sup>th</sup> double diluted plasma (1:256,000) (3.91 ppm) in both linear and logarithmic pattern. Depleted plasma Ig from AD patient showed higher peak currents compared to control subjects indicating the presence of more plasma immunoglobulin in the AD

patient compared to control subject available for conjugation with antibody. This also increased the tendencies of the immune-complex in AD patient to act as electron accelerator between the redox probe and electrode surface compared to the control subject. The result compared to the ELISA method showed that the immunosensor electrode has better sensitivity and reproducibility in detecting plasma Ig at high concentrations linearly compared to the ELISA method.

Secondly the iron oxide core-gold shell nanoparticle (74 nm) was used as the immobilizing substrate for the formation of immunosensor electrode for the depleted plasma immunoglobulin biomarker and antibody (polyclonal rabbit Anti-human IgA, IgG, IgM). The result also showed higher peak current values for plasma obtained from AD patients compared to the control subject. Although the modified electrode could not measure depleted plasma concentrations beyond the 5<sup>th</sup> plasma double dilution (1:32,000) (31.25 ppm) which might be attributed to shifts observed in the cyclic voltammogram due to the gradual diffusion of iron oxide-gold shell nanoparticles ( $\text{Fe}_2\text{O}_3\text{-Au Np}$ ) into the redox solution with time. This is attributed to the poor nanoparticles binding and stability on the surface of the electrode.

In both cases the results have shown that the immunosensor electrode developed with modified gold electrode and nanoparticles can differentiate between the concentrations in plasma Ig for both AD patients and control subjects. This shows that the immunosensor electrodes are highly sensitive and reproducible based on the results obtained and also answers the hypothesis question raised on AD biomarkers as supportive measures for AD diagnosis and monitoring. This also shows that the fabrication of plasma Ig biomarker immunosensor electrode for AD is feasible.

### **6.1 Recommendations for Future work**

The following are recommendations that would help in future research work on iron oxide nanoparticles synthesis, and the use of gold electrode and iron oxide core-gold shell nanoparticles for the fabrication of immunosensor electrode for the detection of plasma immunoglobulin as biomarker for AD monitoring and detection:

1. In synthesizing iron oxide nanoparticles (magnetite or maghemite), the nanoparticles should be well stabilized with good stabilizing agents (PEI) to prevent the aggregation of the nanoparticles with time which also affects the formation of gold shell. .
2. The nanoparticles characterization should be carried out as soon as possible after synthesis to prevent false results which might result if the nanoparticles aggregate with time.
3. Synthesizing magnetite nanoparticles of specific sizes and shapes for specific purposes using the oxidative alkaline hydrolysis of ferrous salt, care should be taken in altering the synthesis parameters to avoid the formation of impurities or side products which might affects the application of the nanoparticles.
4. In using PEI for stabilizing iron oxide nanoparticles and as capping agent for the formation of gold shell nanoparticles on iron oxide nanoparticles, heating the iron oxide nanoparticles at 40°C is most favourable for PEI attachment or stirring the nanoparticles at room temperature (25°C).
5. In the fabrication of immunosensor electrode, the Fe<sub>2</sub>O<sub>3</sub>-Au Np should be properly and strongly immobilized on the surface of the detecting electrode (gold electrode) using good chemical immobilization techniques to prevent the diffusion of the nanoparticles into the redox solution with time during experimentation. This will allow for the maximum detection of the plasma immunoglobulin concentration by the nanoparticles. Other sizes of nanoparticles should be used in the development of the immunosensor electrodes and to determine the sizes that is most favourable for the detection of plasma Ig concentrations.
6. The use of multiple electrode detecting system that can measure multiple electrodes modified with depleted plasma immunoglobulin and polyclonal rabbit Anti-human IgA, IgG, IgM at a go. This will prevent discrepancies often observed when the plasma concentrations are run at different times.
7. The depleted plasma Ig should be double diluted into different concentrations at the same time and used the same time or period. This will be prevent the changes that might occur on the samples if stored for a long time in the freezer due to experimentation time table.

8. The sensing electrode should be properly cleaned to avoid giving false results.
9. The polyclonal rabbit Anti-human IgA, IgG, IgM should be freshly prepared and used once for all depleted plasma concentration during conjugation. This will prevent discrepancies that might result from using differently prepared polyclonal rabbit Anti-human IgA, IgG, IgM or polyclonal rabbit Anti-human IgA, IgG, IgM stored for a long time in the fridge.

## References

- Amarjargal, A., Tijing, L.D., Park, C.H., Im, I.T. and Kim, C.S. (2013) 'Controlled assembly of superparamagnetic iron oxide nanoparticles on electrospun PU nanofibrous membrane: A novel heat-generating substrate for magnetic hyperthermia application', *European Polymer Journal*, 49(12), pp. 3796-3805.
- Armstrong, R.D., Lindholm, B. and Sharp, M. (1986) 'Impedance characteristics of a modified electrode', *Journal of Electroanalytical Chemistry and Interfacial Electrochemistry*, 202(1-2), pp. 69-74.
- Bae, K.H., Park, M., Do, M.J., Lee, N., Ryu, J.H., Kim, G.W., Kim, C., Park, T.G. and Hyeon, T. (2012) 'Chitosan oligosaccharide-stabilized ferrimagnetic iron oxide nanocubes for magnetically modulated cancer hyperthermia', *ACS Nano*, 6(6), pp. 5266-5273.
- Barnett, C.M., Gueorguieva, M., Lees, M.R., McGarvey, D.J. and Hoskins, C. (2013) 'Physical stability, biocompatibility and potential use of hybrid iron oxide-gold nanoparticles as drug carriers', *Journal of Nanoparticle Research*, 15(6).
- Bell, R.D. and Zlokovic, B.V. (2009) 'Neurovascular mechanisms and blood-brain barrier disorder in Alzheimer's disease', *Acta Neuropathologica*, 118(1), pp. 103-113.
- Brown, K.R. and Natan, M.J. (1998) 'Hydroxylamine seeding of colloidal Au nanoparticles in solution and on surfaces', *Langmuir*, 14(4), pp. 726-728.
- Brust, M., Walker, M., Bethell, D., Schiffrin, D.J. and Whyman, R. (1994) 'Synthesis of thiol-derivatised gold nanoparticles in a two-phase liquid-liquid system', *Journal of the Chemical Society, Chemical Communications*, (7), pp. 801-802.
- Chauhan, N. and Pundir, C.S. (2011) 'An amperometric biosensor based on acetylcholinesterase immobilized onto iron oxide nanoparticles/multi-walled carbon nanotubes modified gold electrode for measurement of organophosphorus insecticides', *Analytica Chimica Acta*, 701(1), pp. 66-74.
- Che, X., Yuan, R., Chai, Y., Ma, L., Li, W. and Li, J. (2009) 'Hydrogen peroxide sensor based on horseradish peroxidase immobilized on an electrode modified with DNA-L-cysteine-gold-platinum nanoparticles in polypyrrole film', *Microchimica Acta*, 167(3-4), pp. 159-165.

- Chen, M., Wei, X., Qian, H. and Diao, G. 'Fabrication of GNPs/CDSH-Fc/nafion modified electrode for the detection of dopamine in the presence of ascorbic acid', *Materials Science and Engineering C*.
- Chen, Y., Li, Y., Sun, D., Tian, D., Zhang, J. and Zhu, J.J. (2011) 'Fabrication of gold nanoparticles on bilayer graphene for glucose electrochemical biosensing', *Journal of Materials Chemistry*, 21(21), pp. 7604-7611.
- Chin, A.B. and Yaacob, I.I. (2007) 'Synthesis and characterization of magnetic iron oxide nanoparticles via w/o microemulsion and Massart's procedure', *Journal of Materials Processing Technology*, 191(1–3), pp. 235-237.
- Chung, T.H., Hsiao, J.K., Hsu, S.C., Yao, M., Chen, Y.C., Wang, S.W., Kuo, M.Y.P., Yang, C.S. and Huang, D.M. (2011) 'Iron oxide nanoparticle-induced epidermal growth factor receptor expression in human stem cells for tumor therapy', *ACS Nano*, 5(12), pp. 9807-9816.
- Connoly, J.R (2005) ' Introduction to X-ray powder diffraction', *Spring*, pp. 1-9.
- Daou, T.J., Pourroy, G., Greneche, J.M., Bertin, A., Felder-Flesch, D. and Begin-Colin, S. (2009) 'Water soluble dendronized iron oxide nanoparticles', *Dalton Transactions*, (23), pp. 4442-4449.
- Deslouis, C., Musiani, M.M. and Tribollet, B. (1989) 'The theory of ac and EHD impedances for a mediated reaction on a redox polymer modified electrode', *Journal of Electroanalytical Chemistry*, 264(1-2), pp. 37-55.
- Dronskowski, R. (2001) 'The Little Maghemite Story: A Classic Functional Material', *Advanced Functional Materials*, 11(1), pp. 27-29.
- Dubois, B., Feldman, H.H., Jacova, C., DeKosky, S.T., Barberger-Gateau, P., Cummings, J., Delacourte, A., Galasko, D., Gauthier, S., Jicha, G., Meguro, K., O'Brien, J., Pasquier, F., Robert, P., Rossor, M., Salloway, S., Stern, Y., Visser, P.J. and Scheltens, P. (2007) 'Research criteria for the diagnosis of Alzheimer's disease: revising the NINCDS-ADRDA criteria', *Lancet Neurology*, 6(8), pp. 734-746.
- Egerton, R.F. (2011) 'An Introduction to EELS', in *Electron Energy-Loss Spectroscopy in the Electron Microscope*. Springer US, pp. 1-28.
- Ehret, R., Baumann, W., Brischwein, M., Schwinde, A., Stegbauer, K. and Wolf, B. (1997) 'Monitoring of cellular behaviour by impedance measurements on interdigitated electrode structures', *Biosensors and Bioelectronics*, 12(1), pp. 29-41.

El-Brolossy, T.A., Abdallah, T., Mohamed, M.B., Abdallah, S., Easawi, K., Negm, S. and Talaat, H. (2008) 'Shape and size dependence of the surface plasmon resonance of gold nanoparticles studied by Photoacoustic technique', *European Physical Journal: Special Topics*, 153(1), pp. 361-364.

Ertekin-Taner, N., Younkin, L.H., Yager, D.M., Parfitt, F., Baker, M.C., Asthana, S., Hutton, M.L., Younkin, S.G. and Graff-Radford, N.R. (2008) 'Plasma amyloid  $\beta$  protein is elevated in late-onset Alzheimer disease families', *Neurology*, 70(8), pp. 596-606.

'Fundamentals of Diffraction', (2009) in *Fundamentals of Powder Diffraction and Structural Characterization of Materials*. Springer US, pp. 133-149.

German, N., Ramanaviciene, A., Voronovic, J. and Ramanavicius, A. (2010) 'Glucose biosensor based on graphite electrodes modified with glucose oxidase and colloidal gold nanoparticles', *Microchimica Acta*, 168(3), pp. 221-229.

Goldstein, J., Newbury, D., Echlin, P., Joy, D., Lyman, C., Lifshin, E., Sawyer, L. and Michael, J. (2003) 'The SEM and Its Modes of Operation', in *Scanning Electron Microscopy and X-ray Microanalysis*. Springer US, pp. 21-60.

Goon, I.Y., Lai, L.M.H., Lim, M., Munroe, P., Gooding, J.J. and Amal, R. (2009) 'Fabrication and dispersion of gold-shell-protected magnetite nanoparticles: Systematic control using polyethyleneimine', *Chemistry of Materials*, 21(4), pp. 673-681.

Goon, I.Y., Zhang, C., Lim, M., Gooding, J.J. and Amal, R. (2010) 'Controlled fabrication of polyethylenimine-functionalized magnetic nanoparticles for the sequestration and quantification of free  $\text{Cu}^{2+}$ ', *Langmuir*, 26(14), pp. 12247-12252.

Guo, Y., Zhang, Z., Kim, D.-H., Li, W., Nicolai, J., Procissi, D., Huan, Y., Han, G., Omary, R.A. and Larson, A.C. (2013) 'Photothermal ablation of pancreatic cancer cells with hybrid iron-oxide core gold-shell nanoparticles', *International Journal of Nanomedicine*, 8, pp. 3437-3446.

Gupta, A.K. and Gupta, M. (2005) 'Synthesis and surface engineering of iron oxide nanoparticles for biomedical applications', *Biomaterials*, 26(18), pp. 3995-4021.

Gupta, A.K., Naregalkar, R.R., Vaidya, V.D. and Gupta, M. (2007) 'Recent advances on surface engineering of magnetic iron oxide nanoparticles and their biomedical applications', *Nanomedicine*, 2(1), pp. 23-39.

- Haiss, W., Thanh, N.T.K., Aveyard, J. and Fernig, D.G. (2007) 'Determination of size and concentration of gold nanoparticles from UV-Vis spectra', *Analytical Chemistry*, 79(11), pp. 4215-4221.
- Hall, P.G., Clarke, N.S. and Maynard, S.C.P. (1995) 'Inelastic neutron scattering (TFXA) study of hydrogen modes in  $\alpha$ -FeOOH (goethite) and  $\gamma$ -FeOOH (lepidocrocite)', *Journal of Physical Chemistry*, 99(15), pp. 5666-5673.
- Hansson, O., Zetterberg, H., Buchhave, P., Londos, E., Blennow, K. and Minthon, L. (2006) 'Association between CSF biomarkers and incipient Alzheimer's disease in patients with mild cognitive impairment: A follow-up study', *Lancet Neurology*, 5(3), pp. 228-234.
- Hien Pham, T.T., Cao, C. and Sim, S.J. (2008) 'Application of citrate-stabilized gold-coated ferric oxide composite nanoparticles for biological separations', *Journal of Magnetism and Magnetic Materials*, 320(15), pp. 2049-2055.
- Hofmann, S. (2013) 'Qualitative Analysis (Principle and Spectral Interpretation)', in *Auger- and X-Ray Photoelectron Spectroscopy in Materials Science*. Springer Berlin Heidelberg, pp. 43-76.
- Hoskins, C., Min, Y., Gueorguieva, M., McDougall, C., Volovick, A., Prentice, P., Wang, Z., Melzer, A., Cuschieri, A. and Wang, L. (2012) 'Hybrid gold-iron oxide nanoparticles as a multifunctional platform for biomedical application', *Journal of Nanobiotechnology*, 10.
- Hou, Y., Xu, Z. and Sun, S. (2007) 'Controlled Synthesis and Chemical Conversions of FeO Nanoparticles', *Angewandte Chemie*, 119(33), pp. 6445-6448.
- Huang, X. and El-Sayed, M.A. (2010) 'Gold nanoparticles: Optical properties and implementations in cancer diagnosis and photothermal therapy', *Journal of Advanced Research*, 1(1), pp. 13-28.
- Hye, A., Lynham, S., Thambisetty, M., Causevic, M., Campbell, J., Byers, H.L., Hooper, C., Rijdsdijk, F., Tabrizi, S.J., Banner, S., Shaw, C.E., Foy, C., Poppe, M., Archer, N., Hamilton, G., Powell, J., Brown, R.G., Sham, P., Ward, M. and Lovestone, S. (2006) 'Proteome-based plasma biomarkers for Alzheimer's disease', *Brain*, 129(11), pp. 3042-3050.
- Ishigami, K., Tajima, T., Fujita, N., Nishie, A., Asayama, Y., Kakihara, D., Nakayama, T., Okamoto, D., Taketomi, A., Shirabe, K. and Honda, H. (2011) 'Hepatocellular

carcinoma with marginal superparamagnetic iron oxide uptake on T2\*-weighted magnetic resonance imaging: Histopathologic correlation', *European Journal of Radiology*, 80(3), pp. e293-e298.

Jaganathan, H. and Ivanisevic, A. (2011) 'Gold-iron oxide nanoparticle chains scaffolded on DNA as potential magnetic resonance imaging agents', *Journal of Materials Chemistry*, 21(4), pp. 939-943.

Jain, T.K., Richey, J., Strand, M., Leslie-Pelecky, D.L., Flask, C.A. and Labhasetwar, V. (2008) 'Magnetic nanoparticles with dual functional properties: Drug delivery and magnetic resonance imaging', *Biomaterials*, 29(29), pp. 4012-4021.

Jin, J., Yang, F., Zhang, F., Hu, W., Sun, S.-b. and Ma, J. (2012) '2, 2'-(phenylazanediy) diacetic acid modified Fe<sub>3</sub>O<sub>4</sub>@PEI for selective removal of cadmium ions from blood', *Nanoscale*, 4(3), pp. 733-736.

Jolivet, J.P., Chanéac, C. and Tronc, E. (2004) 'Iron oxide chemistry. From molecular clusters to extended solid networks', *Chemical Communications*, 10(5), pp. 481-487.

Ju, H., Zhang, X. and Wang, J. (2011) 'Nanomaterials for Immunosensors and Immunoassays', in *NanoBiosensing*. Springer New York, pp. 425-452.

Kasuga, K., Tokutake, T., Ishikawa, A., Uchiyama, T., Tokuda, T., Onodera, O., Nishizawa, M. and Ikeuchi, T. (2010) 'Differential levels of  $\alpha$ -synuclein,  $\beta$ -amyloid42 and tau in CSF between patients with dementia with Lewy bodies and Alzheimer's disease', *Journal of Neurology, Neurosurgery and Psychiatry*, 81(6), pp. 608-610.

Kaushik, A., Khan, R., Solanki, P.R., Pandey, P., Alam, J., Ahmad, S. and Malhotra, B.D. (2008) 'Iron oxide nanoparticles-chitosan composite based glucose biosensor', *Biosensors and Bioelectronics*, 24(4), pp. 676-683.

Kim, D., Kim, J.W., Jeong, Y.Y. and Jon, S. (2009) 'Antibiofouling Polymer Coated Gold@Iron Oxide Nanoparticle (GION) as a Dual Contrast Agent for CT and MRI', *Bulletin of the Korean Chemical Society*, 30(8), pp. 1855-1857.

Kim, D.K., Mikhaylova, M., Zhang, Y. and Muhammed, M. (2003) 'Protective coating of superparamagnetic iron oxide nanoparticles', *Chemistry of Materials*, 15(8), pp. 1617-1627.

Kimling, J., Maier, M., Okenve, B., Kotaidis, V., Ballot, H. and Plech, A. (2006) 'Turkevich method for gold nanoparticle synthesis revisited', *Journal of Physical Chemistry B*, 110(32), pp. 15700-15707.

- Kobayashi, T. (2011) 'Cancer hyperthermia using magnetic nanoparticles', *Biotechnology Journal*, 6(11), pp. 1342-1347.
- Kreyling, W.G., Semmler-Behnke, M. and Chaudhry, Q. (2010) 'A complementary definition of nanomaterial', *Nano Today*, 5(3), pp. 165-168.
- Kumagai, Izumi, and Tsumoto, Kouhei (Apr 2010) 'Antigen–Antibody Binding'. In: *eLS*. John Wiley & Sons Ltd, Chichester. <http://www.els.net> [doi: 10.1002/9780470015902.a0001117.pub2]
- Laurent, S., Forge, D., Port, M., Roch, A., Robic, C., Vander Elst, L. and Muller, R.N. (2008) 'Magnetic iron oxide nanoparticles: Synthesis, stabilization, vectorization, physicochemical characterizations and biological applications', *Chemical Reviews*, 108(6), pp. 2064-2110.
- Lee, E.S., Lim, C., Song, H.T., Yun, J.M., Lee, K.S., Lee, B.J., Youn, Y.S., Oh, Y.T. and Oh, K.T. (2012) 'A nanosized delivery system of superparamagnetic iron oxide for tumor MR imaging', *International Journal of Pharmaceutics*, 439(1-2), pp. 342-348.
- Lee, J.E., Seo, J.H., Kim, C.S., Kwon, Y., Ha, J.H., Choi, S.S. and Cha, H.J. (2013) 'A comparative study on antibody immobilization strategies onto solid surface', *Korean Journal of Chemical Engineering*, 30(10), pp. 1934-1938.
- Li, C., Li, D., Wan, G., Xu, J. and Hou, W. (2011a) 'Facile synthesis of concentrated gold nanoparticles with low size-distribution in water: Temperature and pH controls', *Nanoscale Research Letters*, 6, pp. 1-10.
- Li, J., Yuan, R. and Chai, Y. (2011b) 'Simple construction of an enzymatic glucose biosensor based on a nanocomposite film prepared in one step from iron oxide, gold nanoparticles, and chitosan', *Microchimica Acta*, 173(3-4), pp. 369-374.
- Li, K., Lai, Y., Zhang, W. and Jin, L. (2011c) 'Fe<sub>2</sub>O<sub>3</sub>@Au core/shell nanoparticle-based electrochemical DNA biosensor for Escherichia coli detection', *Talanta*, 84(3), pp. 607-613.
- Liang, C.-H., Wang, C.-C., Lin, Y.-C., Chen, C.-H., Wong, C.-H. and Wu, C.-Y. (2009) 'Iron Oxide/Gold Core/Shell Nanoparticles for Ultrasensitive Detection of Carbohydrate-Protein Interactions', *Analytical Chemistry*, 81(18), pp. 7750-7756.
- Lindholm, B. (1990) 'Ac-impedance studies of charge transport and redox capacities at poly-4-vinylpyridine films on electrode surfaces', *Journal of Electroanalytical Chemistry and Interfacial Electrochemistry*, 289(1–2), pp. 85-101.

- Loaiza, T.A., Jubete, E., Ochoteco, E., Cabañero, G., Grande, H. and Rodríguez, J. (2011) 'Gold coated ferric oxide nanoparticles based disposable magnetic genosensors for the detection of DNA hybridization processes', *Biosensors and Bioelectronics*, 26(5), pp. 2194-2200.
- Luo, X., Morrin, A., Killard, A.J. and Smyth, M.R. (2006) 'Application of nanoparticles in electrochemical sensors and biosensors', *Electroanalysis*, 18(4), pp. 319-326.
- Luppa, P.B., Sokoll, L.J. and Chan, D.W. (2001) 'Immunosensors - Principles and applications to clinical chemistry', *Clinica Chimica Acta*, 314(1-2), pp. 1-26.
- Lyon, J.L., Fleming, D.A., Stone, M.B., Schiffer, P. and Williams, M.E. (2004) 'Synthesis of Fe oxide Core/Au shell nanoparticles by iterative hydroxylamine seeding', *Nano Letters*, 4(4), pp. 719-723.
- Ma, M., Zhang, Y., Guo, Z. and Gu, N. (2013) 'Facile synthesis of ultrathin magnetic iron oxide nanoplates by Schikorr reaction', *Nanoscale Research Letters*, 8(1), pp. 1-7.
- Maketon, W. and Ogden, K.L. (2009) 'Synergistic effects of citric acid and polyethyleneimine to remove copper from aqueous solutions', *Chemosphere*, 75(2), pp. 206-211.
- Marcu, A., Pop, S., Dumitrache, F., Mocanu, M., Niculite, C.M., Gherghiceanu, M., Lungu, C.P., Fleaca, C., Ianchis, R., Barbut, A., Grigoriu, C. and Morjan, I. (2013) 'Magnetic iron oxide nanoparticles as drug delivery system in breast cancer', *Applied Surface Science*, 281, pp. 60-65.
- Martin, C., Penner, R. and Dyke, L. (1989) 'Electrochemical Investigation of Electronically Conductive Polymers', in Bergbreiter, D. and Martin, C. (eds.) *Functional Polymers*. Springer US, pp. 119-139.
- Martin, M.N., Basham, J.I., Chando, P. and Eah, S.K. (2010) 'Charged gold nanoparticles in non-polar solvents: 10-min synthesis and 2D self-assembly', *Langmuir*, 26(10), pp. 7410-7417.
- McKhann, G.M., Knopman, D.S., Chertkow, H., Hyman, B.T., Jack Jr, C.R., Kawas, C.H., Klunk, W.E., Koroshetz, W.J., Manly, J.J., Mayeux, R., Mohs, R.C., Morris, J.C., Rossor, M.N., Scheltens, P., Carrillo, M.C., Thies, B., Weintraub, S. and Phelps, C.H. (2011) 'The diagnosis of dementia due to Alzheimer's disease: Recommendations from the National Institute on Aging-Alzheimer's Association workgroups on diagnostic guidelines for Alzheimer's disease', *Alzheimer's and Dementia*, 7(3), pp. 263-269.

- Menichetti, L., Manzoni, L., Paduano, L., Flori, A., Kusmic, C., De Marchi, D., Casciaro, S., Conversano, F., Lombardi, M., Positano, V. and Arosio, D. (2013) 'Iron oxide-gold core-shell nanoparticles as multimodal imaging contrast agent', *IEEE Sensors Journal*, 13(6), pp. 2341-2347.
- Mills, P. and Sullivan, J.L. (1983) 'A study of the core level electrons in iron and its three oxides by means of X-ray photoelectron spectroscopy', *Journal of Physics D: Applied Physics*, 16(5), pp. 723-732.
- Mohanty, S.P. and Koucianos, E. (2006) 'Biosensors: A tutorial review', *IEEE Potentials*, 25(2), pp. 35-40.
- Mohanty, U.S. (2011) 'Electrodeposition: A versatile and inexpensive tool for the synthesis of nanoparticles, nanorods, nanowires, and nanoclusters of metals', *Journal of Applied Electrochemistry*, 41(3), pp. 257-270.
- Morgan, C.L., Newman, D.J. and Price, C.P. (1996) 'Immunosensors: Technology and opportunities in laboratory medicine', *Clinical Chemistry*, 42(2), pp. 193-209.
- Mukaetova-Ladinska, E.B., Abdel-All, Z., Andrade, J., McNally, R.J.Q., James, P.W., Kalaria, R.N. and O'Brien, J.T. (2012) 'Increase in Platelet Immunoglobulin in Alzheimer's Disease is Normalised Following Cholinesterase Inhibitor Treatment: Preliminary Results', *Journal of Alzheimer's Disease*, 32(2), pp. 431-436.
- Mulder, C., Verwey, N.A., Van Der Flier, W.M., Bouwman, F.H., Kok, A., Van Elk, E.J., Scheltens, P. and Blankenstein, M.A. (2010) 'Amyloid- $\beta$ (1-42), total tau, and phosphorylated tau as cerebrospinal fluid biomarkers for the diagnosis of Alzheimer disease', *Clinical Chemistry*, 56(2), pp. 248-253.
- Mürbe, J., Rechtenbach, A. and Töpfer, J. (2008) 'Synthesis and physical characterization of magnetite nanoparticles for biomedical applications', *Materials Chemistry and Physics*, 110(2-3), pp. 426-433.
- Nasibulin, A., Rackauskas, S., Jiang, H., Tian, Y., Mudimela, P., Shandakov, S., Nasibulina, L., Jani, S. and Kauppinen, E. (2009) 'Simple and rapid synthesis of  $\alpha$ -Fe<sub>2</sub>O<sub>3</sub> nanowires under ambient conditions', *Nano Research*, 2(5), pp. 373-379.
- Nguyen, D.T., Kim, D.J., So, M.G. and Kim, K.S. (2010) 'Experimental measurements of gold nanoparticle nucleation and growth by citrate reduction of H<sub>2</sub>AuCl<sub>4</sub>', *Advanced Powder Technology*, 21(2), pp. 111-118.

Omidirad, R., Rajabi, F.H. and Farahani, B.V. (2013) 'Preparation and in vitro drug delivery response of doxorubicinloaded poly(acrylic acid)-coated magnetite nanoparticles', *Journal of the Serbian Chemical Society*, 78(10), pp. 1609-1616.

Perrault, S.D. and Chan, W.C.W. (2009) 'Synthesis and surface modification of highly monodispersed, spherical gold nanoparticles of 50-200 nm', *Journal of the American Chemical Society*, 131(47), pp. 17042-17043.

'Powder Diffractometry', (2009) in *Fundamentals of Powder Diffraction and Structural Characterization of Materials*. Springer US, pp. 263-300.

Qian, J.M., Suo, A.L., Yao, Y. and Jin, Z.H. (2004) 'Polyelectrolyte-stabilized glucose biosensor based on woodceramics as electrode', *Clinical Biochemistry*, 37(2), pp. 155-161.

Rahman, M.A., Shiddiky, M.J.A., Park, J.S. and Shim, Y.B. (2007) 'An impedimetric immunosensor for the label-free detection of bisphenol A', *Biosensors and Bioelectronics*, 22(11), pp. 2464-2470.

Rebodos, R.L. and Vikesland, P.J. (2010) 'Effects of oxidation on the magnetization of nanoparticulate magnetite', *Langmuir*, 26(22), pp. 16745-16753.

Rico, Y., Bidegain, J.C. and Elsner, C.I. (2009) 'Synthetic and natural Iron oxide characterization through microparticle voltammetry', *Geofisica Internacional*, 48(2), pp. 221-236.

Ris, F., Lepetit-Coiffe, M., Meda, P., Crowe, L.A., Toso, C., Armanet, M., Niclauss, N., Parnaud, G., Giovannoni, L., Bosco, D., Morel, P., Vallee, J.P. and Berney, T. (2010) 'Assessment of human islet labeling with clinical grade iron nanoparticles prior to transplantation for graft monitoring by MRI', *Cell Transplantation*, 19(12), pp. 1573-1585.

Rodger, A. (2013) 'Beer-Lambert Law Derivation', in Roberts, G.K. (ed.) *Encyclopedia of Biophysics*. Springer Berlin Heidelberg, pp. 184-185.

Rodríguez Nieto, F.J., Fachini, E., Cabrera, C.R. and Arvia, A.J. (2009) 'X-ray photoelectron spectroscopy of oxygen-containing layers formed by a linear potential scan on stepped gold (111) films in aqueous 1 M sulphuric acid', *Thin Solid Films*, 517(5), pp. 1534-1540.

Sakai, T. and Alexandridis, P. (2005) 'Mechanism of gold metal ion reduction, nanoparticle growth and size control in aqueous amphiphilic block copolymer solutions at ambient conditions', *Journal of Physical Chemistry B*, 109(16), pp. 7766-7777.

Salazar-Alvarez, G., Muhammed, M. and Zagorodni, A.A. (2006) 'Novel flow injection synthesis of iron oxide nanoparticles with narrow size distribution', *Chemical Engineering Science*, 61(14), pp. 4625-4633.

Saxena, U., Chakraborty, M. and Goswami, P. (2011) 'Covalent immobilization of cholesterol oxidase on self-assembled gold nanoparticles for highly sensitive amperometric detection of cholesterol in real samples', *Biosensors and Bioelectronics*, 26(6), pp. 3037-3043.

Scheuner, D., Eckman, C., Jensen, M., Song, X., Citron, M., Suzuki, N., Bird, T.D., Hardy, J., Hutton, M., Kukull, W., Larson, E., Levy-Lahad, E., Viitanen, M., Peskind, E., Poorkaj, P., Schellenberg, G., Tanzi, R., Wasco, W., Lannfelt, L., Selkoe, D. and Younkin, S. (1996) 'Secreted amyloid  $\beta$ -protein similar to that in the senile plaques of Alzheimer's disease is increased in vivo by the presenilin 1 and 2 and APP mutations linked to familial Alzheimer's disease', *Nature Medicine*, 2(8), pp. 864-870.

Scholz, F. (2010) 'Thermodynamics of Electrochemical Reactions', in Scholz, F. (ed.) *Electroanalytical Methods*. Springer Berlin Heidelberg, pp. 11-31.

Sharma, A., Matharu, Z., Sumana, G., Solanki, P.R., Kim, C.G. and Malhotra, B.D. (2010) 'Antibody immobilized cysteamine functionalized-gold nanoparticles for aflatoxin detection', *Thin Solid Films*, 519(3), pp. 1213-1218.

Sharma, G. and Jeevanandam, P. (2013) 'Synthesis of self-assembled prismatic iron oxide nanoparticles by a novel thermal decomposition route', *RSC Advances*, 3(1), pp. 189-200.

Silva, A.C., Oliveira, T.R., Mamani, J.B., Malheiros, S.M., Malavolta, L., Pavon, L.F., Sibov, T.T., Amaro Jr, E., Tannús, A., Vidoto, E.L., Martins, M.J., Santos, R.S. and Gamarra, L.F. (2011) 'Application of hyperthermia induced by superparamagnetic iron oxide nanoparticles in glioma treatment', *International journal of nanomedicine*, 6, pp. 591-603.

Snow, C.L., Smith, S.J., Lang, B.E., Shi, Q., Boerio-Goates, J., Woodfield, B.F. and Navrotsky, A. (2011) 'Heat capacity studies of the iron oxyhydroxides akaganéite ( $\beta$ -

FeOOH) and lepidocrocite ( $\gamma$ -FeOOH)', *Journal of Chemical Thermodynamics*, 43(2), pp. 190-199.

Stojek, Z. (2010) 'The Electrical Double Layer and Its Structure', in Scholz, F. (ed.) *Electroanalytical Methods*. Springer Berlin Heidelberg, pp. 3-9.

Sugimoto, T. and Matijević, E. (1980) 'Formation of uniform spherical magnetite particles by crystallization from ferrous hydroxide gels', *Journal of Colloid and Interface Science*, 74(1), pp. 227-243.

Sun, X., Du, S., Wang, X., Zhao, W. and Li, Q. (2011) 'A label-free electrochemical immunosensor for carbofuran detection based on a sol-gel entrapped antibody', *Sensors*, 11(10), pp. 9520-9531.

Sunderland, T., Gur, R.E. and Arnold, S.E. (2005) 'The use of biomarkers in the elderly: Current and future challenges', *Biological Psychiatry*, 58(4), pp. 272-276.

Suslick, K.S. (1990) 'Sonochemistry', *Science*, 247(4949), pp. 1439-1445.

Tamer, U., Cetin, D., Suludere, Z., Boyaci, I.H., Temiz, H.T., Yegenoglu, H., Daniel, P., Dinçer, I. and Elerman, Y. (2013) 'Gold-coated iron composite nanospheres targeted the detection of Escherichia coli', *International Journal of Molecular Sciences*, 14(3), pp. 6223-6240.

Tan, S., Erol, M., Attygalle, A., Du, H. and Sukhishvili, S. (2007) 'Synthesis of positively charged silver nanoparticles via photoreduction of AgNO<sub>3</sub> in branched polyethyleneimine/HEPES solutions', *Langmuir*, 23(19), pp. 9836-9843.

Teja, A.S. and Koh, P.Y. (2009) 'Synthesis, properties, and applications of magnetic iron oxide nanoparticles', *Progress in Crystal Growth and Characterization of Materials*, 55(1-2), pp. 22-45.

van Oijen, M., Hofman, A., Soares, H.D., Koudstaal, P.J. and Breteler, M.M. (2006) 'Plasma A $\beta$ 1-40 and A $\beta$ 1-42 and the risk of dementia: a prospective case-cohort study', *Lancet Neurology*, 5(8), pp. 655-660.

Vergés, M.A., Costo, R., Roca, A.G., Marco, J.F., Goya, G.F., Serna, C.J. and Morales, M.P. (2008) 'Uniform and water stable magnetite nanoparticles with diameters around the monodomain-multidomain limit', *Journal of Physics D: Applied Physics*, 41(13).

Vidal-Vidal, J., Rivas, J. and López-Quintela, M.A. (2006) 'Synthesis of monodisperse maghemite nanoparticles by the microemulsion method', *Colloids and Surfaces A: Physicochemical and Engineering Aspects*, 288(1-3), pp. 44-51.

- Wang, W., Ying, S., Zhang, Z. and Huang, S. (2011) 'Novel glucose biosensor based on a glassy carbon electrode modified with hollow gold nanoparticles and glucose oxidase', *Microchimica Acta*, pp. 1-6.
- Wang, X., Zhou, L., Ma, Y., Li, X. and Gu, H. (2009) 'Control of aggregate size of polyethyleneimine-coated magnetic nanoparticles for magnetofection', *Nano Research*, 2(5), pp. 365-372.
- Welch, C.M. and Compton, R.G. (2006) 'The use of nanoparticles in electroanalysis: A review', *Analytical and Bioanalytical Chemistry*, 384(3), pp. 601-619.
- Williams, D. and Carter, C.B. (2009a) 'Lenses, Apertures, and Resolution', in *Transmission Electron Microscopy*. Springer US, pp. 91-114.
- Williams, D. and Carter, C.B. (2009b) 'The Transmission Electron Microscope', in *Transmission Electron Microscopy*. Springer US, pp. 3-22.
- Wu, Y., Zhang, T., Zheng, Z., Ding, X. and Peng, Y. (2010) 'A facile approach to Fe<sub>3</sub>O<sub>4</sub>@Au nanoparticles with magnetic recyclable catalytic properties', *Materials Research Bulletin*, 45(4), pp. 513-517.
- Yamashita, T. and Hayes, P. (2008) 'Analysis of XPS spectra of Fe<sup>2+</sup> and Fe<sup>3+</sup> ions in oxide materials', *Applied Surface Science*, 254(8), pp. 2441-2449.
- Yang, Y., Yang, G., Huang, Y., Bai, H. and Lu, X. (2009) 'A new hydrogen peroxide biosensor based on gold nanoelectrode ensembles/multiwalled carbon nanotubes/chitosan film-modified electrode', *Colloids and Surfaces A: Physicochemical and Engineering Aspects*, 340(1-3), pp. 50-55.
- Yates, P.C. (2000) 'Use of a world wide web site evaluation tool in chemistry', *Journal of Science Education and Technology*, 9(4), pp. 357-365.
- Yeu, T., Yin, K.-M., Carbajal, J. and White, R.E. (1991) 'Electrochemical characterization of electronically conductive polypyrrole on cyclic voltammograms', *Journal of the Electrochemical Society*, 138(10), pp. 2868-2877.
- Yiu, H.H.P., Pickard, M.R., Olariu, C.I., Williams, S.R., Chari, D.M. and Rosseinsky, M.J. (2012) 'Fe<sub>3</sub>O<sub>4</sub>-PEI-RITC Magnetic Nanoparticles with Imaging and Gene Transfer Capability: Development of a Tool for Neural Cell Transplantation Therapies', *Pharmaceutical Research*, 29(5), pp. 1328-1343.

- Yocum, A.K., Yu, K., Oe, T. and Blair, I.A. (2005) 'Effect of immunoaffinity depletion of human serum during proteomic investigations', *Journal of Proteome Research*, 4(5), pp. 1722-1731.
- Yoo, M.K., Park, I.K., Lim, H.T., Lee, S.J., Jiang, H.L., Kim, Y.K., Choi, Y.J., Cho, M.H. and Cho, C.S. (2012) 'Folate-PEG-superparamagnetic iron oxide nanoparticles for lung cancer imaging', *Acta Biomaterialia*, 8(8), pp. 3005-3013.
- Zhang, D., Sun, P., Li, P., Xue, A., Zhang, X., Zhang, H. and Jin, X. (2013) 'A magnetic chitosan hydrogel for sustained and prolonged delivery of Bacillus Calmette-Guérin in the treatment of bladder cancer', *Biomaterials*, 34(38), pp. 10258-10266.
- Zhang, J., Du, J., Han, B., Liu, Z., Jiang, T. and Zhang, Z. (2006) 'Sonochemical formation of single-crystalline gold nanobelts', *Angewandte Chemie - International Edition*, 45(7), pp. 1116-1119.
- Zhang, X., Jiang, W., Gong, X. and Zhang, Z. (2010) 'Sonochemical synthesis and characterization of magnetic separable Fe<sub>3</sub>O<sub>4</sub>/Ag composites and its catalytic properties', *Journal of Alloys and Compounds*, 508(2), pp. 400-405.
- Zhou, X., Xu, W., Wang, Y., Kuang, Q., Shi, Y., Zhong, L. and Zhang, Q. (2010) 'Fabrication of Cluster/Shell Fe<sub>3</sub>O<sub>4</sub>/Au Nanoparticles and Application in Protein Detection via a SERS Method', *Journal of Physical Chemistry C*, 114(46), pp. 19607-19613.
- Zolotarjova, N., Martosella, J., Nicol, G., Bailey, J., Boyes, B.E. and Barrett, W.C. (2005) 'Differences among techniques for high-abundant protein depletion', *Proteomics*, 5(13), pp. 3304-3313.
- Zou, P., Yu, Y., Wang, Y.A., Zhong, Y., Welton, A., Galbán, C., Wang, S. and Sun, D. (2010) 'Superparamagnetic iron oxide nanotheranostics for targeted cancer cell imaging and pH-dependent intracellular drug release', *Molecular Pharmaceutics*, 7(6), pp. 1974-1984.

## Chapter 7-Appendices

### 7.1 List of publications and presentations

#### 7.1.1 Publications

Ketebu, O., Yu, E., and Cumpson, P. (2014) ' The Effect of Temperature and Agitation on Polyethyleneimine Adsorption on Iron Oxide Magnetic Nanoparticles in the Synthesis of Iron Oxide-Au Core-Shell Nanoparticles' *Journal of Advance Science, Engineering and Medicine*, 6(5), pp. 531-537.

## The Effect of Temperature and Agitation on Polyethyleneimine Adsorption on Iron Oxide Magnetic Nanoparticles in the Synthesis of Iron Oxide-Au Core-Shell Nanoparticles

Orlando Ketebu<sup>1</sup>, Peter Cumpson<sup>2</sup>, and Eileen Yu<sup>1,\*</sup>

<sup>1</sup>School of Chemical Engineering and Advance Materials, Newcastle University, Newcastle Upon Tyne, NE1 7RU, United Kingdom

<sup>2</sup>Schools of Mechanical Engineering, Newcastle University, Newcastle Upon Tyne, NE1 7RU, United Kingdom

Iron oxide nanoparticles play important role in fields such magnetic fluids, data storage, catalysis and biomedical applications. This is attributed to their unique properties and their ability to be controlled with an external magnet and directed towards specific targets for analysis. This paper looks into the effect of different heating temperatures on polyethyleneimine (PEI) adsorption in the formation of PEI/iron oxide (Fe<sub>2</sub>O<sub>3</sub>-PEI) nanoparticles and the effect of temperature on the capping capabilities of PEI in the formation iron oxide core/gold shell nanoparticles. Cyclic voltammetry (CV) and electrochemical impedance spectroscopy (EIS) were used in the analysis of the effect of PEI adsorption on the Fe<sub>2</sub>O<sub>3</sub>-PEI nanoparticles by measuring change in charge transfer resistance of the particles. The result showed that 40 °C is most favourable for PEI adsorption on iron oxide nanoparticles average particles size 50 nm and also favours capping in the formation of iron oxide core/gold shell nanoparticles. The electrochemical impedance spectroscopy analysis also showed that 40 °C had the least charge transfer ( $R_{ct}$ ) resistance of 38 Ω followed by 25 °C (76 Ω) and highest at 100 °C ( $R_{ct}$  = 207 Ω) due to PEI lost its polycationic nature with increasing temperature. The UV-VIS spectra for Fe<sub>2</sub>O<sub>3</sub>-Au shell nanoparticles formed showed further blue shift of the surface plasmon resonance to 548 nm at 40 °C indicating increased gold shell formation on the nanoparticles. Effect of agitation in synthesis of Fe<sub>2</sub>O<sub>3</sub>/PEI nanoparticles was studied at room temperature (25 °C) with stirring and non-stirring. It showed that stirring increased PEI adsorption on iron oxide nanoparticles.

**KEYWORDS:** Iron Oxide Nanoparticles, Polyethyleneimine, Temperature, Cyclic Voltammetry (CV), Electrochemical Impedance Spectroscopy (EIS), UV-VIS Spectroscopy.

### 1. INTRODUCTION

Iron oxide nanoparticles are iron oxide particles with nanometer diameters (1–100 nm) and they exist in two major forms magnetite (Fe<sub>3</sub>O<sub>4</sub>) also known as triiron-tetraoxide and maghemite (γ-Fe<sub>2</sub>O<sub>3</sub>) which is the oxidized form of magnetite. Magnetite contains both iron II ions (Fe<sup>II</sup>) and iron III ions (Fe<sup>III</sup>) in an inverse cubic spinel structure with the Fe<sup>II</sup> ions in the octahedral site and half Fe<sup>III</sup> ions in octahedral and half in tetrahedral site. Maghemite contains only iron III ions with three quarter of the Fe<sup>3+</sup> cation in the octahedral site and the other quarter is in the tetrahedral site.<sup>1,2</sup> The stoichiometric ratio of

Fe<sup>2+</sup> and Fe<sup>3+</sup> cation in magnetite is 1:2 and its completely oxidized form (maghemite) is zero (Fe<sup>2+</sup>/Fe<sup>3+</sup> = 0).<sup>3</sup> Magnetite and maghemite have nearly identical lattice parameters ( $a = 0.840$  and  $a = 0.835$ ) respectively which also explains their similarities in structures and properties.<sup>4</sup> They are of interest in magnetic fluids, data storage, catalysis and bio-applications fields. They are called magnetic nanoparticles because they can easily be controlled with an external magnet and directed towards specific targets for analysis.

Iron oxide nanoparticles are cost effective and possesses unique properties such chemical stability, biocompatibility, non-toxicity, effective specific power absorption rate and ability to be chemically functionalized and stable in solution of physiological pH. These properties coupled with their strong magnetic properties, high separation

\*Author to whom correspondence should be addressed.  
Email: eileen.yu@ncl.ac.uk  
Received: 30 July 2013  
Accepted: 12 October 2013

efficiency, and high specific surface area makes them useful in biomedical applications such as, drug delivery, hyperthermia, cell separation etc., and the fabrication of DNA and protein biosensors.<sup>5-9</sup>

Magnetic particles are known to be isoelectric at a pH of 7, indicating that they are only stable at high or low pH values thus requiring surface modification through the use of organic or inorganic stabilizers. Organic stabilizers (natural or synthetic) such as dextran, starch, gelatin, chitosan, poly(ethyleneglycol) (PEG), poly(vinyl alcohol) (PVA), poly(lactide acid) (PLA), alginate, polymethylmethacrylate (PMMA), polyacrylic acid (PAA), and inorganic stabilizers (silica, metal, non-metal, metal oxides and sulphides) have been used to functionalized iron oxide nanoparticles. Among the synthetic organic stabilizers used in functionalizing iron oxide nanoparticles, polyethyleneimine (PEI) is known to be effective in stabilizing and preventing aggregation of iron oxide nanoparticles. In solution during synthesis of iron oxide nanoparticles the negatively charged iron oxide nanoparticles binds electrostatically with the positively charge PEI to form a stabilizing polyelectrolyte layer. This enhances the iron oxide stability due to the steric hindrance and electrostatic repulsion between the iron oxide nanoparticles as a result of PEI coatings.<sup>3, 10, 11</sup>

Polyethyleneimine forms stable complex with metal ions at pH 4–12 due to the high amount of amine-nitrogen it contains that can donate electrons and chelate metal ions.<sup>12</sup> The presence of the amine groups also allow for the easy modification of polyethyleneimine to act as coating on inorganic materials, carriers for enzymes immobilization and the neutralization of excess anionic colloidal charges mostly found in acidic and neutral pH conditions. PEI exist in two forms, linear and the branched forms, the branched PEI being a polycation with 25% primary, 50% secondary and 25% tertiary amino groups. It is a liquid at room temperature with melting and boiling points of 59–60 °C and 250 °C respectively and is normally synthesized from its monomer (linear polyethyleneimine which has two methyl groups and a secondary amine group) in the presence of a catalyst.

Goon and co-workers<sup>3</sup> studied the adsorption of PEI on iron oxide nanoparticles ( $\text{Fe}_3\text{O}_4$ ) by varying PEI concentration from 0–50 mg/l at 80 °C. The result showed that increased PEI concentration, increases the amount of PEI adsorbed on the surface of iron oxide nanoparticles due to the greater number of PEI chains present and it also increases the electrophoretic mobility of the particles. The nanoparticles were found to be most stabilized at 50 mg/l and lower or higher concentrations of PEI results in nanoparticle aggregation. They also found in a separate experiment by varying PEI concentration from 0–4  $\text{gl}^{-1}$  at 60 °C that the maximum amount of PEI adsorbed on iron oxide nanoparticles (50 nm) and gold seeded iron oxide nanoparticles was 0.88  $\mu\text{g}$  PEI per  $\text{cm}^3$  particles surface by measuring the solution

organic carbon content since PEI is the only source of carbon.<sup>11</sup>

Zhou and co-workers stabilized and coat iron oxide nanoparticles (40 nm) with gold shell using 5  $\text{gl}^{-1}$  PEI at 60 °C for protein detection<sup>10</sup> although the molecular weight of the PEI used depends on the size of the nanoparticles. Wang et al. controlled the aggregation of iron oxide nanoparticles by agitating the nanoparticles at room temperature with different amount of 5% (m/m) PEI solution.<sup>13</sup> Jinjun and co-workers coated iron oxide nanoparticles with PEI by stirring the nanoparticles with PEI at room temperature for the selective removal of cadmium ion from blood.<sup>14</sup> Also Yiu et al. coated iron oxide nanoparticles with PEI by heating the nanoparticles with PEI at 130 °C for possible neutral cell transplantation therapies.<sup>15</sup>

PEI was used to improve the stability and sensitivity of glucose biosensor up to 200% by reacting PEI and glucose oxidase at room temperature.<sup>16</sup> The result showed that the response of the glucose biosensor increases as PEI concentration increases up to 2.5% (w/v) PEI before decreasing. The biosensor stability was dramatically increased with reduced detection limit due to PEI ability to prevent the oxidation of the enzyme's sulfidic groups.

Although many studies have been carried out on iron oxide magnetic nanoparticles synthesis, there have not been systematic studies on heating temperature for PEI coating. Temperature is a crucial factor for the amount of PEI adsorption on nanoparticle surface and therefore will affect the stability and capping effect of PEI in further gold coating process when preparing gold shell iron oxide core magnetic nanoparticles. The more PEI adsorbed on the surface of the iron oxide nanoparticles, the higher the electrostatic attachment of gold shell nanoparticles which in turn improves the electron transfer properties of the nanoparticles when used for biosensor fabrication.

In this study the effect of different heating temperatures (25 °C, 40 °C, 60 °C, 80 °C and 100 °C) on polyethyleneimine adsorption on magnetic iron oxide nanoparticles was conducted using electrochemical techniques. Comparisons between different temperatures were based on cyclic voltammetry (CV) and electrochemical impedance spectroscopy (EIS). It demonstrates a simple electrochemical method on characterization of the effect of temperature and PEI adsorption in nanoparticles synthesis. UV-Spectroscopy analysis was used to determine the capping effect of PEI at the different temperatures in the formation of iron oxide/gold shell nanoparticles.

## 2. EXPERIMENTAL DETAILS

### 2.1. Materials and Chemicals

Polyethyleneimine (branched 25000 mw), iron II sulphate heptahydrate > 99%, Chitosan powder (deacetylated chitin) were purchased from Sigma Aldrich, sodium

hydroxide 97%, tetramethylammonium hydroxide pentahydrate (TMAOH) and potassium nitrate 99% were from Alfa Aesar. All chemicals were used as received without further purification. Solutions prepared using Millipore deionised water.

## 2.2. Synthesis of Iron Oxide Nanoparticles (Fe<sub>2</sub>O<sub>3</sub>/PEI)

Magnetite (Fe<sub>3</sub>O<sub>4</sub>) was first synthesized following a method by Goon and co-workers<sup>3</sup> and then oxidized to Maghemite ( $\gamma$ -Fe<sub>2</sub>O<sub>3</sub>). Briefly Fe<sub>3</sub>O<sub>4</sub> nanoparticles were separated with the external magnet from 2.4 gl<sup>-1</sup> Fe<sub>3</sub>O<sub>4</sub> solution pH 7.0 and the precipitate washed with 250 ml of 0.01 M HNO<sub>3</sub>. The precipitate was dispersed in 250 ml 0.01 M HNO<sub>3</sub> and heated at 90–100 °C until the solution colour turned to brown.<sup>5</sup> The oxidized nanoparticles were separated with magnet and washed twice with deionised water and dispersed in 250 ml tetramethylammonium hydroxide (TMAOH). Then 5 ml of TMAOH stabilized Fe<sub>2</sub>O<sub>3</sub> nanoparticles were stirred for 30 minutes in 50 ml of 5 gl<sup>-1</sup> PEI to exchange absorbed OH<sup>-</sup> ions with PEI ions and separated with an external magnet. The particles were rinsed to pH 7 with deionised water and dispersed in 50 ml of 5 gl<sup>-1</sup> PEI by sonicating for 3 minutes. For 25 °C synthesis, the particles were allowed to stabilize for 1 hour without stirring and the others were heated for 1 hour at 40 °C, 60 °C, 80 °C and 100 °C respectively.

## 2.3. Preparation of Iron Oxide Modified Electrodes

Iron oxide/polyethyleneimine modified glassy carbon electrodes (GC-Fe<sub>2</sub>O<sub>3</sub>-PEI-CHIT) were prepared by adding 1 ml of iron oxide/PEI nanoparticles synthesized in section 2.2 in 2 ml 0.2 wt.% chitosan (CHIT) solution and sonicated for 3 minutes. 10  $\mu$ l of the mixture was pipetted on a clean glassy carbon electrode and allowed to dry in air. This process was done for iron oxide/PEI nanoparticles synthesized at different temperatures.

## 2.4. Characterization of the Iron Oxide/PEI Nanoparticles

### 2.4.1. Physical Characterization

A Philips XL 30 Electronic scanning electron microscopy (ESEM) operated at 20 kV for both ESEM and energy dispersive X-ray (EDX) were used to determine the surface morphology and elemental composition of the iron oxide nanoparticles. The nature and core electrons of the Fe<sub>2</sub>O<sub>3</sub> nanoparticles were obtained by X-ray photoelectron spectroscopy (XPS) with Thermo Scientific K- $\alpha$  monochromated small spot X-ray Photoelectron Spectrometer system and transmission electron microscopy analysis (TEM) was carried out with Philips CM200 FEGTEM field emission gun TEM/STEM with supertwin objective lens. UV-VIS spectroscopy analysis was carried out with Jenway 6705 model UV-VIS Spectrometer.

### 2.4.2. Electrochemical Characterization

Electrochemical characterizations of the nanoparticles electrode were carried out by Ecochemie BV PGSTAT 302 Autolab (Netherland) using cyclic voltammetry (CV) and electrochemical impedance spectroscopy (EIS). The CV was obtained in 0.1 M phosphate buffer (pH 7) containing 5 mM ferrocyanide/ferricyanide [Fe(CN)<sub>6</sub>]<sup>4-/3-</sup> at a scan rate of 50 mV/s. EIS analysis was carried out in 0.1 M phosphate buffer (pH 7) containing 5 mM ferrocyanide/ferricyanide [Fe(CN)<sub>6</sub>]<sup>4-/3-</sup> in ratio 1:1 by applying an open circuit potential with amplitude 5 mV in frequency range 0.01 Hz–10 kHz. EIS analysis was carried out on the modified electrodes to obtain information on the opposition or resistance (impedance) to alternating current of the electrodes. The resistance determines the movement of electrons of the redox probe (ferrocyanide/ferricyanide) at the electrode interface. A three electrode cell with a 3 mm diameter (area 0.07 cm<sup>2</sup>) glassy carbon electrode (GCE) as working electrode, a Ag/AgCl (3 M NaCl, 0.208 V vs. SHE) as the reference electrode and a platinum wire as the counter electrode was used for the analysis.

## 3. RESULTS AND DISCUSSION

### 3.1. Physical Properties of Nanoparticles

#### 3.1.1. Paramagnetic Effect of As Prepared Iron III Oxide ( $\gamma$ -Fe<sub>2</sub>O<sub>3</sub>) and Their XPS Analysis

Figure 1(a) shows the paramagnetic effect of iron III oxide (maghemite) stabilized in TMAOH solution before and after magnetic separation. Figure 1(b) shows the nanoparticles after heating with PEI in the presence and absence of an external magnet. In both cases, the nanoparticles were attracted to the external magnet within 5 minutes and re-disperse in the absence of the magnet.

The XPS spectra were used to determine the composition of the as-prepared iron oxide nanoparticles. The XPS scan shows the core electrons of the atoms present in the

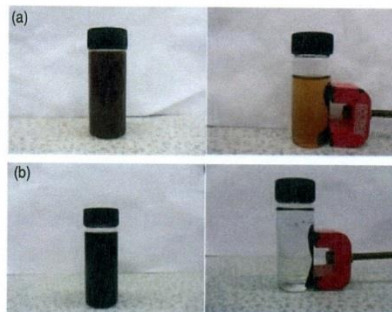


Fig. 1. Fe<sub>2</sub>O<sub>3</sub> nanoparticles stabilized in different solvent before and after 5 minutes magnetic separation (a) TMAOH (b) PEI.

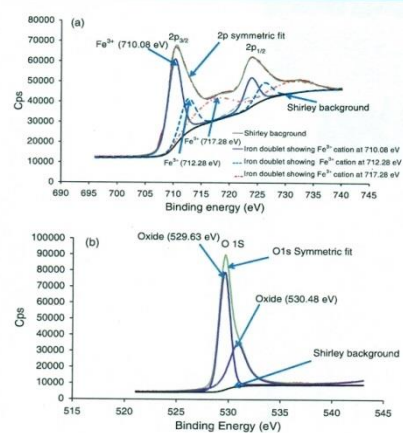


Fig. 2. XPS analysis of  $\text{Fe}_2\text{O}_3$  nanoparticles (a) 2p core electrons (b) 1s core electrons of  $\text{O}_2$ .

samples and their corresponding binding energies which are characteristics of the individual atoms. The core electrons do not participate in bonding (not valence electrons) but exist in orbitals with binding energies that are characteristic of the atoms.

Figure 2(a) shows the characteristic doublet of iron based compounds showing the 2p core electrons for maghemite ( $\gamma\text{-Fe}_2\text{O}_3$ ). The doublets shows peaks indicated by the arrows which can be assigned to iron III cation ( $\text{Fe}^{3+}$ ) at 710.08 eV, 712.28 eV and a characteristic satellite peak at 717.28 eV. These peaks are characteristics of maghemite which contains only iron III oxidation states ( $\gamma\text{-Fe}_2\text{O}_3$ ,  $\text{Fe}^{2+}/\text{Fe}^{3+} = 0$ ).<sup>3</sup> Figure 2(b) shows the XPS spectra for oxygen 1s core electron present in the nanoparticles. The scan shows characteristic oxide peaks at 529.63 eV and 530.48 eV confirming the presence of only oxides in the sample and no hydroxyl species (iron oxy-hydroxide).

### 3.1.2. ESEM, TEM and EDX Analysis of As Prepared Iron III Oxide ( $\gamma\text{-Fe}_2\text{O}_3$ )

The SEM and TEM images of ( $\gamma\text{-Fe}_2\text{O}_3$ ) nanoparticles (NPs) are shown in Figure 3. The SEM image in Figure 3(a) showed the as-prepared  $\gamma\text{-Fe}_2\text{O}_3$  nanoparticles while the TEM in Figure 3(b) indicated that the nanoparticles are cubic in shape with average particle size of 50 nm. The elemental composition from EDX spectra showed that iron and oxygen are the dominant elements in the sample with Fe:O ratio of 46.4%:53.6% atomic.

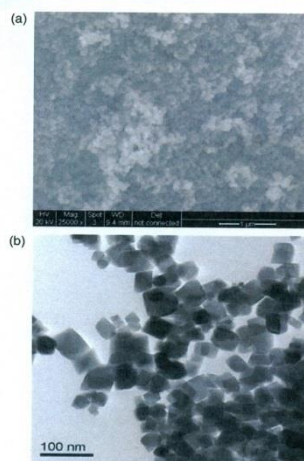


Fig. 3. (a) SEM image of  $\text{Fe}_2\text{O}_3$  nanoparticles (b) TEM image of  $\text{Fe}_2\text{O}_3$  nanoparticles.

### 3.2. Electrochemical Analysis on PEI Adsorption in Iron III Oxide/PEI Nanoparticle Preparation at Various Heating Temperatures

The cyclic voltammetry (CV) can be used to compare the changes on the electrode surface after each modification step with nanoparticles, and its ability to allow the flow of electrons between the redox couple probe and the electrode surface. The result shown in Figure 4(a) is the cyclic voltammogram of the modified electrodes with PEI at different temperatures. The result showed that PEI is well adhered to the surface of  $\gamma\text{-Fe}_2\text{O}_3$  nanoparticles at 40 °C compared to that at 25 °C and heating at 60, 80 and 100 °C for 1 hour. The results showed that PEI heated at 40 °C had the highest oxidation and reduction peaks at 0.3 V and 0.15 V respectively in the cyclic voltammograms followed by 25 °C, 60 °C and the lowest at 100 °C when the solution turned oily. This is an indication that more of the PEI is adhered or adsorbed electrostatically onto the surface of the  $\text{Fe}_2\text{O}_3$  nanoparticles at 40 °C compared to the other temperatures.

The high increase in the oxidation and reduction current of the modified electrode with  $\text{Fe}_2\text{O}_3$ -PEI at 40 °C is due to the presence of more PEI molecules attached to the surface of the iron oxide nanoparticles, which reduces the electron transfer charges between the probe solution and the electrode surface thus, increasing the oxidation and reduction peaks.<sup>17</sup> This result is further verified with the electrochemical impedance spectroscopy (EIS) results

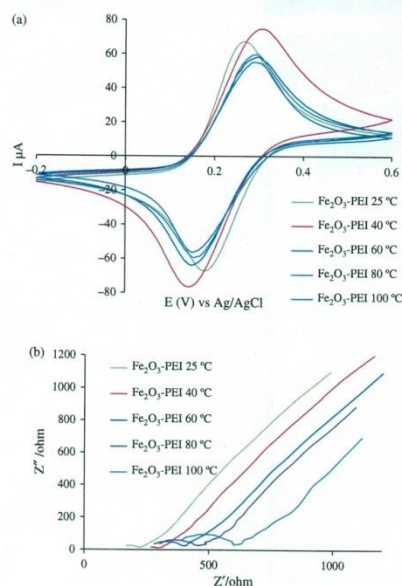


Fig. 4. Electrochemical characterisation of  $\text{Fe}_2\text{O}_3$ -PEI at different temperatures (a) cyclic voltammograms (b) EIS Nyquist plots.

shown in Figure 4(b) demonstrating the ohmic resistance ( $R_s$ ) which includes the ohmic resistance of solution and the coating layer, and the charge transfer resistance ( $R_{ct}$ ). It can be observed that the lowest ohmic resistance was obtained at 25 °C followed by 40 °C which had the lowest charge transfer resistance. The temperatures and their corresponding ohmic and charge transfer resistance are shown in Table I.

The result shows that change in temperatures affects the ohmic resistance and as the heating temperature of PEI on iron oxide nanoparticles increases, the charge transfer resistance increases. This also indicates that the polycationic nature of PEI which neutralizes any negative

Table I.  $\text{Fe}_2\text{O}_3$ -PEI nanoparticles temperatures, ohmic and charge transfer resistance.

$\text{Fe}_2\text{O}_3$ -PEI nanoparticles heating temperatures (°C)	Resistance to charge transfer (Ohm)	Ohmic resistance (Ohm)
25	76	177
40	38	268
60	104	280
80	128	302
100	207	388

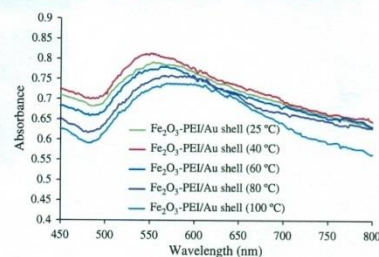


Fig. 5. UV-Vis spectra for  $\text{Fe}_2\text{O}_3$ -PEI/Au shell formation after 5 iteration step at different temperatures.

charge that tends to increase charge transfer resistance diminishes with increasing temperatures on the surface of the iron oxide nanoparticles. A repeat of the experiment was carried out and similar result was obtained with 40 °C showing better PEI adsorption on iron oxide nanoparticles compared to the other temperatures. The reason for this observation might be that 40 °C favoured the electrostatic interaction between positively charged PEI molecule and negatively charged iron oxide nanoparticles.

### 3.3. UV-VIS Spectroscopy Analysis of $\text{Fe}_2\text{O}_3$ -PEI/Au Shell Nanoparticles at the Different Temperatures

The optical properties of the  $\text{Fe}_2\text{O}_3$ -PEI nanoparticles at the different temperatures coated with gold shell was analysed with the aid of UV-Vis spectroscopy and the results shown in Figure 5. The formation of  $\text{Fe}_2\text{O}_3$ -PEI-Au<sub>shell</sub> nanoparticles was achieved after five iterations through the iterative reduction of chloroauric acid with hydroxyl amine.<sup>4,11</sup> The results in Figure 5 shows that after 5 iteration steps for each temperature, the size of gold shell on the surface of the iron oxide nanoparticles increases resulting to a blue shift of the surface plasmon resonance in the UV-Vis spectra. The blue shift indicates an increase in gold shell formation to the iron oxide nanoparticles. The shift in surface plasmon resonance is most observed at 40 °C as the ratio of gold to iron oxide increases with peak wavelength of 548 nm followed by 25 °C (553 nm), 60 °C (562 nm) and the lowest at 100 °C (584 nm). This result indicates the presence of more positively charged PEI ions on the iron oxide nanoparticles at 40 °C that can act as capping agents for gold shell formation.

### 3.4. Effect of Agitation on PEI Adsorption

Comparison was made between stirring iron oxide nanoparticles with PEI at room temperature for 1 hour and the unstirred process at room temperature. It was observed from the cyclic voltammetry results shown in Figure 6(a) that the nanoparticles ( $\text{Fe}_2\text{O}_3$ -PEI) obtained by stirring PEI

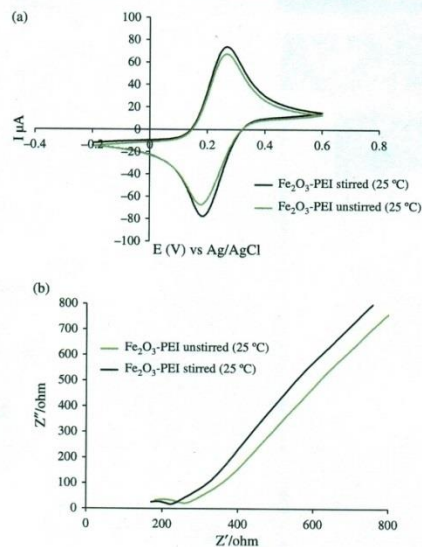


**Fig. 6.** Effects of agitation: on PEI adsorption on  $\text{Fe}_2\text{O}_3$  nanoparticles at room temperatures with and without stirring (a) cyclic voltammograms (b) EIS Nyquist plots.

with iron oxide had the higher oxidation and reduction peaks at 0.25 V and 0.19 V respectively for the redox couple compared to the unstirred process. This result is corroborated with the EIS analysis shown in Figure 6(b) and the results in Table II which showed that the stirred nanoparticles had lower charge transfer resistance compared to the unstirred synthesis. This can be attributed to the stirring process which enables the random mixing of the iron oxide nanoparticles with PEI, resulting in an increased PEI ion attached on the surface of iron oxide nanoparticles due to increased electrostatic attraction between the negatively charged iron oxide and positively charged PEI.

The EIS results (Fig. 6(b)) also showed that the ohmic resistance ( $R_s$ ) is slightly affected at room temperature compared to large variation observed when the particles were heated at increased temperatures as shown in Table I.

**Table II.**  $\text{Fe}_2\text{O}_3$ -PEI nanoparticles at room temperature ohmic and charge transfer resistance.

$\text{Fe}_2\text{O}_3$ -PEI nanoparticles at room Temperatures ( $^{\circ}\text{C}$ )	Resistance to charge transfer (Ohm)	Ohmic resistance (Ohm)
25 (stirred)	44	171
25 (not stirred)	76	177

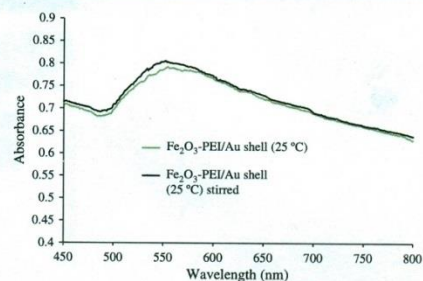


**Fig. 7.** UV-Vis spectra for  $\text{Fe}_2\text{O}_3$ -PEI/Au shell formation after 5 iteration step for stirred and unstirred process at  $25^{\circ}\text{C}$ .

This indicates that PEI synthesized at room temperature and at  $40^{\circ}\text{C}$  had less opposition to the flow of electron of a probe solution due to increased polycationic nature of PEI at this temperatures. Higher heating temperatures results in opposition to flow of electrons as the PEI polycationic nature diminishes. The UV- spectra (Fig. 7) showed that stirred nanoparticles at  $25^{\circ}\text{C}$  had higher absorbance and surface plasmon resonance peak at 550 nm compared to the unstirred nanoparticles 553 nm. This indicates that agitating PEI with iron oxide nanoparticles at room temperature favoured capping capability of the PEI in the attachment of gold shell nanoparticles.

#### 4. CONCLUSIONS

In conclusion it was found out that temperature places a major role in the adsorption of PEI on iron oxide nanoparticles and the ability of PEI to act as capping agents in the formation of gold shell on the iron oxide nanoparticles. The result showed that  $40^{\circ}\text{C}$  is most favourable for PEI adsorption on iron oxide nanoparticles and favours the capping properties of PEI in the formation of iron oxide core/gold shell nanoparticles. The result also indicates that the polycationic nature of PEI on iron oxide nanoparticles diminishes as the heating temperature increases which is reflected on the reduced electrochemical properties observed at  $100^{\circ}\text{C}$  compared to  $40^{\circ}\text{C}$ . Also the ohmic resistance of iron oxide/PEI nanocomposite is affected with increased heating temperatures above  $40^{\circ}\text{C}$ . At room temperature synthesis, the stirred iron oxide/PEI nanoparticles showed better electrochemical properties compared to the unstirred process due to the agitation which encouraged better electrostatic attraction between the negatively charge iron oxide nanoparticles and positively charged PEI ions.

**Acknowledgment:** Orlando Ketebu thanks the Petroleum Technology Development Fund (PTDF) for the scholarship and the authors thank EPSRC Knowledge Transfer Award to support this work.

**References and Notes**

1. A. P. Grosvenor, B. A. Kobe, M. C. Biesinger, and N. S. McIntyre, *Surf. Interface Anal.* 36, 1564 (2004).
2. A. K. Gupta and M. Gupta, *Biomaterials* 26, 3995 (2005).
3. I. Y. Goon, C. Zhang, M. Lim, J. J. Gooding, and R. Amal, *Langmuir* 26, 12247 (2010).
4. J. L. Lyon, D. A. Fleming, M. B. Stone, P. Schiffer, and M. E. Williams, *Nano Lett.* 4, 719 (2004).
5. T. T. Hien Pham, C. Cao, and S. J. Sim, *J. Magn. Magn. Mater.* 320, 2049 (2008).
6. T. K. Jain, J. Richey, M. Strand, D. L. Leslie-Pelecky, C. A. Flask, and V. Labhasetwar, *Biomaterials* 29, 4012 (2008).
7. A. Kaushik, R. Khan, P. R. Solanki, P. Pandey, J. Alam, S. Ahmad, and B. D. Malhotra, *Biosens. Bioelectron.* 24, 676 (2008).
8. S. C. McBain, H. H. P. Yiu, and J. Dobson, *International Journal of Nanomedicine* 3, 169 (2008).
9. K. Li, Y. Lai, W. Zhang, and L. Jin, *Talanta* 84, 607 (2011).
10. X. Zhou, W. Xu, Y. Wang, Q. Kuang, Y. Shi, L. Zhong, and Q. Zhang, *J. Phys. Chem. C* 114, 19607 (2010).
11. I. Y. Goon, L. M. H. Lai, M. Lim, P. Munroe, J. J. Gooding, and R. Amal, *Chem. Mater.* 21, 673 (2009).
12. W. Maketon and K. L. Ogden, *Chemosphere* 75, 206 (2009).
13. X. Wang, L. Zhou, Y. Ma, X. Li, and H. Gu, *Nano Research* 2, 365 (2009).
14. J. Jin, F. Yang, F. Zhang, W. Hu, S.-B. Sun, and J. Ma, *Nanoscale* 4, 733 (2012).
15. H. H. P. Yiu, M. R. Pickard, C. I. Olariu, S. R. Williams, D. M. Chari, and M. J. Rosseinsky, *Pharm. Res.* 29, 1328 (2012).
16. J. M. Qian, A. L. Suo, Y. Yao, and Z. H. Jin, *Clin. Biochem.* 37, 155 (2004).
17. P. Vatsyayan, S. Bordoloi, and P. Goswami, *Biophys. Chem.* 153, 36 (2010).